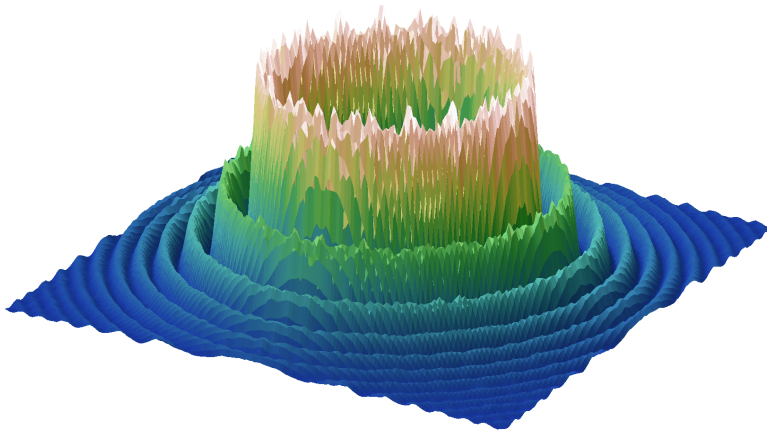




UNIVERSITÄT
BAYREUTH

Non equilibrium fluctuations in polystyrene/toluene mixtures



Daniel Zapf

geboren am 27.06.1990 in Bayreuth

Von der Universität Bayreuth
zur Erlangung des Grades eines
Doktors der Naturwissenschaft (Dr. rer. nat.)
genehmigte Abhandlung

1. Gutachter: Prof. Dr. Werner Köhler
2. Gutachter: Prof. Dr. Lothar Kador

Tag der Einreichung: 23.03.2022

Tag des Kolloquiums: 07.06.2022

Kurzzusammenfassung

Thermische (T-NEFs) und solutale Nichtgleichgewichtsfluktuationen (c-NEFs) in Flüssigkeiten mit aufgeprägten Temperatur- und Konzentrationsgradienten unterscheiden sich von Gleichgewichtsfluktuationen (EFs) grundlegend. Sie werden durch spontane Geschwindigkeitsschwankungen hervorgerufen, welche Volumenpakete und ihre Temperatur- und Konzentrationszustände verschiebt. Diese wirken als starke lokale Störungen, sogenannte Fluktuationen in einem Nichtgleichgewichtszustand oder Nichtgleichgewichtsfluktuationen (NEFs). Sie können auf allen Längenskalen auftreten und wirken langreichweitig mit einem charakteristischen $\sim q^{-4}$ Verhalten, der zugeordneten Amplituden. Wir untersuchen mit einem selbst entwickelten und gebauten Shadowgraphy Setup diese NEFs in binären Polystyrol/Toluol Mischungen, die einem externen Temperaturgradienten ausgesetzt sind. Dieses Messverfahren bietet ebenso eine alternative Detektionsmöglichkeit von wichtigen fluidalen Transportkoeffizienten, ohne dass optische Kontrastfaktoren benötigt werden. Es zeigten sich dabei zunächst von der Literatur abweichende Ergebnisse, die jedoch mit einer komplexen Simulation (der entstehenden Shadowgraphy-Signale) auf unberücksichtigte Nichtlinearitäten in den Gleichungen zurückzuführen waren. Dies ist ein wichtiges Ergebnis für viele ähnliche Experimente, da diese meist ebenfalls nur die lineare Näherung der Diffusionsgleichungen berücksichtigen. Des Weiteren konnten wir im Zuge dieser Arbeit eine alternative Beschreibung der Strukturfunktion aufstellen, die im Fall von Proben mit großer Lewiszahl entscheidende Verbesserungen verspricht.

Abstract

Thermal (T-NEFs) and solutal non equilibrium fluctuations (c-NEFs) in liquids with applied temperature and concentration gradients differ fundamentally from equilibrium fluctuations (EFs). They are caused by spontaneous velocity fluctuations that displace volume elements and their temperature and concentration states. These act as strong local perturbations so-called fluctuations in a non equilibrium state or non equilibrium fluctuations (NEFs). They can occur on all length scales and have a long-range effect due to the characteristic $\sim q^{-4}$ behavior of the associated amplitudes. Using a self developed shadowgraphy setup we have studied these NEFs in binary polystyrene/toluene mixtures exposed to an external temperature gradient. This method offers additionally an alternative way of detecting important fluidic transport coefficients without the need for optical contrast factors. The results initially differed from the literature, but with a complex simulation (of the resulting shadowgraphy signals) they could be attributed to unconsidered non linearities in the diffusion equations. This is an important result for many similar experiments, since these usually only consider the linear approximation. Furthermore, in the course of this work we were able to introduce an alternative description of the structure function, which promises decisive improvements in the case of samples with a large Lewis numbers.

Contents

1	Introduction	1
2	Theory	5
2.1	Brief explanation of equilibrium fluctuations (EFs)	6
2.2	Non equilibrium fluctuations (NEFs)	8
2.3	NEFs in a gravitational field	10
2.4	Fluctuating thermo hydrodynamics	11
2.4.1	Fluctuating variables and the steady state condition	13
2.4.2	Fourier transformation and horizontal projection	15
2.5	Correlation functions of NEFs	19
2.5.1	Equilibrium condition without gravitation (E, g=0)	20
2.5.2	Non equilibrium condition without gravitation (NE, g=0)	21
2.5.3	NEFs due to external gradients and gravity (NE, g)	23
2.6	Mode coupling and structure function	24
3	Experimental	31
3.1	Shadowgraphy setup	32
3.1.1	Light path	33
3.1.2	Soret-cell	35
3.1.3	Camera operation	38
3.2	Sample properties	42
3.2.1	Binary sample composition	42
3.2.2	Viscosity contributions	46
3.3	Image processing	47
3.3.1	Image collection	47
3.3.2	Image processing in real space	49

3.3.3	Image processing in Fourier space	52
3.3.4	Processing of the structure function	54
4	Results and discussions	59
4.1	Evaluation system	60
4.1.1	Application	65
4.2	Simulation of non linearities in NEFs	67
4.2.1	Thermophysical parameters	69
4.2.2	Temperature and concentration cell profiles	74
4.2.3	Simulated relaxation and amplitude signals	77
4.2.4	Evaluation of the simulated data	83
4.2.5	Comparison of simulated and experimental data	87
4.2.6	Application to the results of 4.1	93
4.2.7	Simulation with temperature independent coefficients	93
4.3	NEF static structure factor $S(q)$ analysis	101
4.3.1	Temperature dependence	103
4.3.2	Concentration and molar dependence	108
4.4	Transport coefficient analysis	119
4.4.1	Temperature dependence	121
4.4.2	Concentration and molar mass dependence	128
5	Summary and outlook	139
6	Appendix	143
6.1	Structure function comparison with literature	143
6.2	Sealing of the inner cell	144
6.3	Alignment of the Soret-cell	145
6.4	Alignment of the camera mirror	146
6.5	Camera telescope control	147
6.6	Pixel illustration of the normalization steps	148
6.7	Normalized A^c , q_{ro}^c illustrations	149
6.8	TDFRS measured simulation data	151
6.9	List of transport coefficients	152

Bibliography	163
7 List of publications	173

1 Introduction

In 1991, an article with the fitting title: 'What interests physicist today in fluids?'^[1] (original german title: 'Was interessiert den Physiker heute an Fluiden?') was published. The author mentions that recently simple and complex fluids and their physical behaviors have rapidly grown in interest. Further he explicitly emphasizes non equilibrium phenomena under the influence of external fields. In addition to this rheological research field, all kinds of non linear processes are a young topic as well, which often impresses with analytically unsolvable equations, solutions that differ substantially from the linear ones and sometimes even contain instabilities. A fundamental physical principle that unites various of these topics is the analysis of the smallest possible system deviations as a basis for the description. All these themes: complex fluids, non equilibrium, non linear and small variations, are combined in our topic of thermodynamic non equilibrium fluctuations in complex mixtures.

These non equilibrium fluctuations (NEFs) are fundamentally different from equilibrium fluctuations (EF). They are caused by random velocity fluctuations in stationary temperature and concentration fields. These displaced volumes carry their initial temperature and concentration states and act as strong thermal (T-NEFs) and solutal fluctuations (c-NEFs) in the shifted environments. In contrast to EFs, they appear long ranged and with a characteristic amplitude increase proportional to $\sim q^{-4}$ as the wavevector q becomes smaller. The size of the fluctuation is in micro gravity only limited by the container and the resulting finite-size effects^[2]. Under gravitational conditions, further sedimentation and buoyancy effects limit the amplitude growth^[3]. As the method of choice for the research of NEFs and as a measuring tool for the transport coefficients the shadowgraphy technique evolved^[4,5,6,7,8,9]. The basis was prepared by two projects: the 'gradient-driven fluctuations experiment' (GRADFLEX) project of the European Space Agency

(ESA), in which simple, binary, benign systems were examined under micro gravity conditions, and the 'diffusion and thermodiffusion Coefficients Measurements in ternary mIXtures' (DCMIX) project, where first microgravity experiments on ternary mixtures and complex fluids were performed. This resulted in a linear description of the NEFs in the steady state and a fundamental understanding of multi component mixtures under micro gravity. Subsequently, in cooperation with ESA and the German Aerospace Center (DLR), the GIANT-FLUCTUATIONS, formerly called 'Non-EqUilibrium Fluctuation: DIffusion in compleX liquids' (NEUF-DIX), project was created, in which this thesis is embedded. The project includes many different topics of the participating research groups. For example, complex solutions in non-ideal conditions, such as strongly asymmetric ternary polymer solutions near the glass temperature (our topic) or the investigation of the Casimir effect in liquids due to colloidal particles. Follow-up projects are already in progress, such as the CORA-MAP project 'Technologies for Non-Equilibrium Systems' (TechNES), which aims at the development of technologies that enable the investigation of NEFs in complex systems.

For an easier understanding of the micro gravity experiments and for ground-based reference measurements, we constructed and established a completely new two-color shadowgraphy setup, inspired by one of the existing ones of our partner groups in Anglet and Milan. The Soret-cell, a liquid container, which allows the application of external temperature and concentration gradients, was totally redesigned and own built in the machine shop of the University of Bayreuth. Thereby special attention was paid to reliably uniform and strong temperature differences. In addition, the image evaluation script, optimized for our needs, was entirely new and self-programmed. Furthermore, the analysis scripts for the resulting structure functions were created, which provides next to the NEF-nature, the included transport coefficients.

The first 'theory' and second 'experimental' chapters introduce the essential thermo hydrodynamic equation basis of the NEFs in a steady state condition and the complete experimental background for the understanding of the measurements. Already during the first measurements of known polymer solutions, deviations in

the resulting transport coefficients and literature benchmarks were found. This leads to a simulation campaign of the signals in our shadowgraphy setup, which specifically targets the non linearity of the underlying diffusion equation and which is the most important achievement of the result chapter. Due to the relatively strong temperature differences (≈ 50 K) in the case of the shadowgraphy, in contrast to 'thermal diffusion forced Rayleigh scattering' (TDFRS, few mK)^[10,11,12], 'optical beam deflection' (OBD, ≈ 1 K)^[10,13,14,15] and 'optical digital interferometry' (ODI, ≈ 5 K), we have found that the non linearity of the diffusion equation cannot be neglected. Usually, due to the small temperature differences, only the linear diffusion equation is used and it is additionally assumed that the resulting transport quantities belong to the average concentrations and temperature. The simulation is based on thermophysical descriptions of all participating transport variables and generates the temperature and concentration distributions inside the cell. With these we calculated the resulting structure function signals. The outcomes were then ultimately compared and confirmed with real measurements. In addition to the simulations, another innovation is a new evaluation approach for the structure functions, which is also presented in the results chapter. Finally, all experimental and simulated transport coefficients are compared with the literature values and the differences are explained.

2 Theory

The first three of the six theory sections are intended to provide an easy access to non equilibrium fluctuations. The connection with the experimental light scattering method is also briefly demonstrated. The first [section 2.1](#) introduces equilibrium fluctuation with Brownian particle motion. The second one [2.2](#) demonstrates the actual non equilibrium state and defines non equilibrium fluctuations (NEFs). The last of these sections expands the observation to include gravitational effects. These three sections [2.1-2.3](#) can easily be skipped, if the reader already is familiar with NEFs, their formation and detection.

Subsequently to these preparation sections, the underlying thermo hydrodynamic equations are introduced in [section 2.4](#) and considered in a fluctuating steady state condition. The required functions of the visible refractive index correlations are calculated with the thermo hydrodynamic equations in [section 2.5](#). Finally, [section 2.6](#) shows the interaction of the established structure function modes in different constellations (equilibrium and non equilibrium, with and without gravity), which arise from the correlation equations.

2.1 Brief explanation of equilibrium fluctuations (EFs)

An easy and simple explanation for fluctuations in an equilibrium system, which we want to call: equilibrium fluctuations (EFs), is offered by random Brownian motion^[16] of evenly distributed particles (blue dots in [fig. 2.1](#)).

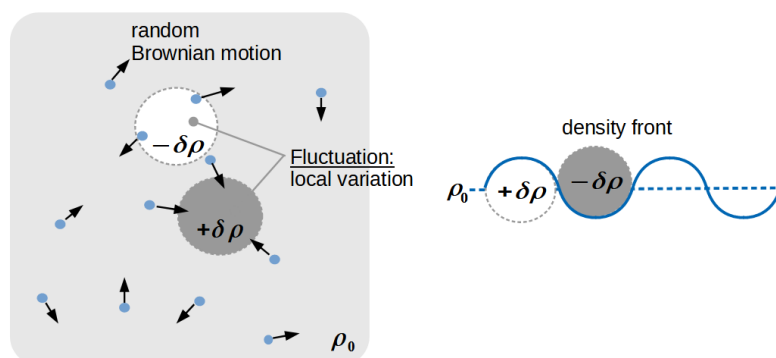


[Fig. 2.1](#): LEFT: Schematic illustration of density fluctuations (local volumes which deviate from the average density ρ_0) in an equilibrium state, resulting from random Brownian motions of solved particles (blue dots). RIGHT: Locally arranged fluctuations ($\pm\delta\rho$) of the left panel, which form a associated density wave front (blue line).

These movements result in local density variations ($\rho_{loc} \neq \rho_0$, where ρ_0 is the average density and ρ_{loc} is the density in a certain volume) and are called fluctuations, or in this case more specific, density fluctuations

$$\delta\rho = \rho_{loc} - \rho_0 . \quad (2.1)$$

The amplitude (strength) of these EFs is very small (vs. the non equilibrium fluctuations of [section 2.2](#)) and can be described by a statistical distribution^[17]¹. In doing so, for every increasing fluctuation ($+\delta\rho$) an equally strong decreasing fluctuation ($-\delta\rho$) can be assigned. The local density front ρ_{loc} can now be calculated with these rearranged fluctuations as:

$$\rho_{loc} = \rho_0 + \delta\rho \cdot \sin(kx) , \quad (2.2)$$

¹Know from salt fingers (instability) effects and the start from Rayleigh-Bernard convection.

where $\delta\rho$ represents the amplitude of the fluctuation and the associated parameter kx (k wavevector)^[18] describes the spatial expansion of the fluctuation (blue line). The illustration of [fig. 2.2](#) shows the diffusive relaxation process of a certain

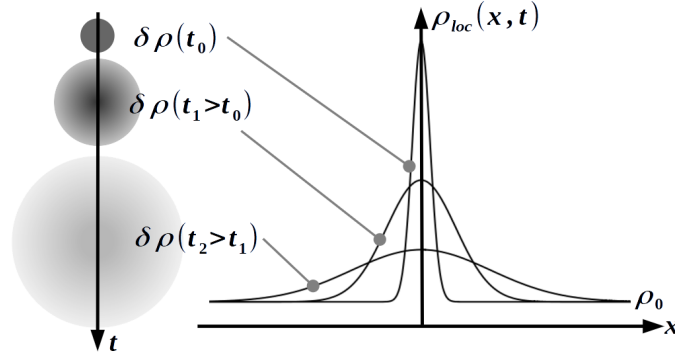


[Fig. 2.2](#): Diffusive relaxation of equilibrium fluctuations $\delta\rho$, starting at the time t_0 . On the left in the illustration style of [fig. 2.1](#), on the right as the Gaussian-bell function, both decreases over time.

density fluctuation $\delta\rho(t_0)$ over time and is an alternative imagination model of the diffuse relaxation. The left side demonstrates the growth of the fluctuation with simultaneous intensity decreasing (starting from the border). The right side illustrates how these steps spread out over time and how they creep back into the average density ρ_0 . This process can be calculated by a Gaussian-bell function^[19] (normal distribution), where at all times the area under the function has the same value.

Light scattering connection

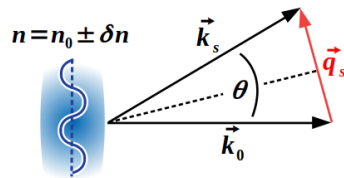


[Fig. 2.3](#): Scattering illustration, where the scattering vector \vec{q}_s , the two wavevectors k_i ($i = 0, s$) and the associated angle θ are shown as functions of n . The oscillating refractive index front n is shown in the medium (blue line) and originates from [eq. 2.2](#).

Due to these density fluctuations, the local refractive index $n = c_0/c_m$ (c_0 speed of light in vacuum, c_m speed of light in medium) also fluctuates proportionally². The scattering arises due to the differences in the speed of light in different media compositions of the corresponding refractive index wave front $n = n_0 \pm \delta\rho$ (fig. 2.3). The connected local differences of these refractive index fluctuations δn leading to different light scattering amplitudes. The scattering vector^[21]

$$q_s = 2n \frac{2\pi}{\lambda} \sin\left(\frac{\theta}{2}\right) \quad (2.3)$$

is described as a function of the local refractive index n , the wavelength of the detection light λ and the resulting scattering angle θ . More details about the scattering is given in chapter 3, where the experiment will be introduced. The important aspect, which should be highlighted, is the experimental access to the thermodynamic transport properties (e.g. diffusion) due to the connection of the density and the refractive index fluctuations, which can be measured by light scattering.

2.2 Non equilibrium fluctuations (NEFs)

To explain non equilibrium fluctuations we start with the establishment of the non equilibrium state, which includes a constant density gradient $\vec{\nabla}\rho$. Experimentally the density gradient (gray arrow in fig. 2.4) is established by an external temperature gradient $\vec{\nabla}T$ (reddish arrow) and a concentration gradient $\vec{\nabla}c$ (bluish arrow) in the opposite direction, which is formed due to the Soret-effect^[22]:

$$\vec{\nabla}c = -S_T c(1-c) \vec{\nabla}T . \quad (2.4)$$

It is a migration effect of molecules in temperature fields for which there is still no microscopic description. Eq. 2.4 contains therefore the concentration c of the denser component and the associated Soret coefficient S_T . After a certain amount of time the system is in the steady state (a quasi equilibrium condition), where

²Described by a Lorentz-Lorenz-approach^[20] or similar functions.

the two opposite gradients and the connected Fickian $\vec{\nabla}j_{\rho,c}$ and Soret mass flows $\vec{\nabla}j_{\rho,T}$ are canceling each other out. The result is a density gradient $\vec{\nabla}\rho$, which is shown in [fig. 2.4](#). In the following sections more to this will follow, here just a small introduction.

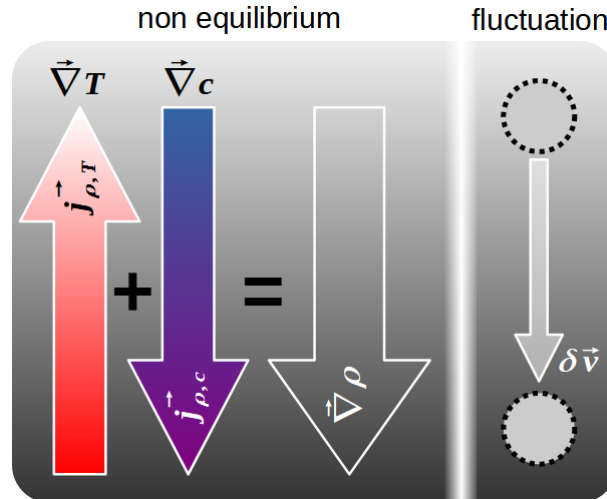


[Fig. 2.4](#): Illustration of a non equilibrium system state with a density gradient $\vec{\nabla}\rho$. This gradient is formed by the temperature $\vec{\nabla}T$, the concentration gradient $\vec{\nabla}c$ and the associated mass flows $j_{\rho,i}$. Furthermore we can see a displacement of a certain volume due to velocity fluctuations $\delta\vec{v}$, the non equilibrium fluctuations.

Now we want to explain non equilibrium fluctuations. But we don't want to consider the very small random Brownian fluctuations of [section 2.1](#) any more. The much larger effects are local fluctuations of the temperature and concentration due to displacements in their respective gradient fields. These displacements result from velocity fluctuations $\delta\vec{v}$, which can push certain volumes (portions) in to regions, where they act as strong local disturbances. This is illustrated in the right part of [fig. 2.4](#). These temperature δT and concentration fluctuations δc , which are generated by velocity fluctuations $\delta\vec{v}$, are called non equilibrium fluctuations (or short: NEFs).

2.3 NEFs in a gravitational field

The last important external effect which we need to introduce in our fluctuation image is gravity. Due to the explained density differences of NEFs, they are influenced by gravity and experience buoyancy and sedimentation effects^[23]. This additional force and the associated acceleration also affects the system dynamics.

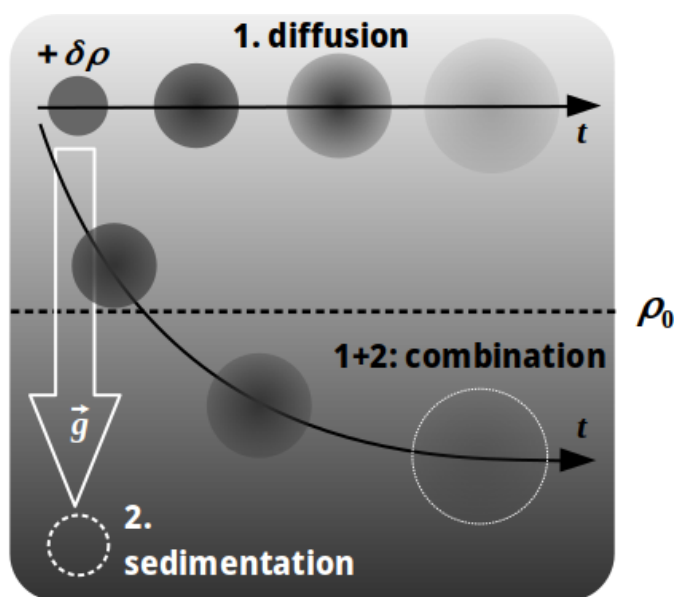


Fig. 2.5: Representation of the temporal relaxation of a density fluctuation ($\delta\rho(t)$) in a non equilibrium state with gravity (\vec{g}). The sedimentation of the volume (step 2) and the diffusive relaxation (step 1) of fluctuation form the transport and relaxation processes.

The illustration of [fig. 2.5](#) deals with the two relaxation processes. Labeled with 'step 1. diffusion' is the relaxation due to diffusion into the outer regions. It is basically the same process as the one demonstrated in [fig. 2.2](#). In addition, such a fluctuation with an increased local density $\delta\rho$ sediments in a gravitational field \vec{g} , which causes the volume to sink simultaneously ('step 2. sedimentation'). In all of our experiments a combination of both effects appears, which is demonstrated with '1+2: combination'.

For the sake of completeness, it must be mentioned that convection effects and the reflection of very large fluctuations at the cell boundaries (finite-size effects^[24]) can

also occur. These effects arise only in the case of small q values and under certain circumstances.

2.4 Fluctuating thermo hydrodynamics

Now that we have a picture of what NEFs are, we establish the corresponding theoretical equations. As the name of the section already suggests, the thermo hydrodynamics serves as the basis for the description. We already know that the refractive index fluctuations

$$\delta n(\vec{x}, t) = \left. \frac{\partial n}{\partial T} \right|_{p,c} \delta T(\vec{x}, t) + \left. \frac{\partial n}{\partial c} \right|_{p,T} \delta c(\vec{x}, t) \quad (2.5)$$

are the relevant quantities, because they are accessible with light scattering experiments. This derivation follows the calculations of *Law and Nieuwoudt*^[25] and will focus on the NEF with neglected gravitational impact (for the moment). In [eq. 2.5](#) the pressure p is a constant value in space \vec{x} and time t and the $\partial n/\partial i$ -terms, with $i = T$ for temperature and $i = c$ for concentration, are called optical contrast factors. The shown functional expression of the refractive index fluctuation δn is dependent on the thermal $\delta T(\vec{x}, t)$ and solutal NEFs $\delta c(\vec{x}, t)$. These quantities will be derived in this first theoretical section.

The basis of the thermo hydrodynamics description form the necessary conservation equations³ of the heat (temperature T), concentration c and velocity \vec{v} . These are the continuity equation (mass conservation)^[26]

$$\overbrace{\frac{\partial c}{\partial t} + \vec{v} \cdot \vec{\nabla} c + c \nabla \cdot \vec{v}}^{\substack{= \frac{dc}{dt} \\ = \nabla \cdot (c\vec{v})}} = \frac{-1}{\rho} \nabla \cdot \vec{j}_\rho, \quad (2.6)$$

³A conserved quantity does not change in certain physical processes.

the momentum conservation equation (Navier-Stokes equation)^[27]

$$\overbrace{\frac{\partial \vec{v}}{\partial t} + (\vec{v} \cdot \vec{\nabla}) \vec{v}}^{=\frac{d\vec{v}}{dt}} = \frac{-1}{\rho} \overbrace{\left[\vec{\nabla} p - \eta \nabla^2 \vec{v} - \left(\xi + \frac{\eta}{3} \right) \vec{\nabla} (\nabla \cdot \vec{v}) \right]}^{=\nabla \cdot \vec{j}_v} \quad (2.7)$$

and the entropy balance equation^[28]

$$\overbrace{\frac{\partial s}{\partial t} + \nabla \cdot (s\vec{v})}^{=\frac{ds}{dt}} = \frac{-1}{\rho} \frac{1}{T} \overbrace{\left(-\kappa \nabla^2 T + \vec{j}_\rho \cdot \vec{\nabla} \mu \right)}^{=\nabla \cdot \vec{j}_s - \sigma} . \quad (2.8)$$

This entropy equation follows from the second law of thermodynamics^[29] and includes the entropy production term σ . This is the reason, why it is called a balance equation. The included parameters are, ρ the density, η the dynamic viscosity, ξ the bulk viscosity, s the entropy density, κ the thermal conductivity and μ the chemical potential. All these quantities refer to the denser of the two components, which in our case will be the polymer.

For a further description of the three conservation equations we especially need the density $\rho(c, T)$, the chemical potential $\mu(c, T)$ ^[30] and the entropy density $s(c, T)$ as functions of concentration c and temperature T . Additionally the associated thermal Soret mass flow^[22] with the thermodiffusion coefficient D_T and the solutal Fickian mass flow^[31] with the related diffusion coefficient D must be considered in [eq. 2.6](#).

$$\vec{j}_\rho = -\rho \left(\underbrace{D \vec{\nabla} c}_{\text{Fickian}} + \underbrace{D_T c [1 - c] \vec{\nabla} T}_{\text{Soret}} \right) \quad (2.9)$$

In many cases it is helpful to replace the thermodiffusion coefficient with the Soret coefficient S_T or the thermodiffusion ratio k_T . Both will be very important in this thesis, especially in the result [chapter 4](#).

$$S_T = \frac{D_T}{D} \quad \rightarrow \quad \vec{j}_\rho = -\rho D \left(\vec{\nabla} c + S_T c [1 - c] \vec{\nabla} T \right) \quad (2.10)$$

$$k_T = T S_T c (1 - c) \quad \rightarrow \quad \vec{j}_\rho = -\rho D \left(\vec{\nabla} c + \frac{k_T}{T} \vec{\nabla} T \right) \quad (2.11)$$

The term \vec{j}_v is the momentum flux density^[32] and is used in the Navier-Stokes equation (NSE) 2.7. We use this equation, which has not yet been mathematically proven⁴, in the solvable, weak, slow-moving form, where we know from *Evans*^[33] that a solution exists. Similar to the mass flow of eq. 2.6 and the momentum flux density in eq. 2.7 the entropy balance equation 2.8 contains the entropy flow

$$\vec{j}_s = \frac{1}{T} (\vec{q} - \mu \vec{j}_\rho) \quad (2.12)$$

as well as the mentioned entropy production

$$\sigma = -\frac{1}{T^2} \vec{q} \cdot \vec{\nabla} T - \frac{1}{T} \vec{j}_\rho \cdot \vec{\nabla} \mu . \quad (2.13)$$

These follow from the Gibbs fundamental relationship^[34]

$$ds = \frac{1}{T} (dq - \mu dc) \quad (2.14)$$

and the heat conduction equation^{[35]5}

$$\frac{dq}{dt} = \frac{-T}{\rho T} \nabla \cdot \vec{q} , \text{ with: } \vec{q} = -\kappa \vec{\nabla} T + \mu \vec{j}_\rho . \quad (2.15)$$

This can be especially well seen in the Phd-thesis of *Hartung*^[36]. All required variables, their functional temperature and concentration dependencies and the conservation laws have now been introduced.

2.4.1 Fluctuating variables and the steady state condition

Next we want to bring the fluctuations of the three important variables temperature ($i = T$), concentration ($i = c$) and velocity ($i = \vec{v}$) into the conservation equations 2.6-2.8:

$$i = i_0 + \delta i . \quad (2.16)$$

⁴It is not proven that solutions always exist in 3D.

⁵Here \vec{q} is the heat flow, but only in this short explanation of eq. 2.8. In the following not to be mixed up with \mathbf{q} , the wave vector.

For this purpose, the variables are replaced by a sum of the average value i_0 and a fluctuation δi . If we do so, we formally also have to include corresponding spontaneous initiation forces of these fluctuations^[37], where \vec{F}_c describes the force of the concentration fluctuations, \vec{F}_v that of the velocity fluctuations and \vec{F}_T that of the temperature fluctuations.

$$\text{in eq. 2.6: } + \rho \nabla \cdot \vec{F}_c \quad (2.17)$$

$$\text{in eq. 2.7: } + \rho \nabla \cdot \vec{F}_v \quad (2.18)$$

$$\text{in eq. 2.8: } + \nabla \cdot \vec{F}_T - \rho T \left. \frac{\partial \mu}{\partial T} \right|_{p,c} \nabla \cdot \vec{F}_c \quad (2.19)$$

Theoretically, the thermodynamic equations only apply in case of equilibrium states. Therefore we only consider the simplified steady state condition^[38], where we can assume local equilibria and no global mass flows ($\vec{j}_0 = 0$), because the Soret $j_{\rho,T}^{\vec{}}$ and the Fickian mass flow $j_{\rho,c}^{\vec{}}$ of eq. 2.9 balance each other out.

$$\vec{j}_0 = 0 \leftrightarrow \vec{v}_0 = 0 \Rightarrow j_{\rho,T}^{\vec{}} = -j_{\rho,c}^{\vec{}} \quad (2.20)$$

The equations 2.21-2.23 arise, if the in eq. 2.16 described fluctuations and if the steady state condition of eq. 2.20 are used in the conservation equations 2.6-2.8.

$$\overbrace{\frac{\partial(c_0 + \delta c)}{\partial t}}^{= \frac{\partial \delta c}{\partial t}} + \delta \vec{v} \cdot \vec{\nabla} c + \overbrace{(c_0 + \delta c)}^{\approx c_0} \nabla \cdot \delta \vec{v} = \underbrace{\frac{-1}{\rho_0 + \delta \rho}}_{\approx \rho_0} \nabla \cdot \overbrace{((\rho_0 + \delta \rho) \delta \vec{v})}^{\approx \rho_0 \delta \vec{v}} + \rho_0 \nabla \cdot \vec{F}_c \quad (2.21)$$

$$\frac{\partial \delta \vec{v}}{\partial t} + \overbrace{(\delta \vec{v} \cdot \vec{\nabla})}^{\sim \delta v^2 \ll 1} \delta \vec{v} = \underbrace{\frac{-1}{\rho_0 + \delta \rho}}_{\approx \rho_0} \left[\vec{\nabla} p - \eta \nabla^2 \delta \vec{v} - \left(\xi + \frac{\eta}{3} \right) \underbrace{\vec{\nabla} (\nabla \cdot \delta \vec{v})}_{\ll 1} \right] + \rho_0 \nabla \cdot \vec{F}_v \quad (2.22)$$

$$\begin{aligned}
 & \overbrace{\frac{\partial(s_0 + \delta s)}{\partial t}}^{=\frac{\partial \delta s}{\partial t}} + \nabla \cdot \overbrace{\left((s_0 + \delta s) \vec{\delta v} \right)}{\approx s_0 \vec{\delta v}} = \\
 & = \underbrace{\frac{-1}{\rho_0 + \delta \rho}}_{\approx \rho_0} \underbrace{\frac{1}{T_0 + \delta T}}_{\approx T_0} \left(-\kappa \nabla^2 T + \delta \vec{j}_\rho \cdot \vec{\nabla} \mu \right) + \nabla \cdot \vec{F}_T - \rho_0 T_0 \left. \frac{\partial \mu}{\partial T} \right|_{p,c} \nabla \cdot \vec{F}_c
 \end{aligned} \tag{2.23}$$

Additionally, we use the assumptions, that the fluctuations are small against the average value (e.g. $\rho_0 + \delta \rho \approx \rho_0$) and that these average values are time independent (e.g. $\partial c_0 / \partial t = 0$). This follows directly from *Vailati and Giglio*^[39].

2.4.2 Fourier transformation and horizontal projection

A mathematically easier accessible approach to solve the three differential equations 2.21-2.23 is to consider them in Fourier space. A typical Fourier transformation

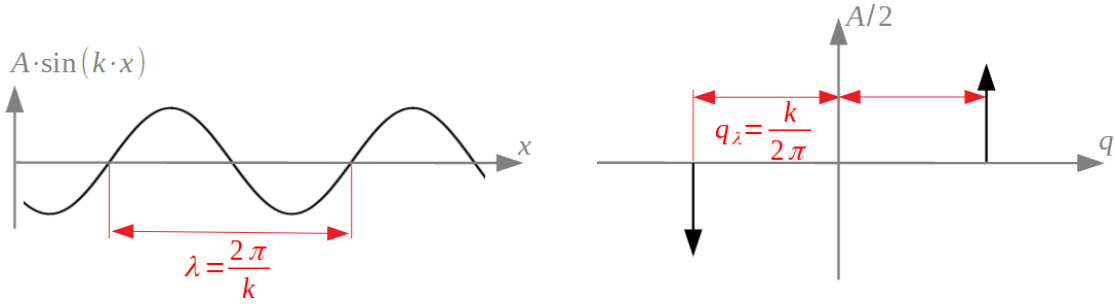


Fig. 2.6: LEFT: Typical representation of a Fourier transformation of a real space sine wave function with a wave length of $\lambda = \frac{2\pi}{k}$ (wavevector k). RIGHT: It transforms into two peaks in the frequency domain with q -value of the inverse wave length: $q_\lambda = 1/\lambda$.

\mathcal{F} ^[40] is shown mathematically in eq. 2.24, where the variable $z(\vec{x}, t) \rightarrow z(\vec{q}, \omega)$ transforms from real (depending of \vec{x}, t) to Fourier space (\vec{q}, ω).

$$z(\vec{q}, \omega) = \mathcal{F} \{ z(\vec{x}, t) \} = \frac{2}{\sqrt{2\pi}} \iint dx dt \cdot z(x, t) \cdot \exp(-i(qx + \omega t)) \tag{2.24}$$

The for our understanding important transformation of a fluctuating wave front, which was introduced in section 2.1, is shown in fig. 2.6. Therefore all variables and parameters of the fluctuating conservation equations 2.21-2.23 need to be Fourier

transformed. An easy transformation operation can be formulated from eq. 2.24, which concludes in the two following variables.

$$\begin{aligned} \text{temporal frequency } \omega : \mathcal{F} \left\{ \frac{\partial}{\partial t} z(\vec{x}, t) \right\} &\rightarrow i\omega z(\vec{q}, \omega) \\ \text{spatial frequency } \vec{q} : \mathcal{F} \{ \nabla \cdot \vec{z}(\vec{x}, t) \} &\rightarrow -i\vec{q}z(\vec{q}, \omega) \end{aligned}$$

Additionally, the initiation forces appear in Fourier space with the same but now lower-case letters (e.g. $\vec{f}_i = \mathcal{F}\{\vec{F}_i\}$).

Horizontal projection

The established model of the density front (fig. 2.7) with the oscillations parallel to the light direction \vec{e}_k defines in perpendicular direction the spatial fluctuation

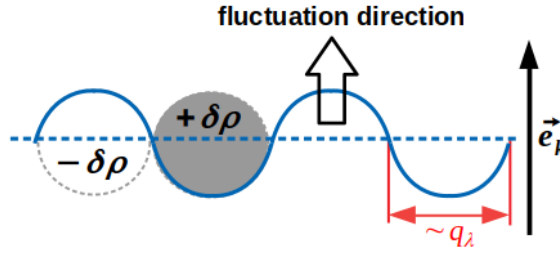


Fig. 2.7: Well-known representation of the density wave front from fig. 2.1, where the fluctuation direction is parallel to the light direction (\vec{e}_k) and the spatial extension is observed in the perpendicular direction (\parallel scattering vector q_λ).

size (half of the wave length). Which means, the oscillation wavevector and the connected variable q_λ is the necessary information of the NEFs (size). Therefore we investigate only in the projection of the fluctuation on to the q -direction ($\perp \vec{g}$), whereby many (unimportant) terms of eq. 2.21-2.23 disappear due to the scalar products:

$$\vec{q} \cdot (\delta\vec{v}, \vec{\nabla}\rho, \vec{\nabla}T, \vec{\nabla}c) \stackrel{\perp}{=} 0 . \quad (2.25)$$

The in eqs. 2.26-2.28 shown three coupled differential equations result from the Fourier transformation of the fluctuating conservation equations 2.21-2.23 and the

simultaneous projection in q -direction.

$$\text{eq. 2.22} \Rightarrow (i\omega + q^2 \nu) \delta \vec{v}_{q,\omega} = -i \frac{\vec{q} \cdot \vec{f}_v}{\rho_0} \quad (2.26)$$

$$\text{eq. 2.21} \Rightarrow (i\omega + q^2 D) \delta c_{q,\omega} = -q^2 \cdot D \frac{k_T}{T_0} \delta T_{q,\omega} - \delta \vec{v}_{q,\omega} \cdot \vec{\nabla} c - \vec{q} \cdot \vec{f}_c \quad (2.27)$$

$$\begin{aligned} \text{eq. 2.23} \Rightarrow (i\omega + q^2 D_{th}) \delta T_{q,\omega} &= \frac{-1}{\rho_0} \delta \vec{v}_{q,\omega} (\vec{\nabla} T - \hat{T} \vec{\nabla} c) + i\omega \hat{T} \delta c_{q,\omega} - \\ &- i \vec{q} \cdot \left(\frac{\vec{f}_T}{\rho_0 C_p} - \hat{T} \vec{f}_c \right) \end{aligned} \quad (2.28)$$

In these equations, which can again be found in [39], the kinematic viscosity $\nu = \eta/\rho$ and the thermal diffusivity D_{th} arise. The solutal terms of the entropy equation 2.28 contain a temperature-like coefficient: $\hat{T} := \frac{k_T}{C_p} \frac{\partial \mu}{\partial c} \Big|_{p,T}$, which results from the Onsager relations, where $D \sim L_{\rho\rho} \frac{\partial \mu}{\partial c} \Big|_{p,T}$.

Note

The Onsager coefficients^[41] L_{lk} arise when the considered flows of the conservation equations (cf. eq. 2.9 and eq. 2.12) are rewritten as generalized flows \vec{j}_l (with $l = \rho$ (mass), q (heat)) and they are thus determined from a generalized force $\vec{\chi}_l$:

$$\vec{j}_l = \sum_{k=\rho,q} L_{lk} \vec{\chi}_k. \quad (2.29)$$

The sum in eq. 2.29 derives from the direct transport coefficients (with the same indices) and the cross-connected transport coefficients (different indices). Direct means, for example: mass flow through a concentration gradient and diffusion D as the related transport variable. Cross connected means for example Soret-flow, a mass flow (index 1: ρ) driven by temperature effects (index 2: q) with the thermodiffusion coefficient $D_T \sim L_{\rho q}$ as the variable.

Back to the fluctuating and projected conservation equations of eqs. 2.26-2.28 in Fourier space. The right side of eq. 2.26 shows that the considered velocity fluctuations $\delta \vec{v}_{q,\omega}$ ($\vec{q} \perp \vec{e}_k$) arise directly from the spontaneous fluctuation forces \vec{f}_v and relaxes (in this simplified model) completely independently from the other

	index 2: ρ	index 2: q
index 1: ρ	$L_{\rho\rho} = D \left. \frac{\partial \mu}{\partial c} \right ^{-1} \rho_0 T_0 c_2$	$L_{\rho q} = D_T \rho_0 c_1 c_2 T_0^2$
index 1: q	$L_{q\rho} = D_D \rho_0 c_1 c_2 T_0^2$	$L_{qq} = \kappa T_0^2$

Tab. 2.1: Representation of the functional dependencies of the thermodynamic coefficients and the Onsager coefficients (L). The Duffour coefficient is negligible for liquids (gray one).

fluctuations with the mode

$$i\omega + \nu q^2 \quad \rightarrow \quad \tau_v = 1/(\nu q^2) \quad (2.30)$$

and the corresponding viscous relaxation time $\tau_v(q)$. As indicated describes the left side of these equations the relaxation mode, which transforms in time to the associated relaxation times τ_i . The remaining two coupled differential equations 2.27 and 2.28 can be shown as a matrix and have a similar structure.

$$\begin{aligned} & \begin{bmatrix} q^2 \cdot D_T c_1 c_2 & i\omega + q^2 \cdot D \\ i\omega + q^2 \cdot D_{th} & -i\omega \hat{T} \end{bmatrix} \begin{bmatrix} \delta T_{q,\omega} \\ \delta c_{q,\omega} \end{bmatrix} = \\ & = -\delta \vec{v}_{q,\omega} \cdot \underbrace{\begin{bmatrix} \vec{\nabla} c \\ \frac{1}{\rho_0} (\vec{\nabla} T - \hat{T} \vec{\nabla} c) \end{bmatrix}}_{\text{external gradients}} + \underbrace{\begin{bmatrix} -\vec{q} \cdot \vec{f}_c \\ i\vec{q} \cdot \left(\hat{T} \vec{f}_c - \frac{\vec{f}_T}{\rho_0 C_p} \right) \end{bmatrix}}_{\text{initiation forces}} \end{aligned} \quad (2.31)$$

If we look for example, at the concentration fluctuation δc in eq. 2.32, which is the matrix-vector multiplication of the upper row, we can see the conceptual structure of these fluctuation terms.

$$\delta c_{q,\omega} = \underbrace{(i\omega + q^2 D)^{-1}}_{\text{relax. mode}} \left[\underbrace{\delta \vec{v}_{q,\omega} \cdot \vec{\nabla} c}_{\text{direct source}} - \underbrace{q^2 D_T c c' \delta T_{q,\omega}}_{\text{cross connection}} - \underbrace{\vec{q} \cdot \vec{f}_c}_{\text{initial force term}} \right] \quad (2.32)$$

Comparing eq. 2.32 with the easier to understand eq. 2.30 of the viscosity fluctuation $\delta \vec{v}$, we understand, that the term '0' is the solutal relaxation mode.

$$i\omega + Dq^2 \quad \rightarrow \quad \tau_c = (q^2 D)^{-1} \quad (2.33)$$

The terms in the square brackets are the various possible causes of c-NEFs (δc). The most important of these fluctuation sources is term 'I', which describes the displacement of a local concentration in the concentration field $\vec{\nabla}c$ due to the velocity fluctuation $\delta\vec{v}$. Analogous to eq. 2.30, the solutal relaxation time τ_c (as shown in eq. 2.33) follows from the relaxation mode. Without gravity it contains only the diffusion coefficient D ⁶. The last two terms of eq. 2.32 describe the c-NEF due the initiation force \vec{f}_c (III, very small against I) and the cross coupled c-NEFs due to the temperature fluctuation and the thermodiffusion coefficient D_T (II). The thermal fluctuation $\delta T_{q,\omega}$ has a similar structure as we will see in the next section.

2.5 Correlation functions of NEFs

After the long derivation of the two individual NEF, δT and δc , we now want to calculate the correlation functions $C^i(q, t) = \langle \delta i(q, 0) \delta i(q, t) \rangle$ ($i = c, T$). In eq. 2.34, the important experimental correlation function^[42] of the refractive index fluctuation δn (eq. 2.5) is shown.

$$\begin{aligned} \langle \delta n(\vec{q}, 0) \delta n(\vec{q}, t) \rangle &= \left. \frac{\partial n}{\partial T} \right|_{p,c}^2 \langle \delta T(\vec{q}, 0) \delta T(\vec{q}, t) \rangle + \left. \frac{\partial n}{\partial c} \right|_{p,T}^2 \langle \delta c(\vec{q}, 0) \delta c(\vec{q}, t) \rangle \\ &\quad + \frac{\partial n}{\partial T} \frac{\partial n}{\partial c} \left(\langle \delta T(\vec{q}, 0) \delta c(\vec{q}, t) \rangle + \langle \delta c(\vec{q}, 0) \delta T(\vec{q}, t) \rangle \right) \end{aligned} \quad (2.34)$$

The cross correlated third term ($\langle \delta T \delta c \rangle$, gray) of eq. 2.34 is considered uncorrelated and is therefore neglected^{[43]7}. The purpose of this section is to describe the two important correlation functions of eq. 2.34, which are the temperature fluctuation correlation function $C^T(q, t) = \langle \delta T(\vec{q}, 0) \delta T(\vec{q}, t) \rangle$ and the concentration fluctuation correlation function $C^c(q, t) = \langle \delta c(\vec{q}, 0) \delta c(\vec{q}, t) \rangle$. From the start, we want to decompose these individual correlation functions (eq. 2.35) in a sum of two parts, the

⁶The graphs of these relaxation times $\tau_i(q)$ ($i = c, T$) and the connection to the individual static structure factor $S^i(q)$ will follow in section 2.6.

⁷It should be mentioned, that under special circumstances, such as high pressures, there are cross coupling effects^[44].

equilibrium (index: E) and the non equilibrium part (index: NE).

$$C^i(q, t) = C_E^i(q, t) + C_{NE}^i(q, t) \quad (2.35)$$

$$= A_E^i \cdot f\left(t, \tau_E^i(q)\right) + A_{NE}^i(q) \cdot f\left(t, \tau_{NE}^i(q)\right) \quad (2.36)$$

We will follow in this section *Croccolo et al.*^[45] and will describe the correlation functions in the time domain, instead of the initially introduced frequency ω -domain of the Fourier transformation, where the intermediate scattering function ($f(t, \tau)$) describes the development over time t :

$$f(t, \tau) = \exp\left(\frac{-t}{\tau}\right). \quad (2.37)$$

The two correlation equations $C_j^i(q, t)$ of [eq. 2.36](#) are constructed in a similar way, with an amplitude A_j^i and a relaxation time τ_j^i . The exponents indicate the thermodynamic variable: $i = c$ for solutal and $i = T$ for thermal, the indices describes the equilibrium $j = E$ or non equilibrium $j = NE$ part. The next three sub-sections describe the NEF amplitudes A_j^i and relaxation times τ_j^i of [eq. 2.36](#) and build upon each other.

2.5.1 Equilibrium condition without gravitation ($\mathbf{E}, \mathbf{g}=0$)

First we discuss pure equilibrium fluctuations $\delta i = i_{loc} - i_0$ (for $i = c, T$, as in [section 2.4](#)), where we can neglect the non equilibrium part ($C_{NE}^i(q, t) = 0$) and gravitational effects ($g = 0$).

$$C^i(q, t) = C_E^i(q, t) = A_E^i \cdot f\left(t, \tau_E^i(q)\right) \quad (2.38)$$

The resulting correlation functions $C^i(q, t)$ ($i = c, T$) include the equilibrium amplitudes A_E^i and the equilibrium relaxation times $\tau_E^i(q)$, which are demonstrated in [fig. 2.8](#) and [tab. 2.2](#). The individual equilibrium relaxation dynamics show the characteristic q^{-2} -dependencies (cf. [eq. 2.33](#)), whereas the amplitudes have no q -dependence and they are also very weak (compared with the following ones). This squared q dependency originates from the former 'nabla'-terms (∇) in the conservation equations, which often refers to the diffusion characteristic in these

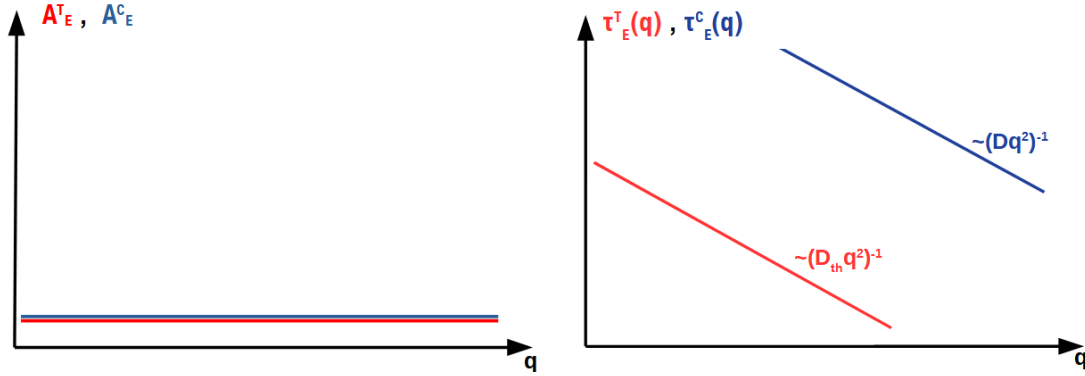


Fig. 2.8: LEFT: Representation of the individual constant amplitudes A_E^i in a spacial diagram of the individual correlation function. RIGHT: Representation of the equilibrium relaxation behavior with the fundamental q^{-2} -dependency of the relaxation times $\tau_E^i(q)$.

equations. As tab. 2.2 shows, the equilibrium amplitudes A_E^i are described by delta-distributions and are to be understood like the Brownian fluctuation of section 2.1.

thermal	amplitude: $A_E^T = \frac{k_B T_0}{\rho_0 V} \frac{T_0}{c_p} \cdot (2\pi)^3 \delta(\Delta q)$
	relax. time: $\tau_E^T(q) = (D_{th} q^2)^{-1}$
solutal	amplitude: $A_E^c = \frac{k_B T_0}{\rho_0 V} \chi_p \cdot (2\pi)^3 \delta(\Delta q)$, $\chi_p = \left(\frac{\partial \mu}{\partial c}\right)_{p,T}^{-1}$
	relax. time: $\tau_E^c(q) = (D q^2)^{-1}$

Tab. 2.2: Application of the resulting equilibrium amplitudes A_E^i and relaxation times of the components $\tau^i(q)$. The shown equations can be found in [46].

In the next sub-sections, we will successively expand the shown fig. 2.8 and tab. 2.2 and determine the gravitationally limited NEF, we are looking for.

2.5.2 Non equilibrium condition without gravitation (NE, $g=0$)

Now the non equilibrium components of the correlation functions due to the external gradients ($\vec{\nabla}c$ and $\vec{\nabla}T$) are considered, but the gravitation is still neglected ($g = 0$). This results in non equilibrium amplitudes $A_{NE}^i(q)$ (eq. 2.39) which are a product of three parts: the equilibrium amplitude A_E^i (same as in section 2.5.1), the term

\tilde{A}^i , which includes the transport coefficients and a third term, which includes the external temperature field (applied stimulation) and the q -dependency:

$$C^i(q, t) = A_E^i \cdot f(t, \tau_E^i(q)) + \overbrace{A_E^i \cdot \tilde{A}^i}^{A_{NE}^i(q)} \cdot \frac{|\vec{\nabla}T|^2}{q^4} \cdot f(t, \tau_E^i(q)) . \quad (2.39)$$

The amplitudes and time constants are listed in [tab. 2.3](#). In the course of this sub-section the terms $S_T R_n$ and R appear in the NE amplitudes. The factor $S_T R_n$ describes a dimensionless number of the refractive index ratios due to the external gradients:

$$S_T \cdot R_n = \left(-\frac{\vec{\nabla}c}{\vec{\nabla}T} \frac{1}{c_1 c_2} \right) \cdot \left(-2c_1 c_2 \frac{\frac{\partial n}{\partial c} \Big|_{p,T}}{\frac{\partial n}{\partial T} \Big|_{p,c}} \right) = 2 \frac{\vec{\nabla}n_c}{\vec{\nabla}n_T}, \quad \vec{\nabla}n_i = \frac{\partial n}{\partial i} \Big|_p \vec{\nabla}i \quad (2.40)$$

and the term R is the scattering intensity ratio of the individual modes in absence of gradients:

$$R = \frac{\partial \mu}{\partial c} \Big|_{p,T}^{-1} \frac{c_{p,c}}{T_0} \frac{\frac{\partial n}{\partial c} \Big|_{p,T}}{\frac{\partial n}{\partial T} \Big|_{p,c}}^2 . \quad (2.41)$$

In $A_{NE}^c(q)$, there is even a combination of both:

$$\frac{(S_T R_n)^2}{2R} = 2 \frac{\partial \mu}{\partial c} \Big|_{p,T} \frac{T_0}{c_{p,c}} \left| \frac{\vec{\nabla}c}{\vec{\nabla}T} \right|^2 . \quad (2.42)$$

If we first look at the relaxation times τ_E^i in [tab. 2.3](#), we can see that these do not differ from the equilibrium case. We have already seen this in [eq. 2.32](#), in which only the equilibrium mode (term 0.) occurred in the relaxation dynamics. However, the amplitudes $A_{NE}^i(q)$ change drastically (shown due to the comparison of [fig. 2.8](#) and [fig. 2.9](#)) due to the thermodynamic coefficients (D , D_{th} , ν), the gradients $\vec{\nabla}i$ ($i = c, T$) and the emerging (q^{-4})-dependency. Especially the NEF amplitude proportionality of $\sim q^{-4}$ is the most important difference between NEFs and EFs. The point where the amplitude curves crossover to the constant equilibrium signal (dashed gray line in [fig. 2.9](#)) is called the cut-off wavevector q_c^i and will be important

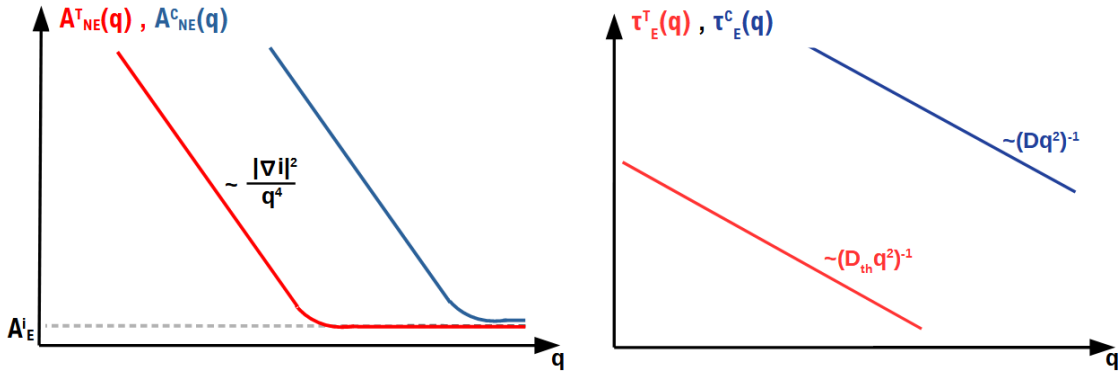


Fig. 2.9: LEFT: From the constant equilibrium amplitude A_E^i the non equilibrium amplitude $A_{NE}^i(q) \sim q^{-4}$ lifts of. RIGHT: The relaxation time remains in the equilibrium mode: $\tau_E^i(q) \sim q^{-2}$.

thermal	amplitude:	$\tilde{A}^T = \frac{c_{p,c}}{T_0(\nu^2 - D_{th}^2)} \frac{\nu}{D_{th}} \left[1 + S_T R_n \left(1 - \frac{D}{D_{th}} \right) \right]$
	NE-amplitude:	$A_{NE}^T(q) \simeq \frac{k_B T_0}{\rho_0 V} \cdot \frac{1 + S_T R_n}{\nu D_{th}} \cdot \frac{ \vec{\nabla} T ^2}{q^4}$
	relax. time:	$\tau_E^T(q) = (D_{th} q^2)^{-1}$
solutal	amplitude:	$\tilde{A}^c = \frac{c_{p,c}}{T_0(\nu^2 - D^2)} \frac{(S_T R_n)^2}{2R} \frac{\nu}{D} \left\{ 1 + 2 \frac{D}{D_{th}} \left[1 + \frac{2}{S_T R_n} \right] \right\}$
	NE-amplitude:	$A_{NE}^c \simeq 2 \frac{k_B T_0}{\rho_0 V} \cdot \frac{1}{D\nu} \cdot \frac{ \vec{\nabla} c ^2}{q^4}$
	relax. time:	$\tau_E^c(q) = (D q^2)^{-1}$

Tab. 2.3: Representation of the non equilibrium amplitudes \tilde{A}^i , $A_{NE}^i(q)$ and the relaxation times $\tau_E^i(q)$ ($i = c, T$). The approximations in the NE-amplitudes contain the assumption $Le = D_{th}/D \gg 1$. The shown equations can be found in [46].

in the fitting of the experiments (chapter 4).

2.5.3 NEFs due to external gradients and gravity (NE, g)

In all earth based laboratory experiments, however, gravity cannot be neglected. Now additional q -dependencies in the non equilibrium amplitudes $A_{NE,g}^i(q)$ and in

the relaxation times $\tau_{NE}^i(q)$ occur:

$$C^i(q, t) = A_E^i \cdot f(t, \tau_E^i(q)) + \overbrace{A_{NE,g}^i(q)} \cdot \tilde{A}^i \cdot \frac{|\vec{\nabla}T|^2}{1 - (q/q_{ro}^i)^4} \cdot f(t, \tau_{NE}^i(q)) \quad (2.43)$$

$$\tau_{NE}^i(q)^{-1} = \tau_E^i(q)^{-1} + \tau_g^i(q)^{-1} . \quad (2.44)$$

These new terms are limited by the gravitational buoyancy and sedimentation effects. Both in the amplitude and in the relaxation time plots (fig. 2.10), the curves now deviate from the known q^{-4} behavior below a certain q -value. This value, the so-called q roll-off wavevector q_{ro}^i (eq. 2.45), describes a physical balance point between the limitations of the gravity effects and the disturbances of the fluctuations. As mentioned, the roll-off values q_{ro}^i arise from a buoyancy or sedimentation effect in the gravitational field. They can be described by the expansion of the fluctuations due to the density gradients: $\vec{\nabla}\rho_i = \beta_i\vec{\nabla}i_0$ and the gravitational acceleration in a viscous medium: g/ν . The time scale of the fluctuation given quantities are the thermal diffusivity D_{th} (in the thermal case) and diffusion coefficient D (in the solutal case). The roll-off wavevectors are given by

$$q_{ro}^c = \left(\frac{g \cdot \vec{\nabla}\rho_c}{\eta D} \right)^{1/4} = \left(\frac{g \cdot \beta_c \vec{\nabla}c}{\nu D} \right)^{1/4} \quad (2.45)$$

$$q_{ro}^T = \left(\frac{g \cdot \vec{\nabla}\rho_T}{\eta D_{th}} \right)^{1/4} = \left(\frac{g \cdot \beta_T \vec{\nabla}T}{\nu D_{th}} \right)^{1/4} . \quad (2.46)$$

The curves shown in fig. 2.10, the NEFs amplitudes $A_{NE,g}^i(q)$ as well as the bell shaped relaxation times $\tau_{NE}^T(q)$, are important for the results in chapter 4.

2.6 Mode coupling and structure function

After the derivation of the individual relaxation times $\tau_j^i(q)$ and the amplitudes $A_j^i(q)$ of the correlation functions $C_j^i(q, t)$, we now want to connect these thermal and solutal modes to the time dependent structure factors $S^i(q, \Delta t)$, which we

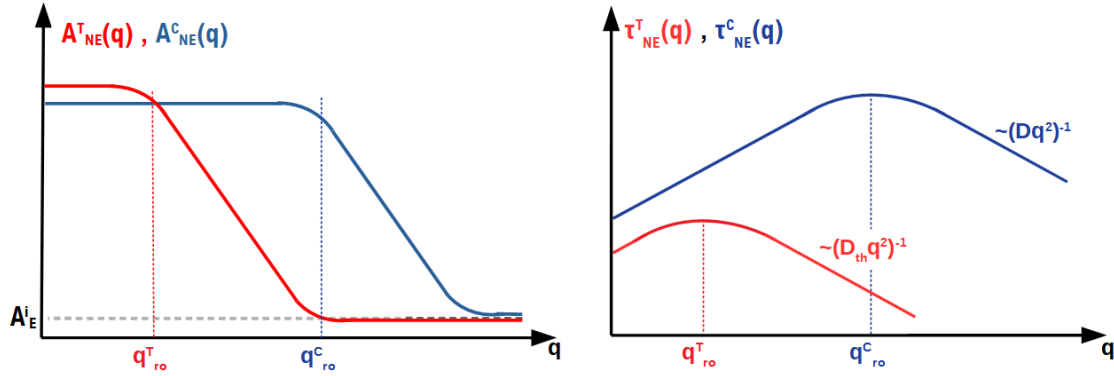


Fig. 2.10: LEFT: The gravitational dependence results in limiting of the amplitude for q smaller q_{ro}^i . RIGHT: This gravitational q dependence is also shown in the relaxation times τ_{NE}^i by a q^2 slope for q smaller q_{ro}^i .

thermal	amplitude:	$\tilde{A}^T = \frac{c_{p,c}}{T_0(\nu^2 - D_{th}^2)} \frac{\nu}{D_{th}} \left[1 + S_T R_n \left(1 - \frac{D}{D_{th}} \right) \right]$
	NE-amplitude:	$A_{NE,g}^T(q) \simeq \frac{k_B T_0}{\rho_0 V} \cdot \frac{1 + S_T R_n}{\nu D_{th}} \cdot \frac{ \vec{\nabla} T ^2}{1 - (q/q_{ro}^T)^4}$
	relax. time:	$\tau_{NE}^T(q) = \left(D_{th} q^2 \left[1 + (q_{ro}^T/q)^4 \right] \right)^{-1}$
solutal	amplitude:	$\tilde{A}^c = \frac{c_{p,c}}{T_0(\nu^2 - D^2)} \frac{R_n^2}{2R} \frac{\nu}{D} S_T^2 \left\{ 1 + 2 \frac{D}{D_{th}} \left[1 + \frac{2}{S_T R_n} \right] \right\}$
	NE-amplitude:	$A_{NE,g}^c(q) \simeq 2 \frac{k_B T_0}{\rho_0 V} \cdot \frac{1}{\nu D} \cdot \frac{ \vec{\nabla} c ^2}{1 - (q/q_{ro}^c)^4}$
	relax. time:	$\tau_{NE}^c(q) = \left(D q^2 \left[1 + (q_{ro}^c/q)^4 \right] \right)^{-1}$

Tab. 2.4: Representation of the non equilibrium amplitudes \tilde{A}^i , $A_{NE,g}^i(q)$ (simplified representation, $Le = D_{th}/D \gg 1$) and the relaxation times $\tau_{NE}^i(q)$ ($i = c, T$). In both terms the roll-off value q_{ro}^i appears. The shown equations can be found in [46].

can detect by light scattering. In this section we will follow our publication [47] where the derivation of the two important functions (eq. 2.54 and eq. 2.55) and the experimental validation is shown. This derivation follows directly from the correlation function of the refractive index fluctuations and can be confirmed experimentally, which follows in the first result section. It differs somewhat from the empirically motivated, purely solutal, approach proposed in the literature. This will be addressed around fig. 2.11 and is discussed in the appendix. Especially for our polymer samples with large Lewis numbers ($Le = D_{th}/D \approx 100$), which means easily distinguishable thermal and solutal modes, our treatment of the structure function leads to dramatically better results.

As already mentioned, the important experimental quantity is the correlation function of the refractive index fluctuations $C^n(q, t)$. Following [eq. 2.34](#) this function can be written as a sum of the two individual correlation functions (without the neglected cross correlation term).

$$C^n(q, t) = \langle \delta n(q, 0) \delta n(q, t) \rangle = \sum_{i=T,c} \left. \frac{\partial n}{\partial i} \right|_p^2 C^i(q, t) \quad (2.47)$$

The exponent indicates the different correlation modes of $i = n$ (refractive index fluctuations), $i = T$ (temperature fluctuations) and $i = c$ (concentration fluctuations). As shown in the previous [section 2.5](#) the individual correlation functions $C^i(q, t)$ are themselves a sum of an equilibrium (index E) and a non equilibrium part (index NE).

$$C^i(q, t) = \overbrace{A_E^i \cdot f(t, \tau_E^i(q))}^{=C_E^i(q,t)} + \overbrace{A_{NE}^i(q) \cdot f(t, \tau_{NE}^i(q))}^{=C_{NE}^i(q,t)} \quad (2.48)$$

Both parts decay in time with the mono-exponential ISF and the introduced relaxation times $\tau_j^i(q)$.

$$f(t, \tau_j^i(q)) = \exp(-t/\tau_j^i(q)) \quad (2.49)$$

In the case of our experiments we are interested in NEF in a gravitational field, as described and shown in [section 2.5.3](#). Since we are observing the correlations of difference images (shown in the experimental [section 3.3](#)) we need to consider the temporal variations of the correlation function $\Delta C^i(t, \Delta t) = C^i(t) - C^i(t + \Delta t)$. Due to the calculation rules for the exponential function, the term $f(t, \tau_j^i(q))$ can be excluded from both terms.

$$\begin{aligned} \Delta C^i(q, t, \Delta t) &= A_E^i \cdot f(t, \tau_E^i(q)) [1 - f(\Delta t, \tau_E^i(q))] + \\ &+ A_{NE}^i(q) \cdot f(t, \tau_{NE}^i(q)) [1 - f(\Delta t, \tau_{NE}^i(q))] \end{aligned} \quad (2.50)$$

Therefore, we can understand that the starting time t is unimportant and will be neglected (time invariant). The resulting correlation function difference $\Delta C^i(q, t =$

$0, \Delta t) = C^i(q, \Delta t)$ is only a function of q and Δt , and can be written as

$$C^i(q, \Delta t) = A_E^i \left[1 - f \left(\Delta t, \tau_E^i(q) \right) \right] + A_{NE}^i(q) \left[1 - f \left(\Delta t, \tau_{NE}^i(q) \right) \right] . \quad (2.51)$$

These functions are called structure functions^[48] of the thermal ($i = T$) and solutal ($i = c$) components. If we compare [eq. 2.48](#) and [eq. 2.51](#) it becomes clear, what the effect of the difference formation does with the correlation function. In order to bring the individual structure functions $C^i(q, \Delta t)$ into connection with the visible refractive index correlations, the individual time dependent structure factors $S^i(q, \Delta t)$ must be considered:

$$C^i(q, \Delta t) = \left. \frac{\partial n}{\partial i} \right|^2 S^i(q, \Delta t) . \quad (2.52)$$

The experiments have shown that the small ($S_E^i \ll S_{NE}^i$) constant equilibrium component (all E terms) of the individual time dependent structure factors cannot be distinguished from a background signal and are therefore regarded as such:

$$B^i(q, \Delta t) = S_E^i \left[1 - ISF \left(\Delta t, \tau_E^i(q) \right) \right] . \quad (2.53)$$

Consequently, the individual time dependent structure factors $S^i(q, \Delta t)$ are now written as

$$S^i(q, \Delta t) = S_{NE}^i(q) \left[1 - f \left(\Delta t, \tau_{NE}^i(q) \right) \right] + B^i(q, \Delta t) . \quad (2.54)$$

This is the important and noteworthy function of this section, since all of our experimental results ([chapter 4](#)) will be fitted with a combination of the thermal and solutal contributions. The illustration of [fig. 2.11](#) shows both individual modes $S^i(q, \Delta t)$ and the total time dependent structure factor $S(q, \Delta t)$ as the sum of both:

$$S(q, \Delta t) = \sum_{i=T,c} S^i(q, \Delta t) . \quad (2.55)$$

The blue line illustrates the solutal component, which rises from the associated background signal B_c and runs into the plateau of the amplitude A_{NE}^c with the relaxation time τ_{NE}^c . An analogous behavior is described by the red curve for

the thermal mode and for the sum of both, which describes the total signal

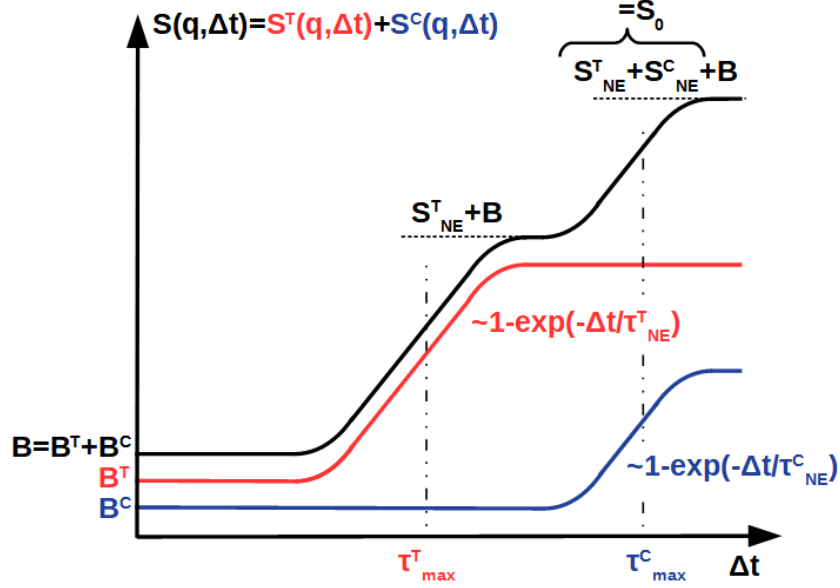


Fig. 2.11: In this demonstration, the equilibrium term and its small amplitude is shifted to the background as $B^i(q, \Delta t)$. Representation of the total structure function $S(q, \Delta t)$ (black, cf. eq. 2.55) as the sum of thermal (red) and solute mode (blue), both exponential functions with a relaxation time τ_{NE}^i and a amplitude S_{NE}^i (eq. 2.54).

(black line). From now on we will omit the index specifications in the amplitudes ($A_{NE}^i(q) \rightarrow A^i(q)$) and the relaxation times ($\tau_{NE}^i(q) \rightarrow \tau^i(q)$). As mentioned, we follow our own publication [47] for this derivation, in the literature the time dependent structure factor $S(q, \Delta t)$ is sometimes calculated differently. However, these approaches can be transformed into each other. This is briefly presented in the [appendix 6.1](#).

Finally the two illustrations [fig. 2.12](#) and [2.13](#) show the structure factor equations [2.54](#) and [eq. 2.55](#) in spatial and temporal behavior. [Fig. 2.12](#) shows the static (over q) and the time dependent (over Δt) behaviors of the individual structure factors $S^i(q, \Delta t)$ ($i = T$: in red, $i = c$: in blue) and the total function $S(q, \Delta t)$ (in black). The bridge between these two are the relaxation times $\tau^i(q)$ in the upper τ -plot. The important parts are the dotted lines, which illustrate the connection between the static and dynamic plateaus. The asymptotic plateaus ($\Delta t \rightarrow \infty$) in the dynamic plot connect to the associated q -values in the static plot. These amplitudes are formed by the introduced gravitational quench. Therefore we also

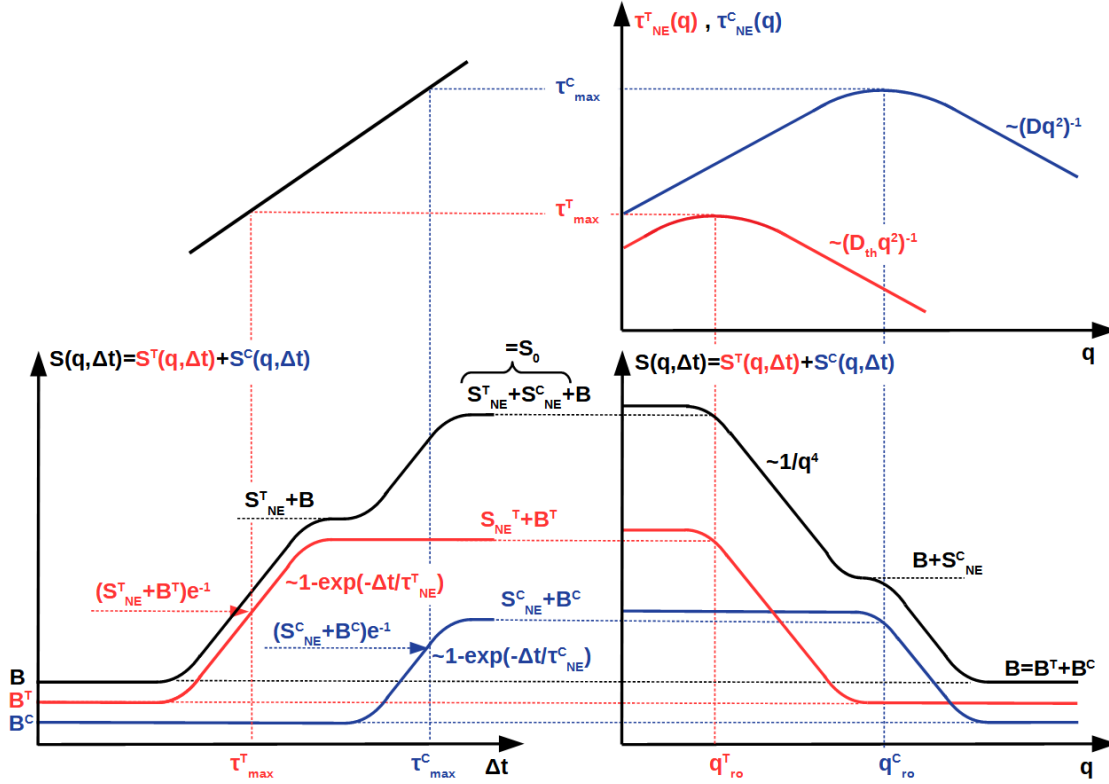


Fig. 2.12: Temporal ($S(q, \Delta t)$ over Δt) and spatial ($S(q, \Delta t)$ over q) representation of the total structure functions $S(q, \Delta t)$ as a sum of the individual structure functions of the thermal $S^T(q, \Delta t)$ and the solutal contribution $S^C(q, \Delta t)$. Furthermore a schematic demonstration of the resulting relaxation dynamics $\tau^i(q)$ (cf. tab. 2.4), which are the connection between both sides.

can find the roll-off wavevectors q_{ro}^i in the τ -plot at the maxima $\tau_{max}^i(q)$ of the bell shaped curves (cf. tab. 2.4) and in the static plot $S^i(q)$ at the transition from the gravitational plateau into the q^{-4} behaviors.

Illustration fig. 2.13 shows the 3-dimensional sketches of fig. 2.12. The mathematical (x, y) -plane of the Cartesian coordinate system represents the $(q, \Delta t)$ -plane and the z-direction shows the three structure factors (same color code). The panel on the left shows the superimposed individual time dependent structure factors of the thermal $S^T(q, \Delta t)$ and solutal $S^C(q, \Delta t)$ modes. It becomes clear that there are three different regions: either both modes together build the total signal (for example: $q \rightarrow 0$ and $\Delta t \rightarrow \infty$) or one of the two dominates (for example: the solutal mode for large q or the thermal mode for small Δt). The right (sketched) illustration

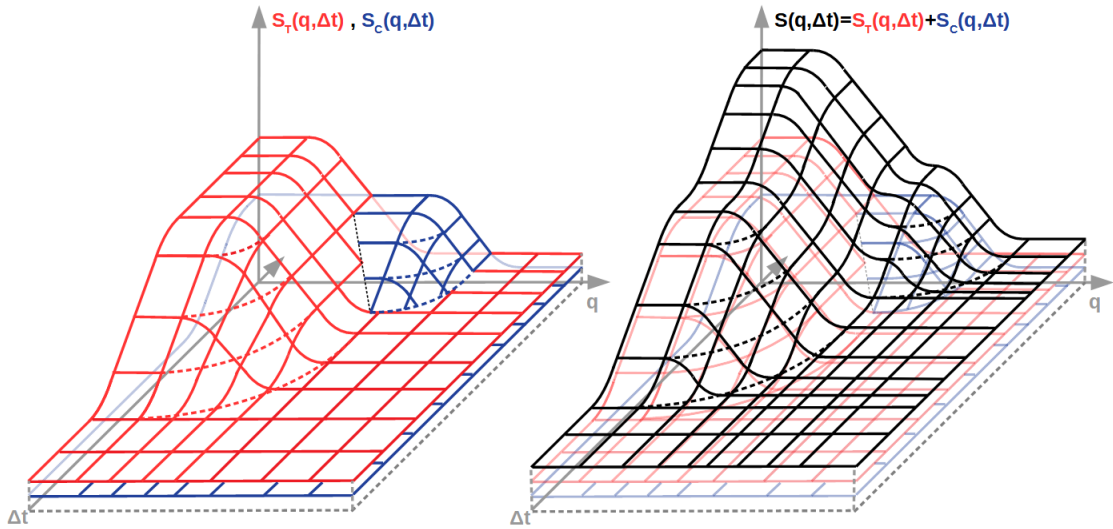


Fig. 2.13: LEFT: 3D illustration of the individual structure factors $S^i(q, \Delta t)$ from fig. 2.12 shown over the $(q, \Delta t)$ plane, where we can see, in which areas which contribution dominates. RIGHT: 3D illustration of the complete structure factors $S(q, \Delta t)$ over the $(q, \Delta t)$ plane.

shows the resulting total time dependent structure factor $S(q, \Delta t)$ as the sum of the two individual ones. This black curve (or plane) is the final result of the theory chapter 2 and is the signal which we will detect with the shadowgraphy setup of chapter 3. As shown, the total signal results from the correlation functions of the thermal and solutal NEFs. These themselves form the two parts of the correlation function of the refractive index fluctuations, which represents the experimentally accessible quantity.

3 Experimental

This chapter is divided into three individual sections, each implements a certain part in the understanding of the experiment.

The topic of the first [section 3.1](#) is the 'shadowgraphy setup' and therefore contains sub-sections for the light path, the Soret-cell and the camera operation, which are the key components of the measurement.

[Section 3.2](#) starts with the pure components of all the observed binary polymer mixtures and afterwards introduces the main parameters, such as the density, of the resulting samples. Another focus of this section is the explanation of the individual viscosity contributions.

The final [section 3.3](#) explains the self-written image analysis program, which is based on a *Differential Dynamic Analysis* (DDA) method. It additionally connects the experimentally generated structure factors with the in [chapter 2](#) theoretically derived ones of [eq. 2.54](#) and [eq. 2.55](#).

It should also be mentioned that almost every section includes a larger appendix. They are especially important when it comes to alignment and adjustment details of the setup. However, these additional sections are not absolutely necessary for an understanding of the experiments and the results. As part of the laboratory work in this thesis, the experimental setup was completely redesigned, built and put into operation. Therefore this experimental chapter is a bit more detailed.

3.1 Shadowgraphy setup

The motivation of this first experimental [section 3.1](#) is to introduce the important details of our shadowgraphy setup. In general it is a 'schlieren'-method related process, which detects refractive index changes of the transmitted light^[49]. The following three subdivisions focus on the key components. [Subsection 3.1.1](#) starts with an introduction of the light path, followed by [section 3.1.2](#), which explains the Soret-cell and ends with [section 3.1.3](#), where the camera operation is addressed. [Fig. 3.1](#) sketches the entire setup with a focus on the mentioned components.

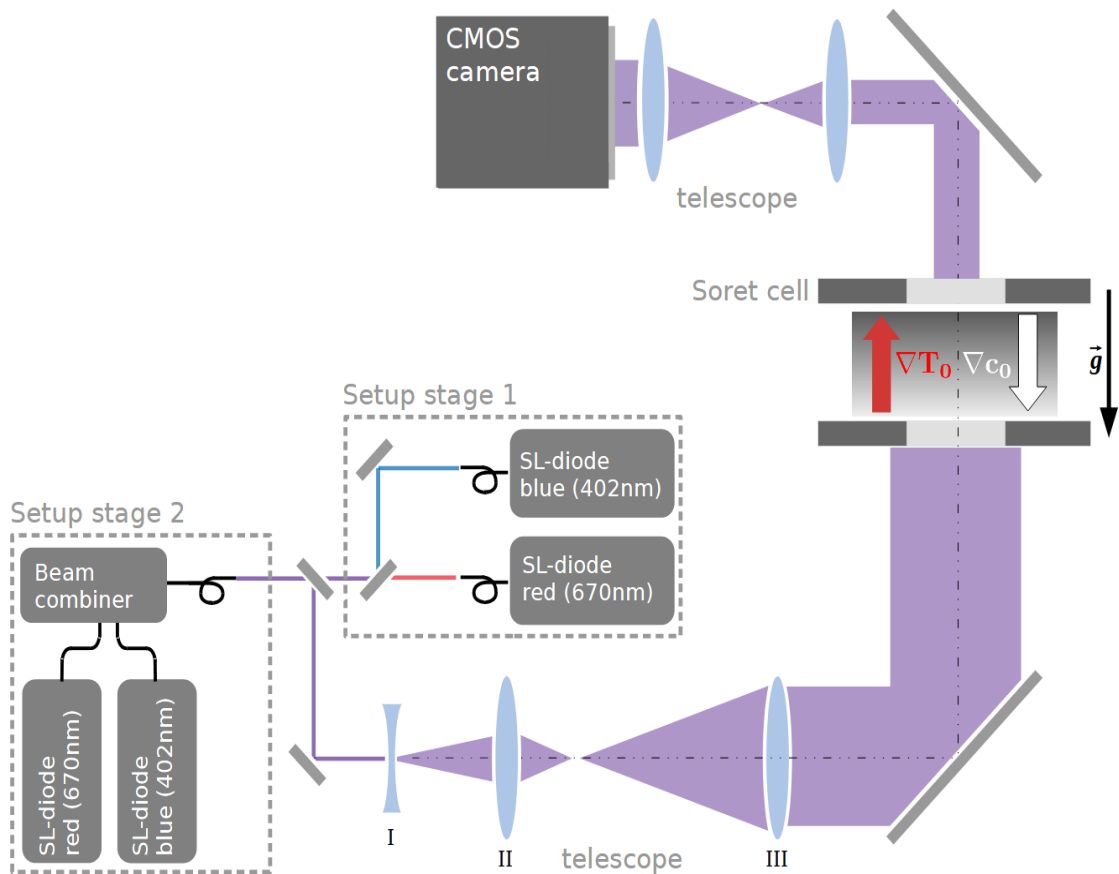


Fig. 3.1: Simplified sketch of the shadowgraphy setup, which shows the light path of the two beams. The overlapped common light path of the red and blue beam is shown in purple. Additionally the two telescopes, the Soret-cell and the camera are pictured.

3.1.1 Light path

The path and manipulation of the detection light are the topic of this [section 3.1.1](#). The 3D setup construction of [fig. 3.2](#) is a more detailed illustration, focusing on the light path (superimposed beam is shown in purple) of the two superluminescent light emitting diodes (SLED). The superimposing of the two SLED¹ lights is mana-

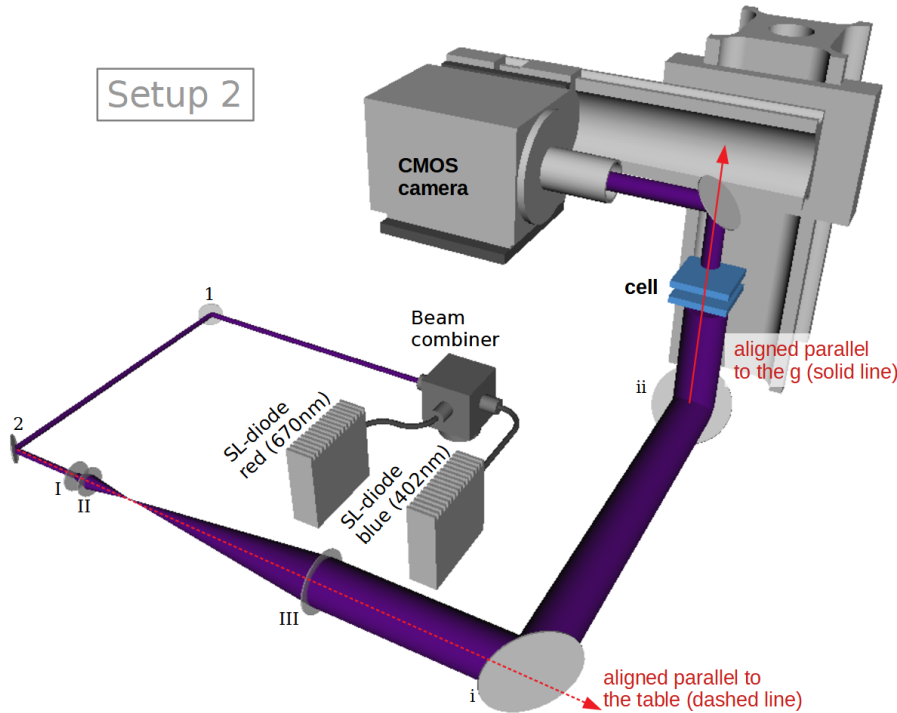


Fig. 3.2: 3D Arrangement of the optical path. The final version ('Setup2' from [fig. 3.1](#)) starts with a beam combiner for the superposition of the red and blue beams. The two important optical axes (red arrows) are shown, which each are aligned with the help of two mirrors. Installed on the first axis is the expansion telescope, on the second, vertical axis, the Soret-cell is mounted. In front of the camera the last mirror can be seen, which will be explained together with the camera in [section 3.1.3](#).

ged by a fiber-coupled beam combiner². This is the starting point of the purple light beam in [fig. 3.2](#). To avoid undesirable longitudinal interference effects, the use of SLED light sources with very short coherence lengths is inevitable. Even if this thesis only deals with binary samples, the future aim is to investigate ternary

¹SLED's are particularly bright LED light sources.

²Beam Splitter: 48-MCS-008 in the 2 → 1 configuration, Schäfter-Kirchhoff.

mixtures, therefore two easily distinguishable wavelengths are required. For this reason we installed a blue ($\lambda_{\text{blue}} = 402 \text{ nm}$)³ and a red ($\lambda_{\text{red}} = 670 \text{ nm}$)⁴ SLED. They have been selected based on the expertise of our partner groups in the GIANT FLUCTUATIONS project. After the beam combiner, the next two mirrors⁵ (arabic numbers) align the beam on the first optical axis (dashed red line in fig. 3.2). Along this telescope axis, which is adjusted parallel to the table plane (x, y), the beam is expanded with the help of two achromatic lenses⁶, in a telescopic arrangement (II: $f_1 = 30 \text{ mm}$, III: $f_2 = 150 \text{ mm}$). To expand a beam effectively a minimal diameter

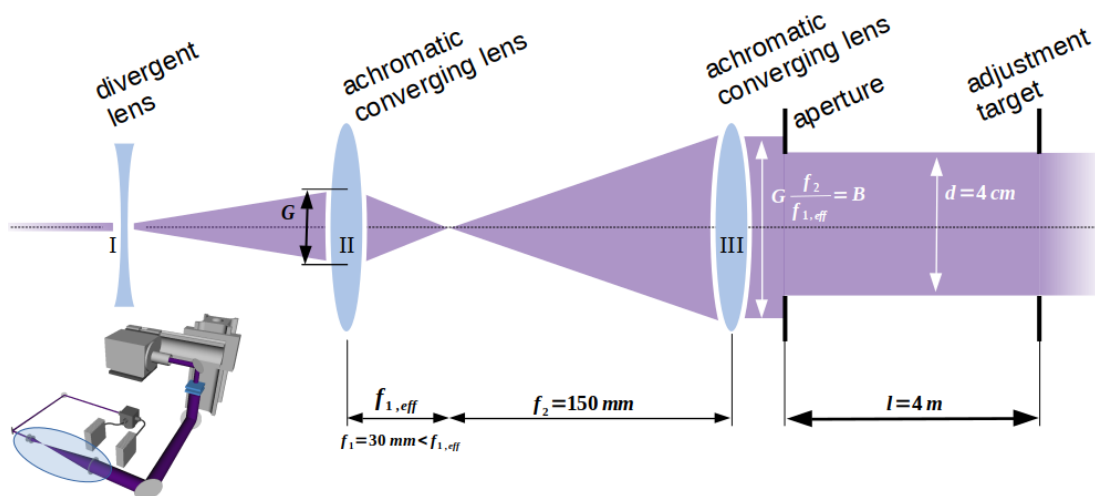


Fig. 3.3: Illustration of the Kepler-telescope arrangement. In front of the objective lens (II) a divergent lens (I) is positioned, which causes a divergent light beam and consequently a larger cross-section. The telescope itself consists of two converging lenses (II, III), the second lens (the ocular) being in the focus of the first. The parallelism of the flanks is controlled with the help of an iris and a target of the same size at a greater distance.

G is required. This is created with a diverging lens (I: $f_d = -50 \text{ mm}$) in front of the telescope (shown in fig. 3.3). Since the incoming light beam is now divergent, the distance to the focal plane of the first lens $f_{1,eff} > f_1$ is slightly longer than the corresponding focus length f_1 . As illustrated in fig. 3.3 the focus of the second lens is adjusted to this distance. In a perfect telescopic arrangement, the resulting

³EXS210084-01 from Exalos.

⁴SLD-261-MD-670 from Superlum.

⁵Thorlabs, silica broadband dielectric mirrors.

⁶Thorlabs, achromatic doublets.

beam diameter $B = G \cdot f_2/f_{1,eff}$ can be calculated from of the beam diameter G and the ratio of the focal lengths. In our case the generated beam diameter at the first lens is approximately $G \approx 10.5$ mm and the resulting diameter of the telescope is $B \approx 50.5$ mm. The parallelism of the expanded beam was checked with the help of an aperture and a corresponding target. This target⁷ was positioned at to a long distance, where the diameter was then checked. Behind the telescope the Gaussian beam is set to $d = 40$ mm (2σ -value). The entire telescope could in future be replaced by one, to the divergence of the fiber end tuned, achromatic lens. But especially for the start of this setup, it was very helpful to know and be able to manipulate every single component.

The Soret-cell needs to be in a horizontal orientation and the direction of the observing light beams must be parallel to the direction of gravity (solid line in [fig. 3.2](#)). For this reason the following two mirrors⁸ (small roman numbers in [fig. 3.2](#)) lifting the expanded beam up in a vertical running axis (parallel to the direction of gravity: $\parallel \vec{e}_g$). On this optical axis the Soret-cell, which will follow in the next [section 3.1.2](#), is positioned perfectly orthogonal to the light direction.

In [fig. 3.1](#) and [fig. 3.2](#) also the last mirror (cam mirror), the second telescope and the camera are shown. These parts will be addressed in [section 3.1.3](#).

3.1.2 Soret-cell

The Soret-cell (illustrated in [fig. 3.4](#)) is a special container for a liquid sample, which allows to apply a controlled external temperature gradient $|\vec{\nabla}T| = \Delta T/h$ ⁹. The inner radius of the cylindrical sample volume is 10 mm and has a height of 5 mm¹⁰. Due to the Soret-effect (explained in [section 2.2](#)), the applied temperature gradient $\vec{\nabla}T$ creates an opposing concentration gradient $\vec{\nabla}c$, which gives the cell its name. The explained cell-type, with the two gradients, is a very common experimental component. It can also be found in other setups, such as the 'optical beam

⁷Inner diameter: $D = 20$ mm in a distance of $l \approx 5$ m.

⁸Thorlabs, 2 inch silica broadband dielectric mirrors.

⁹The temperature gradient is generated by two surrounding Peltier-elements: AMS TB-109.

¹⁰There are also two other cells with heights of $h = 2, 3$ mm, which aren't covered in this thesis.

deflection’^[50] (OBD) or the ‘optical digital interferometry’^[51] (ODI). The main difference is that in these two cells the light direction and the thermal gradient are perpendicular, whereas the shadowgraphy operates in a parallel alignment. The

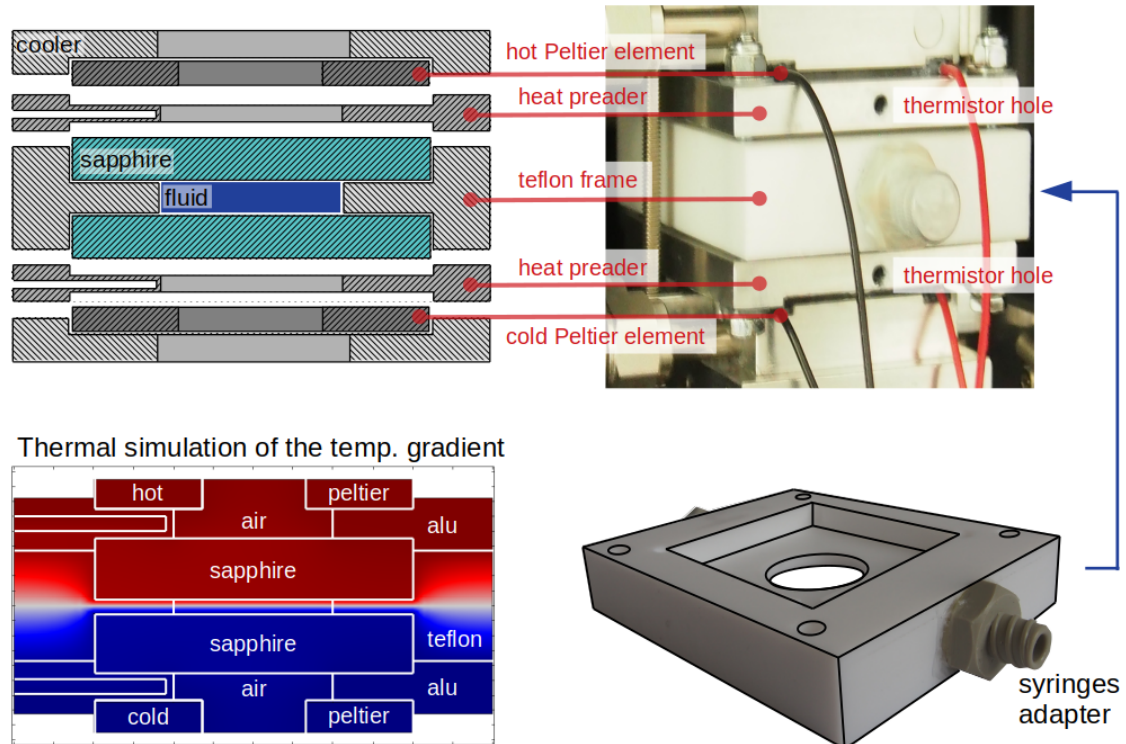


Fig. 3.4: ABOVE: Comparison of the cell picture (right) with a technical drawing (left) that names the individual components. BELOW, RIGHT: Photo of the Teflon frame with the visualization of the sample volume (cylindric) and the recesses of the sapphire windows (squared). BELOW, LEFT: Temperature simulation with the real sizes and the right materials. Colored representation of the temperature profile.

large illustration of fig. 3.4 explains in several independent sub-figures the design of the Soret-cell. The following introduction of the cell structure can be seen in the exploded drawing (upper left). We start in the center, with the two sapphire windows ($40 \times 40 \times 8 \text{ mm}^3$)¹¹ (cyan), which are embedded in the Teflon-frame and serve as the transparent and highly thermal conductive bottom and top enclosures of the liquid. Below and above the windows the mentioned Peltier-elements are positioned. These components have a central hole ($d = 13 \text{ mm}$), which allows the light to shine

¹¹Sapphire windows from Korth Kristalle.

directly vertically through the elements¹², into the sample. The outward pumped heat, of the Peltier-elements, is dissipated with water-cooled plates and a connected water thermostat¹³, which always runs at the required measuring temperature T_0 of 25 °C. The Teflon-frame, shown in fig. 3.4 (lower right), is the horizontal non-heat-conductive wall of the liquid. Since the sapphire windows are embedded in the Teflon-frame, they are thermally decoupled from each other. The applied temperature of the Peltier-elements form the temperature difference ΔT and are controlled by two commercial control units (LFI)¹⁴. Therefore every LFI has an own thermistor¹⁵, which is measuring the temperature in a 2 mm thick aluminum heat

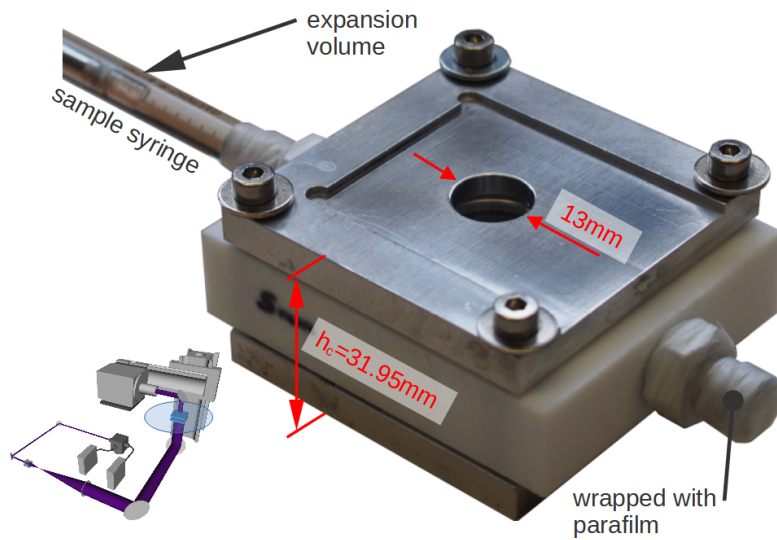


Fig. 3.5: Image of the assembled inner cell. The main part of the cell is built with the inner Teflon frame (white part), the upper and lower heat spreader plates (with the holes for the thermistors) and between these parts are the sapphire windows. The attached syringe and the cap are additionally wrapped with parafilm. Far from the inner cell a little air bubble remains, as a expansion volume.

spreader plate between the Peltier-elements and the sapphire windows¹⁶. These heat spreader plates are screwed together and construct with the embedded sapphire

¹²Conceptually are Peltier-elements to be understood as current-controlled heat exchanger.

¹³Thermostat: Julabo F-32.

¹⁴LFI-3751 from Wavelength electronics.

¹⁵Semiconductor NTC, $R = 1000 \Omega$.

¹⁶Thermal conductivity: $\kappa_{alu} = 205 \text{ W/mK}$ ^[52], $\kappa_{sapphire} = 42 \text{ W/mK}$ ^[53], $\kappa_{Teflon} = 0.25 \text{ W/mK}$ ^[53].

windows and the Teflon-frame, the inner capsuled cell, which is demonstrated in [fig. 3.5](#). At the horizontal center of the Teflon-frame the adapters for the sample syringes are mounted. For our measurements one syringe (far from the cell) always remains with a little air volume for thermal expansion. It is important that no bubbles are present inside the cell, since they would cause unwanted mixing due to Marangoni convection along their surface. Future details to the sealing of the inner cell are given in [section 6.2](#). The horizontal alignment of the cell, as well as the perpendicular orientation are described in [section 6.3](#). Finally, the entire cell is isolated from the ambient temperature (laboratory temperature: $T_l \simeq 20^\circ\text{C}$) with an styrofoam layer (thickness ≈ 1 cm), which surrounds the complete Soret-cell.

The structure and temperature distribution of the entire cell was in a first step computer simulated¹⁷, which is demonstrated in the lower left panel of [fig. 3.4](#). The aim was to achieve a temperature gradient that is as uniform and stable as possible, with liquid temperatures that did not differ from those of the thermistors. Based on these results, the structure of the Soret-cell was then completely redesigned and built in the machine shop of the University of Bayreuth.

3.1.3 Camera operation

In many common light scattering experiments, for example 'photon correlation spectroscopy' (PCS) or the mentioned OBD, the detection is far from the sample (FFS: far field scattering). This is to isolate a certain scattering angle θ and avoid interference effects. Contrary to this, the camera in our setup is very close to the sample, this measuring type is called near field scattering (NFS). The sketch of [fig. 3.6](#) compares these two variants illustratively. A useful consequence is that all of the scattering vectors

$$\text{eq. 2.3: } q_s = 2n \frac{2\pi}{\lambda} \sin(\theta/2) \quad (3.1)$$

are detected simultaneously. The simultaneous method is called heterodyne detection^[54]. In reverse all the different fluctuations are included in every camera

¹⁷Thermal computer simulation with Comsol (finite element programm).

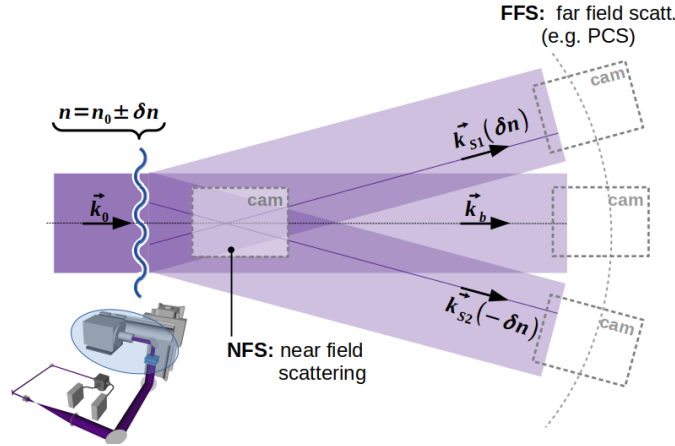


Fig. 3.6: The camera is in a NFS arrangement. In contrast to the FFS, in which only a certain scattering angle θ is viewed in isolation at a certain point in time, in the NFS a heterodyne signal is viewed as a overlap of all possible scattering angles at the same time.

image. The 3D illustration of the setup [fig. 3.2](#) shows the horizontal rail where the CMOS-camera¹⁸ is attached. Due to the weight of the camera, an additional lifting platform is installed beneath. The alignment of the camera is controlled with a bubble leveling glass. The mentioned cam mirror, the last mirror, which reflects the scattered light onto the camera, must be very carefully aligned. This is absolutely necessary, since otherwise unacceptable interference signals outshine the signal at small scattering vectors. The alignment and control procedure of the cam mirror, which is done by the congruent superposition of two irises interference ring-pattern, is explained in the [appendix 6.4](#).

The CMOS-camera is equipped with a large sensor surface of $A_{cam} = 2304 \text{ px}^2$, but to avoid very long calculation times we measure with a reduced effective area of $A_{eff} = 1000 \text{ px}^2$. However, this area should be increased in the future, because the step size in the Fourier-space shrinks in return, as we will see below. The individual pixel size is $px = 6.5 \mu\text{m}$ and has no unnecessary gap. The precise distance $z = 20.87 \text{ cm}$ between the cell center and the camera-sensor is calculated

¹⁸CMOS: complementary metal-oxide-semiconductor, Hamamatsu Orca-Fusion.

by the transfer-function^[55,56]

$$T(q) = 4 \sin^2 \left(\frac{z}{2k} \cdot q^2 \right) , \quad (3.2)$$

which modulates the total time dependent structure factor $S(q, \Delta t)$ with the included sine-oscillations. More precisely, with the measured oscillation minima of the structure function (blue line in [fig. 3.8](#)) and the known wavevector $k = 2\pi/\lambda$ we can calculate the distance z from the derivative $\partial T(q)/\partial q$. Depending on the used sensor area and the accessible buffer memory size, the sampling rate can differ quite a bit. In our case, with an effective area $A_{eff} = 1000 \text{ px}^2$, buffer size of 1000 images and in the water cooled operation mode¹⁹, the camera can record approximately 100 fps (frames per second). In case of NEFs, the most interesting q -values are the small ones ($q \rightarrow 0$). Therefore an additional telescope²⁰ is mounted in front of the camera. Thereby the small scattering vectors are distributed over a larger sensor area. The telescopic beam direction manipulation of the scattered light is shown in [fig. 3.7](#). This was checked using the real image and the resulting

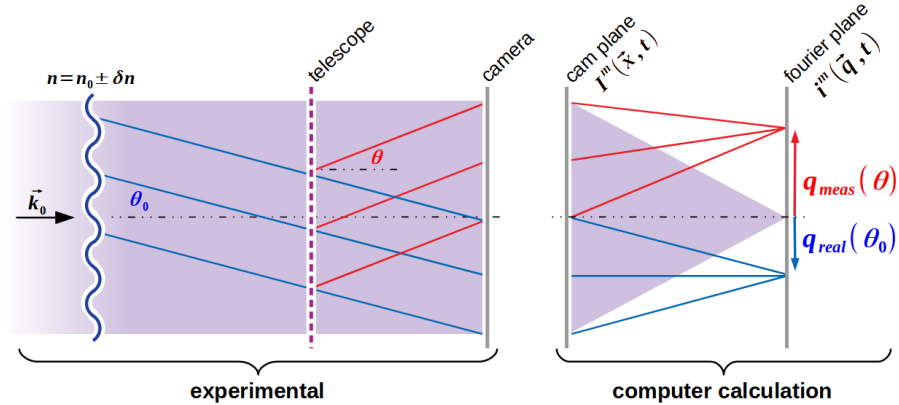


Fig. 3.7: Directly at the camera a telescope is connected by C-mount. Therefore the scattering angles are distorted, which leads to different q -values. This figure illustrates the beam path of a specific scattering vector (blue) and shows how it is distorted (red) through the telescope (dashed purple line). It also shows that parallel beams through the telescope remain parallel and that the q -values can therefore be corrected later (shown in [fig. 3.8](#)).

¹⁹Water cooled camera-mode is faster than air cooled mode.

²⁰KOPPACE, 0.5x C-mount camera adapter.

Fourier transformation of a scale made with a gap width and gap distance of 1 mm. This is shown in the [appendix 6.4](#). Illustrated in [fig. 3.7](#) is a certain scattering angle θ_0 , resulting from the associated refractive index fluctuations δn . The blue lines demonstrates the mentioned scattering direction θ_0 without the telescope. In the sketch the telescope is represented by the dashed violet line. The red lines behind shows the still parallel light paths of emerging new scattering angle θ with the telescope. The resulting two different q -values, the measured q_{meas} (with telescope,

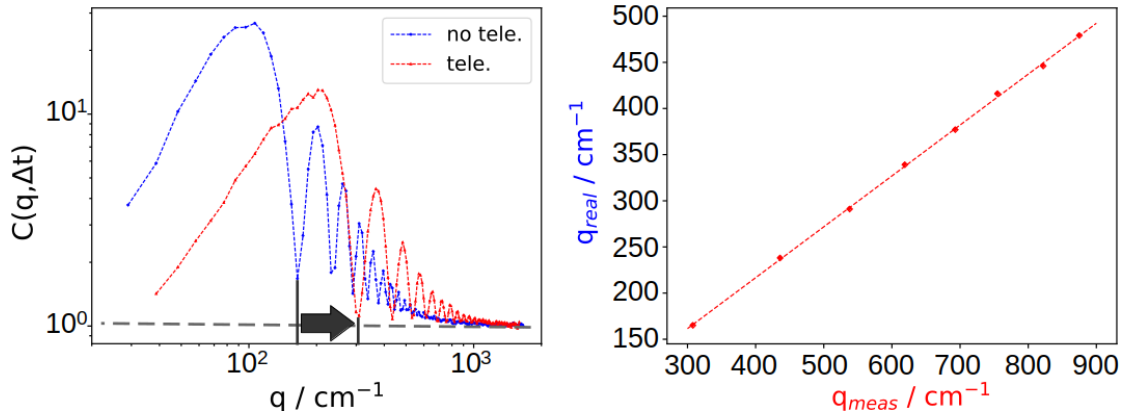


Fig. 3.8: LEFT: Comparison of the static structure factors with (red) and without (blue) the camera telescope (slightly different diode intensities). RIGHT: The q values can subsequently be transformed back into the correct lengths using the shown linear function [eq. 3.3](#). Parameters: $\Delta T = 40$ K, $c = 0.01$ [w/w], $M = 17.9$ kg/mol.

red) and the real scattering vector q_{real} (without telescope, blue), are shown in the last plane of [fig. 3.7](#). This Fourier-plane is an imagination layer, were in reality this is included in the analysis due to numerical Fourier-transformation (FFT). The two panels of [fig. 3.8](#) compare these two q -values and calculate the linear transformation function

$$q_{real} = 0.65 \cdot q_{meas} - 3.89 \text{ cm}^{-1} . \quad (3.3)$$

The left side of [fig. 3.8](#) is a comparison of the same structure functions $C(q, \Delta t_{max} = 99s)$. In blue measured without the telescope and in red with. The black arrow illustrated the mentioned telescopic shift of the q -value towards larger ones. With the easy localizable minima of these functions, the demonstrated linear shift function [eq. 3.3](#) is calculated from the identification plot (right side). This panel plots the measured q_{meas} (red, with telescope) on the x-axis and real q_{real} (blue,

without telescope) on the y-axis. The red dashed line illustrates the fitted q value transformation function of [eq. 3.3](#).

Note

Not all measurements were taken with this last camera positioning. In the continuous optimization process, various distances and optics were tested. For all configurations, the q transformation of [eq. 3.3](#) must be determined new. However, this always follows the same shown logic.

3.2 Sample properties

This section, which focuses on the measured samples, is divided in two sub-sections. The first [section 3.2.1](#) introduces the parameters of the pure substances and connects these to the important ones of the observed binary mixtures. The second [section 3.2.2](#) focuses mainly on the viscosity of the polymer solutions.

3.2.1 Binary sample composition

All the samples are binary mixtures of extra-pure toluene²¹ (tol) and dissolved polystyrene²² (PS). The primary goal is to define the thermodynamic coefficients and to explain the dependencies of the polymer concentrations c , as well as the molar masses M ²³. In [tab. 3.1](#) some important parameters of the two pure substances are shown, where in case of the polymer, the repetition unit is presented. This table is augmented by [tab. 3.2](#), which shows the measured densities and the below calculated expansion coefficients for different concentrations. All the density measurements are accomplished with a commercial density-meter (Anton Paar, DMA 4500 M). A selection of these densities is shown by the blue triangles in the right panel of [fig. 3.9](#).

²¹Toluene, AnalaR NORMAPUR from VWR with a purity=99.98%.

²²All polystyrene's are from Polymer Standards Service (PSS).

²³The molar mass of a certain polymer defines the chain length of the carbon backbone.

component	property	
toluene	molar mass:	$M_{tol} = 92.14 \text{ g/mol}$
	density:	$\rho_{tol} = 0.862 \text{ g/cm}^3$
	refractive index:	$n_{0,tol} = 1.497$
polystyrene (ru)	molar mass:	$M_{PS} = 104.15 \text{ g/mol}$
	density (solid):	$\rho_{PS} = 1.05 \text{ g/cm}^3$
	refractive index (solvent):	$n_{0,PS} = 1.57$

Tab. 3.1: List of the specific sizes of the two basic substances toluene and polystyrene (repeating unit).

It illustrates the density $\rho(c, T_0 = 25 \text{ }^\circ\text{C})$ as a function of the concentration. More on this in a moment. Completed is [fig. 3.9](#) with the left demonstration, where we can see the density $\rho(T)$ of various samples as a function of temperature T . There

concentration	$\rho_0 / \frac{\text{g}}{\text{cm}^3}$	$\beta_T / 10^{-3}\text{K}^{-1}$	β_c
c=0.2%	0.863	-1.086	0.211
c=1.0%	0.864	-1.084	0.211
c=2.0%	0.866	-1.070	0.210
c=5.0%	0.871	-1.073	0.209
c=10%	0.880	-1.030	0.207
c=20%	0.897	-0.973	0.203
c=30%	0.914	-0.916	0.199
c=40%	0.931	-0.859	0.195
c=50%	0.949	-0.802	0.192

Tab. 3.2: List of the density ($\rho_0(T_0)$, at $T_0 = 298.15 \text{ K}$) and the two expansion coefficients (thermal β_T of [eq. 3.4](#) and solutal β_c of [eq. 3.6](#)) of the different concentrations.

are several groups of curves, which reflect the different polymer concentrations $c = 0.2, 2, 5, 10, 20, 30, 40\%$ (from bottom to top). The different molar masses are all in these same bunches (superimposed), which means they have no effect on the density, if the concentration is measured in mass fraction. The thermal expansion coefficient $\beta_T = \rho_0^{-1} \partial \rho / \partial T$ (ρ_0 is the average density at $T_0 = 25 \text{ }^\circ\text{C}$) can be determined from the slope: $\partial \rho / \partial T = 0.571$ and varies slightly for the different

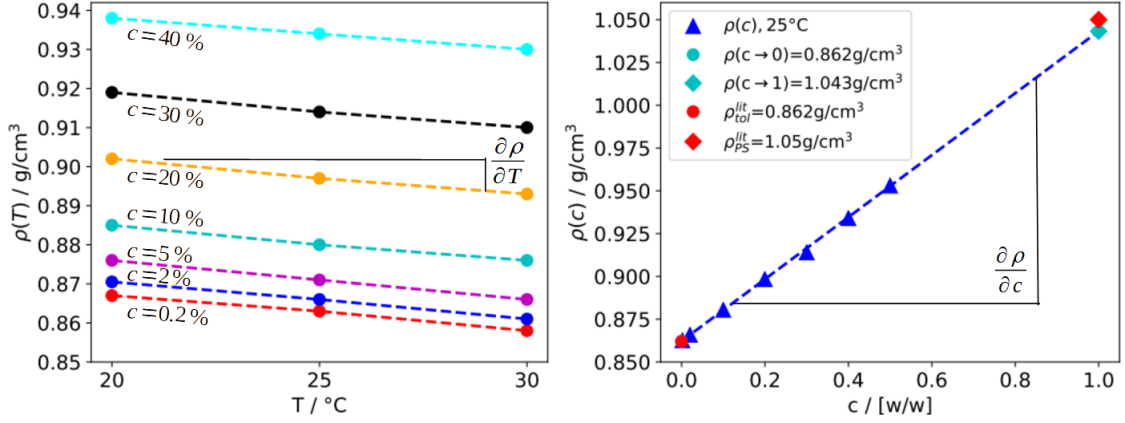


Fig. 3.9: LEFT: Thermal density dependency of different binary mixtures. All with slightly different $\partial\rho/\partial T$, which is used in the thermal expansion coefficients β_T are shown in [tab. 3.2](#). RIGHT: Analogue representation of the solutal density dependency. Interestingly, the density function of the mixed density ([eq. 3.5](#)) with increasing polystyrene concentration (blue triangles) shows a perfect straight line from the pure toluene up to pure polystyrene.

concentrations.

$$\beta_T(c) = \frac{1}{\rho_0(c)} \cdot \left. \frac{\partial \rho}{\partial T} \right|_{p,c} \approx (-1.087 + 0.571 \cdot c) \cdot 10^{-3} \quad (3.4)$$

The empirical [eq. 3.4](#) can be used to approximate the thermal expansion coefficient β_T for a given polystyrene concentration in a binary mixture with toluene. From the right panel of [fig. 3.9](#) and the linear fit of the measured densities we derive the slope of $\partial\rho/\partial c = 0.182$, which allows us to calculate the density $\rho(c)$ for any concentration. Consequently, we can also estimate the solutal expansion coefficient with the derivation-term $\partial\rho/\partial c$ and the density of [eq. 3.5](#).

$$\rho_0(c) = \rho_{\text{tol}} + \left. \frac{\partial \rho}{\partial c} \right|_{p,T} \cdot c \quad (3.5)$$

$$\beta_c(c) = \frac{1}{\rho_0(c)} \cdot \frac{\partial \rho}{\partial c} \quad (3.6)$$

As a control, the fit of [eq. 3.5](#) is extrapolated to the pure substances, which are the limits in the plot (shown in red). It turns out that this linear approximation fits not only the pure toluene (the suspension point, green dot) it also nearly perfectly

connects to the pure polymer density (which is a solid, green diamond). This result is surprising, since we increase with this approximation the concentration, starting from the dilute state ($c < c^*$), over the overlap concentration c^* ^[57] up to the pure polymer. A wide variety of system states are covered, from completely uncoupled polymer chains, floating in the solvent, to chains that sense each other (around the overlap concentration $c \approx c^*$), entangled chains with severely limited dynamics (entangled region, more details in [section 3.2.2](#)), to the glassy state of the solution. However, we never exhausted this approximation and never went beyond 50/50 solutions with our measurements.

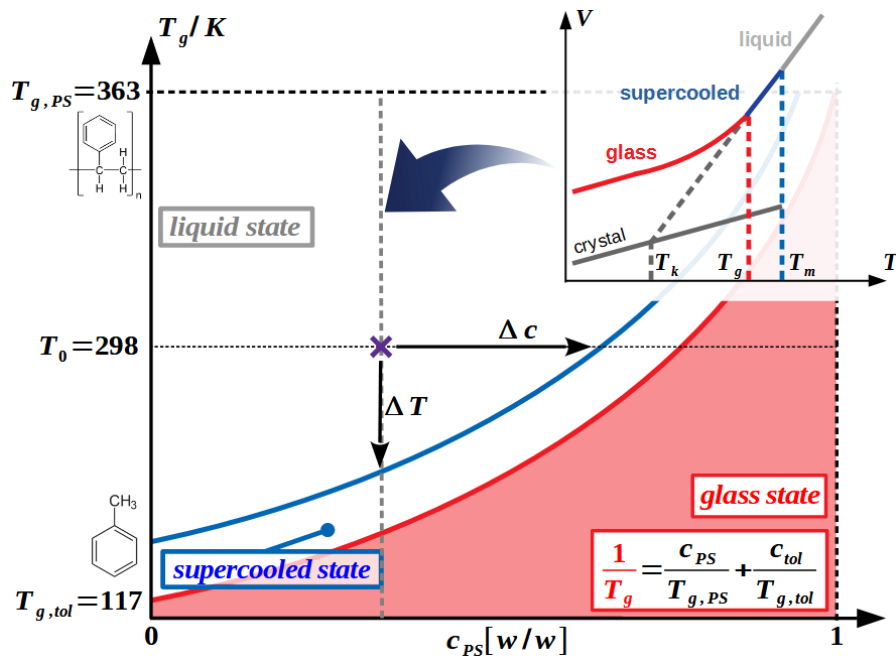


Fig. 3.10: The large plot is a phase diagram of a mixture of two glass formers. The white area is the liquid and the red the glass system state. The region between the blue and the red lines describes the supercooled state. Vertical temperature reduction ΔT as well as horizontal concentration increase Δc ensures an approach to the glass temperature. For a specific concentration the insert shows a $V(T)$ -diagram, which compares the glass transition with crystallization. It refers the crystallization T_k , glass T_g and the melting temperature T_m .

These binary solutions can be understood as a mixture of two glass formers with the individual glass temperatures: $T_{g,tol} = 117$ K and $T_{g,PS} = 363$ K. The *Fox-equation*^[58] can be employed to estimate the glass temperature T_g of the mixture

as

$$\frac{1}{T_g} = \frac{c_{PS}}{T_{g,PS}} + \frac{c_{tol} = (1 - c_{PS})}{T_{g,tol}} . \quad (3.7)$$

The current state of research is that additional effects are present, such as intermolecular interactions^[59,60] and that even two glass temperatures exist^[61]. But for our purpose this simpler approach is sufficient. Naively said, the glass temperature is that temperature where the liquid starts to solidify. In contrast to liquids that form crystal structures, where the melting T_m and the crystallising temperature T_k can be easily defined and measured, the glass transition temperature is not sharply defined (illustrated in the inset of [fig. 3.10](#)). If we cool a glass forming liquid, the sample can reach the supercooled regime, an area between the melting temperature (blue line) and the glass temperature (red line).

3.2.2 Viscosity contributions

A glass solidifies, not because it forms certain structures (as crystals), but because its viscosity tends to infinity and therefore all the system dynamics are 'frozen'. From this very interesting point of view, polymer solutions are suitable to investigate the important coefficients, which describe the system dynamics, because the total viscosity changes dramatically, depending on the concentration and the molar mass of the polymer. For all of our measurements the viscosity is estimated with the empirical approximation of *Schwaiger*^[62]:

$$\log \eta(c, M, T_0) = \underbrace{\log [\eta_{poly}(c, M, T_0)]}_{\text{polymer viscosities}} + \underbrace{\log \left[\frac{a_{Tg,0}(c, M, T_0)}{a_{Tg,tol}(T_0)} \right]}_{II.} + \log [\eta_{sol}(T_0)] , \quad (3.8)$$

where the total viscosity $\eta(c, M, T_0)$ is build up with three individual parts. This section describes the easily distinguishable three viscosity contributions of [eq. 3.8](#). It should be noted, that in the result [section 4.2](#), an alternative calculation of the viscosity is described. This calculates the total contribution via the specific and intrinsic viscosity and delivers better results, especially for small concentrations.

The last term the viscosity of the pure solvent η_{sol} is the basis of [eq. 3.8](#) and is in the case of toluene a constant quantity. The second polymer part (II) is viscosity contribution due to the distance from the glass temperature. The closer the sample is to the glass temperature, the larger this viscosity contribution will be. The first polymer part (I) is a contribution due to entanglements of the polymer chains η_{poly} . Thereby is the rule the larger the polymer concentration, the more frequent the occurrence of entanglements. These severely restrict the mobility and therefore increase the viscosity.

Illustration model

A very useful approach is to imagine a polymer solution as a pot of spaghetti. A certain spaghetti can only move along its contour length and all movements perpendicular to it are severely limited. This consideration only describes solutions above the overlap concentration, but for this molecular effect it is unimportant whether the polymer is entwined by neighbored chains or by itself.

3.3 Image processing

This last section of the experimental chapter focuses on all the necessary image processing steps. The description starts with an explanation of the image collection in [section 3.3.1](#). Afterwards the images are pre-processed, which is detailed in [section 3.3.2](#). Before the actual time dependent structure factors are calculated in [section 3.3.4](#), the [section 3.3.3](#) demonstrates the mentioned Fourier-transformation with focus on the experimental image analysis.

3.3.1 Image collection

For our target to investigate both, the solutal and the thermal effects of the polymer mixtures, we need not only a very high sampling rate (primary for the thermal effects), we also need low sampling rate (for the solutal effects). Therefore the camera measures in a quasi-logarithmic way. As in [fig. 3.11](#) demonstrated several

different interval times: $\tau_s = 0.01, 0.1, 1$ s (sometimes, additional $\tau_s = 10$ s) are chosen, all with the same sampling number, of 300 images. This ensures that images are recorded over many decades, but that the total amount of data is manageable. There is no need for thousands of images which are recorded in 10 ms steps, if

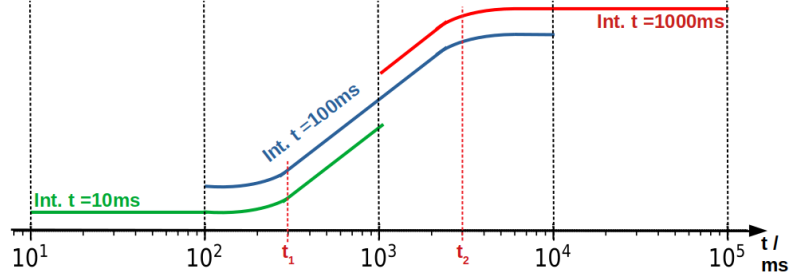


Fig. 3.11: The total measurement time is created from the combination of three various interval times: $\tau_s = 0.01, 0.1, 1$ s. This quasi-logarithmic procedure generates the same number of images for all sampling times.

the solutal variation changes significantly over a time of approximately 1 s. A simplification of the associated curves (green: 10 ms, blue: 100 ms, red: 1 s) is shown in [fig. 3.11](#). The two defined times $t_1 = 300$ ms and $t_2 = 3$ s are also demonstrated, these are the points where the contributing interval times are normalized to each other and thereby connected to generate the master curve. The schematic curve of [fig. 3.11](#) shows an ideal time dependent structure factor $S(q, \Delta t)$, which is determined by only one relaxation process and demonstrated for one specific q -value. This corresponds to [fig. 3.12](#), where the right side shows all different q -values and the measured structure functions $S(q, \Delta t)$. For the sake of completeness, the left side shows all associated structure functions $S(q, \Delta t)$ for the different time differences Δt and as a function of the q -value. The color scheme of [fig. 3.12](#) is based on [fig. 3.11](#) and illustrates the time dependent structure factors $S(q, \Delta t)$ in the color of the sampling rate.

The following [sections 3.3.2-3.3.4](#) explain how these time depended structure factor curves are extracted from the calculated images.

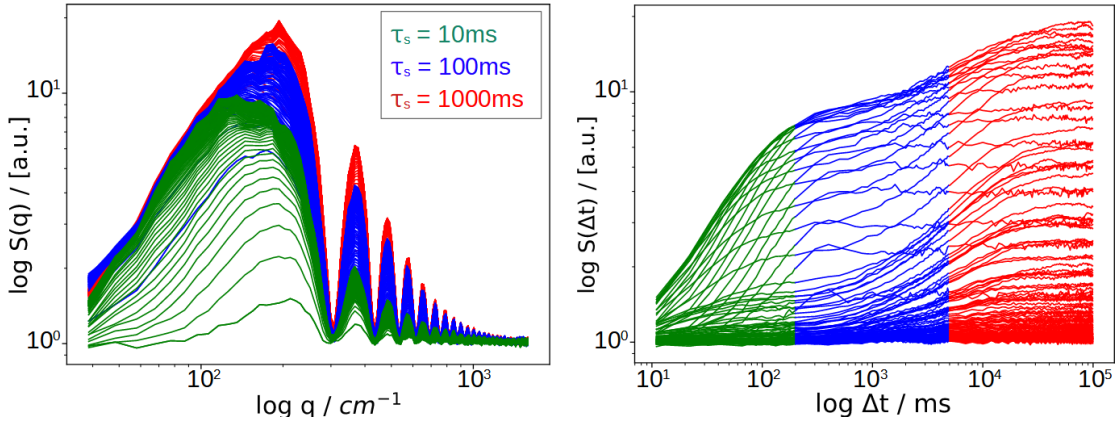


Fig. 3.12: LEFT: Representation of the various time dependent structure factors. The interval times are differentiated by color, so that the green curves are recorded with $\tau_s = 10\text{ms}$, the blue ones with $\tau_s = 100\text{ms}$ and the red ones with $\tau_s = 1\text{s}$. RIGHT: Illustration how the different interval times of the same q values are connected at points t_1 and t_2 . With very slow dynamics, a fourth interval time with $\tau_s = 10\text{s}$ was used.

3.3.2 Image processing in real space

As [fig. 3.13](#) explains, it is necessary to pre-process the measured images. Every spatial pixel intensity (in the camera plane $\sim \vec{x}$) of the measured images $I^m(\vec{x}, t)$ (m : measured) is formed due to a heterodyne overlap intensity signal, of the scattering amplitudes $I^f(\vec{x}, t) \propto \delta n$ (f , contains all fluctuations) and the transmitting background intensity $I^b(\vec{x})$ (b : background).

$$I^m(\vec{x}, t) = I^b(\vec{x}, t) + I^f(\vec{x}, t) \quad (3.9)$$

To separate the different overlapping fluctuation parts (in $I^f(\vec{x}, t)$) we use a Fourier analysis of the images, which will follow in [fig. 3.15](#). This method enables the individual contributing scattering signals to be isolated and plotted against the associated scattering vectors (q -values). But before we introduce the Fourier analysis, the images are pre-processed. As a first step, all the measured images $I^m(\vec{x}, t)$ are normalized to their own spatial mean grey-value, in order to exclude power fluctuations of the light source, which could result in temporal intensity changes.

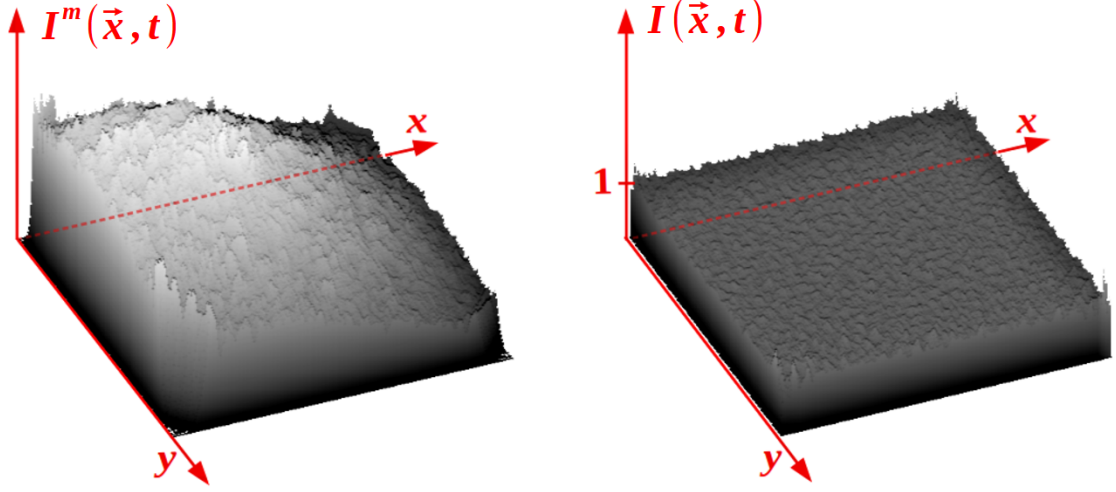


Fig. 3.13: LEFT: Actual measured image $I^m(\vec{x}, t)$, which includes the intensity beam profile and the fluctuations. RIGHT: Spatial and temporal normalized image $I(\vec{x}, t) = \langle \langle I^m(\vec{x}, t) \rangle_x \rangle_t$. The remaining roughness is the dominating fluctuation intensity in the images (easier to see on the PC). Fig. 6.5 of the appendix represents this process stylized from the point of view of individual pixels.

For that reason they are eliminated. The calculation of the spatial mean grey-value

$$gv^{av}(t) = \frac{\sum_{x=1}^X \sum_{y=1}^Y I^m(x, y, t)}{X \cdot Y} \quad (3.10)$$

is done by averaging over all pixels in the image, with the total pixel number X in x-direction and Y in y-direction. The generated intensity profiles of the spatial averaged images

$$\frac{I^m(\vec{x}, t)}{gv^{av}(t)} = \overbrace{\frac{I^b(\vec{x}, t)}{gv^{av}(t)}}^{=I^b(\vec{x})} + \frac{I^f(\vec{x}, t)}{gv^{av}(t)} \quad (3.11)$$

are a sum of the static (time independent) background $I^b(\vec{x})$ and the time dependent fluctuation intensities $I^f(\vec{x}, t)/gv^{av}(t)$. Afterwards all images are also averaged temporally, which means a normalization with the static image:

$$I^{st}(\vec{x}) = \frac{\sum_i^N \langle I^m(\vec{x}, t_i) \rangle_{\vec{x}}}{N} \hat{=} I^b(\vec{x}) . \quad (3.12)$$

As mentioned, in the introduction of the fluctuation (section 2.4.1), fluctuations occur randomly, which means the temporally averaged result vanishes: $\sum_i^N \langle I^f(\vec{x}, t_i) \rangle_{\vec{x}} / N = 0$. The static information $I^{st}(\vec{x})$ contains thereby only the Gaussian profile of the light beam.

$$\begin{aligned} I(\vec{x}, t) &:= \frac{\langle I^m(\vec{x}, t) \rangle_{\vec{x}}}{I^{st}(\vec{x})} = \frac{I^b(\vec{x})}{I^{st}(\vec{x})} + \frac{\langle I^f(\vec{x}, t) \rangle_{\vec{x}}}{I^{st}(\vec{x})} \\ &= 1 + I_n^f(\vec{x}, t) \end{aligned} \quad (3.13)$$

The result of the temporal averaging is shown in the small calculation of eq. 3.13. The background signal of the spatial and temporal normalized images $I(\vec{x}, t)$ is a constant value of 1, on top we can find the fluctuation information $I_n^f(\vec{x}, t)$ (n : normalized). This is demonstrated on the right side in fig. 3.13. In appendix 6.6 the two described normalization steps are shown from the perspective of the image pixels.

Windowing

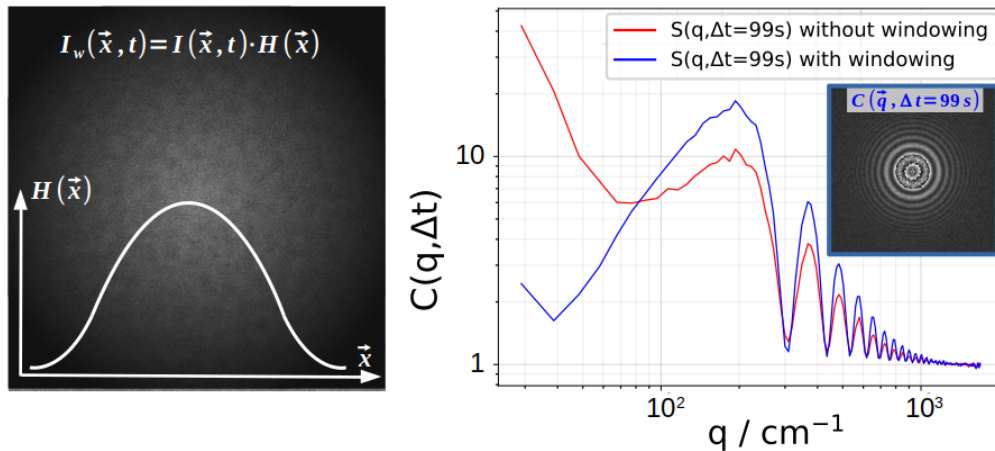


Fig. 3.14: RIGHT: Representation of $I_w(\vec{x}, t)$, the multiplication of the normalized image $I(\vec{x}, t)$ with the Hann-window-function $H(\vec{x})$. LEFT: Comparison of the resulting structure functions, in red without the windowing and in blue with windowing. The inset shows the image of the structure function $C(\vec{q}, \Delta t)$ of the blue curve. Parameters: $c = 0.02$, $M = 17.9 \text{ kg/mol}$, $\Delta T = 50 \text{ K}$, $T_0 = 25 \text{ }^\circ\text{C}$.

Before the image differences and the spatial Fourier-transformation can finally be

calculated, it is useful to multiply the normalized images with a window function^[63]. We use the Hann-function $H(\vec{x})$ ^[64].

$$I_w(\vec{x}, t) = I(\vec{x}, t) \cdot H(\vec{x}) \quad (3.14)$$

The favorable effect is shown in [fig. 3.14](#). The left side illustrates how the pixel intensity of the normalized images $I(\vec{x}, t)$ is modified by the window-function $H(\vec{x})$. By doing so, the fluctuations near the cell borders are weighted less than those in the center, which minimizes the border-effects. This is visible when the structure functions $C_{DDA}(q, \Delta t)$ are compared, shown on the right. It is clearly shown, that due to the windowing of the images, the introduced structure function is now modulated by a nearly perfect transfer function ($\sim \sin^2$). Otherwise the modulating transfer function $T(q)$, itself would be influenced by a Talbot-effect^[65]²⁴.

3.3.3 Image processing in Fourier space

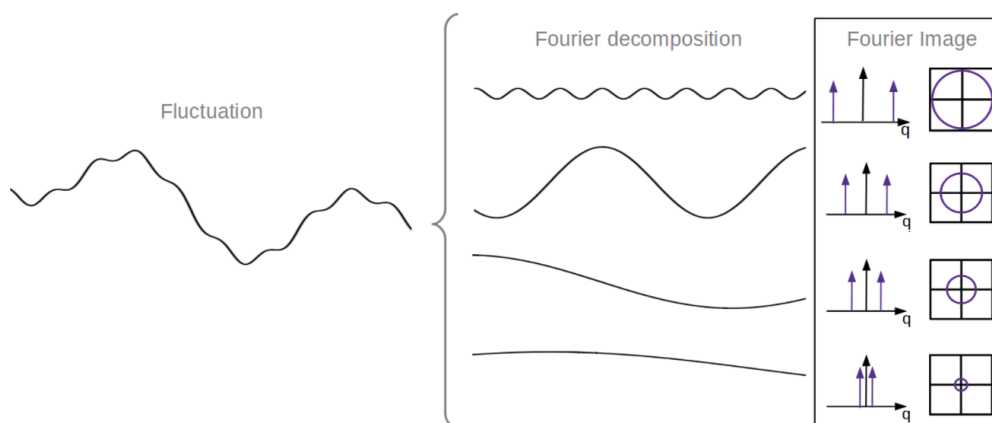


[Fig. 3.15](#): Decomposition of the individual refractive index fluctuations δn due to the Fourier-transformation. Additional illustration of the scattering vector peaks in the Fourier space of the individual fluctuations and the representation in the static structure factor images $S(\vec{q})$ (cf. [fig. 3.17](#)).

The sketch of [fig. 3.15](#) demonstrates the decomposition of the measured (heterodyne) fluctuation wave front (left side) into the individual wave fronts (middle), which are

²⁴A Talbot-effect is an additional exponential function, which deforms the sine-square oscillations.

each related to specific refractive index fluctuations δn . The right side connects the wave fronts to the calculated scattering vectors q in the Fourier-space (fig. 3.17). Before we calculate the q -values, we need to Fourier-transform the pre-processed images and perform the DDA. In eq. 3.15 the Fourier-transformation ($\mathcal{F}_x\{..\}$) of a certain image $I_w(\vec{x}, t)$ is shown:

$$i(\vec{q}, t) = \mathcal{F}_x\{I_w(\vec{x}, t)\} = \overbrace{\delta(\vec{q})}^{=\mathcal{F}_x\{1\}} + \overbrace{i_f(\vec{q}, t)}^{=\mathcal{F}_x\{I_n^f(\vec{x}, t) \cdot H(\vec{x})\}}. \quad (3.15)$$

As in section 2.4.1, lower case letters are used for the Fourier-transformed images ($I_w(\vec{x}) \rightarrow i(\vec{q})$). The next DDA-step is the image correlation and the calculation of the time differences Δt . These are evaluated as a squared absolute value ($|\cdot|^2$) to generate the structure functions $C_{DDA}(\vec{q}, \Delta t)$. $N = 200^{25}$ identical structure functions of the same time differences Δt are averaged together (temporal averaging $\langle \cdot \rangle_t$, eq. 3.16) to improve the signal to noise ratio. In this case, identical time

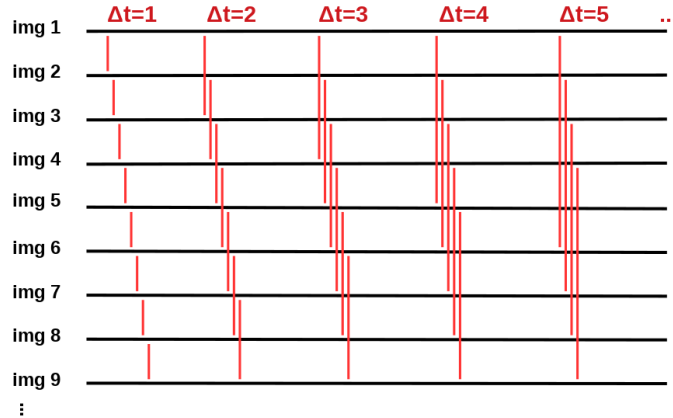


Fig. 3.16: Selection of the images for certain time differences Δt . For example, if $\Delta t = 2$ the image differences are calculated with the images $I_1(\vec{x}, 1) - I_3(\vec{x}, 3 \cdot \Delta t)$, so as with $I_2(\vec{x}, 2 \cdot \Delta t) - I_4(\vec{x}, 4 \cdot \Delta t)$ and so on.

differences Δt means that the image differences: $i(\vec{q}, t) - i(\vec{q}, t + \Delta t)$, formed with

²⁵With 200 identical time shifts of the 300 total images we generate 100 averaged correlation functions.

the same time shift of the detected images, which is demonstrated in [fig. 3.16](#).

$$\begin{aligned} C_{DDA}(\vec{q}, \Delta t) &= \left\langle \left| i^f(\vec{q}, t) - i^f(\vec{q}, t + \Delta t) \right|^2 \right\rangle_t \\ &= 2 \cdot C^f(\vec{q}, \Delta t) + B_0(\vec{q}, \Delta t) \end{aligned} \quad (3.16)$$

The in [eq. 3.16](#) shown value $(|..|^2)$ can be calculated with the binomial formula $((a - b)^2 = -2ab + a^2 + b^2)$. The mixed term (ab) is the dynamic contribution of the fluctuations (f : fluctuation).

$$C^f(\vec{q}, \Delta t) = \left\langle \left| i^f(\vec{q}, t) \right| \cdot \left| i^f(\vec{q}, t + \Delta t) \right| \right\rangle_t \quad (3.17)$$

The two squared terms (a^2, b^2) are static contributions

$$B_0(\vec{q}, \Delta t) = \left\langle \left| i^f(\vec{q}, t) \right|^2 \right\rangle_t + \left\langle \left| i^f(\vec{q}, t + \Delta t) \right|^2 \right\rangle_t \approx B_0, \quad (3.18)$$

because they don't include different times. This static part is neither q nor time dependent. Therefore the static part is a constant value B_0 . The experimental result of the refractive index structure function, calculated by the DDA, is:

$$C_{DDA}(\vec{q}, \Delta t) = 2 \cdot C^f(\vec{q}, \Delta t) + B_0. \quad (3.19)$$

The resulting structure function C_{DDA} is twice the structure function of the fluctuations C^f and an added constant background B_0 (static). The factor two, which comes from the binomial formula, can be explained, since two fluctuating images contribute to this one correlation calculation due to the image difference.

3.3.4 Processing of the structure function

As on the right side in [fig. 3.15](#) already indicated, demonstrates [fig. 3.17](#) how a certain refractive index fluctuation δn and the associated wave front (blue line) lead to a certain q -value in the Fourier-transformed images. If we shift $\vec{q} = (0, 0)$ into the center, these q -values are symmetrical rings. The center describes the transmitted light and the radii the magnitude of the scattering vectors (lower plot). For every correlation time Δt , we get from the DDA²⁶ a structure function

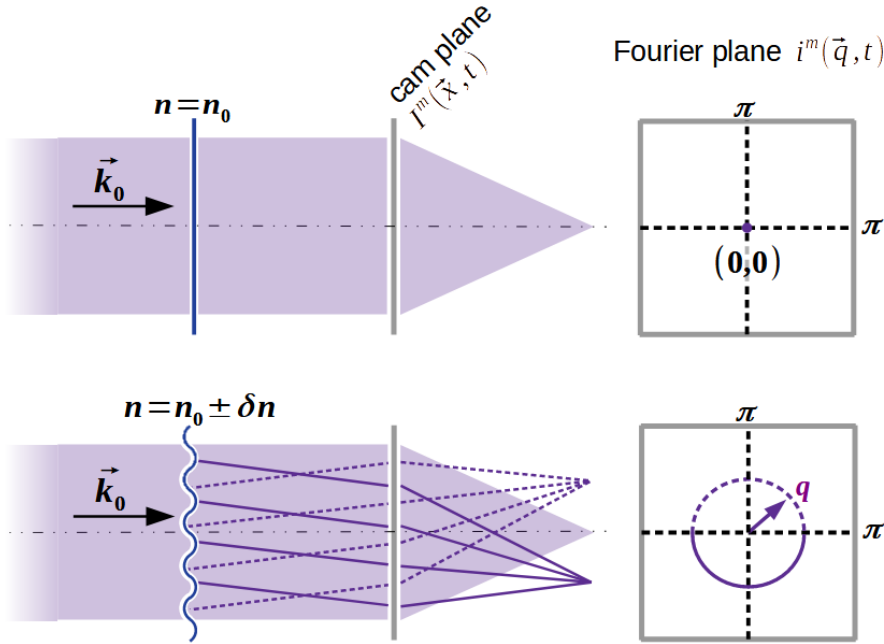


Fig. 3.17: Comparative illustration of the effects of refractive index fluctuations δn and the visualization of the fluctuation variables dependent scatter intensities in the Fourier image of the camera image.

image $C_{DDA}(\vec{q}, \Delta t)$, which is shown on the left side in fig. 3.18. The blue box demonstrates the smaller 'region of interest' (ROI) of $250 \times 250 \text{ px}^{-1}$, since in the larger q -area we detected only the background noise B_0 . The larger the original image (in real space), the smaller the q -step size of the inverse pixels. This leads to a q -step size of: $q_{min} = 9.67 \text{ cm}^{-1}$. The chosen maximum radius is thereby $q_{max} = 200 \cdot q_{min} \approx 1900 \text{ cm}^{-1}$. The right side of fig. 3.18 shows a quasi-anti-aliasing method, which defines which inverse pixels contribute to a certain q -value. The red colored squares are the contributing inverse pixels and the ratio of the covered to the uncovered area is the statistical weight of this pixel to the selected q -value ring (middle plot). This way of crediting the pixel values to a certain q -value corresponds to an azimuthal averaging $((\cdot)_{\phi_q})$ in polar coordinates $((q_x, q_y) \rightarrow (q, \phi_q))$ and

²⁶The associated program, 'DDA_100820_long.py', is saved under:
 $\sim / \text{DOC} / \text{Python} / \text{Shadowgraphie} / \text{Auswertung} / \text{DDA_SORT}$.

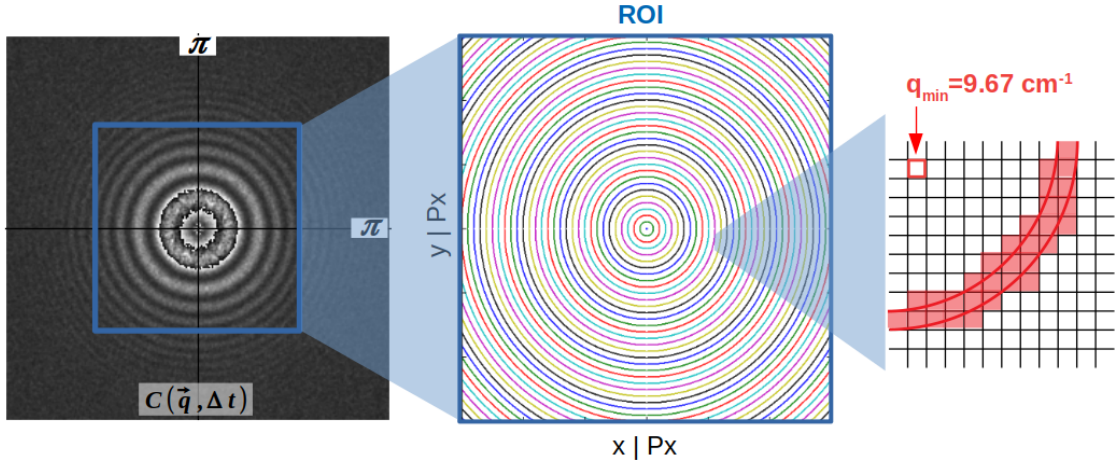


Fig. 3.18: LEFT: Representation of $C(\vec{q}, \Delta t)$ and the Region Of Interest (ROI). MIDDLE: Illustration of the look up matrix which specifies which pixels belong to which q . Some pixels that belong together are shown in the same color. RIGHT: The pixels belonging to a certain q value are assigned to the corresponding q based on their statistical weight. This is derived from the anti-aliasing method.

ultimately determines the experimental structure functions

$$C_{DDA}(q, \Delta t) = \langle C_{DDA}(\vec{q}, \Delta t) \rangle_{\phi_q} = 2 \cdot C_f(q, \Delta t) + B_0 . \quad (3.20)$$

The last function we need to consider is the intensity modulation due to the transfer function^[56] $T(q)$, which we can see in the left plot of [fig. 3.18](#). It is an interference effect of the two scattered beams ($\pm \delta n \rightarrow \pm q$) and the transmitted one ($n_0 \rightarrow q = 0$):

$$T(q) = 4 \cdot \sin^2 \left(\frac{z}{2k} q^2 \right) . \quad (3.21)$$

As in [section 2.6](#) explained, the fluctuation theory provides a structure function of the refractive index fluctuations ([eq. 2.47](#)), which is related to the time dependent structure factor $S(q, \Delta t)$ ([eq. 2.54](#), [eq. 2.55](#)). Finally it is necessary to connect the theoretical and experimental functions:

$$\begin{aligned} C_{DDA}(q, \Delta t) &= 2T(q) \cdot S(q, \Delta t) + B_0 \quad (3.22) \\ &= 2T(q) \cdot \left(\sum_{i=T,c} S^i(q) [1 - f(\Delta t, \tau^i(q))] \right) + \overbrace{B^T + B^c + B_0}^{\approx B_0} . \end{aligned}$$

In eq. 3.22 is the final result and the required connection of the theory and the experimental images analysis shown. It is assumed that the thermal B^T and solutal background terms B^c (cf. eq. 2.54) are dominated by experimental background noise B_0 . Additionally we can see, that the transfer function $T(q)$ and the theoretical structure factor replace the fluctuating term $C_f(q, \Delta t)$ of eq. 3.20.

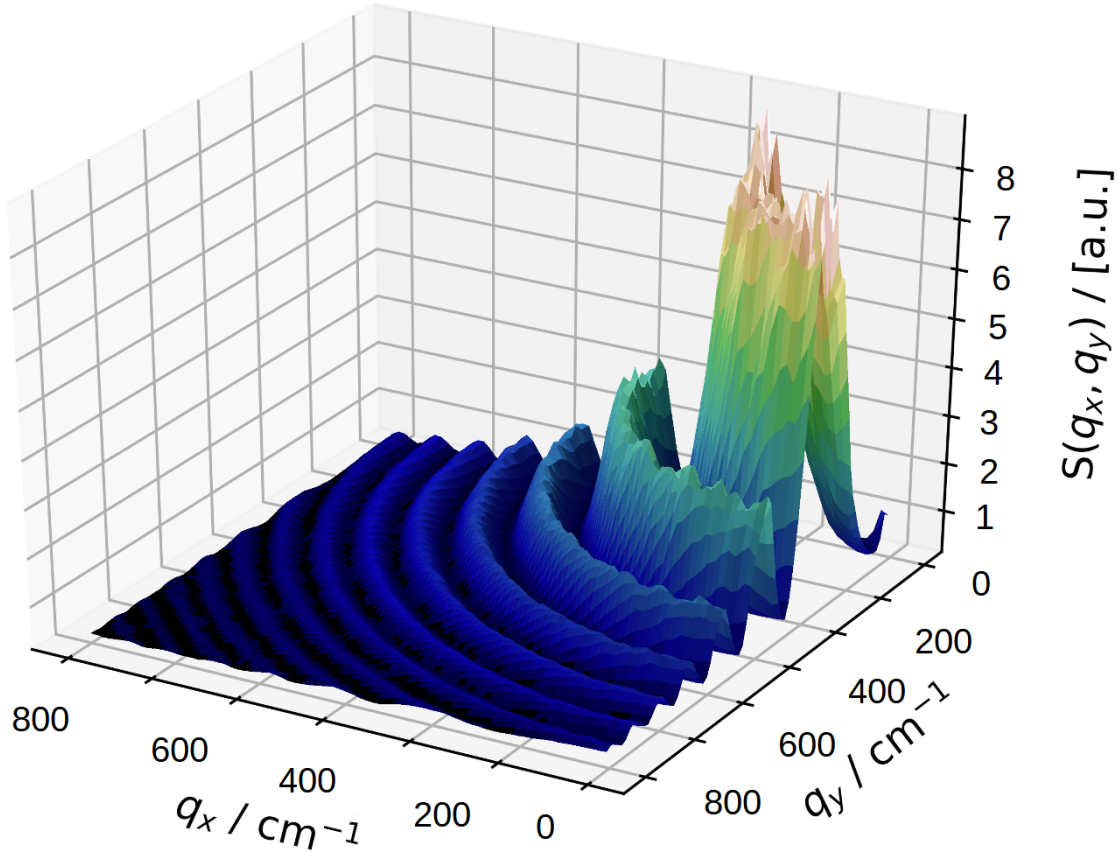


Fig. 3.19: Actual 3D surface presentation of a quarter of the static structure factor from fig. 3.18, where the transfer function $T(q)$ is still included in the form of the oscillations. Sample: $c = 50\%$ polystyrene ($M = 4.8 \text{ kg/mol}$) in toluene, with $\Delta T = 30 \text{ K}$ around $T_0 = 298.15 \text{ K}$.

The last, additional figure of fig. 3.19 shows a sectional view of a real structure function. It can be clearly seen that the amplitudes increase noticeably towards $q \rightarrow 0$ and run into a background plateau in the opposite direction ($q \rightarrow \infty$). All in chapter 4 following structure functions of the experimental results are produced with the now presented, self-written, image analysis program.

4 Results and discussions

The first [section 4.1](#) demonstrates the critical evaluation steps of the final structure function [eq. 3.22](#) from the experimental [section 3.3.4](#), at an actual measurement. It introduces the significant fit parameters and their further implications. In addition it relates these parameters to [fig. 2.12](#) from [section 2.6](#), which was the final illustration of the theory [chapter 2](#).

[Section 4.2](#) introduces a complete simulation of our NEF measurements, which provides the most important achievement of this thesis. Therefore the simulation first establishes all the necessary thermophysical parameters. Subsequently these are used to calculate the non linear temperature and concentration distributions inside the cell, which finally deliver the NEF signals of the structure functions. The simulated signals and the resulting transport coefficients are then compared with actual experiments. The most important result of this work is the non linearity of the diffusion equation, which has significant effects on the NEF signals and the transport coefficients involved.

Then [section 4.3](#) provides a systematic analysis of the experimental static structure factor. It isolates certain external influences and describes their dependencies. We start in the first sub-section with the thermal characterization and follow with a simultaneously description of the concentration and the molar mass effects. In both sub-sections we focus on the q roll-off values and the resulting NEF amplitudes, in which we pay attention to collective movements of multiple curves in the included c -, M -limits.

The final [section 4.4](#) ultimately connects the most important achievements and shows the dependencies of the fluidal transport quantities. These are the diffusion coefficient, the Soret coefficient and the thermodiffusion coefficient. Again we consider the external parameters and group them in the thermal and solutal sub-sections. In addition an overview of all simulated and experimental samples is provided.

4.1 Evaluation system

This first section serves as a reminder of the final theoretical presentation [fig. 2.12](#) in [section 2.6](#). Therefore, we evaluate¹ exemplarily an actual experiment, which is generated with the image preparation routine, introduced in [section 3.3](#). Every highlighted evaluation step refers to one of the three subplots in [fig. 2.12](#). For that reason, to each of the following experimental figures a stylized version is attached, which describes the essential parameters and helps to connect the plot to its theoretical pendant. The presented sample is a dilute ($c = 0.02$ g/g) binary mixture of polystyrene ($M = 90.9$ kg/mol) dissolved in toluene. The measurement is detected with three decadal interval times $\tau_s = 10, 100, 1000$ ms and for 300 images each. The applied temperature gradient $\vec{\nabla}T_0 = 10^4$ K/m originates from the temperature difference of 50 K between the 5 mm separated sapphire boundaries. For the calculation of the structure functions $C(q, \Delta t)$ of every q value, we averaged 200 difference images of the same time steps, as introduced in [fig. 3.16](#).

Following our publication [47] and as explained in [eq. 3.22](#), the first step is to consider the total structure functions $C(q, \Delta t)$ as a sum of two individual contributions $C^i(q, \Delta t)$, with one fast thermal ($i = T$) and a slower solutal ($i = c$) mode.

$$C(q, \Delta t) = \sum_{i=c,T} \overbrace{a^i(q) \cdot \left[1 - \exp\left(-\frac{\Delta t}{\tau^i(q)}\right) \right]}{=C^i(q, \Delta t)} + B_0 \quad (4.1)$$

Three of these total structure functions and the associated fits are shown as the dots and the solid lines in the left plot of [fig. 4.1](#). The right illustration demonstrates a simplified version of the lower left plot of [fig. 2.12](#) and links especially the greenish q -value of 89 cm^{-1} to the theoretical representation. The shown functions are conceptionally different. Starting from the top, the light green one, visualizes the mentioned q value of 89 cm^{-1} . It's a signal where both thermal and solutal contributions appear, despite their different time scales ($\tau^T \approx 0.2$ s, $\tau^c \approx 20$ s). The magenta curve shows a relatively small q -value of 40 cm^{-1} , where mainly the fast

¹The associated program: '*STRUCT_FIT_210621.py*', is located at
 $\sim /DOC/Python/Shadowgraphie/Auswertung/STRUCTURE_FCT$.

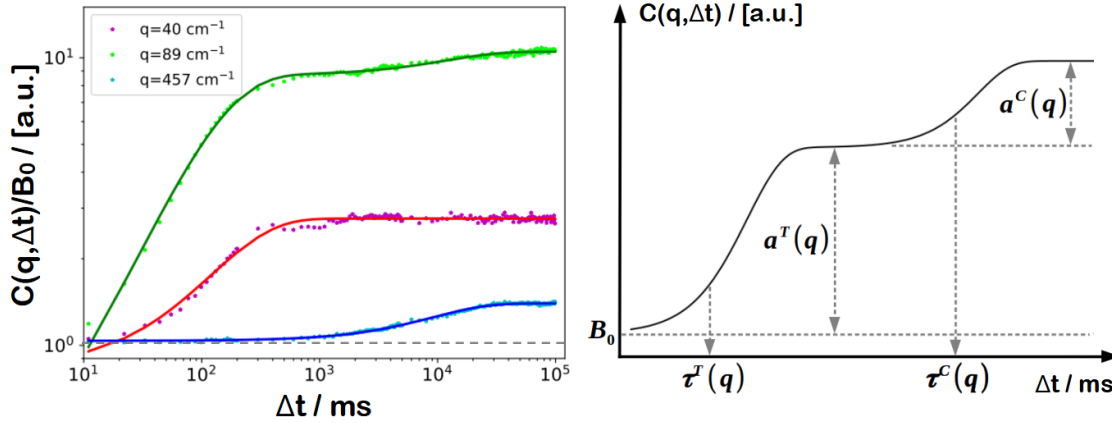


Fig. 4.1: Illustration of three different structure functions (dots) of a $c = 0.02$ [w/w], $M = 90.9$ kg/mol mixture and the associated fit curves (lines). Shown is a fast purely thermal process in magenta ($q = 40$ cm $^{-1}$), a slow solutal one in cyan ($q = 457$ cm $^{-1}$) and in light green, a combination of both ($q = 89$ cm $^{-1}$). Superimposed the associated fit curves are shown with the red, blue and green solid lines. The right panel is a sketch with all four fit parameters. It builds the connection to the lower left sub-plot of fig. 2.12.

thermal signal can be found (C^T). On the other hand, the large $q = 457$ cm $^{-1}$ value of the blue curve is a pure (slow) solutal signal (C^c). As indicated in the right sketch, each of the contributions ($i = c, T$) includes an own amplitude $a^i(q)$ and a relaxation time $\tau^i(q)$. These are the important, q value specific quantities of the next two evaluation steps.

$$\tau^i(q) = \frac{1}{\chi q^2 \cdot [1 + (q_{ro}^i/q)^4]}, \quad \text{for } i = \begin{cases} c : \chi = D \\ T : \chi = D_{th} \end{cases} \quad (4.2)$$

$$a^i(q) = 2 \cdot T(q) \cdot S^i(q) \quad (4.3)$$

The second step is the analysis of the thermal ($i = T$) and solutal ($i = c$) relaxation dynamics $\tau^i(q)$. This is shown in fig. 4.2. The left side demonstrates our actual fitted relaxation times (of eq. 4.1) as the magenta (thermal) and turquoise (solutal) dots. Additionally, the solid red and blue lines show the bell shaped fit functions of eq. 4.2. The right panel visualizes one of these modes and is the connection to the upper right plot of fig. 2.12. In there, the blue area represents the gravitationally limited q -region. The maximum of the curve, or in other words the end of this region, defines the associated roll-off value q_{ro}^i . The right flank of the bell-shaped

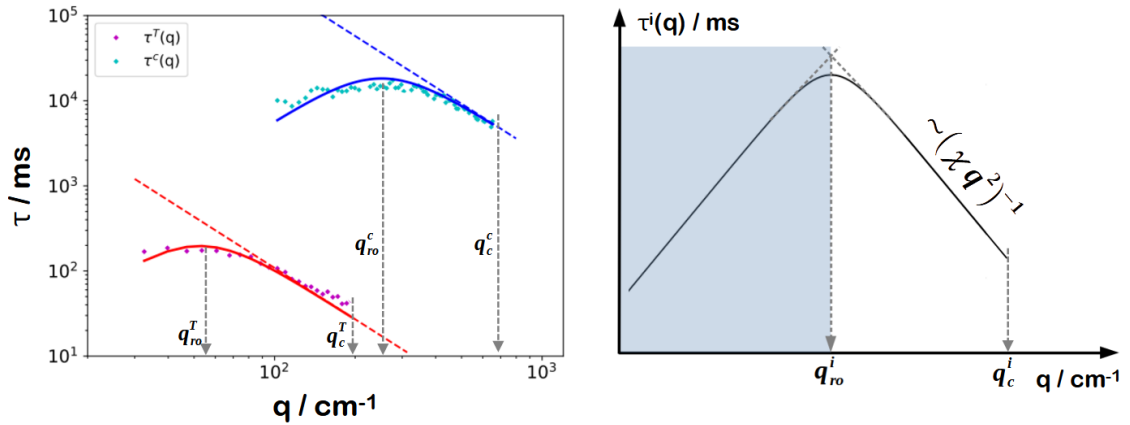


Fig. 4.2: Demonstration of the thermal (shown in magenta) and solutal (turquoise) relaxation time behaviors. Both show a maximum, which determines the individual roll-off values q_{ro}^i and a cut-off threshold q_c^i . The right flanks demonstrate the direct transport coefficients, the thermal diffusivity $\chi = D_{th}$ and the diffusion coefficient $\chi = D$ respectively. The blue region in the right plot indicates the gravitationally limited area, where the dynamics of the individual modes is slowed down or quenched due to buoyancy effects.

curves is the non equilibrium region, where free diffusion ($\chi = D$), or free heat diffusion ($\chi = D_{th}$), occurs. The dashed lines in the left plot illustrate these free diffusion processes $\sim q^{-2}$, which would occur under micro gravity. These right flanks end, for large q values, at the associated cut-off thresholds q_c^i . That is the point where the NEF amplitudes ($\sim q^{-4}$) are dominated by the background B_0 , which can be seen in [fig. 4.3](#), indicated with the red arrow.

In the third step we analyse the NEF amplitudes $a^i(q)$ of the static structure factors in combination with the total static structure factor², which is determined in our evaluation routine by the longest possible correlation time $C(q, \Delta t \rightarrow \infty) \rightarrow S(q)$. Towards the end of the evaluation work, it was shown that the total static structure factor is better replaced with the sum of the fit amplitudes $a(q) = \sum a^i(q)$. In future projects this will be implemented³. The right illustration of [fig. 4.3](#) again is a connection to [fig. 2.12](#) and shows one individual static structure factor contribution

²total: sum of the thermal and solutal contribution.

³This filters additional modulations of the longest correlation times. For example, long-wave building vibrations that the tables cannot dampen.

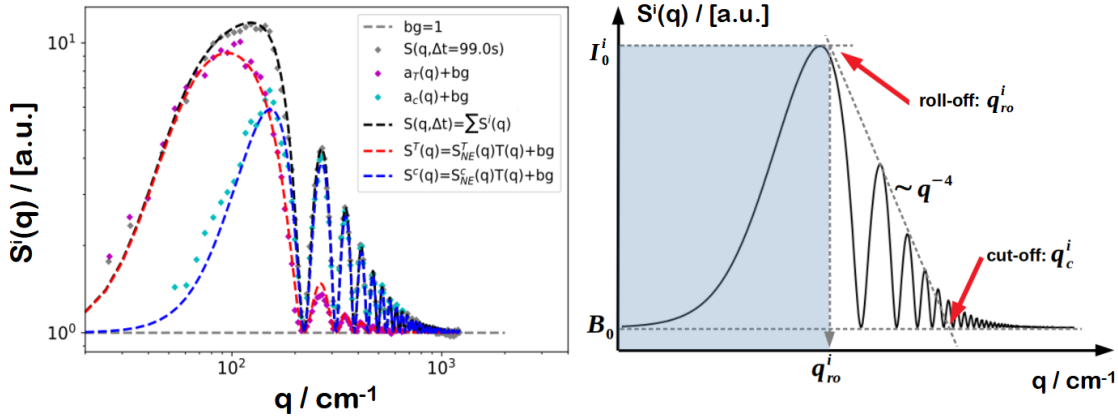


Fig. 4.3: Representation of the thermal and solutal amplitudes a^i of fig. 4.1 (colored dots) and their fits (dashed lines). In addition, the static structure factor is shown (gray dots), which is fitted by the sum of the two modes (black dashed line). The right panel explains the important aspects, such as the roll-off and cut-off thresholds or the gravitationally limited amplitude I_0^i (of one mode), in a simplified illustration.

$S^i(q)$ ($i = T, c$):

$$S^i(q) = \left(\frac{\partial n}{\partial i} \right)^2 \frac{I_0^i}{1 + \left(\frac{q}{q_{ro}^i} \right)^4} + B_0. \quad (4.4)$$

We can see the characteristic $\sim q^{-4}$ dependency of the NEF amplitudes, which is located between the roll-off q_{ro}^i and cut-off q_c^i thresholds of q ($q_{ro}^i < q < q_c^i$, highlighted by the red arrows). In the introduced blue q -region, the gravitationally limited intensity I_0^i ($q \rightarrow 0$) can be seen, which is magnitudes smaller than in micro gravity conditions (extension of the q^{-4} proportionality). The oscillations in the amplitudes are caused by the experimental transfer function $T(q)$ (already included in eq. 4.3), an interference effect, which is explained in eq. 3.2. Our fit algorithm combines in a simultaneous process both individual amplitudes a^i (magenta, cyan dots in fig. 4.3) with the total static factor (grey dots) and fits the coupled intensities I_0^i ($q \rightarrow 0$) and the static roll-off values q_{ro}^i simultaneously to all three curves. This is explained in detail in our publication [47]. The results are the three dashed lines, in red and blue the thermal and solutal static structure factors $S^i(q)$, respectively. Additionally we get the total static structure factor $S(q) = \sum S^i(q)$ (black dashed line) by the sum of both modes. This sum fits perfectly the experimental static structure factor $S(q)$ (amplitudes of the longest correlation time $C(q, \Delta t = 99 \text{ s})$).

Finally, we calculate the Soret-coefficient S_T from the concentration gradient $\vec{\nabla}c$, which is included in the solutal q roll-off value q_{ro}^c and the Soret equation 2.4 (shown in eq. 4.6):

$$q_{ro}^c = \left[\frac{g \cdot \beta_c \cdot |\vec{\nabla}c|}{\nu \cdot D} \right]^{1/4} \quad (4.5)$$

$$S_T = \frac{-\vec{\nabla}c}{\vec{\nabla}T \cdot c(1-c)} = \frac{-1}{\vec{\nabla}T \cdot c(1-c)} \cdot \frac{(q_{ro}^c)^4 \cdot \nu \cdot D}{g \cdot \beta_c}. \quad (4.6)$$

The roll-off value q_{ro}^c appears in the solutal relaxation time $\tau^c(q)$ as well as in the static solutal structure factor $S^c(q)$ and is experimentally not always the same. Therefore we follow *Croccolo et al.*^[66] and differentiate them as the dynamic (from $\tau(q)$) and the static (from $S(q)$) q roll-off values. We will return to this in section 4.2 and provide an explanation for the differences. But the actual NEF theory states, that these two values must be identical.

The necessary parameters for the fit functions of eq. 4.5 and eq. 4.6, are the kinematic viscosity $\nu = \eta\rho$ and the solutal expansion coefficient β_c , which can be measured and estimated as shown in eq. 3.6 and eq. 3.8. Finally, the diffusion coefficient D is obtained from the fit of the solutal relaxation time $\tau^c(q)$ and explains the free diffusion section (right flank and micro gravity behavior). The resulting

	experiment $c = 0.2\%$	literature $c = 1\%$ [67]
$S_T / 10^{-2}\text{K}^{-1}$	$44.36 \pm 4^*$	21.5 ± 2
$D / 10^{-10}\text{m}^2/\text{s}$	$0.43 \pm 0.04^*$	0.54 ± 0.05

Tab. 4.1: Comparison of the resulting experimental transport coefficients ($T_0 = 298.15$ K, with $\Delta T = 50$ K) of a $c = 0.02$ [w/w], $M = 90.9$ kg/mol polystyrene/toluene mixture and the associated literature values of *Schwaiger*^[67].

transport properties are listed in tab. 4.1, where we compare them with the literature values^[67] of a slightly different concentration $c = 1\%$. In general the transport properties of such small concentrations should not change or change only slightly (at least for smaller molar masses). However, especially the experimental Soret coefficient differs notably from the literature value. The demonstrated experimental

properties, which are marked with a star (*), are affected by the same effects, which provide the differences in the q roll-off values. Therefore these values are not well suited for an actual comparison and for now should be simply viewed as preliminary experimental results. The effects meant, are on the one hand non linearities of primary the solutal mode and on the other hand thermal dependencies of the transport coefficients ($D(\Delta T)$, $S_T(\Delta T)$, etc.). We will look into these effects in more detail in [section 4.2](#) and [section 4.4](#), where we will also bring back this table and correct the results.

Note

There is an alternative way of estimating the Soret-coefficient S_T , which we have suggested as a possibility in our publication [47]. For this, the ratios of the expansion coefficients, the transport parameters and the roll-off wavevectors are used:

$$S_T = \frac{-1}{c(1-c)} \frac{\beta_T}{\beta_c} \frac{D}{D_{th}} \left(\frac{q_{ro}^c}{q_{ro}^T} \right)^4. \quad (4.7)$$

The advantage is that no optical contrast factors are required and that the viscosity dependence disappears. Consequently, no external measurements are required.

4.1.1 Application

The evaluation just shown, which is based on the theory already presented in [section 2.6](#), was proposed in our publication [47]. Therein we specified that for polymer samples with large Lewis numbers ($Le = D_{th}/D \approx 100$), which means easily distinguishable thermal and solutal modes, our treatments [eq. 2.54](#) and [eq. 2.55](#) of the structure function leads to notably better results. This was shown experimentally with a $c = 0.02$ polystyrene ($M = 4.84$ kg/mol) in toluene mixture. The shadowgraphy setup used was an earlier, monochrome ($\lambda_{red} = 670$ nm), state of the current one with the same Soret-cell but without the additional second telescope in front of the camera. [Fig. 4.4](#) shows plots of the evaluated relaxation times τ^i and structure functions C_i , which are very similar to the ones in [47]. The amplitudes of the right panel and especially the resulting relaxation times of the

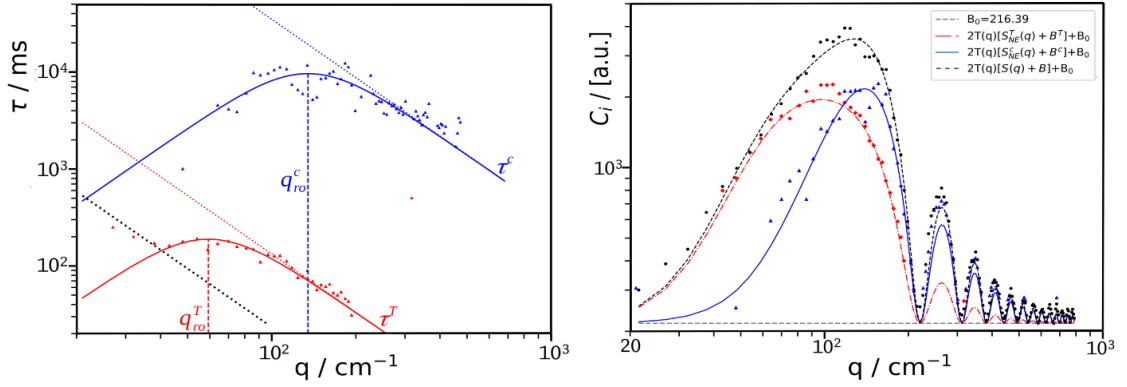


Fig. 4.4: Plot of the evaluated thermal ($i = T$) and solutal ($i = c$) relaxation times τ^i and structure functions C_i of [47]. Parameters: $c = 0.02$ g/g, $M = 4.84$ kg/mol, $\Delta T = 30$ K, $T_0 = 298$ K.

left one showed a greater scatter at that time. Comparing these results with the two plots on the left in fig. 4.2 and fig. 4.3, it is easy to see that the setup and the evaluation have further developed, resulting in better signal-to-noise ratios and generally smoother curves. Tab. 4.2 shows the resulting transport coefficients and the comparison of TABLE II. in [47].

		Kan	Rau	Cro	Maz	Zapf
M	kg/mol	4.84	4.75	9.1	9.1	4.84
c	g/g	0.02	0.02	0.018	0.018	0.02
T	K	298	295	-	-	298
D	10^{-10} m ² /s		2.4 ± 0.07	2.03 ± 0.04	1.83 ± 0.37	2.75 ± 0.5
D_{th}	10^{-8} m ² /s	8.37 ± 0.15				7.5 ± 0.7
q_{ro}^T	cm ⁻¹				69	45.5 ± 2.5
q_{ro}^c	cm ⁻¹				233	144 ± 20
S_T	10^{-2} K ⁻¹		4.3 ± 0.2			2.9 ± 1.5
D_T	10^{-12} m ² /(sK)		10.3 ± 0.7			7.1 ± 4.0

Tab. 4.2: Representation of the final results of [47], where Zapf are our ones, Kan (*Kantelhardt*), Rau (*Rauch*^[68]), Cro (*Croccolo*^[4]), and Maz (*Mazzoni*^[69]).

4.2 Simulation of non linearities in NEFs

The intention of this section is to introduce and confirm a completely simulated description for the resulting structure functions $C(q, \Delta t)$ of our shadowgraphy setup. Special attention will be paid to the non linearities of the Soret-equation 2.4 (results from the diffusion equation)

$$\vec{\nabla}c = -S_T \vec{\nabla}T \cdot c(1 - c) , \quad (4.8)$$

which are neglected in the case of many other methods, such as *optical beam deflection* (OBD)^[10,13,14,15] and *thermal diffusion forced Rayleigh scattering* (TDFRS)^[10,11,12]. This can be explained by their very small temperature differences, OBD approximately 1 K and TDFRS a few mK. In the case of shadowgraphy, however, we work with differences up to 50 K over a cell height of 5 mm. As this section will show, these are circumstances in which a linear approximation no longer applies.

The simulation⁴ interprets the entire signal as a layer model of $N = 100$ individual and independent (index i) structure functions $C_i(q, \Delta t, z)$. Every layer (height variable z) contributes thereby with an own non linearly related composition, which will be explained in section 4.2.1 and 4.2.2. The plot of fig. 4.5 illustrates, for a specific $q = 115 \text{ cm}^{-1}$ value, all the related structure functions $C_i(q, \Delta t, z)$ as thin cyan lines. On top, three signature layers are highlighted with thicker dark blue lines. This way of representation is used in several of the following figures, where the signals of the boundary layers at $z = 0$ and $z = h$ are shown with thick solid and dashed blue lines and where the central layer at $z = h/2$ is highlighted by the dotted thick blue line. The graphs are completed by the thick black lines, which represents the averaged signal of all involved layers:

$$C(q, \Delta t) = \frac{1}{h} \int_0^h C_i(q, \Delta t, z) dz . \quad (4.9)$$

We interpret this average quantity as the experimentally available counterparts of our simulation model. In addition to the mentioned, highlighted signature layers,

⁴The simulation program, 'TOTAL_TC_SIM_NEW.py', can be found under:

'~/DOC/SIMULAT_Temp_Abh/SIM_PS_TOL_TOT'.

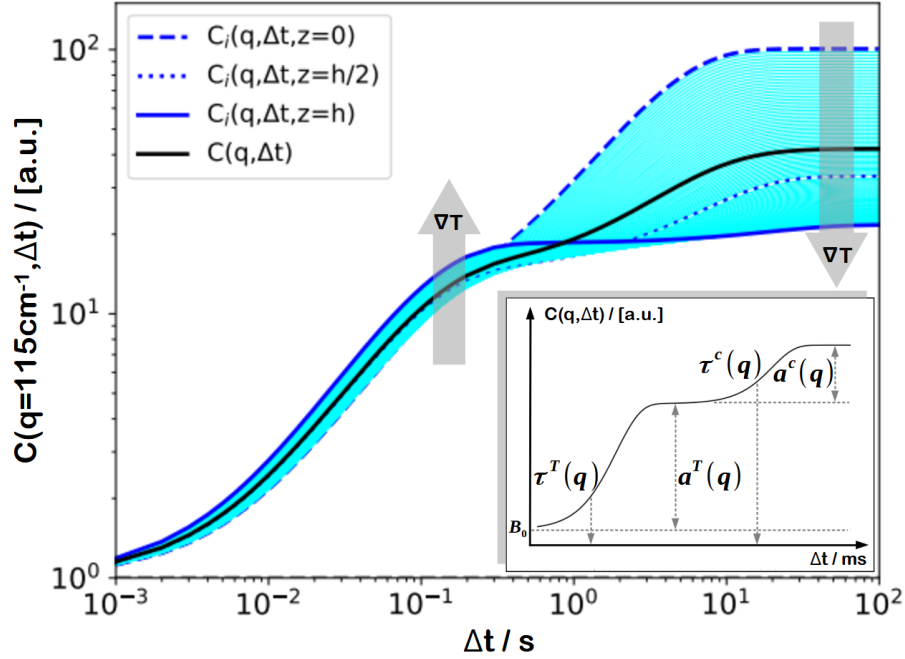


Fig. 4.5: Illustration of all the individual correlation signals $C_i(q, \Delta t, z)$ for a specific $q = 115 \text{ cm}^{-1}$ value^[70]. The three blue highlighted curves are the signature heights $z = 0, h/2, h$. The black line reflects the structure function $C(115 \text{ cm}^{-1}, \Delta t)$, which is the averaged portion of all the contributing layers and which is available through the experiment. The thermal and solutal parts of every layer are demonstrated in the inset. Due to the gray arrows the direction of the temperature gradient $\vec{\nabla}T$ is shown. It should help to understand which cell side provides the dominant signal.

the direction of the temperature difference is indicated by large gray arrows. This is intended to give a sense when the hot, upper layers and when the cold, lower ones provide the dominant signal. Especially since the hot cell side dominates in the thermal signal part and the cold side in the solutal part. The simulated sample of this section is a dilute solution of polystyrene ($M = 17.9 \text{ kg/mol}$) in toluene with a concentration of $c_0 = 0.01 \text{ g/g}$, for which a complete temperature series is present. The temperature difference $\Delta T = 30 \text{ K}$ is applied symmetrically around the average temperature of $T_0 = 298.15 \text{ K}$ and over the mentioned cell height of $h = 5 \text{ mm}$.

At first we present in [section 4.2.1](#) the essential thermophysical parameters, which form the base of the simulation. Afterwards we show in [section 4.2.2](#) the resulting

non linear temperature and concentration distributions. Finally, [section 4.2.3](#) demonstrates the calculations of the structure functions and the resulting measurable signals (of τ^i and a^i). [Section 4.2.4](#) evaluates these functions in the introduced way, where we get the resulting transport properties. The last [section 4.2.5](#) compares in step one the simulated signals of [section 4.2.3](#) and in step two the resulting transport coefficients of [section 4.2.4](#) with actual experiments of the temperature series. With that we then can ultimately confirm our simulations and use the knowledge in the following chapters.

4.2.1 Thermophysical parameters

This sub-section presents the calculation methods for the thermophysical parameters. Those are the diffusion (D), Soret (S_T) and thermodiffusion coefficient (D_T), as well as the thermal diffusivity (D_{th}) and the kinematic viscosity (ν). To avoid problems, we simplified our region of interest and only considered polymer mixtures far from glass transition effects (introduced in [fig. 3.10](#)). For this purpose, *J. Kantelhardt* measured with our TDFRS-setup^[10,11,12] $S_T(T)$, $D(T)$, $D_T(T)$ and $D_{th}(T)$ of a certain sample ($c = 1\%[\text{w/w}]$, $M = 4.84 \text{ kg/mol}$) for several different ambient temperatures: between 10°C and 50°C . The procedure and the evaluation

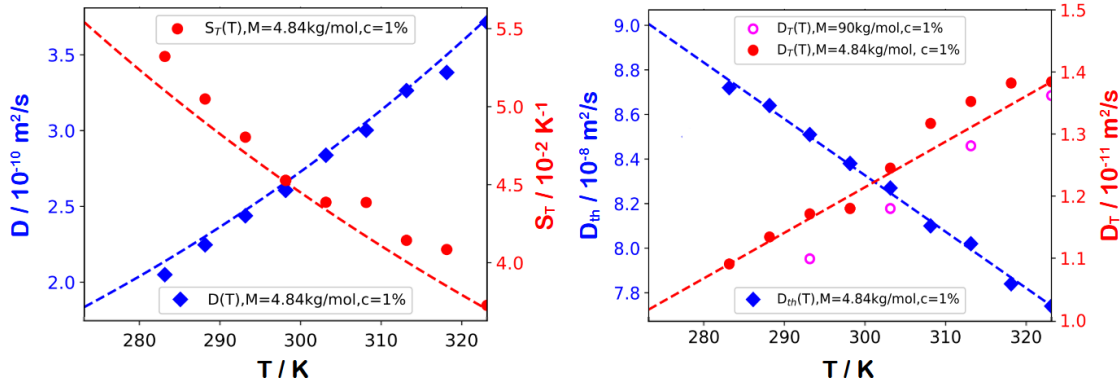


Fig. 4.6: Comparison of the measured (markers) transport properties, $S_T(T)$, $D(T)$, $D_T(T)$ and $D_{th}(T)$, with the simulation models (dashed lines). For a $c = 0.01$, $M = 4.84 \text{ kg/mol}$ mixture *J. Kantelhardt* measured, with our TDFRS setup, the transport properties for different temperatures (more details in [section 6.8](#)). In order to show the solutal independence of D_T , a further molar mass ($M = 90 \text{ kg/mol}$, magenta open dots) from *Schwaiger*^[71] is embedded. Based on [70].

method is briefly explained in [appendix 6.8](#). Both, the red circles and blue diamond values of [fig. 4.6](#) show his comparison quantities, they serve as control values of our calculations or as actual fit values.

a) Soret coefficient

We start with the model for the Soret coefficient $S_T(M, c, T)$, which is demonstrated by the red dashed line in the left panel of [fig. 4.6](#). It is the most important parameter in the Soret-equation [4.8](#), since it directly affects the concentration distribution. The parameterization follows *Schwaiger*^[62]. The coefficient is thereby constructed out of two individual parts, one temperature $\tilde{S}_T(T)$ and the other one molar mass and concentration $\hat{S}_T(M, c)$ dependent.

$$S_T(M, c, T) = \tilde{S}_T(T) \cdot \hat{S}_T(M, c) \quad (4.10)$$

$$S_T(M, c, T) = \left(\frac{T_0}{T}\right)^{2.4} \cdot \frac{a(M)}{1 + b(M) \cdot c^{\beta(M)}} \quad (4.11)$$

Included are the molar mass⁵ dependent parameters: $a(M)$, $b(M)$ and $\beta(M)$. These are empirically motivated quantities, modified for the measurements of *Schwaiger* and presented in [62].

$$a(M) = 3.294 \cdot 10^{-4} \cdot M^{0.58} \quad (4.12)$$

$$b(M) = \frac{a(M)}{0.012} - 1 \quad (4.13)$$

$$\beta(M) = \frac{35.42}{\sqrt{M}} + 0.82 \quad (4.14)$$

As [fig. 4.6](#) illustrates, the calculated curve of the Soret coefficient $S_T(T)$ (dashed red line) show slight deviations to the measured values of *J. Kantelhardt*. However, since the diffusion $D(T)$ and the thermodiffusion coefficient $D_T(T)$ fit almost perfectly, measurement inaccuracies could have influenced the S_T results of *J. Kantelhardt*.

b) Diffusion and thermodiffusion coefficient

Next we want to focus on the diffusion coefficient $D(M, c, T)$, which can be calculated with the definition of the Soret coefficient (established in [eq. 2.10](#)) and the

⁵M in g/mol.

thermodiffusion coefficient $D_T(T)$.

$$D(M, c, T) = \frac{D_T(T)}{S_T(M, c, T)} \quad (4.15)$$

If we reflect again [fig. 4.6](#), we can see that the model of [eq. 4.15](#) (dashed blue line, left) matches the measured values (blue diamonds) exactly. Therefore we needed a calculation basis for the thermodiffusion coefficient $D_T(T)$. It is known from *Rauch*^[72], that D_T is molar mass independent and that its concentration dependence can be neglected for $c \lesssim 0.1$ ⁶. That means we only need a description of the temperature dependence, which we can fit (red dashed line, right) to the TDFRS measurements of *J. Kantelhardt*:

$$D_T(T) = D_T(T_0) + 7.339 \cdot 10^{-14} \frac{\text{m}^2}{\text{sK}^2} (T - T_0) \quad (4.16)$$

The in [eq. 4.16](#) used average thermodiffusion coefficient at $T_0 = 298.15$ K is $D_T(T_0) = 1.201 \cdot 10^{-11} \text{m}^2/\text{sK}$. To illustrate, the mentioned, molar mass independence of $D_T(T)$, the right panel of [fig. 4.6](#) shows, additional to the fitted values ($M = 4.84$ kg/mol, red circles) also magenta colored open circles for a $M = 90$ kg/mol, $c = 0.01$ g/g mixture^[71]. The points of the very different molar masses are close to each other and the temperature dependence (slope) is the same.

c) Thermal diffusivity

In a similar way we fit (dashed blue line, right in [fig. 4.6](#)) the temperature dependence of the thermal diffusivity $D_{th}(T)$ to the TDFRS measurements of *J. Kantelhardt* (blue diamonds, right). With an average value of $D_{th}(T_0) = 8.374 \cdot 10^{-8} \text{m}^2/\text{s}$.

$$D_{th}(T) = D_{th}(T_0) - 2.529 \cdot 10^{-10} \frac{\text{m}^2}{\text{sK}} (T - T_0) \quad (4.17)$$

There is no concentration dependence of the thermal diffusivity for our mixtures.

d) Expansion coefficients

⁶Molar mass independent for polymer chains longer than the Kuhn segment of around $M \approx 1$ kg/mol.

Additionally, we also need the expansion coefficients β_i ($i = c, T$) and a calculation method for the kinetic viscosity $\nu(M, c, T)$. The expansion coefficients β_i of eqs. 3.4 and 3.6, illustrated on the left in fig. 4.7, show no significant temperature or concentration dependency ($\beta_c \approx 4\%$, $\beta_T \approx 2\%$). That means we assume them as constant parameters:

$$\beta_T = -1.081 \cdot 10^{-3} \text{K}^{-1} \quad (4.18)$$

$$\beta_c = 0.211 \quad (4.19)$$

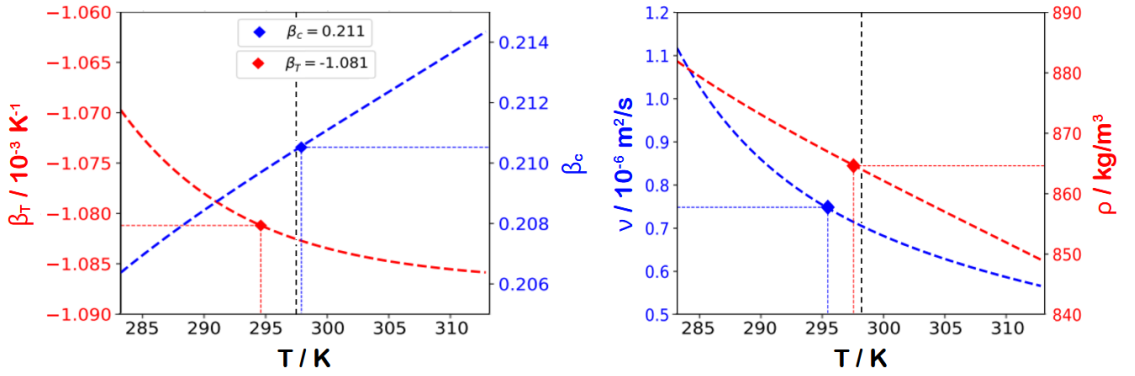


Fig. 4.7: LEFT: Illustration of the minor deviations of the thermal and solutal expansion coefficients β_T (red, eq. 3.4) and β_c (blue, eq. 3.6) from the average values. These marked values are our constant quantities. RIGHT: Representation of the kinematic viscosity ν (blue, eq. 4.20) and density ρ (red, eq. 4.21) in the cell. The average values are again shown with the corresponding markers and the attached guide lines. Parameters: $M = 17.9 \text{ kg/mol}$, $\Delta T = 30 \text{ K}$, $c_0 = 0.01$, $T_0 = 298.15 \text{ K}$.

e) Kinematic viscosity and density

The kinematic viscosity

$$\nu(M, c, T) = \frac{\eta(M, c, T)}{\rho(c, T)} \quad (4.20)$$

is the quotient of dynamic viscosity $\eta(M, c, T)$ and density $\rho(c, T)$. As explained in section 3.2, the density was measured by a density meter. In combination with the temperature dependency of toluene (from [73]) the parameterization

$$\rho(c, T) = \rho_{sol}(T_0) + 182 \cdot c - 0.933 \frac{\text{kg}}{\text{m}^3 \text{K}} (T - T_0) \quad (4.21)$$

results, with an average value of $\rho_{sol}(T_0) = 863 \text{ kg/m}^3$. Finally, we need a temperature and concentration dependent formulation for the dynamic viscosity $\eta(M, c, T)$. Following our assumptions, the temperature dependency is exclusively described by the solvent $\eta_{sol}(T)$. The solutal dependency follows *Matsuoka and Cowman*^[74], where it is calculated due to the specific $\eta_{sp}(M, c)$ and the intrinsic viscosity $[\eta](M)$.

$$\eta(M, c, T) = \eta_{sol}(T) \cdot (\eta_{sp}(M, c) + 1) \quad (4.22)$$

For the mentioned temperature dependencies of eq. 4.23 we use the formulation of *Santos et al.*^[75], where the average viscosity of toluene is given as $\eta_{sol}(T_0) = 0.632 \text{ mPas}$.

$$\eta_{sol}(T) = \eta_{sol}(T_0) \cdot \exp\left(-5.22 + \frac{8.964}{T/T_0} - \frac{5.834}{(T/T_0)^2} + \frac{2.084}{(T/T_0)^3}\right) \quad (4.23)$$

The concentration dependency is represented in the specific viscosity

$$\eta_{sp}(M, c) = c\rho(c, T) \cdot 10^{-3} [\eta](M) \cdot \left[1 + \sum_{i=1}^3 \frac{(0.4c\rho(c, T) \cdot 10^{-3} [\eta](M))^i}{i!}\right], \quad (4.24)$$

which follows *Matsuoka and Cowman*^[74]. The molar mass dependency is included in the intrinsic viscosity $[\eta](M)$, which usually would be described by the *Mark–Houwink–Sakurada equation* $[\eta] = KM^a$. In [76] *Wagner* proposes an advanced parameterization

$$\log([\eta](M)) = -0.538 + 0.203 \cdot \log(M) + 0.0471 \cdot \log(M)^2 \quad (4.25)$$

for the intrinsic viscosity. Therein η is in mL/g and M in g/mol^[70]. The right panel in fig. 4.7 demonstrates, in a familiar way, the calculated kinematic viscosity $\nu(T)$ (eq. 4.20) and the density $\rho(T)$ (eq. 4.21), both as function of the temperature T . Therefore it is not surprising that both, the average density and the viscosity are shifted in the right graph of fig. 4.7 towards the denser, cold side. These values are shown by the associated markers, which are connected, due to the thin dashed lines, to their respective axes.

Now we have all the necessary parameterizations for the calculation of the NEF

signals. This enables us to simulate, in the next sub-section, the temperature $T(z)$ and concentration distributions $c(z)$ in the cell.

4.2.2 Temperature and concentration cell profiles

With the now established Soret-coefficient $S_T(M, c, T)$ we can calculate the non-linear concentration $c(z)$ and temperature distribution $T(z)$ inside the cell.

a) Temperature distribution

The temperature profile

$$T(z) = \vec{\nabla}T_0 h \cdot \frac{-1 + \sqrt{1 + \beta_\kappa \frac{z}{h} (2 + \beta_\kappa)}}{\beta_\kappa} + \left(T_0 - \frac{\Delta T}{2} \right) \quad (4.26)$$

is calculated with $\beta = \alpha\Delta T/h$ and the temperature difference ΔT symmetrically around the average temperature T_0 of 298.15 K. Therefore we consider the temperature dependence of the thermal conductivity

$$\kappa(T) = \kappa(T_0) + \alpha (T - T_0) , \quad (4.27)$$

which includes the average thermal conductivity of toluene $\kappa(T_0) = 0.1307 \text{ W/Km}$ ^[77] and for the temperature dependency $\alpha = -2.88 \cdot 10^{-4} \text{ W/m}$ ^[78]. Details are given in our recently submitted publication [70], but conceptionally the temperature gradient originates from the solution of the heat equation

$$\nabla \cdot (\kappa(T) \vec{\nabla}T) = 0 . \quad (4.28)$$

The resulting slightly non linear temperature profile $T(z)$ is shown, as a red curve, in the left illustration of [fig. 4.8](#). Due to the slightly off centered location of the average temperature T_0 and due to the minor variations of the temperature gradient $\vec{\nabla}T(z)$ (red curve, right panel) around the average value of $\vec{\nabla}T_0 = 6 \cdot 10^3 \text{ K/m}$, we see the slightly non linear temperature distribution.

b) Concentration profile

Now we turn our attention to the concentration distribution $c(z)$, which is shown as the blue curve in the left panel of [fig. 4.8](#). As introduced in [equation 2.6](#), the concentration $c(z)$ is the solution of the diffusion-equation [4.29](#). In our case with the additional premise of the steady state condition ($dc/dt = 0$):

$$\frac{dc}{dt} = \nabla \cdot \left\{ D(M, c, T(z)) \cdot \vec{\nabla}c + D_T(T(z)) \cdot c[1 - c] \cdot \vec{\nabla}T(z) \right\} . \quad (4.29)$$

The resulting ordinary differential equation is the in [eq. 4.30](#), shown Soret-equation, which can be solved, in our model, by *separation of the variables*^[79].

$$\vec{\nabla}c = \frac{dc}{dz} = -S_T(M, c, T(z)) \cdot c[1 - c] \cdot \vec{\nabla}T(z) \quad (4.30)$$

This leads to the integral equation [4.31](#), where only a numerical solution yields an expression for concentration distribution $c(z)$. Consequently, in combination with [eq. 4.30](#) also an expression for the solutal gradient $\vec{\nabla}c(z)$ can be obtained.

$$\int_{c(0)}^{c(z)} dc \frac{1}{\hat{S}_T(M, c) \cdot c[1 - c]} = \int_0^z dz' \tilde{S}_T(T(z')) \cdot \vec{\nabla}T(z') \quad (4.31)$$

The integration constant appearing in the solution of the integral still needs to be calculated with the initial condition of [eq. 4.32](#) (mass conservation):

$$c_0 = \frac{1}{h} \int_0^h c(z) dz . \quad (4.32)$$

The two blue curves of [fig. 4.8](#) demonstrate the strong non linearities of the concentration distributions. This results in average values (blue markers), which are shifted outwards from the center, towards the cold side, as well as in the strong variation of the associated gradient $\vec{\nabla}c(z)$.

The now calculated concentration $c(z)$ and temperature distribution $T(z)$ are shown in the left panel of [fig. 4.8](#). The associated markers illustrate the average values, $T_0 = 298.15$ K and $c_0 = 0.01$ and their locations along the vertical z-axis. The common gradient estimations would be, that the temperature difference $\Delta T = 30$ K and cell height of $h = 5$ mm construct the constant temperature gradient $\vec{\nabla}T_0$ of [eq. 4.33](#). With that and a constant Soret coefficient, here $S_T(T_0) = 9.21 \cdot 10^{-2} \text{K}^{-1}$,

we would calculate the constant concentration gradient $\vec{\nabla}c_0$ as:

$$\vec{\nabla}T_0 = \frac{30 \text{ K}}{5 \text{ mm}} = 6 \cdot 10^3 \text{ K/m} \quad (4.33)$$

$$\vec{\nabla}c_0 = -S_T(T_0)\vec{\nabla}T_0 \cdot c_0(1 - c_0) = -5.5 \text{ m}^{-1} . \quad (4.34)$$

By comparing these common assumptions with the right plot from [fig. 4.8](#), it is easy to see, that these are very inadequate. It should be noted that the average values are not that far away from the assumed values from [eq. 4.33](#) and [eq. 4.34](#). But this

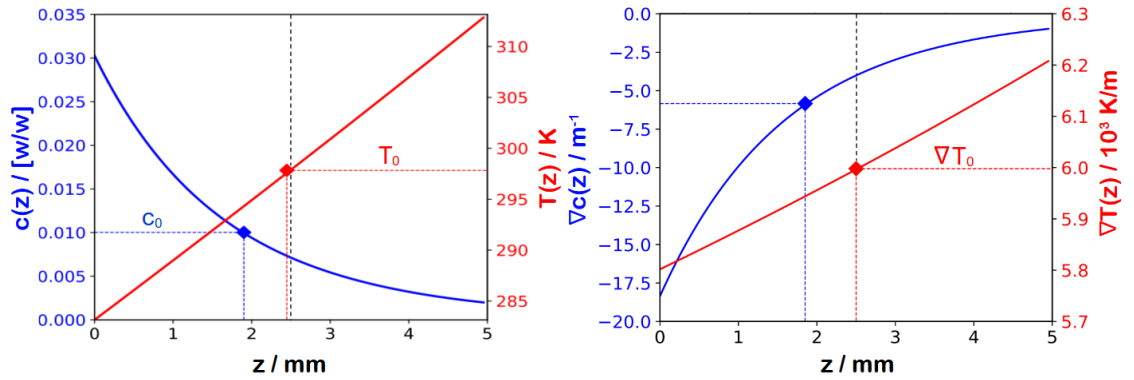


Fig. 4.8: LEFT: Illustration of the temperature $T(z)$ (red) and concentration profile $c(z)$ (blue) in the cell. Marked are the, due to the non linearities of both equations, off-centered average values. RIGHT: Slightly non linear temperature $\vec{\nabla}T(z)$ (red) and strongly non linear concentration gradient $\vec{\nabla}c(z)$ (blue). With an average concentration gradient, which is shifted towards the cold side, whereas the average temperature gradient $\vec{\nabla}T_0$ close to the cell center.

is only true in average, at the borders of the cell however, which contribute the dominant signals, the assumptions do not match the functions at all. To illustrate this a little better, [tab. 4.3](#) shows for $T(z)$ and $c(z)$, as well as for their gradients, $\vec{\nabla}T(z)$ and $\vec{\nabla}c(z)$, the values of the signature cell height ($z = 0, h/2, h$). The additional last row give the locations of the average values (markers). It becomes clear that the general assumption of describing $\vec{\nabla}c(z)$ by $\vec{\nabla}c_0(z)$ does not fit more than in exactly one point. In the left panel of [fig. 4.8](#) as well as in the [tab. 4.3](#), we can clearly see, that due to the strong non linearity of the concentration distribution $c(z)$, the location of average concentration $\langle c(z) \rangle_z = c_0$ is shifted out of the center ($z \approx 2.5$ mm, dashed black line), towards the cold side ($z = 0$). The average

	$c(z)$	$T(z) / \text{K}$	$\vec{\nabla}c(z) / \text{m}^{-1}$	$\vec{\nabla}T(z) / \text{K/m}$
$z = 0$	0.0303	283.15	-18.26	5.80
$z = h/2$	0.0071	297.91	-4.01	6.00
$z = h$	0.0018	313.15	-0.99	6.21
$\langle \dots \rangle_z / \text{mm}$	$z = 1.90$	$z = 2.44$	$z = 1.85$	$z = 2.50$

Tab. 4.3: Breakdown of critical values in fig. 4.8 of the three signature heights $z = 0, h/2, h$.

temperature $\langle T(z) \rangle_z = T_0$ on the other hand remains centrally, which means the temperature profile is not as much affected by the included non linearity as the concentration counterpart. In a similar way the right panel of fig. 4.8 demonstrates the distributions of the local thermal $\vec{\nabla}T(z)$ and solutal gradients $\vec{\nabla}c(z)$, as the red and blue functions. Also with the marked positions of the average values.

The important message here is, that the thermal gradient varies weakly (around 6%) and is largest on the hot cell side ($z = h$). The magnitude of the solutal counterpart varies significantly ($c(0) \approx 18 \cdot c(h)$) and is largest on the cold cell side ($z = 0$). These gradients are the determining quantities of the amplitudes in the NEF signals

$$A_{NE}^i \sim |\vec{\nabla}i|^2, \quad (4.35)$$

which we have introduced in the time dependent structure factor section 4.3, especially in eq. 4.57 and 4.60. In the next section we use the thermophysical parameters with the now established temperature and concentration distributions and calculate the shadowgraphy signals in our layer model. Beyond that, we compare the simulation with actual experiments.

4.2.3 Simulated relaxation and amplitude signals

The last theoretical section 2.6 introduced the relaxation times $\tau^j(q)$ and the static structure factors $S^j(q)$ as the two important quantities in the structure functions $C^j(q, \Delta t)$ ($j = T, c$)⁷. This section demonstrates the associated calculation steps of

⁷The previously used i , which differentiated between T for thermal and c for concentration, becomes a j in this section. Because the index i is used here as the notation of the individual layers, this follows the notation of the paper (ref).

these three contributions and reflects the resulting average signals as our measuring observables. We assume that, in a realistic cell the generated structure function

$$C(q, \Delta t) = \frac{1}{h} \int_0^h C_i(q, \Delta t, z) dz \quad (4.36)$$

is a multi-component signal of all contributing layers $C_i(q, \Delta t, z)$. We construct our model with the assumption that these layer signals do not interfere with each other. Therefore an additional fluctuation size restriction is introduced, which limits q to $q \gg 2\pi/h$, within the cell. The calculation of the structure functions of the individual layers $C_i(q, \Delta t, z)$ follows our publication [47], which was introduced in [section 2.6](#). There, the total signal is divided into two separated contributions $C_i^j(q, \Delta t, z)$, which have analogous expressions for the thermal ($j = T$) and solutal ($j = c$) component.

$$C_i(q, \Delta t, z) = 2T(q, Z) \cdot \sum_{j=c,T} S^j(q, z) \cdot \left[1 - \exp\left(\frac{-\Delta t}{\tau^j(q, z)}\right) \right] + B_0 \quad (4.37)$$

For better comparison with the experimental signals, we included a constant background $B_0 = 1$, as well as the oscillating transfer function $T(q, Z)$ (cf. [eq. 3.2](#))⁸. It should be mentioned that the weak concentration and temperature dependence of the contrast factor was neglected. The previously shown black curve of [fig. 4.5](#) demonstrates the resulting correlation function $C(q = 115 \text{ cm}^{-1}, \Delta t)$ of all the 100 individual contributions of the different layers $C_i(q = 115 \text{ cm}^{-1}, \Delta t, z)$ (light blue curves). The visible overlap of the curves, at around $\Delta t \approx 0.1 - 1 \text{ ms}$, is due to the non linear temperature profile. As mentioned, the thermal part, which is the fast mode, is dominated by the hot cell side ($z = h$). For longer correlation times $\Delta t > 1 \text{ ms}$, the cold side ($z = 0$) dominates the slower, solutal mode. These different dominance's, in which cell side contributes the main signal portion, are one of many points, which were not noticed before this detailed simulation. Now we discuss the calculation methods of the relaxation times

$$\tau^j(q, z) = \frac{1}{\chi q^2 \cdot \left[1 + \left(q_{ro}^j(z)/q \right)^4 \right]}, \text{ for } j = \begin{cases} c : \chi = D(T) \\ T : \chi = D_{th}(T) \end{cases} \quad (4.38)$$

⁸Pay attention to the transfer function $T(q, Z)$, with the cell-layer to camera distance Z , which shouldn't be mixed up with the temperature profile $T(z)$.

and the static structure factors

$$S^j(q, z) = \frac{I_0^j(z)}{1 + (q/q_{ro}^j(z))^4} \quad (4.39)$$

of both modes ($j = T, c$). The corresponding curves are illustrated in the two figures 4.9 and 4.10. Therein the thermal related contributions ($j = T$) are shown in reddish colors and the solutal component ($j = c$) in bluish ones. The entire signal of each mode, formed out of the layer contributions, have a band like appearance, with different widths at different q values. Following fig. 4.5, the three layers, $z = 0, h/2, h$ are again highlighted with thicker solid, dashed and dotted blue lines, respectively. In addition, the direction of the temperature gradient $\vec{\nabla}T$ is indicated by the transparent gray arrows to give a quick understanding of which cell side is providing the dominant signal. It is important to understand that the experimental temperature gradient does not change, only the dominant signal contribution. Finally, the thinner black vertical lines demonstrate the embedded q roll-off $q_{ro}^j(z)$ ~~Station~~ with the description of relaxation time plot 4.9, where we find for both the thermal and solutal components a similar progression. For an easier analysis, we divide the entire relaxation dynamic $\tau^j(q, z)$, into the left $\tau_l^j(q, z)$ and right flanks $\tau_r^j(q, z)$ of the bell-shaped curves. The associated functions are shown in eq. 4.40 and 4.41.

$$\tau_l^j(q, z) = \frac{\nu(M, c, T)}{g \cdot \beta_j} \cdot \frac{q^2}{|\vec{\nabla}j(z)|} \quad , \text{ for } j = \begin{cases} c : \vec{\nabla}j(z) = \vec{\nabla}c(z) \\ T : \vec{\nabla}j(z) = \vec{\nabla}T(z) \end{cases} \quad (4.40)$$

The more complex left side is the one, where the bands are determined by the inverse magnitude of the associated gradients, $|\vec{\nabla}T(z)|$, respectively $|\vec{\nabla}c(z)|$. But this is the non linear component, which explains the large variations and the width bands, especially in the solutal case. Therefore, the hot side ($z = h$, solid line) is dominant in the solutal and the cold side ($z = 0$, dashed line) in the thermal signal.

$$\tau_r^j(q, z) = \frac{1}{\chi \cdot q^2} \quad , \text{ for } j = \begin{cases} c : \chi = D(T) \\ T : \chi = D_{th}(T) \end{cases} \quad (4.41)$$

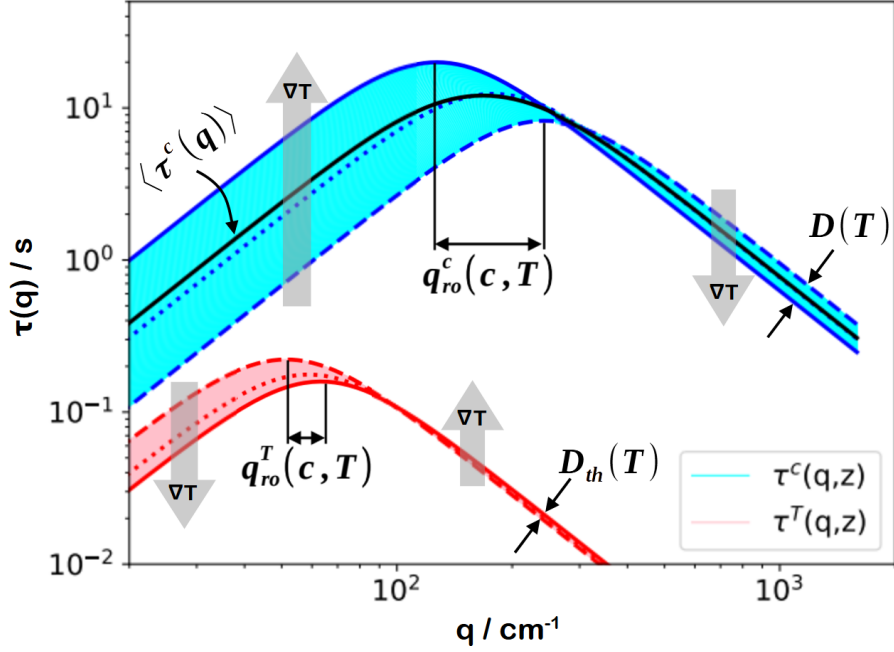


Fig. 4.9: Demonstration of all relaxation times $\tau^j(q, z)$ of the individual layers, where in reddish the thermal part and in bluish the solutal contributions are shown. For both modes the introduced signature heights, $z = 0, h/2/h$, are highlighted. Additionally the black lines demonstrate the q roll-off variances $q_{ro}^j(c, T)$ and the thermal dependencies of the embedded transport coefficient. Parameters: $M = 17.9$ kg/mol, $\Delta T = 30$ K, $c_0 = 0.01$, $T_0 = 298.15$ K. Based on [70].

The right, free diffusion, flank on the other hand is simpler. Here, only the thermal dependencies of the diffusion coefficient $D(T)$ and the thermal diffusivity $D_{th}(T)$ determine the signals, also in an inverse relation. For these transport coefficients we only have to remember back to fig. 4.6, this explains the dominance of the cold side in the solutal signal and the hot in the thermal one. The swap in the dominance from the left to the right flank finally explains the crossing of the layer curves, which occurs in both components slightly after the maximum values. This is also the reason for the mentioned dominance change in the structure function plot 4.5 (at around $\Delta t = 0.3$ s). The black horizontal arrows in fig. 4.9 illustrate the variations in the q roll-off values $q_{ro}^j(z)$, which is also indicated in fig. 4.10. For each layer the two, mainly independent, flank contributions generate in their

intersection the associated q roll-off value $q_{ro}^j(z)$:

$$q_{ro}^c(z) = \left[\frac{g \cdot \beta_c}{\nu(M, c, T)} \right]^{1/4} \cdot \left[\frac{|\vec{\nabla}c(z)|}{D} \right]^{1/4} \quad (4.42)$$

$$q_{ro}^T(z) = \left[\frac{g \cdot \beta_T}{\nu(M, c, T)} \right]^{1/4} \cdot \left[\frac{|\vec{\nabla}T(z)|}{D_{th}} \right]^{1/4} . \quad (4.43)$$

The solutal (bluish) band shows a strong variation, that is created due to the included magnitude of the concentration gradient $\vec{\nabla}c(z)$. This non linearly related modification of the resulting q roll-off value in the average solutal relaxation time $\tau^c(q)$ (solid black line) is one of the biggest problems in our experiments, because the curve is artificially widened (stretched). This can be seen better in [fig. 4.12](#) of [section 4.2.4](#). The problem is that the thermal and solutal roll-off values q_{ro}^j determine, as demonstrated in [eq. 4.7](#), the Soret-coefficient S_T . This non linearity footprint in both roll-off values, is the reason for the 'note' at the end of the last section, where we explained that [eq. 4.7](#) (via q_{ro}^c/q_{ro}^T) is a better calculation method than [eq. 4.6](#) (approach via $\vec{\nabla}c$).

For the NEF static structure factors $S^j(q, z)$ of [fig. 4.10](#) similar explanations can be formulated. This time we only need to consider the intensity

$$I_0^c(z) = \frac{|\vec{\nabla}c(z)|^2}{\nu(M, c, T) \cdot D(T)} \quad (4.44)$$

$$I_0^T(z) = \frac{|\vec{\nabla}T(z)|^2}{\nu(M, c, T) \cdot D_{th}(T)} \quad (4.45)$$

of the gravitational plateau and the mentioned considerations of the q roll-off values $q_{ro}^j(z)$. The shown band widths are again created due to the in [eqs. 4.44](#) and [4.45](#) included magnitude of the associated gradients. This results again in a narrow thermal and a wide solutal band. In the solutal case always the cold ($z = 0$, dashed line) and in the thermal one always the hot cell side ($z = h$, solid line) is the dominating one. The black line demonstrates the average solutal static structure factor $S^c(q)$, which together with the related average relaxation time

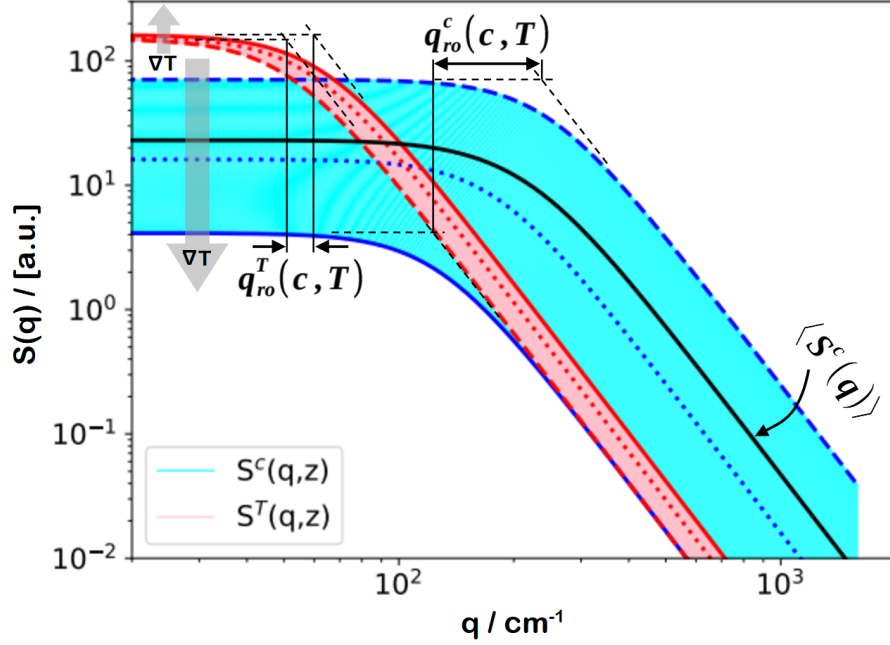


Fig. 4.10: Demonstration of all static structure factors $S^j(q, z)$ of the individual layers, where in reddish the thermal part and in bluish the solutal contributions are shown. For both modes the introduced signature heights, $z = 0, h/2/h$, are highlighted. Additionally the construction lines demonstrate the q roll-off variances $q_{ro}^j(c, T)$ and the thermal dependencies of the embedded transport coefficient. Parameters: $M = 17.9$ kg/mol, $\Delta T = 30$ K, $c_0 = 0.01$, $T_0 = 298.15$ K. Based on [70].

$\tau^c(q)$ generates the simulated solutal structure signals $C^c(q, \Delta t)$. Finally, as the sum of the solutal signal $C^c(q, \Delta t)$ and the thermal counterpart $C^T(q, \Delta t)$, the total structure function $C(q, \Delta t)$ (black line in fig. 4.5) is completed.

All the required quantities of the necessary structure functions have now been introduced and the calculations in the simulation have been explained. The next section 4.2.4 briefly discusses the evaluation of the simulated signals, which, however, is similar to the evaluation already shown in section 4.1. That means, we evaluate our simulated averaged structure functions $C(q, \Delta t)$ as if they were experimental ones.

4.2.4 Evaluation of the simulated data

Following the steps of the previous introduced explanations in [section 4.1](#), we are now evaluating the simulated structure functions. The plot of [fig. 4.11](#) illustrates the simulated (index: sim) structure functions $C_{\text{sim}}(q, \Delta t)$ for three q values. The magenta colored dots (behind the red line) shows a small q value of 49 cm^{-1} , which contains only the fast, thermal mode. The cyan (behind the blue line) counterpart of $q = 360 \text{ cm}^{-1}$ illustrates a slow, purely solutal mode. Lastly the gray correlation function of $q = 115 \text{ cm}^{-1}$ combines both modes (behind the black line). This signal is the average structure function $C_{\text{sim}}(q = 115 \text{ cm}^{-1}, \Delta t)$ already known from [fig. 4.5](#).

$$C_{\text{sim}}(q, \Delta t) = \sum_{i=1}^N \frac{\sum_{j=c,T} \overbrace{C_{i,\text{sim}}^j(q, \Delta t, z)}^{\sim \text{exp}}}{N} \quad (4.46)$$

Our evaluation (index. eva) method interprets the multi-exponential total corre-

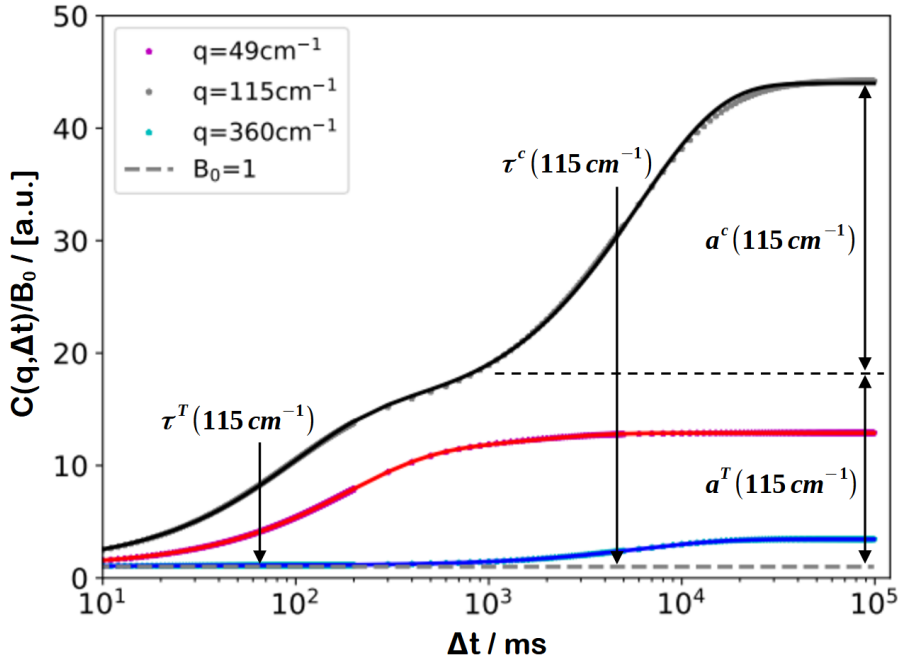


[Fig. 4.11](#): Illustration of three simulated structure functions (dots, [eq. 4.46](#)) and the associated fitted curves (solid lines, [eq. 4.47](#)). The four important fit parameters ($a^c(q)$, $a^T(q)$, $\tau^c(q)$, $\tau^T(q)$) of [eq. 4.47](#) are shown for the curve of $q = 115 \text{ cm}^{-1}$ (same as in [fig. 4.5](#)). Based on [70].

lation function $C_{\text{sim}}(q, \Delta t)$ of eq. 4.46 as a binodal sum of two mono-exponential contributions $C_{\text{eva}}^j(q, \Delta t)$ ($j = T, c$).

$$C_{\text{eva}}(q, \Delta t) = \sum_{j=c,T} \overbrace{a_{\text{eva}}^j(q) \cdot \left[1 - \exp\left(\frac{-\Delta t}{\tau_{\text{eva}}^j(q)}\right) \right]}^{=C_{\text{eva}}^j(q, \Delta t)} + B_0 \quad (4.47)$$

Each mode, which is itself a multi-exponential contribution, is thereby approximated with a mono-exponential part. We added on top of the signals a background of $B_0 = 1$, which experimentally would be an additional fit parameter. The thermal ($j = T$) and solutal ($j = c$) contributions of the evaluated structure functions $C_{\text{eva}}^j(q, \Delta t)$, include again, own amplitudes $a_{\text{eva}}^j(q)$ and relaxation times $\tau_{\text{eva}}^j(q)$. These four associated fit parameters of the structure functions are demonstrated in fig. 4.11 for the black fit curve of $q = 115 \text{ cm}^{-1}$ by the thin construction lines. As a first glimpse they match very well, only on a closer inspection, especially in the areas of the strongest bends ($\Delta t \approx 10 - 30 \text{ s}$), minor deviations become apparent. These result from the original strong variations in the correlation signals, which are embedded in the multi-exponential portions of the simulated signals. The next steps are the fits of the relaxation times $\tau_{\text{eva}}^j(q)$ (eq. 4.48) and the NEF amplitudes $a_{\text{eva}}^j(q)$ (eq. 4.49). This is shown in eq. 4.48 and 4.49, as well as in fig. 4.12 and fig. 4.13.

$$\tau_{\text{eva}}^j(q) = \frac{1}{\chi_{\text{eva}} \cdot q^2 \cdot \left[1 + \left(\frac{q_{ro}^j}{q} \right)^4 \right]}, \quad \text{for } j = \begin{cases} c : \chi = D_{\text{eva}} \\ T : \chi = D_{\text{th,eva}} \end{cases} \quad (4.48)$$

$$a_{\text{eva}}^j(q) = 2 \cdot T_{\text{eva}}(q) \cdot \frac{\overbrace{I_{0,\text{eva}}^j(q)}^{=S_{\text{eva}}^j(q)}}{1 + \left(\frac{q}{q_{ro}^j} \right)^4} \quad (4.49)$$

The evaluated amplitudes $a_{\text{eva}}^j(q)$ include the static structure factors $S_{\text{eva}}^j(q)$, the transfer function $T_{\text{eva}}(q)$ (optical interference effect) and the factor '2', which is an attribute of the doubled fluctuation dependency (explained in eq. 3.16). The structure factor term, under the brace, is a function of the gravitationally limited intensities $I_{0,\text{eva}}^j$ (cf. fig. 4.3) and the associated static q roll-off values q_{ro}^j . The

roll-off value also appears in the relaxation times, where we call it dynamic, since they are experimentally not always the same^[66].

The left panel of [fig. 4.12](#) is a reminder and shows the solutal (cyan) and thermal (pink) relaxation time bands of the simulation ([fig. 4.9](#)). The right side demonstrates

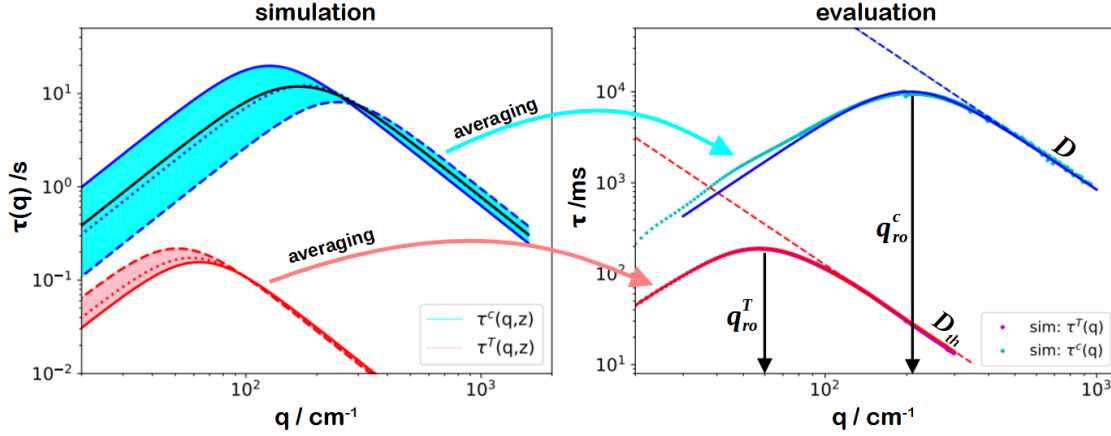


Fig. 4.12: The right plot is the actual plot of the relaxation times $\tau^j(q)$ (dots) and associated fit functions (4.48, solid lines) of the thermal (red) and solutal (blue) modes. The left plot is a reminder, it shows again all the embedded relaxation times bands of the simulation. The dashed lines in the right panel are the pure transport properties in micro gravity (μg). Also marked are the dynamic q roll-off values q_{ro}^j of both components.

for every q value the fitted average relaxation times $\tau_{eva}^j(q)$ as the turquoise (solutal) and magenta (thermal) dots. The embedded band structures collapse due to the averaging process. The two solid lines in the right panel are the resulting bell-shaped fit functions of [eq. 4.48](#), with the contained roll-off values q_{ro}^j and the pure transport quantities D and D_{th} , of the solutal ($j = c$) and thermal ($j = T$) modes. As we can see, especially on the left flank of the solutal relaxation time, minor deviations from the bell-shaped function can be found. This is due to the non linearity of the included concentration gradient $\vec{\nabla}c$, which we explained in [eq. 4.40](#). It should be mentioned that in these areas additional finite-size effects^{[80], [24]} can occur, which aren't included in our simulation model. A closer look at the solutal fit curve in conjunction with the simulated relaxation times makes it clear that these are not only slightly above the fit curve on left side, they are also above it on the right side and slightly below it in the middle. This is the indicated artificial widening

of the solutal relaxation dynamics due to the non linearity, which complicates the positioning of the q roll-off values.

The illustrations of the static structure factors in fig. 4.13 follow the same style as fig. 4.12. We see the two band like time dependent structure factors of all the

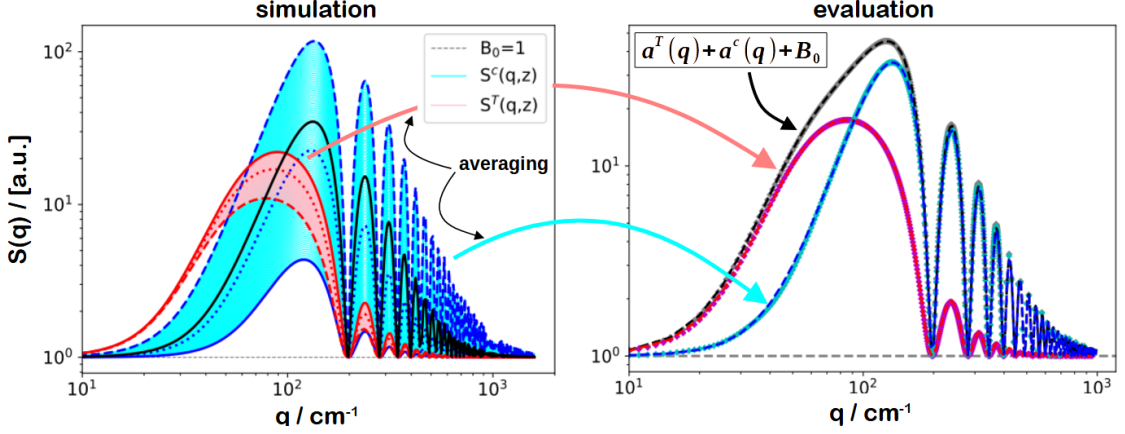


Fig. 4.13: The right plot is the actual plot of the static structure factor $S^j(q)$ and associated fit functions (4.49, dashed lines) of the thermal (red) and solutal (blue) modes. Additionally the sum of both modes (total contribution) is shown with the gray dots and the black dashed line. The left plot is a reminder, it shows again all the embedded static structure factor bands of the simulation.

individual layers on the left and the evaluated NEF amplitudes $a_{eva}^j(q)$ of eq. 4.47 on the right. As explained before, the gray dots demonstrate the sum of the two amplitudes $a^T(q) + a^c(q) + B_0$. This is the analogue to the static structure factor $S_{eva}(q)$. Our fitting algorithm calculates eq. 4.49 not only for the individual structure factors $S_{eva}^j(q)$, it fits parallel to these two functions, the sum of both as the total static structure factor $S_{eva}(q)$. The only fit parameters are the gravitational limited intensities $I_{0,eva}^j$ and the static q roll-off values q_{ro}^j of the thermal and solutal contributions. The resulting functions are the associated red, blue and black dashed lines, which are perfectly matching the simulated curves.

We have now shown how the important parameters of our evaluation interact due to the embedded non linearities and discussed the mono-exponential analysis. However, we don't know yet, whether the calculated signals and the resulting

transport coefficients indeed describe real experiments. This will be addressed in the following [section 4.2.5](#), where we compare first the simulated signals and finally the evaluated transport properties with literature values.

4.2.5 Comparison of simulated and experimental data

This section is divided into two parts. First we will compare the simulated relaxation times $\tau^j(q)$ and the NEF amplitudes $a^j(q)$ with experimental ones. Afterwards we will compare the resulting transport coefficients.

Experimental signals

Starting with the relaxation times, [fig. 4.14](#) demonstrates the already known plot of [fig. 4.12](#), where the small cyan and magenta colored diamonds show the simulated relaxation times $\tau^j(q)$. The blue (solulal) and red (thermal) solid lines represent the associated fits ([eq. 4.48](#)) of these data and the dashed extrapolations the micro-gravitational behaviors. Additionally we can see the dark blue (solulal) and brown (thermal) x-symbols, which are the experimental analogs. We can see that the experimental values are exactly where the simulation predicts them, this is especially true for the right flanks of the bell-shaped curves. On the left flank, on which the non linear effects are predominant, the experiments differ slightly from the simulations. This behavior was to be expected, since real experiments can not be as smooth and perfect as simulations. Additionally, the mentioned finite-size effect^{[80], [24]} could play a role at these small q values, which is not included in the simulation.

[Fig. 4.15](#) compares in a similar way as [fig. 4.14](#), the simulated (diamonds) and the experimental (x-symbols) static structure factors $S^j(q)$ of the thermal ($j = T$, reddish) and solulal ($j = c$, bluish) contributions. As introduced in [eq. 4.49](#), the gray diamonds are the static structure factor $a(q) = a^T(q) + a^c(q)$. The dashed red, blue and black lines are the simultaneously fitted static structure factors [4.49](#) (under the brace). The additional demonstrated experimental NEF structure factor amplitudes (x-symbols), match with each of the three simulated counterparts nearly perfectly. Where the black symbols are the experimental static structure factor,

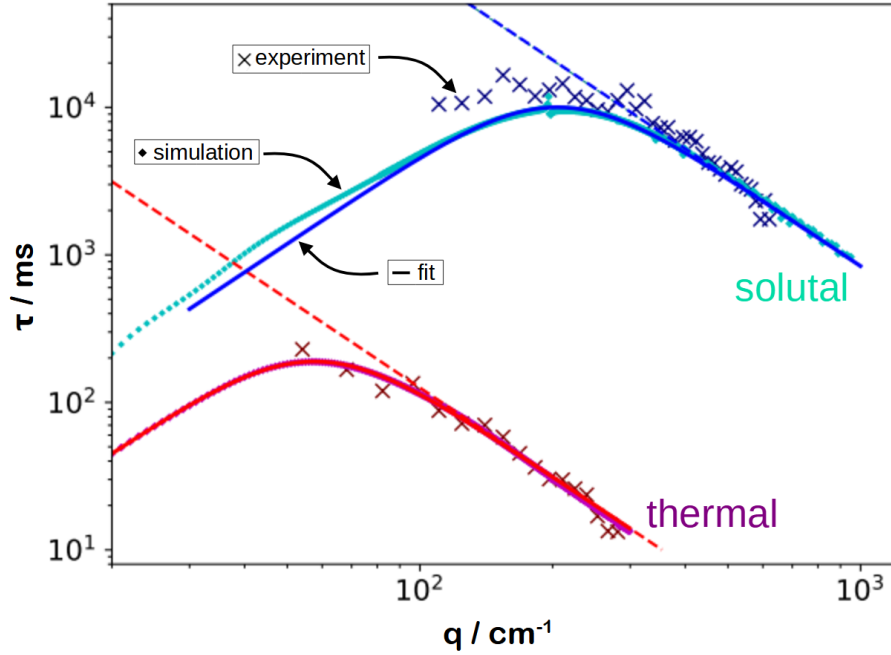


Fig. 4.14: Known plot of fig. 4.12, with the cyan and magenta dots, which are the evaluated solutal and thermal relaxation times of the simulation. The solid red and blue lines illustrate the associated fits (eq. 4.48) and the dashed attachments the micro gravitational behaviors. Additionally we can see the dark blue (solutal) and brown (thermal) x-symbols. These are the experimental counterparts of the same system. Parameters: $M = 17.9 \text{ kg/mol}$, $c = 1\%[\text{w/w}]$, $\Delta T = 30 \text{ K}$. Based on [70].

the brown ones, the thermal and the blue ones the solutal, contributions.

Ultimately, the comparison of the relaxation dynamics (fig. 4.14) and the structure functions (fig. 4.15), in both modes ($j = T, c$), confirms the correctness of the simulated signals. In the next and last step we also compare the actual resulting transport properties to generate a complete picture.

Transport coefficients

After the NEF signal comparison, we now start the last confirmation step. In it we compare the resulting experimental and simulated transport coefficients. These are the diffusion D , Soret S_T and thermodiffusion coefficient D_T , as well as the thermal diffusivity D_{th} . The first two plots, fig. 4.16 and fig. 4.17, consider the

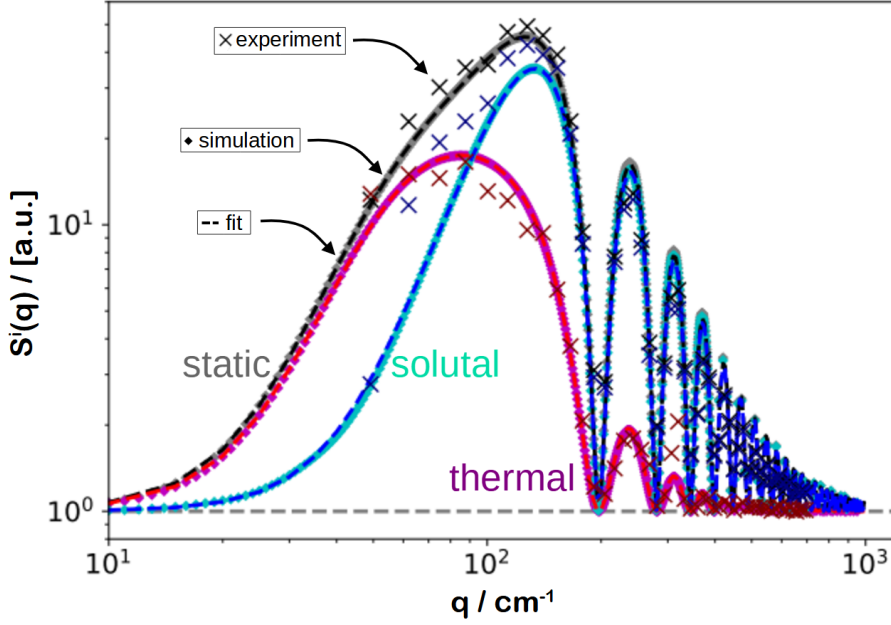


Fig. 4.15: Similar illustration as fig. 4.14, here for the static structure factors. We can see in the bluish and reddish colors the solutal and thermal simulated (diamonds) and experimental (x-symbols) structure factor amplitudes $a^j(q)$. Additionally, the gray diamonds show the total static structure factor. The dashed lines are the simultaneous fits of eq. 4.49 to these three simulated curves. Parameters: PS/toluene $c = 1\%$, $M = 4.84$ kg/mol, $\Delta T = 50$ K. Based on [70].

temperature dependence. Afterwards fig. 4.18 illustrates a comparison of an entire concentration series.

Temperature dependence

The in fig. 4.16 and fig. 4.17 demonstrated experimental measurements, were investigated with the temperature differences of $\Delta T = 10, 20, 30, 40, 50$ K. The simulated series is calculated in 5 K steps, within the limits of $\Delta T = 1 - 50$ K. The left and right panel of fig. 4.16 show the diffusion $D(\Delta T)$ and Soret coefficients $S_T(\Delta T)$ over the applied temperature difference ΔT . For both plots and also in fig. 4.17, the same illustration and symbol style is used. Where the experimental values (index: exp) are shown with the black stars and the associated simulated counterparts (index: sim) with gray circles. Additionally we plot at $\Delta T = 1$ K the corresponding literature values of *Rauch*^[68], which are marked with black diamond symbols. We can see in both panels that the simulated and experimental series match nearly

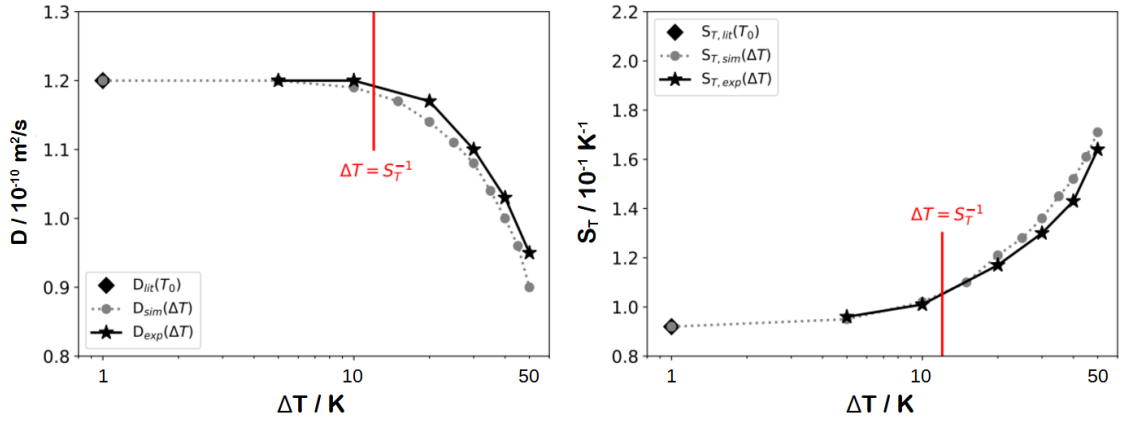


Fig. 4.16: Comparison of the experimental transport properties, shown as black stars with the simulated pendants, as gray dots. The additional diamond markers are the literature values of [68]. The left side shows the diffusion coefficients $D(\Delta T)$ and the right side the Soret coefficients $S_T(\Delta T)$. The red line is the calculated threshold were the coefficients start to deviate. Based on [70].

perfectly. For small temperature differences ΔT they reach the plateau of the literature value and for larger temperature differences ΔT they diverge from it. As the boundary of this plateau we used the criterion

$$|S_T \Delta T| = 1, \quad (4.50)$$

which is shown with the red line. The important message is, that for temperature differences $\Delta T < S_T^{-1}$ the linear approximation of the concentration profile is sufficient and for larger ones additional effects due to the non linearity of the concentration distribution must be taken into account. They result in smaller diffusion and, therefore larger Soret coefficients. This is explained in more detail and for more samples in section 4.4.1, the analysis of the experimental transport coefficients. In principle, the larger the applied temperature difference, the more dominant are the cold regions in the cell. For the moment we only want to compare the simulated and experimental curves to give a final confirmation for the simulations. The quintessence is that, the simulation can not only predict individual experimental data but also the transport coefficients of entire temperature series.

For the sake of completeness, fig. 4.17 shows on the left the results of the thermo-

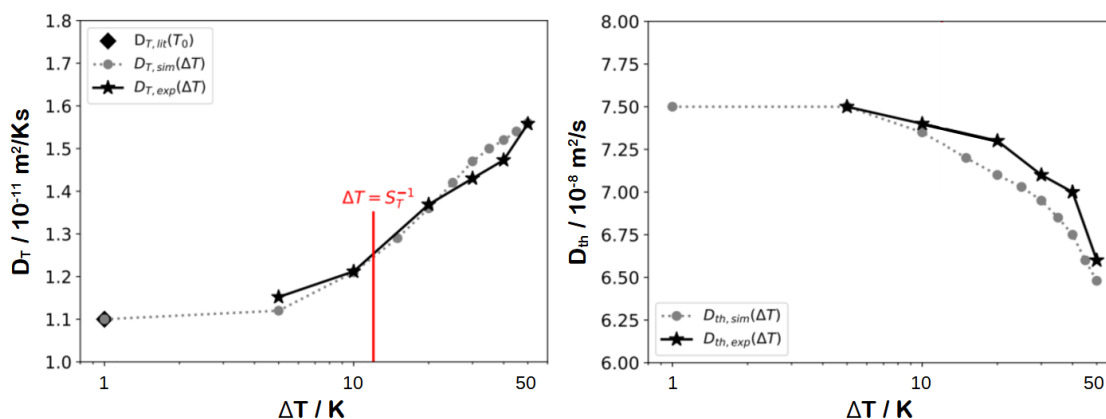


Fig. 4.17: Comparison of the experimental transport properties, shown as black stars with the simulated pendants, as gray dots. The additional diamond markers are the comparison literature values of [68]. The left side shows the thermodiffusion coefficients $D_T(\Delta T)$ and the right side the thermal diffusivity $D_{th}(\Delta T)$. The red line, is the calculated threshold were the coefficients start to deviate. Based on [70].

diffusion coefficients $D_T(\Delta T)$, and the thermal diffusivity $D_{th}(\Delta T)$ on the right. It need to be said, that the thermal diffusivity includes mainly temperature dependent effects, which are shown in fig. 4.6, but additionally small non linearity effects due to the temperature dependent thermal conductivity $\kappa(\Delta T)$ (shown in eq. 4.27). The thermodiffusion coefficient D_T on the other hand is in both cases (experiment and simulation) calculated as: $D_T = S_T \cdot D$. In both panels, we see again the literature plateau for small values of ΔT and a diverging effect for larger ones, which we know from fig. 4.16. In the case of the thermal diffusivity D_{th} , a little bit larger differences of the experimental values to the simulated ones, can be seen. But in general both experimental curves match their simulated pendants reasonably well.

Concentration dependence

The next logical step is to consider in fig. 4.18 a complete concentration series and to explain due to the simulation, the differences between the literature and the experimental values. Therefore we again use the known chain length of $M = 17.9 \text{ kg/mol}$. Additionally to the experimental $(D_{\text{exp}}(c), S_{T, \text{exp}}(c))$ temperature series of fig. 4.16, where we changed the temperature differences ΔT and which is shown with black stars (located at $c = 0.01 \text{ [w/w]}$), the black hexagons demonstrate our experimental concentration series, performed with $\Delta T = 50 \text{ K}$. The black diamonds indicate the literature values of Rauch^[68] $(D_{\text{lit}}(c), S_{T, \text{lit}}(c))$ and fit again perfectly the simulated

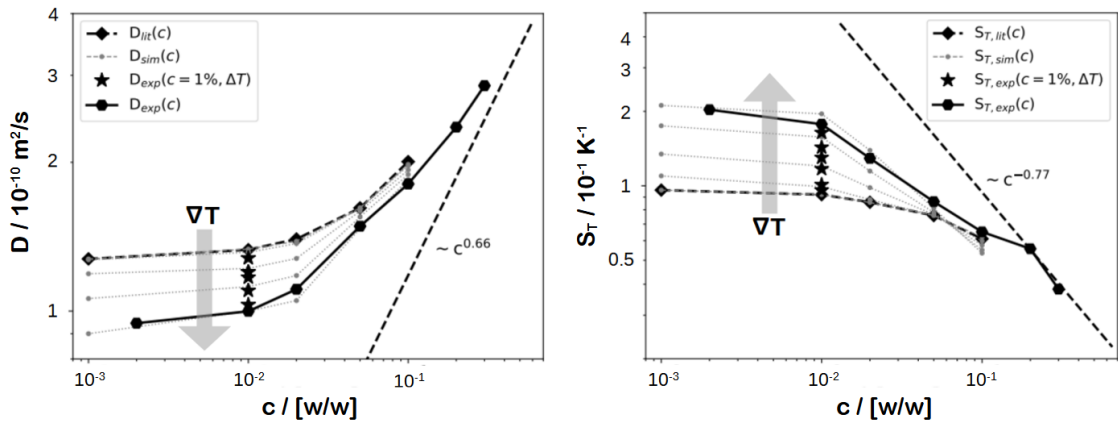


Fig. 4.18: Comparison of own experimental (black stars and hexagons), literature (black diamonds) and simulated values (gray dots) of the diffusion (left) and Soret coefficient (right), as functions of the concentrations c . Experimentally we see the thermal series of fig. 4.16 marked with stars at $c = 1\%$. The experiments of all different $M = 17.9 \text{ kg/mol}$ samples, all measured with $\Delta T = 50 \text{ K}$, are illustrated with the black hexagons. Our reference literature values^[68] are displayed with the black diamonds. All the connected gray dots are the simulated series, with different ΔT . The shown scale laws are also from Rauch^[68]. Parameter: PS/toluene $M = 17.9 \text{ kg/mol}$, $T_0 = 298.15 \text{ K}$.

($D_{\text{sim}}(c)$, $S_{T,\text{sim}}(c)$) results (gray dots) for small temperature differences $\Delta T \leq 10 \text{ K}$. The different simulation series, with increasing temperature differences ΔT , fill the gap between our literature and the experimental values, which is indicated by the big transparent gray arrows. Once again we can see impressively, that the simulations for small temperature differences $\Delta T \leq 10 \text{ K}$ reflect the literature values and for large differences $\Delta T = 50 \text{ K}$ our experiments. This means, the calculation can fully explain the gap in between, which was the initial reason for the non linearity consideration and this simulation campaign. A large part of this simulation and the non linearity influence has also been published in our recent paper [70]. This was the last check of our simulations, we can now confirm, that the simulation fit our data perfectly and reflect both experiment and literature values.

4.2.6 Application to the results of 4.1

With the now introduced and confirmed simulation, we can briefly return to our final problem of [section 4.1](#), that was left open. As a quick reminder, we evaluated a binary mixture of $c = 0.2\%$ polystyrene ($M = 90.9 \text{ kg/mol}$) in toluene, which was measured with a temperature difference of $\Delta T = 50 \text{ K}$. The resulting diffusion and Soret coefficients, shown in [tab. 4.1](#), deviated strongly from the associated literature values. [Tab. 4.4](#) expands on the familiar [tab. 4.1](#) and adds appropriate simulations values. In the new expanded table, the old values are indicated in gray

	$c = 0.2\%, \vec{\nabla}T_0 = 10^4 \text{K/m}$		$c = 1\%, T_0 = 298.15 \text{ K}$	
	experiment	simulation	literature	simulation
$S_T \mid 10^{-2} \text{K}^{-1}$	44.36±4	47.89±5	21.5±2	20.4±2
$D \mid 10^{-10} \text{m}^2/\text{s}$	0.43±0.04	0.40±0.04	0.54±0.05	0.59±0.06

[Tab. 4.4](#): Extension of the [tab. 4.1](#) (gray marked values), with additional simulation values for both experiment and literature. The agreement is convincing.

and in the same columns additional simulation values are shown in black. These new quantities match the experimental as well as the literature values very well. The initial differences of the experimental and the literature values can therefore be explained by the non linearities in the Soret-equation and by the temperature dependencies of the transport coefficients.

4.2.7 Simulation with temperature independent coefficients

In the final statements of [tab. 4.4](#), where we explained the differences between the measured and the reference values, we found two reasons for the deviations. First, the non linearity in the concentration gradient $\vec{\nabla}c(z)$ ⁹, which comes from the $c(1-c)$ term in the Soret-equation ([eq. 4.8](#)). Secondly the temperature dependencies of the transport coefficients and other thermophysical parameters. In this sub-section we want to decompose these two effects, focusing on the supposedly stronger non linearity effect. For this purpose, we will assume all thermodynamically relevant

⁹The non linearity in $\vec{\nabla}T(z)$ is neglected.

parameters to be constant. The naming scheme will call the former simulation approach 'total' simulation, where all components were considered temperature and concentration dependent. Contrary we call the new one 'constant' simulation. We use again the $c_0 = 0.01$ [w/w], $M = 17.9$ kg/mol sample, where the associated fixed parameters can be seen in [tab. 4.5](#).

parameter			value			parameter			value		
D	m^2/s	$1.20 \cdot 10^{-10}$	ρ	kg/m^3	864	$\frac{\partial n}{\partial T}$	$1/\text{K}$	$-5.64 \cdot 10^{-4}$	$\frac{\partial n}{\partial c}$	$9.80 \cdot 10^{-2}$	
S_T	$1/\text{K}$	$9.21 \cdot 10^{-2}$	β_T	$1/\text{K}$	$-1.09 \cdot 10^{-3}$	β_c		0.21			
D_T	m^2/Ks	$1.20 \cdot 10^{-11}$									
D_{th}	m^2/s	$7.50 \cdot 10^{-8}$									
ν	m^2/s	$7.42 \cdot 10^{-7}$									
κ	W/Km	0.1307									

[Tab. 4.5](#): Specification of the prime parameters and their values in the 'constant' simulation. The left side shown the transport coefficients and the right side additional parameters of the sample.

[Eq. 4.26](#) now yields a linear temperature profile $T(z)$ symmetrical around $T_0 = 298.15$ K, which is shown in [eq. 4.51](#).

$$T(z) = \vec{\nabla}T_0 \cdot z + \left(T_0 - \frac{\Delta T}{2}\right) \quad (4.51)$$

$$\vec{\nabla}T_0 = \frac{30 \text{ K}}{5 \text{ mm}} = 6 \cdot 10^3 \text{ K/m} \quad (4.52)$$

Due to the constant Soret coefficient S_T , the Soret equation of [eq. 4.53](#) is an analytically solvable first-order, non linear differential equation. The included $|S_T \Delta T| = 2.76$ term shows that the non linearity ($c(1 - c)$) still can not be neglected, since the defined threshold is $|S_T|^{-1} = \Delta T$.

$$\frac{\partial c}{\partial z} = -S_T \Delta T \cdot c(1 - c) \quad (4.53)$$

For the solution of the concentration distribution $c(z)$ we get [eq. 4.54](#). Involved is the term $c_{lin}(z)$ of [eq. 4.55](#), which is the solution of the linear approximation

$(c(1 - c) \approx c)$.

$$c(z) = A_0 \frac{c_{lin}(z)}{1 + c_{lin}(z)} \quad (4.54)$$

$$c_{lin}(z) = \exp(-S_T \Delta T \cdot z) \quad (4.55)$$

The integration constant A_0 can again be solved by the condition for mass conservation (eq. 4.32), which was also used in the numerical approach of the 'total' simulation.

To get a feeling for the differences of the two simulation approaches, the left

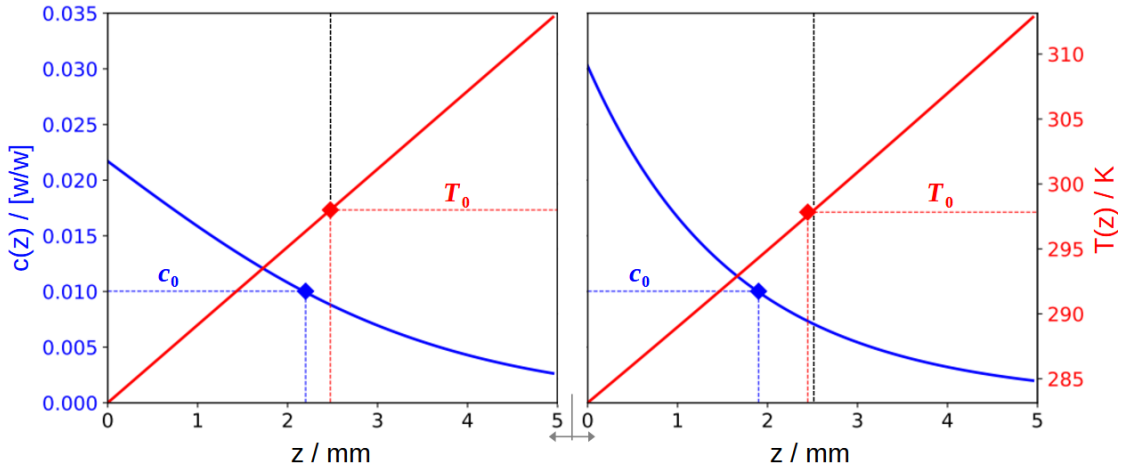


Fig. 4.19: Comparison of the temperature $T(z)$ (red) and concentration distributions $c(z)$ (blue). The left side demonstrates the 'constant' simulation, whereas the 'total' simulation is shown on the right. The markers and the connected dashed lines illustrate the locations of the associated average values c_0 and T_0 .

panel of fig. 4.19 shows the temperature $T(z)$ (red) and concentration distribution $c(z)$ (blue) of eq. 4.51 and eq. 4.54 and compares these with the in fig. 4.8 established distributions of the 'total' simulation (right plot in fig. 4.19). Note, that both plots share the same y-axes. This style we will see again in the following comparison plots. The average values T_0 and c_0 are marked by the diamond symbols and their location is indicated by the attached dashed lines. We can clearly see, the two important differences. First, the 'constant' simulation has a perfectly linear temperature profile $T(z)$ with the centered average value T_0 . Secondly, the

concentration distribution $c(z)$ shows a non linear progression, but especially at the cold side ($z = 0$) the curve isn't as steep as in the case of the 'total' simulation (right side in fig. 4.19). This means the magnitude of the concentration gradient $\vec{\nabla}c(z)$ in this area is smaller than in the other approach.

Signal comparison

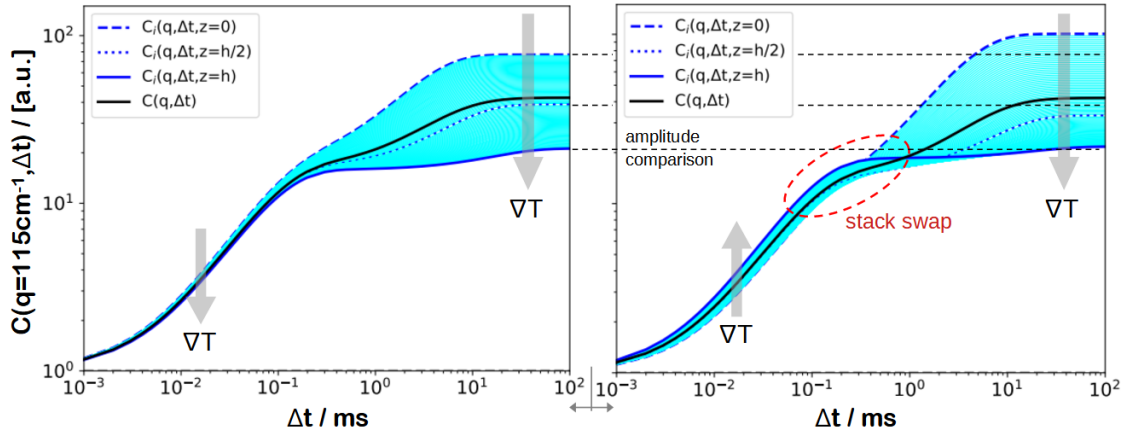


Fig. 4.20: Comparison of all the layer structure functions $C_i(q = 115 \text{ cm}^{-1}, \Delta t, z)$ resulting from the 'constant' (left) and the 'total' simulation (right). The illustration style, with the highlighted layers and the direction of the temperature gradient is known from fig. 4.5. The red circle illustrating, the main difference of these approaches, where the curves overlapping in the 'total' simulation and are perfectly stacked in the 'constant' simulation. The dashed lines connect, for an easier comparison, the amplitudes from the left to the right side.

Starting with fig. 4.20, a comparison of all the contributing structure functions $C_i(115 \text{ cm}^{-1}, \Delta t, z)$, where the right side is the already known illustration from fig. 4.5 with the same scale as the left, 'constant' simulation analogue. Besides the larger amplitudes of the 'total' simulation, which result from the mentioned larger concentration gradients on the cold side ($z = 0$, dashed blue line), the first thing to notice is that, the 'constant' simulation does not show the overlap of the layer curves, instead appears perfectly stacked (red circle). Due to the constant contribution of the temperature gradient $\vec{\nabla}T_0$, all thermal modes $C^T(q, \Delta t)$ are equally strong and the solutal part $C^c(q, \Delta t)$ is simply added on top. Therefore the previously described 'swap' of the dominant layer (which was caused by the

dominance of the hot side ($z = h$) in the thermal mode) does not occur here. This is indicated by the always downward pointing temperature direction (gray arrows).

Next, [fig. 4.21](#) compares the resulting static structure factors $S^j(q, z)$ of both

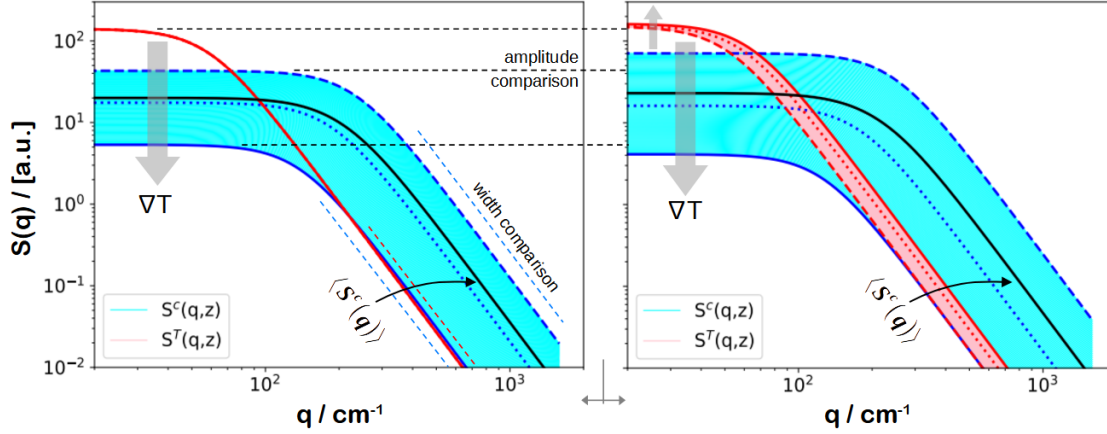


Fig. 4.21: Comparison of all the layer static structure factors $S_i(q, z)$ resulting from the 'constant' simulation on the left and the 'total' simulation on the right. The style and the highlighted layers follow [fig. 4.13](#). The black dashed lines are guides to the eye, for an easier amplitude comparison. Also the blue dashed lines in the left panel, illustrates, for a better comparison, the solutal band width of the 'total' simulation.

components ($j = T$ in reddish, $j = c$ in bluish colors) and for every layer ($z \in [0, h]$). The right panel is the illustration of [fig. 4.10](#) ('total' simulation) and the left one again the 'constant' simulation pendant. For a better understanding, the black dashed lines connect certain amplitudes ($z = 0, h$) of the 'constant' simulation to the 'total' one. The thick black line in both panels is the average solutal static structure factor $S_c(q)$. We can see in the left illustration that all the thermal contributions are collapsed to a single line. That is due to the constant temperature gradient $\vec{\nabla}T_0$ and the constant viscosity ν and thermal diffusivity D_{th} . The solutal band width of the 'constant' simulation is a bit smaller than in the 'total' case, this is additionally indicated by the thin blue dashed lines, which demonstrate the width of the 'total' simulation on the 'constant' side. These differences can be traced back to the smaller concentration gradients $\vec{\nabla}c(z)$. Otherwise, the plots do not differ significantly.

Fig. 4.22 shows the comparison of the individual relaxation times $\tau_i^j(q, z)$, again

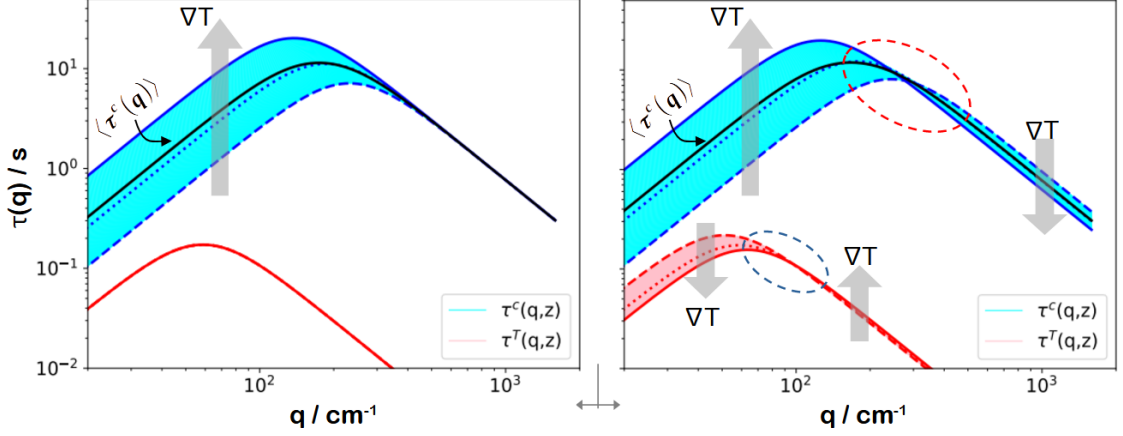


Fig. 4.22: Comparison of all the layer relaxation functions $\tau_i(q, z)$ resulting from the 'constant' simulation on the left and the 'total' simulation on the right. The style follows fig. 4.10. The two ellipses highlight the stack swap in both modes.

of both modes ($j = T, c$) and all layers ($z \in [0, h]$). Similar to the static structure factor analysis of fig. 4.21, all the thermal relaxation time contributions $\tau^T(q, z)$ (red) are falling, due to the constant parameters, onto each other. The main point is indicated with the two ellipses, where for both modes slightly after the q roll-off maximum, the dominance in the layers is swapping. This was shown before, in the discussion of fig. 4.9, where we mentioned that, the direction of the temperature gradient $\vec{\nabla}T$ is flipping from upwards to downwards and in the thermal case the other way around. This effect can not be found in the left, 'constant' simulation plot, which means, it's a thermal dependency effect of the transport properties. As we know from eq. 4.41, the right flanks are determined by the diffusion coefficient D , in the solutal case, and the thermal diffusivity D_{th} in the thermal case. On the left flank, however, the band width of the 'total' simulation is again slightly wider than that of the 'constant' one, but the curves do not really differ otherwise. In conclusion, it should be noted that the relaxation time dynamics of the NEF is a very complex quantity. The left flanks, in the gravitationally limited region, are mainly determined by the non linearities. The right flanks, on the other hand, are only affected by the temperature dependencies of the transport coefficients. These two fundamentally different effects have so far been neglected in the literature, since

for small molecules and weaker temperature gradients they are not as dominant as in our case with stronger temperature and concentration gradients.

Transport coefficient comparison

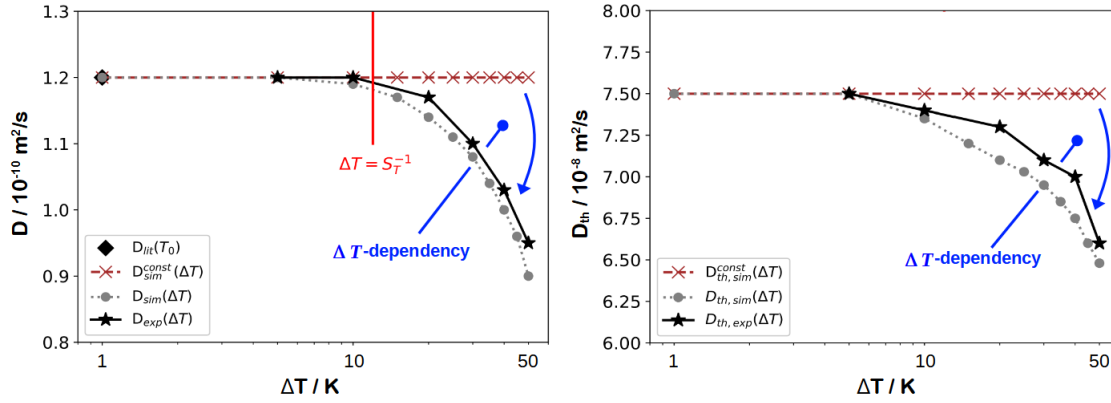


Fig. 4.23: Plots of fig. 4.16 and fig. 4.17 extended by the constant values of D (left) and D_{th} (right), shown by the brown x-symbols. The blue arrows show the area between the two simulated curves, which reflects the temperature dependencies of the quantities.

We start with the comparison of the diffusion coefficient D and the thermal diffusivity D_{th} of the two simulation approaches (index: *sim*) and the experimental results (index: *exp*), which is shown in fig. 4.23. The black stars and the gray dots are the experimental and 'total' simulation coefficient results, known from fig. 4.16 and fig. 4.17. The new ones of the 'constant' simulation are demonstrated as the brown x-symbols and reflect, in these two cases the constancy of the associated parameter. Since these originate from the fit of the right flanks of the relaxation times, for which we know that they are only temperature dependent, the difference between the two simulations must be the temperature dependence of $D(\Delta T)$ and respectively $D_{th}(\Delta T)$, which is indicated by the blue arrows.

The last panel of this entire simulation section demonstrates in fig. 4.24 the comparison of the resulting Soret coefficients S_T . The illustration style remains the same, where the black stars symbolize the experimental value and the two simulations are shown with the gray dots ('total' simulation) and brown x-symbols ('constant' simulation). The red line visualizes our threshold $\Delta T = S_T^{-1} = 11.3$ K. The message is, that for larger temperature differences the non linearity of the diffusion or Soret

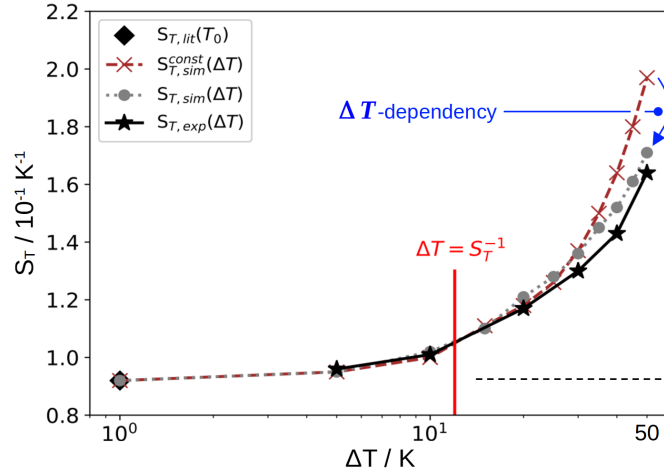


Fig. 4.24: Expanded illustration of the Soret coefficient half of fig. 4.16. The additional brown x-symbols demonstrate the resulting Soret coefficients $S_{T, sim}^{const}(\Delta T)$ of the 'constant' simulation.

equation ($c(1 - c)$) is not negligible any more. The blue arrow shows again the differences between the two simulation approaches and is, following fig. 4.23, the temperature dependency of the Soret coefficient $S_T(\Delta T)$. This means that the thermal dependence is a much smaller but opposing process to the effect of non linearity. As we will see in fig. 4.34 of section 4.4, there are also sample compositions (different c , M), where the nonlinear effect is smaller and the temperature dependency is the dominant effect. In contrast to the here shown increasing values, this leads to falling Soret and thermodiffusion coefficients and to rising diffusion coefficients (cf. pink arrow in fig. 4.38).

This concludes the simulation section. Based on the empirical discrepancies between the measured and the literature transport properties, we searched for a reasonable explanation and found it in the neglected nonlinearity of the diffusion equation. For this purpose we calculated our structure function signals as a layer model and compared the included signal contributions with experiments. We extended the simulation and included the temperature dependencies of the thermophysical parameters. For the confirmation, not only the signals themselves but also the resulting transport coefficients were considered. In all points the simulation agrees with the experiments and was thus verified. Finally, we have considered a second

simulation approach, which treats the nonlinearity of the equations separately from the temperature dependencies. However, it is difficult to predict when this nonlinear consideration will be useful, we found that in the case of polymer systems it is always necessary, especially if the applied temperature difference is larger than the inverse Soret coefficient ($\Delta T > S_T^{-1}$).

4.3 NEF static structure factor $S(q)$ analysis

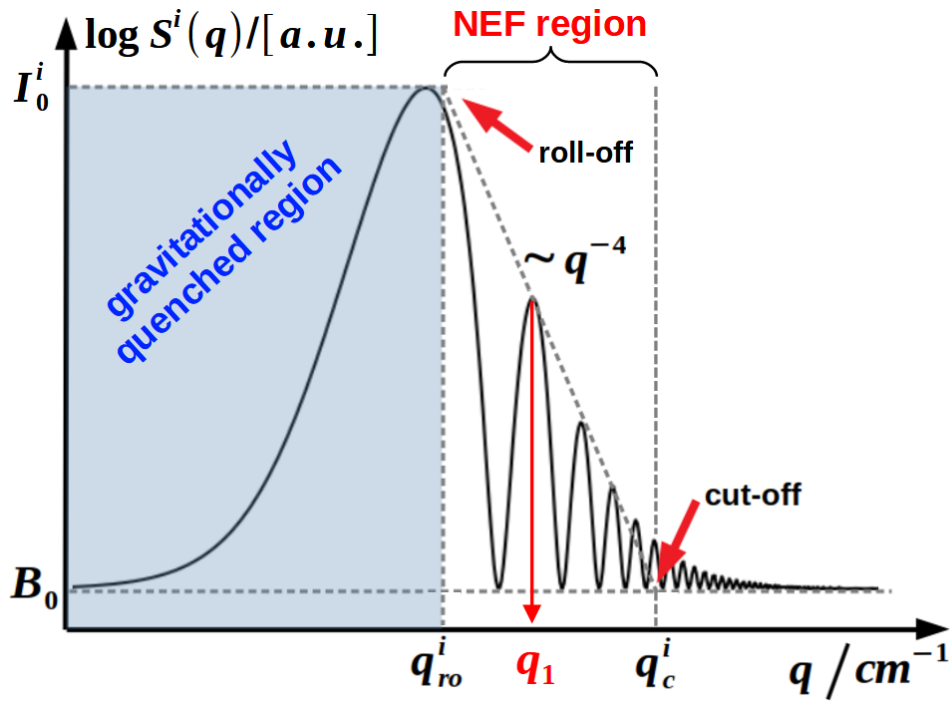


Fig. 4.25: Static structure factor sketch, which is known from the right plot of fig. 4.3, where one of the two analog modes $S^i(q)$ ($i = T, c$) is shown. The blue area is the gravitationally quenched region for q values smaller than the roll-off threshold q_{ro}^i . The interesting NEF region is located between the roll-off and cut-off values and shows the characteristic $\sim q^{-4}$ -dependency.

This section is intended to give a closer look at the experimental static structure factors $S(q)$, which are a key component in the characterization of the NEFs. Additionally, it serves as a conformation for the embedded theory, which is conceptually a theory of small molecules in a fluid mixture. A priori it was not clear, to what

extent it can be applied to highly asymmetric systems, such as entangled or glass-forming polymer solutions. The section is designed as a semi-empirical analysis and does not always provide complete explanations. Usually it addresses certain circumstances and gives perspectives on how these could be further analyzed. In our experiments we have three external parameters: the applied temperature difference ΔT as the thermal quantity and the two solutal ones, the concentration c as well as the molar mass M of the polymers. These two groups and their associated dependencies define the two following sub-sections, where we will characterize the thermal and solutal conditions of the NEF static structure factor. As we have seen already, we construct the total static structure factor $S(q)$ as a sum of the individual contributing thermal ($i = T$)¹⁰ and solutal ($i = c$) modes $S^i(q)$, which are recalled by the sketch of [fig. 4.25](#) (slightly modified version of [fig. 4.3](#)).

$$S(q) = \overbrace{\frac{\partial n}{\partial c} \Big|_{T,p}^2 \cdot \frac{I_0^c}{1 - (q/q_{ro}^c)^4}}^{=S^c(q)} + \overbrace{\frac{\partial n}{\partial T} \Big|_{c,p}^2 \cdot \frac{I_0^T}{1 - (q/q_{ro}^T)^4}}^{=S^T(q)} + B_0 \quad (4.56)$$

$=A_{NE}^c(q)$ $=A_{NE}^T(q)$

Therein we find the q -dependent NEF amplitudes $A_{NE}^i(q)$ (for $i = T, c$). In [eq. 2.43](#) of the theory [section 2.5](#) we explained, that these amplitudes themselves consist of several parts. To focus on the most important non equilibrium portions, we analyze a certain q value¹¹ of $q_1 = 367 \text{ cm}^{-1}$ in the NEF region (red marked in [fig. 4.25](#)), between roll-off and cut-off thresholds ($q_{ro}^i < q < q_c^i$) of both modes. If the amplitude is evaluated for this value, it is represented by the superscript q in $A^i|_q$. Additionally we normalize the amplitudes for better comparison to their individual backgrounds B_0 , which leads to the observables $A^i|_q$ (for $i = T, c$).

$$A^c|_q = \frac{A_{NE}^c(q_1)}{B_0} = \frac{1}{B_0} \cdot \frac{\frac{|\vec{\nabla}c|^2}{\nu \cdot D}}{1 - (q/q_{ro}^c)^4} \sim \frac{|\vec{\nabla}c|^2}{\nu \cdot D} \quad (4.57)$$

$$A^T|_q = \frac{A_{NE}^T(q_1)}{B_0} = \frac{1}{B_0} \cdot \frac{\frac{|\vec{\nabla}T|^2}{\nu \cdot D_{th}}}{1 - (q/q_{ro}^T)^4} \sim \frac{|\vec{\nabla}T|^2}{\nu \cdot D_{th}} \quad (4.58)$$

¹⁰Note that we are back in our notation of i , to differentiate the thermal and solutal contributions.

¹¹Second oscillation maxima of the transfer function (compare [fig. 4.25](#), [fig. 4.26](#)).

Since we are primarily interested in the temperature¹², concentration and molar mass dependencies, it is sufficient to consider only the proportionalities shown in eqs. 4.57 and 4.58 (last terms). Of interest is also the temperature and concentration dependence of the two roll-off wavevectors

$$q_{ro}^T = \left[\frac{g \cdot \beta_T \cdot |\vec{\nabla} T|}{\nu \cdot D_{th}} \right]^{1/4} \quad (4.59)$$

$$q_{ro}^c = \left[\frac{g \cdot \beta_c \cdot |\vec{\nabla} c|}{\nu \cdot D} \right]^{1/4}, \quad (4.60)$$

which is neglected for a better understanding of the amplitude dependencies in the approximations of eq. 4.57 and 4.58. More important are the in eq. 4.7 already tapped, temperature and concentration dependencies of the roll-off wavevector ratio q_{ro}^c/q_{ro}^T , which decisively determines the Soret coefficient:

$$S_T = \frac{-1}{c(1-c)} \cdot \frac{\beta_T}{\beta_c} \cdot \frac{D}{D_{th}} \cdot \left(\frac{q_{ro}^c}{q_{ro}^T} \right)^4. \quad (4.61)$$

As mentioned, the following sub-section 4.3.1 starts with the thermal analysis, which then will be followed by a large solutal section, where the concentration and molar mass dependencies are analysed in parallel.

4.3.1 Temperature dependence

We start with the thermal analysis of the NEF static structure factor. For this purpose we studied a dilute solution ($c = 0.01$ [w/w]) of polystyrene ($M = 17.9$ kg/mol) in toluene, where we varied for each measurement the applied temperature differences $\Delta T = 10, 20, 30, 40, 50$ K. This series is already known from the experimental comparison in the simulation section 4.2. Illustration 4.26 shows in the central plot all associated static structure factors $S(q)/B_0$, which are normalized to their individual backgrounds B_0 . The black solid line represents an equilibrium measurement without an applied temperature field. The curves are the resulting static structure

¹²Temperature dependence means correctly, the dependence of the temperature difference.

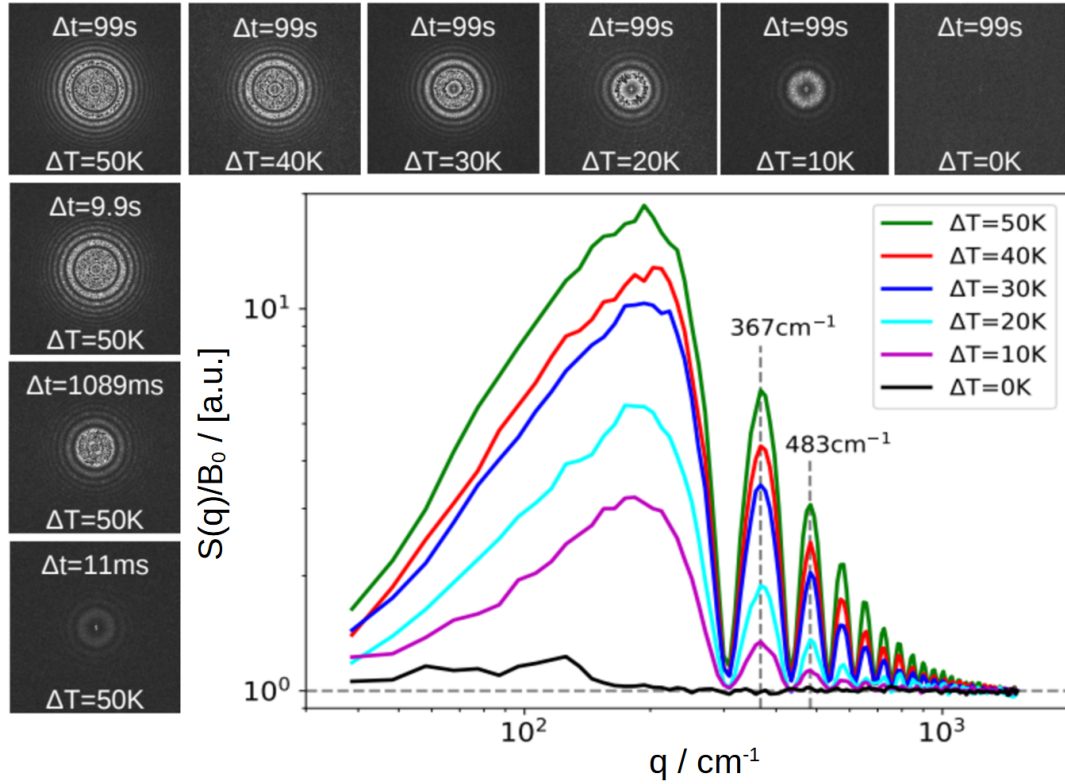


Fig. 4.26: Illustration of different total static structure factors $S(q)$, of the same mixture ($M = 17.9 \text{ kg/mol}$, $c = 0.01 \text{ [w/w]}$), with varied external temperature gradient. The surrounding pictures are the evaluated static structure factor images $S(\vec{q})$ at different temperatures ΔT and correlation times Δt . The two marked q values are the second and third oscillation maxima and serve as a orientation for [fig. 4.27](#).

factors of the associated structure functions $C(q, \Delta t = 99 \text{ s})$ at the maximum correlation time of 99 s. As an additional information, the surrounding pictures show the resulting images of specific structure functions $C(\vec{q}, \Delta t)$, before the azimuthal averaging of the q values (introduced in [fig. 3.18](#)). For the longest correlation time of $\Delta t = 99 \text{ s}$ the upper horizontal row demonstrates all temperature differences ΔT . Additionally, left vertical column shows for 50 K different correlation time steps¹³. We can clearly see, from right to left, how, with increasing temperature difference the central intensity increases and the cut-off values is pushed outwards, which exposes more and more oscillations.

¹³If we compare these images with [fig. 6.2](#) from the appendix, the purity of the plots envisioned that the setup has been adjusted as best as possible.

The next sub-section focuses specifically on the NEF amplitudes of these temperature depended structure factors. This is followed by an analysis of the q roll-off values.

a) NEF amplitudes

At a first glimpse we understand immediately, that all the curves of [fig. 4.26](#) reflect the same q^{-4} -behavior (in the NEF region) and that the NEF amplitudes increase according the applied temperature difference ΔT . For a detailed discussion of the temperature dependency, two specific q values (367 and 483 cm^{-1}) are marked in [fig. 4.26](#). Their amplitudes are shown as a function ΔT in the left panel of [fig. 4.27](#) together with a quadratic fit

$$\frac{S(q)}{B_0} - 1 = a(q) \cdot \Delta T^2 . \quad (4.62)$$

The previously shown [eq. 4.58](#) already suggests this quadratic dependency, which in turn confirms this behavior for our polymer samples. As a second step we

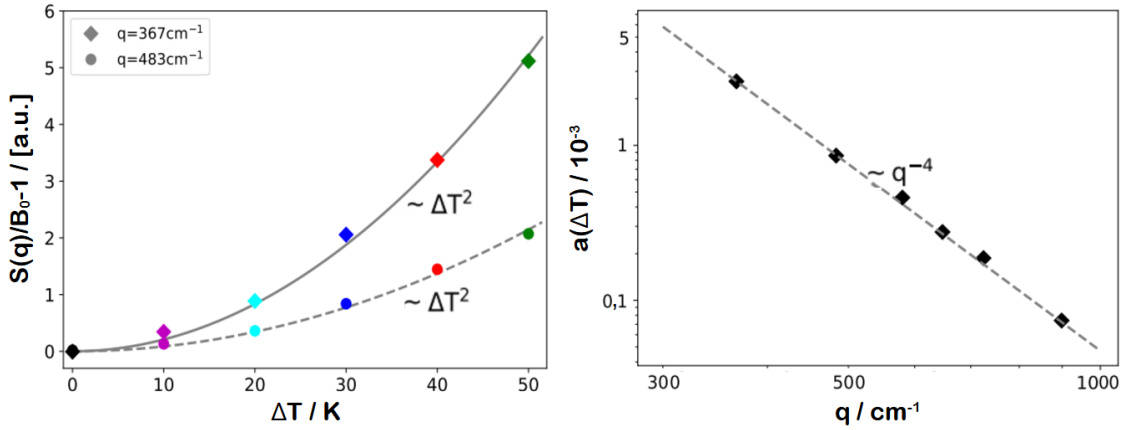


Fig. 4.27: LEFT: Quadratic fitted amplitudes (same color scheme as in [fig. 4.26](#)) of the normalized total static structure factor $S(q)/B_0 - 1$. RIGHT: Further analysis of the amplitude factor $a(q)$ of the different q values (more then the two marked ones). In it we can clearly see the characteristic $\sim q^{-4}$ dependency of non equilibrium amplitudes.

analyse the q -dependent amplitude factor $a(q)$. If we do this for the first six

oscillation maxima (not only the first two), we get the right illustration of [fig. 4.27](#). This method provides a demonstration of the characteristic q^{-4} -dependency of the NEF amplitudes. In future projects it would be possible to take a closer look at the amplitude factor $a(q)$, which is an isolated description of the total amplitude of the NEF.

$$a(q) = \frac{1}{\nu B_0 h^2} \cdot \left[\left. \frac{\partial n}{\partial T} \right|_{c,p}^2 \frac{\frac{1}{D_{th}}}{1 - (q/q_{ro}^T)^4} + \left. \frac{\partial n}{\partial c} \right|_{T,p}^2 \frac{\frac{S_T^2}{D} [c(1-c)]^2}{1 - (q/q_{ro}^c)^4} \right] \quad (4.63)$$

The equation is calculated, with [eq. 4.56-4.61](#) used in [eq. 4.62](#). It contains several transport properties, as the Soret-coefficient S_T , the diffusion coefficient D , the thermal diffusivity D_{th} and the kinematic viscosity ν .

b) Roll-off wavevectors

Now we want to change our focus to the temperature dependency of the two roll-off wavevectors $q_{ro}^i(\Delta T)$ ($i = c, T$) and the cut-off wavevector $q_c(\Delta T)$. For the thermal

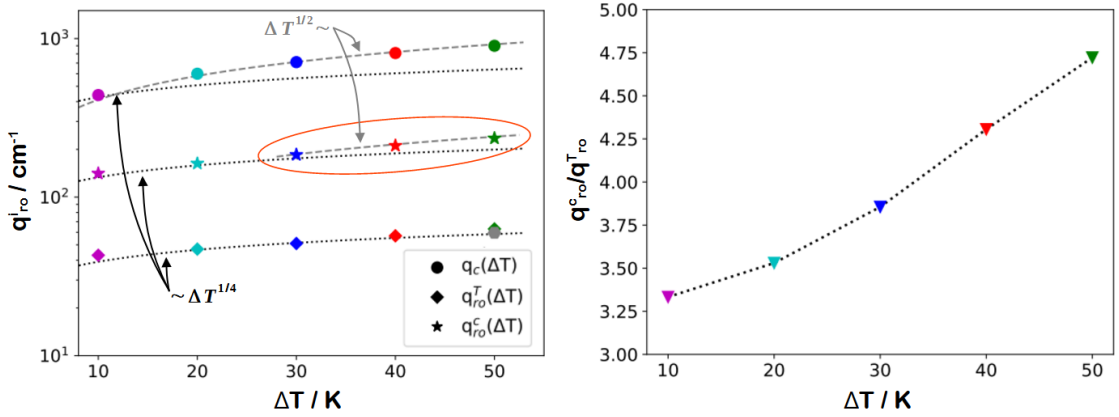


[Fig. 4.28](#): LEFT: Illustration of the thermal dependencies of the two roll-off values $q_{ro}^i(\Delta T)$ and the cut-off value $q_c(\Delta T)$. The progression of the thermal q roll-off value (diamonds) can be fitted proportional to the fourth root ($q_{ro}^T(\Delta T) \sim \Delta T^{1/4}$) and reaches for $\Delta T = 50$ K the value of pure toluene (gray hexagon). The solutal q roll-off value (stars) starts with the shown $q_{ro}^c(\Delta T) \sim \Delta T^{1/4}$ proportionality, however, deviates upward for large ΔT . The cut-off threshold seems to be proportional to the root of the temperature difference ($q_c(\Delta T) \sim \Delta T^{1/2}$). RIGHT: Demonstration of the in [eq. 4.61](#) mentioned q roll-off ratio, which determines the Soret coefficient behavior of [fig. 4.24](#).

roll-off values $q_{ro}^T(\Delta T)$ we find a proportionality to the fourth root ($\sim \Delta T^{1/4}$) of the applied temperature difference ΔT , which is shown with the dotted black lines in [fig. 4.28](#). This was expected, due to the temperature gradient $\vec{\nabla}T = \Delta T/h$ dependency, mentioned in [eq. 4.59](#). In the case of the solutal roll-off value $q_{ro}^c(\Delta T)$, the small temperature differences follow also the $\Delta T^{1/4}$ proportionality (black dotted line). The values of the large temperature differences, especially the three in the red ellipse, however, deviate increasingly. This is due to the in [section 4.2](#) explained non linearity effect of the Soret equation, which enters via the dependence on the concentration gradient $\vec{\nabla}c$, shown in [eq. 4.60](#). Finally, for the cut-off values q_c we find a proportionality to the square of the applied temperature difference:

$$q_c(\Delta T) \sim \Delta T^{1/2} . \quad (4.64)$$

This is illustrated with the gray dashed line, which deviates significant from the black dotted line ($\sim \Delta T^{1/4}$). For the time being, this should be accepted as an empirical measurement result, that cannot be explained yet. However, it should be taken up again in future investigations.

The right panel of [fig. 4.28](#) shows the ratio of the solutal and thermal q roll-off values (q_{ro}^c/q_{ro}^T) in dependency of the applied temperature difference ΔT . As in [fig. 4.24](#) of [section 4.2](#) demonstrated, this nonlinear factor is the dominant reason for the successively from the literature value diverging Soret coefficient $S_T(\Delta T)$.

$$S_{T,exp}(\Delta T) \sim \left(\frac{q_{ro}^c(\Delta T)}{q_{ro}^T(\Delta T)} \right)^4 \sim \begin{cases} \Delta T \leq S_{T,lit}^{-1} : \frac{\Delta T^{1/4}}{\Delta T^{1/4}} \sim 1 \\ \Delta T \geq S_{T,lit}^{-1} : \frac{\Delta T^{1/2}}{\Delta T^{1/4}} \sim \Delta T^{1/4} \end{cases} \quad (4.65)$$

More information will follow in [section 4.4](#) in [fig. 4.35](#), where this topic is analyzed in detail. Of course, the thermal effects of the transport coefficients should not be completely forgotten, but it is advisable to further explore the temperature dependent relationship of q_{ro}^c/q_{ro}^T , which is shown in the right plot of [fig. 4.28](#).

This concludes the thermal analysis of the NEF structure factor and we come to the solutal dependencies in the next sub-section.

4.3.2 Concentration and molar dependence

In this sub-section we shift our attention to the solutal dependencies of the NEF structure factor analysis. This means, we show the NEF amplitudes $A^i|{}^q(c, M)$ and of the q roll-off values $q_{ro}^i(c, M)$, as functions of the polymer concentration c and the molar mass M , which has never been done before systematically. For a pure solutal comparison, all measurements are performed with the same temperature difference of $\Delta T = 50$ K. Due to the concentration independence of the thermal contributions (A^T, q_{ro}^T) it become clear to priorities the solutal effects of the solutal components. This we will see soon in [eq. 4.68](#) and [4.78](#). The two equations [4.66](#) and [4.67](#) are [eq. 4.57](#) and [4.60](#), where the concentration gradient $\vec{\nabla}c$ is replaced by the Soret coefficient S_T and where additionally only the solutal dependencies (c, M) are considered.

$$A^c|{}^q(c, M) \sim \frac{|-S_T(c, M)|^2}{\nu(c, M) \cdot D(c, M)} \cdot (c \cdot (1 - c))^2 \quad (4.66)$$

$$q_{ro}^c(c, M) \sim \left[\frac{|-S_T(c, M)|}{\nu(c, M) \cdot D(c, M)} \right]^{1/4} \cdot (c \cdot (1 - c))^{1/4} \quad (4.67)$$

As a first step, the two illustrations of [fig. 4.29](#) demonstrate several structure functions as a concentration series (same $M = 4.8$ kg/mol) on the left and a molar mass series (same $c = 0.05$ [w/w]) on the right. The remarkable fact of these series is, that for a successively increasing parameter, which is on the left c and on the right M , the amplitudes do not increase uniformly, as we have seen it for ΔT . In both cases a certain threshold appears, which leads to a decrease of the amplitudes, after the initial increase. This is coded in the line types of [fig. 4.29](#), where the curves, with increasing amplitudes are shown with solid lines and the decreasing curve amplitudes are illustrated with dashed lines. More explicitly, we see on the left side that the NEF amplitudes increase from $c = 1\%$ (red line) up to 10% (cyan). The $c = 20\%$ (orange) is just behind the 10% curve and for even larger concentrations the amplitudes decrease again. On the right side the situation is similar, for $M = 2.1$ kg/mol (red) to $M = 17.9$ kg/mol (green) the NEF amplitudes increase, remains equal for $M = 90$ kg/mol (violet) and then falls to $M = 1070$ kg/mol (orange). The causes of these behaviors will be examined in more

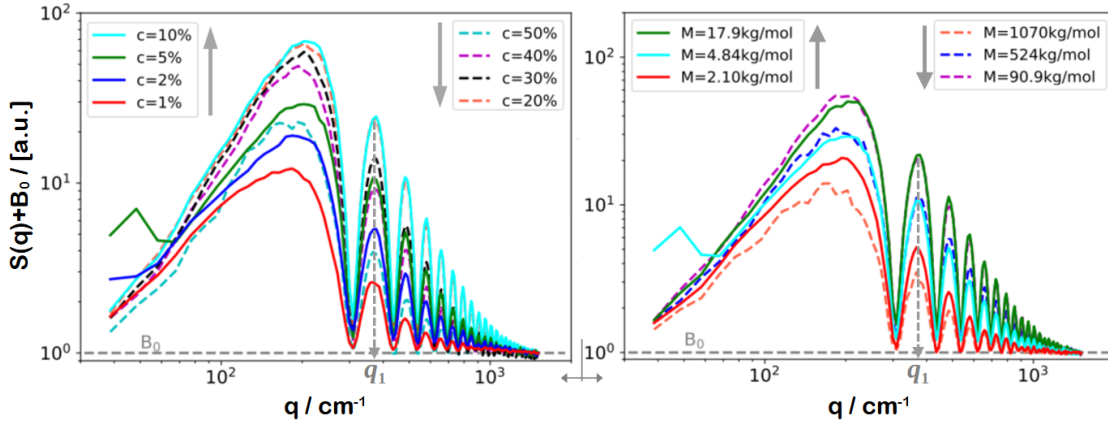


Fig. 4.29: LEFT: Concentration series of a mixture with a molar mass of $M = 4.84$ kg/mol in toluene, which are all measured with a temperature gradient of $\vec{\nabla}T = 10^4$ K/m. The curves with a solid line show an increasing amplitude as a function of the concentration c , where the dashed curves decrease in the amplitude with further increasing c . RIGHT: Molar mass series of mixtures with a constant concentration $c = 0.05$ [w/w], also with temperature gradient of $\vec{\nabla}T = 10^4$ K/m. Similar to the concentration series the curves with a solid line show a increasing amplitude with rising molar mass M and the dashed curves a decreasing amplitude with a further rising M . The arrows (next to the legend) point in the direction of increasing amplitude.

detail. For this purpose, we first consider the q roll-off values and then take a close look at the NEF amplitudes.

a) Roll-off wavevector

A detailed understanding of solutal structure factor effects is given, among others, by the roll-off wavevectors, which is the focus of this sub-section. The first point, which we can see in fig. 4.30 is that the thermal roll-off values q_{ro}^T (diamond markers) show no solute dependency, neither in the concentration c (right), nor in molar mass M (left).

$$q_{ro}^T|_{tol} = 59.6 \pm 2 \text{ cm}^{-1} \quad (4.68)$$

They all fluctuate around the constant value of pure toluene $q_{ro}^T|_{tol}$ ¹⁴, which is shown with the grey diamond markers and the attached dashed lines. This means that the thermal q roll-off values q_{ro}^T , despite the involved kinematic viscosity $\nu(c, M)$,

¹⁴Notation: Thermal q roll-off value q_{ro}^T of toluene (index *tol*).

do not show any significant dependencies on the concentration c or the molar mass M .

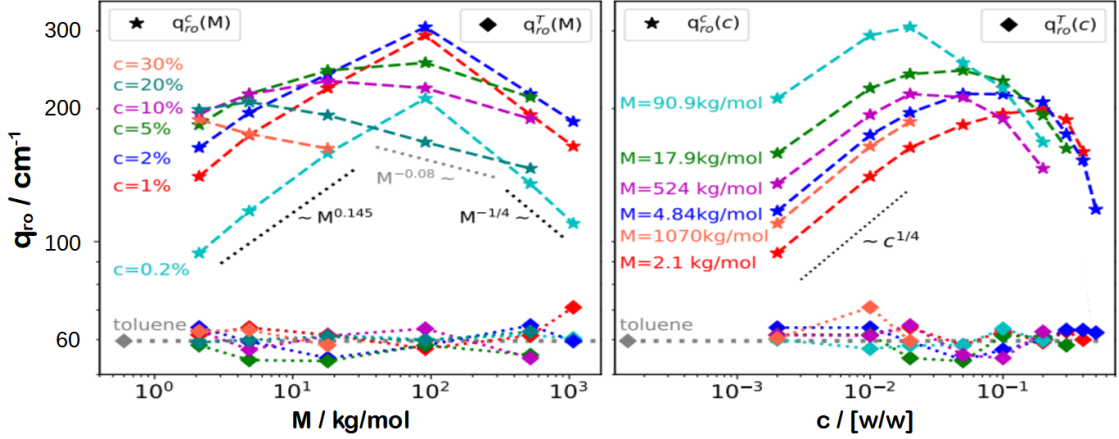


Fig. 4.30: Illustration of the solutal dependencies of the roll-off values q_{ro}^i . Left as a function of the molar mass M , where the colors differentiate the concentration series. On the right as a function of the concentration c , where the color show different molar masses M . Additionally the gray diamond markers and the dashed line visualize the thermal roll-off value of pure toluene. Note that they share the y-axis. [Fig. 6.6](#) of the appendix shows a normalized alternative illustration style.

The star symbols in both panels of [fig. 4.30](#) show the solutal q roll-off values as concentration series $q_{ro}^c|_c(M)^{15}$ (color coded and named in the plot) on the left and molar mass series $q_{ro}^c|_M(c)$ (also differentiated by the colors) on the right. The curve progressions are more or less similar, where the curves increase to a maximum value of the essential variable (x-axis) and afterward decrease. But the proportionalities (dotted lines) of the series are very different. This will now be addressed.

Summary of the proportionalities

Brief empirical summary of the demonstrated q roll-off value curves and the collective proportionalities. The left plot of [fig. 4.30](#) shows, in the limit of small molar masses ($\tilde{M} = M \rightarrow 0$), the same proportionality ($\tilde{M}^{0.145}$) for all concentration

¹⁵Notation: Solutal q roll-off q_{ro}^c , for a specific c and as a function of M .

curves¹⁶, which is illustrated by the dotted black line.

$$q_{ro|c}^c(\tilde{M}) \sim \left[\frac{S_T|_c(\tilde{M})}{\nu|_c(\tilde{M}) \cdot D|_c(\tilde{M})} \right]^{1/4} \stackrel{\text{comp.}}{\sim} \tilde{M}^{0.145} \quad (4.69)$$

The impression is, that the (left) inclining branches are shifted with increasing c to smaller M values. Therefore eq. 4.69 condenses eq. 4.67 and considers only the molar mass proportionalities. Fig. 6.6 of the appendix offers an alternative, normalized illustration style, which can be considered as well, especially if a described proportionality seems unclear. Now we have to ask the question, can we somehow explain the shown proportionality or can it tell us something about the involved transport coefficients? With the in section 4.2.1 mentioned concentration and molar mass constancy of the thermodiffusion coefficient D_T (in our c, M ranges), the Soret coefficient is determined by the inverse diffusion coefficient, $S_T \sim D^{-1}$. For more precise statements, we briefly refer to figs. 4.41, 4.42 and 4.43 in advance, which give us molar mass proportionality for Soret and diffusion coefficients.

$$D|_c(\tilde{M}) \sim \tilde{M}^{-0.6} \quad (4.70)$$

$$S_T|_c(\tilde{M}) \sim \tilde{M}^{0.6} \quad (4.71)$$

With these limitations, we can consider again eq. 4.69 and determine a consequence for the kinematic viscosity $\nu|_c(\tilde{M})$.

$$q_{ro|c}^c(\tilde{M}) \sim \left[\frac{\tilde{M}^{1.2}}{\nu|_c(\tilde{M})} \right]^{1/4} \stackrel{\text{comp.}}{\sim} \tilde{M}^{0.145} \Rightarrow \nu|_c(\tilde{M}) \sim \tilde{M}^{+0.62} \quad (4.72)$$

The result is a proportionality of the kinematic viscosity, for small molar masses (\tilde{M}), to $\nu|_c(\tilde{M}) \sim \tilde{M}^{+0.62}$. An exponent similar to the Flory-Huggins-exponent of 0.66^[81] is a reasonableness expectation. It should be made clear that eq. 4.72 is a purely phenomenological result and should not be overestimated, especially with regard to small concentrations.

¹⁶The note 'comp.' in eq. 4.69 indicates a comparison of the plotted proportionality and the dependencies in the equation.

For large molar masses ($\hat{M} = M \rightarrow \infty$) two proportionalities are visible in the left panel of [fig. 4.30](#) (alternatively in [fig. 6.6](#)). One for small concentrations $c_- \lesssim 5\%$, where the progression of the roll-off values goes like $q_{ro}^c|_{c_-}(\hat{M}) \sim \hat{M}^{-1/4}$ (black decreasing dotted line), and one for bigger concentrations ($c_+ \gtrsim 5\%$) with a proportionality to $q_{ro}^c|_{c_+} \sim \hat{M}^{-0.08}$ (gray dotted line):

$$q_{ro}^c|_c(\hat{M}) \sim \left[\frac{S_T|_c(\hat{M})}{\nu|_c(\hat{M}) \cdot D|_c(\hat{M})} \right]^{1/4} \underset{\text{comp.}}{\sim} \begin{cases} \text{for } c_- : \hat{M}^{-1/4} \\ \text{for } c_+ : \hat{M}^{-0.08} \end{cases} . \quad (4.73)$$

For these two concentration and molar mass ranges, estimations in the form of [eq. 4.70](#) and [eq. 4.71](#) are difficult or impossible to make. But we will need these estimations later again and should keep them in mind.

Now we want to consider the right panel of [fig. 4.30](#), where we can see the solutal q roll-off values ($q_{ro}^c|_M(c)$) of several molar masses M , as a function of the concentration c . For small concentrations ($\tilde{c} = c \rightarrow 0$) we find a general proportionality to $q_{ro}^c|_M(\tilde{c}) \sim \tilde{c}^{1/4}$.

$$q_{ro}^c|_M(\tilde{c}) \sim \left[\frac{S_T|_M(\tilde{c})}{\nu|_M(\tilde{c}) \cdot D|_M(\tilde{c})} \right]^{1/4} \cdot \tilde{c}^{1/4} \underset{\text{comp.}}{\sim} \tilde{c}^{1/4} \quad (4.74)$$

Once again, we take advantage of the results that will follow in [fig. 4.38](#) and [fig. 4.39](#), which deliver a constant proportionality for the diffusion D and Soret coefficients S_T in the limit of small concentrations ($\tilde{c} = c \rightarrow 0$).

$$D|_M(\tilde{c}) \sim \text{const} \quad (4.75)$$

$$S_T|_M(\tilde{c}) \sim \text{const} \quad (4.76)$$

With [eq. 4.74](#) and these two approximations, we find that the kinematic viscosity is also a constant value, in the limit for small polymer concentrations $\nu|_M(\tilde{c})$.

$$q_{ro}^c|_M(\tilde{c}) \sim \left[\frac{1}{\nu|_M(\tilde{c})} \right]^{1/4} \sim \text{const} \Rightarrow \nu|_M(\tilde{c}) \sim \text{const} \quad (4.77)$$

This was expected, since the viscosity of the mixture starts with the constant viscosity contribution of the pure toluene solvent $\nu|_M(\tilde{c}) = \nu_{tol}$. That could mean, if we use these curves and the associated diffusion and Soret coefficients (follow in [section 4.4](#)), we could measure in our experiments the kinematic viscosity. This would be a comparison option to conventional measurement methods, but not a replacement.

b) NEF amplitudes

In a similar way as in the previous sub-section, we want to formulate the solutal dependencies of the NEF amplitudes $A_{NE}^c(q)$. The two panels of [fig. 4.31](#) illustrate the same concentration and molar mass series, we know from [fig. 4.30](#). This time for the normalized NEF amplitudes $A^i|_q$ ([eq. 4.57](#)). First of all, we can record, that the thermal NEF amplitudes $A^T|_q$ (diamonds) show only tiny solutal dependencies and vary again close to the limit of pure toluene. Especially in the right case, we note a slight collective increase in the amplitudes with increasing concentration, but in general the thermal NEF amplitude contribution is dominated by the toluene value.

$$A^T|_{tol}^q = 5.58 \cdot 10^{-2} \pm 0.5 \cdot 10^{-2} \quad (4.78)$$

To see this is remarkable but consistent with [eq. 4.68](#), since the thermal NEF amplitude of [eq. 4.58](#) includes in the denominator the kinematic viscosity $\nu(c, M)$. Therefore, we initially expected a similar progression as for the solutal curves. However, we were not able to confirm this for our measurements.

[Fig. 4.31](#) shows seven different concentrations c as functions of the molar mass M on the left. In addition, the dotted lines show two proportionalities, which are discussed in more detail below. The illustration on the right shows six molar masses M as functions of concentration c , likewise with a proportionality. [Fig. 6.7](#) of the appendix shows again normalized, alternative illustrations of the curve in [fig. 4.31](#).

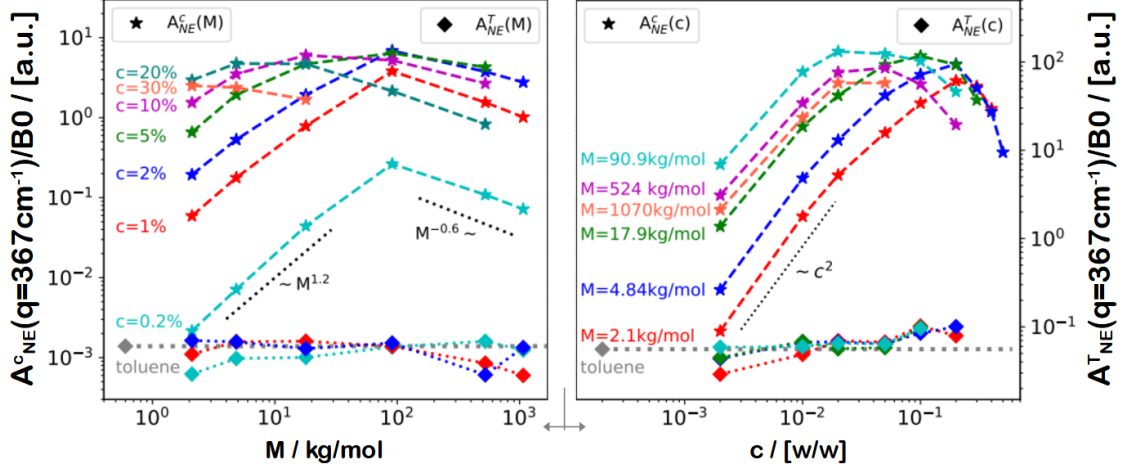


Fig. 4.31: Illustration of the solutal dependencies of the NEF amplitudes A_{NE}^i for a certain $q = 367 \text{ cm}^{-1}$ value. Left as a function of the molar mass M , where the colors reflect concentration series. On the right as a function of the concentration c , where the colors are the different molar masses. Additionally the gray diamond markers and the dashed line visualize the thermal amplitude of pure toluene. Note that the panels share the y-axes. Fig. 6.7 of the appendix shows a normalized alternative illustration style.

Summary of the proportionalities

Similar to the summary in the previous sub-section, we will characterize in the following the in fig. 4.31 shown proportionalities of the solutal NEF amplitudes. In the left panel most curves (up to $c \simeq 20\%$) of the concentration series $A_c^q(M)^{17}$ start for small molar masses ($\tilde{M} = M \rightarrow 0$, left flank) with a proportionality of $\sim \tilde{M}^{1.2}$ (dotted black line).

$$A_c^q(\tilde{M}) \sim \frac{(S_T|_c(\tilde{M}))^2}{\nu|_c(\tilde{M}) \cdot D|_c(\tilde{M})} \stackrel{\text{comp.}}{\sim} \tilde{M}^{1.2} \quad (4.79)$$

Using the already established estimates from eq. 4.70 and eq. 4.71, we find the same proportionality of the kinematic viscosity as in the q roll-off case (eq. 4.72).

$$A_c^q(\tilde{M}) \sim \frac{\tilde{M}^{1.8}}{\nu|_c(\tilde{M})} \sim \tilde{M}^{1.2} \quad \Rightarrow \quad \nu|_c(\tilde{M}) \sim \tilde{M}^{0.6} \quad (4.80)$$

¹⁷Notation: Normalized solutal NEF amplitude A^c for a constant q value ($A^c|_q$), a specific concentration ($A^c|_c$) and as a function of the molar mass ($A^c|_c(M)$).

Since the same proportionality for the kinematic viscosity¹⁸, in the limit of small molar masses (\tilde{M}), arises from two different quantities ($q_{ro}^c(\tilde{M})$, $A^c(\tilde{M})$), we can combine them and get estimations for the embedded transport coefficients. More precisely, we convert eq. 4.69 to the kinematic viscosity $\nu|_c(\tilde{M})$ and substitute this term into eq. 4.79. Thereby we get the following two estimations, which show a consistency to the assumptions of eq. 4.70 ($D|_c(\tilde{M}) \sim \tilde{M}^{-0.6}$) and eq. 4.71 ($S_T|_c(\tilde{M}) \sim \tilde{M}^{0.6}$).

$$\text{exp: } D|_c(\tilde{M}) \sim \tilde{M}^{-0.58} \quad (4.81)$$

$$\text{exp: } S_T|_c(\tilde{M}) \sim \tilde{M}^{0.62} \quad (4.82)$$

On the other side, for large molar masses ($\hat{M} : M \rightarrow \infty$) we find in fig. 4.31 a general progression of all curves, which is falling proportional to $A^c|_c(\hat{M}) \sim \hat{M}^{-0.6}$.

$$A^c|_c(\hat{M}) \sim \frac{(S_T|_c(\hat{M}))^2}{\nu|_c(\hat{M}) \cdot D|_c(\hat{M})} \stackrel{\text{comp.}}{\sim} \hat{M}^{-0.6} \quad (4.83)$$

In the first moment we have the same problem as in eq. 4.73, where general expressions for $D(\hat{M})$ and $S_T(\hat{M})$ can not be found. However, we can combine these two equations, similar to eq. 4.79. Therefore we convert eq. 4.83 to the kinematic viscosity $\nu|_c(\hat{M})$ and replace this term in eq. 4.73. Thereby the diffusion coefficient disappears and creates two dependencies for the Soret coefficient $S_T|_c(\hat{M})$ (each one for one of the two proportionalities of eq. 4.73):

$$\text{exp: } S_T|_c(\hat{M}) \sim \begin{cases} \text{for } c_- : \hat{M}^{0.4} \\ \text{for } c_+ : \hat{M}^{-0.28} \end{cases} \cdot \quad (4.84)$$

As a reminder, c_- defines concentrations smaller than five percent ($c \lesssim 5\%$) and c_+ describes in turn concentration bigger then five percent ($c \gtrsim 5\%$). The calculated proportionality $\sim \hat{M}^{0.4}$ can also be found in fig. 4.39 (upper dashed line). It seems to be an effect of the 'temperature sensitive', which was mentioned in the simulation section and will be further analysed in fig. 4.35. On the other hand, the second proportionality $\sim \hat{M}^{-0.28}$, can not be verified experimentally.

¹⁸This can also be seen in the right panel of fig. 6.7.

From the right panel of [fig. 4.31](#) we get for small concentrations ($\tilde{c} = c \rightarrow 0$) a quadratic proportionality for the amplitudes of the molar mass series $A^c|_M^q(c)$, which we already know from the diffusion and the Soret equation ([eq. 2.4](#)).

$$A^c|_M^q(\tilde{c}) \sim \frac{(S_T|_M(\tilde{c}))^2}{\nu|_M(\tilde{c}) \cdot D|_M(\tilde{c})} \cdot \tilde{c}^2 \stackrel{\text{comp.}}{\sim} \tilde{c}^2 \quad (4.85)$$

If we consider again [eq. 4.75](#) and [eq. 4.76](#), we find also, that the kinematic viscosity $\nu|_M(\tilde{c})$ is for small concentrations a constant term. This is the same result as in [eq. 4.77](#).

$$A^c|_M^q(\tilde{c}) \sim \frac{1}{\nu|_M(\tilde{c})} \sim \text{const} \quad \Rightarrow \quad \nu|_M(\tilde{c}) \sim \text{const} \quad (4.86)$$

In the following sub-section, we will dive a little bit deeper into the characterization of the solutal NEF amplitudes. For this purpose, some of the described proportionalities are analyzed more precisely. With that we find the exact threshold values from which on the amplitudes in [fig. 4.29](#) begin to decrease.

Proportionality factors

The three shown proportionalities of [eq. 4.79](#), [4.83](#) and [4.85](#) are behaviors of the solutal NEF amplitudes $A^c|_M^q(c, M)$ ¹⁹ for small concentrations (\tilde{c}) as well as small (\tilde{M}) and large molar masses (\hat{M}). These scale laws will be fitted with the following three equations:

$$\text{eq. 4.85} \rightarrow A^c|_M^q(\tilde{c}) = d|_{\tilde{c}}(M) \cdot \tilde{c}^{+2} \quad (4.87)$$

$$\text{eq. 4.79} \rightarrow A^c|_c^q(\tilde{M}) = a|_{\tilde{M}}(c) \cdot \tilde{M}^{+1.2} \quad (4.88)$$

$$\text{eq. 4.83} \rightarrow A^c|_c^q(\hat{M}) = b|_{\hat{M}}(c) \cdot \hat{M}^{-0.6} . \quad (4.89)$$

The new coefficients (a, b, d) are shift parameters, which change the y -intercept in the two log-log-plots of [fig. 4.31](#). If these are now plotted against their concentrations c and molar masses M (variable of the various curves), [fig. 4.32](#) is obtained. The resulting curve progressions are similar to the experimental ones, from which they

¹⁹Reminder: solutal amplitude A^c , for a specific q and as functions of c, M .

were derived. For a better understanding and for comparison some experimental curves (known from fig. 4.31) are added. According to our understanding, the resulting curves of the shift parameters (a : gray triangles, b : black dots, d : black triangles) describe the lower and upper solutal bounds of our description.

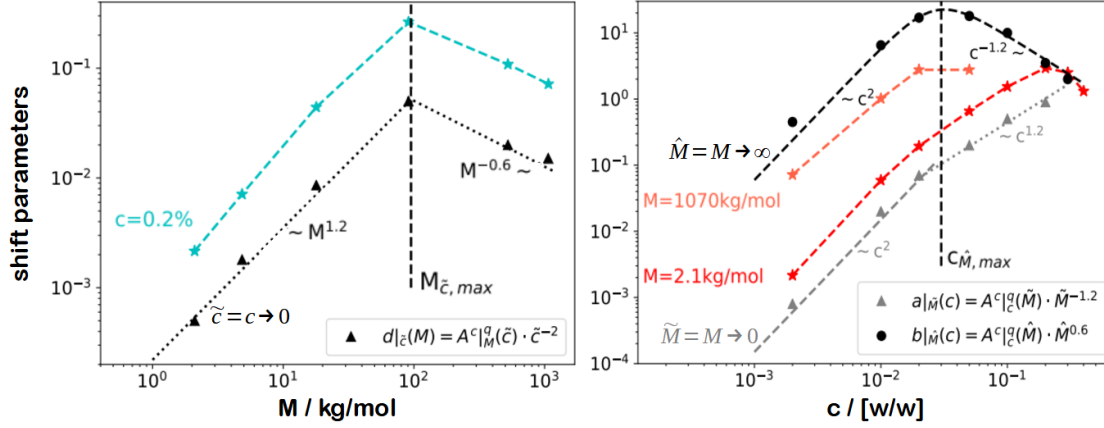


Fig. 4.32: LEFT: Plot of the parallel-shifting parameter $d(M)$ of the scale law for \tilde{c}^2 in the right illustration of fig. 4.31. Supplementary the smallest measured concentration (cyan, $c = 0.2\%$) is added as a comparison curve. RIGHT: Progression of the parallel-shifting parameters $a(c)$ and $b(c)$ of the two scale laws in the left illustration of fig. 4.31. Here also the smallest (red, $M = 2.1 \text{ kg/mol}$) and largest (orange, $M = 1070 \text{ kg/mol}$) measured molar mass curves are added.

In the left panel we see the curve of $d|_{\tilde{c}}(M)$, which results from the quadratic concentration dependency (diffusion equation) of the right panel in fig. 4.31. Added is the smallest measured concentration ($c = 0.2\%$), which is shown in turquoise. We see the exact same curve progression and describe the new curve as the lowest possible concentration estimation of the NEF amplitudes. Additionally we can find the molar mass

$$M_{\tilde{c}, max} = 95 \text{ kg/mol} , \quad (4.90)$$

where the curves reach their maxima. This is the already in fig. 4.29 mentioned molar mass with the largest amplitude. It is also an experimentally useful result and indicates, that in the limit of small concentrations (\tilde{c}) the largest solutal NEF amplitudes $A^c|_c^q(\tilde{c}, M)$ are achieved for a molar mass of $M = 95 \text{ kg/mol}$. For smaller molar masses the amplitude increases and for larger ones it decreases with increasing M .

A similar procedure can be used for the right panel of [fig. 4.32](#), where we illustrated the curve progressions of $a|_{\tilde{M}}(c)$ and $b|_{\hat{M}}(c)$ as a function of concentration. These curves construct, similar to the one on the left, the smallest (\tilde{M}) and largest (\hat{M}) possible estimations for the molar mass. For easier comparison we added the smallest measured molar mass of 2.1 kg/mol in red and the largest one of 1070 kg/mol in orange. Analogous to [eq. 4.90](#) we find here a concentration

$$c_{\hat{M},max} = 0.03 \text{ g/g} . \quad (4.91)$$

This means, in the limit of long polymer chains (large molar masses \hat{M}), the largest solutal NEF amplitudes $A^{c|q}(c, \hat{M})$ are possible for a concentration of $c = 3\%$. This threshold separates both new curves in two different phases, which are summarized in the following relations.

$$a|_{\tilde{M}}(c) \sim \frac{(S_T|_{\tilde{M}}(c))^2}{\nu|_{\tilde{M}}(c) \cdot D|_{\tilde{M}}(c)} [c \cdot (1 - c)]^2 \underset{\text{comp.}}{\sim} \begin{cases} \text{for } c < c_{\hat{M},max} : \tilde{c}^2 \\ \text{for } c > c_{\hat{M},max} : c^{1.2} \end{cases} \quad (4.92)$$

$$b|_{\hat{M}}(c) \sim \frac{(S_T|_{\hat{M}}(c))^2}{\nu|_{\hat{M}}(c) \cdot D|_{\hat{M}}(c)} [c \cdot (1 - c)]^2 \underset{\text{comp.}}{\sim} \begin{cases} \text{for } c < c_{\hat{M},max} : \tilde{c}^2 \\ \text{for } c > c_{\hat{M},max} : c^{-1.2} \end{cases} \quad (4.93)$$

If we compare the curve of [eq. 4.93](#) (black dots in [fig. 4.32](#)) with the orange experimental one we can see the similarity immediately. Both increase quadratically up to $c_{\hat{M},max}$ and then decrease proportionally to $\sim c^{-1.2}$. In the comparison of [eq. 4.92](#) (gray triangles in [fig. 4.32](#)) with the red experimental one we find something new in the curve progressions. From $c_{\hat{M},max}$ onward, the slope flattens from the former $\sim c^2$ proportionality to one of $\sim c^{1.2}$. This was not noticeable before but is also included in the experimental curve. It remains until the curves begin to decrease proportional to $\sim c^{-1.2}$, at large concentrations.

The entire [section 4.3](#) analyzed the two key components of NEF structure functions. Therefore we used our measurements and supplied for the q roll-off values q_{ro}^i and the NEF amplitudes A^i a temperature, concentration and molar mass descriptions. For the amplitudes we focused at characteristic $\sim q^{-4}$ region, but in subsequent

work it is also possible to investigate the gravitational intensities I_0^i ($i = c, T$). Further studies on the briefly mentioned q cut-off values q_c^i would also be advisable.

4.4 Transport coefficient analysis

This last chapter discusses the resulting transport coefficients of the first measurements with our new shadowgraphy setup and shows the resulting discoveries in two sections. Before we characterize the temperature²⁰, concentration and molar mass dependencies of the diffusion coefficient $D(\Delta T, c, M)$, the Soret coefficient $S_T(\Delta T, c, M)$ and the thermodiffusion coefficient $D_T(\Delta T)$ ²¹, we start with an overview of all explored simulated and experimental samples. These are the collected data, which are already known from [sections 4.1, 4.2 and 4.3](#).

Simulation samples

The following [tab. 4.6](#) gives an overview of all simulated sample compositions. In [section 4.2](#) we formulated our concentration ranges. Therein we wanted specifically to stay far away from the glass transition temperature, in the ranges of the dilute to semidilute solutions²². Every single one of these compositions is calculated for several temperature differences ΔT . The chosen temperatures are varying, in $dT = 5$ K steps, between $\Delta T_{\min} = 1$ K and $\Delta T_{\max} = 50$ K and are all listed in the first row of [tab. 4.6](#). As shown in the simulation [section 4.2](#), this was done in order to explain the differences between the experimental (measured with ΔT_{\max}) and literature values (approach of ΔT_{\min}). The answer to the disagreement of the experimental and the literature values was the neglected non linearity in the

²⁰Temperature dependence means again dependence on the temperature difference.

²¹ D_T is solutal independent.

²²Under certain circumstances it might be possible to go to even larger M and c , but this would require additional effects of the increased viscosity^[80] and deviating descriptions of the transport parameters^[72].

$\Delta T = 1, 5, 10, 15, 20, 25, 30, 35, 40, 45, 50 \text{ K}$					
$M \mid \text{kg/mol}$	$c \mid [\text{w/w}]$				
2.10	0.001	0.01	0.02	0.05	0.10
4.84	0.001	0.01	0.02	0.05	0.10
17.9	0.001	0.01	0.02	0.05	0.10
50.0	0.001	0.01	0.02	0.05	0.10
90.9	0.001	0.01	0.02	0.05	0.10

Tab. 4.6: Overview of all simulated samples. The molar mass range is indicated in the vertical direction, the concentration range on the horizontal. Every sample is calculated for all above shown temperature differences ΔT .

diffusion equation. This has already been shown in [section 4.2](#) and will now be taken to its logical conclusion.

Experimental samples

The considered experimental samples, which we used in the structure factor analysis of [section 4.3](#), are shown in the two [tables 4.7](#) and [4.8](#). The first one demonstrates the concentration and molar mass variances in the way of [tab. 4.6](#). For each molar mass, the corresponding row lists all studied concentrations. Each series was started in the limit of small concentrations and successively taken to higher ones. For easy comparison, all experiments were measured with the same temperature difference of $\Delta T = 50 \text{ K}$ over the same cell height of $h = 5 \text{ mm}$. The larger the molar mass became, the fewer concentrations could be measured, because the increased viscosity caused problems with cell filling (bubble formation) or because the measured signals could no longer be evaluated (decreasing amplitudes of [section 4.3](#))²³. The highlighted blue row ($M = 4.84 \text{ kg/mol}$) and red column ($c = 5\%$) are the series of the two panels in the previously shown [fig. 4.29](#), which demonstrated several static structure factors at the start of associated analysis. [Table 4.8](#) illustrates the already known temperature series. This mixture with a concentration of 1% and a molar mass of 17.9 kg/mol is measured for several temperature differences $\Delta T = 10, 20, 30, 40, 50 \text{ K}$ and was shown before in the

²³Note: Automated vacuum filling or smaller temperature differences could provide further results, but have not yet been tested.

M kg/mol	$\Delta T = 50$ K								
	c [w/w]								
2.10	0.002	0.01	0.02	0.05	0.10	0.2	0.3	0.4	\
4.84	0.002	0.01	0.02	0.05	0.10	0.2	0.3	0.4	0.5
17.9	0.002	0.01	0.02	0.05	0.10	0.2	0.3	\	\
90.9	0.002	0.01	0.02	0.05	0.10	0.2	\	\	\
524	0.002	0.01	0.02	0.05	0.10	0.2	\	\	\
1070	0.002	0.01	0.02	0.05	\	\	\	\	\

Tab. 4.7: Overview of all experimental binary mixtures. All here shown samples are measured with an applied temperature gradient of $\vec{\nabla}T_0 = 10^4$ K/m ($\Delta T = 50$ K, $h = 5$ mm). The blue row ($M = 4.84$ kg/mol) indicates the concentration and the red column ($c = 5\%$ g/g) the molar mass series, both of [fig. 4.29](#) (left, right).

experimental comparison of the simulation section and in the thermal analysis of the static structure factor.

combination	ΔT / K
$M = 17.9$ kg/mol $c = 0.01$ [w/w]	10, 20, 30, 40, 50

Tab. 4.8: The sample, with a polymer concentration of $c = 1\%$ and a molar mass of $M = 17.9$ kg/mol, is measured for several temperature differences. It is known from [fig. 4.26](#).

As in the structure factor analysis of [section 4.3](#), the transport coefficients D , S_T and D_T are also dependent on the three external parameters ΔT , c and M . Therefore, we follow here the previous logic and subdivide the two sub-sections into the thermal and solutal analysis of the transport coefficients.

4.4.1 Temperature dependence

Similar to [section 4.3.1](#) we first focus on the temperature dependencies of the transport coefficients. In addition to the experimental series of [tab. 4.8](#) we discuss the 275 independent simulations, which are shown in [tab. 4.6](#). The color scheme in the three following plots (of $D(\Delta T)$, $S_T(\Delta T)$ and $D_T(\Delta T)$) is identical, where

the molar masses are referred to in the plots. The simulations for $\Delta T_{min} = 1$ K represent the calculated reference values (index: *sim*, T_0) and are shown with diamonds. They perfectly match with the available literature values at the ambient temperature of $T_0 = 298.15$ K. This different illustration is to set them apart from all other simulations, which are demonstrated with small colored dot symbols. The experimental transport coefficients (tab. 4.8) are demonstrated with dark blue star-symbols and a dashed line. These are already known from the experimental comparisons in the simulation section (fig. 4.17, 4.16). Both the figures of the diffusion coefficient and the Soret coefficient are illustrations with two adjacent plots. The left one focuses only on the $M = 17.9$ kg/mol results and compares the different concentration curves. Next to all these curves the experimental comparison can be seen again. The right panel shows all molar masses, with the associated concentrations, and allows a comparison of the general behaviors of these entire molar mass groups.

Diffusion coefficient

Fig. 4.33 starts with the diffusion coefficient $D(\Delta T)$ and shows these values as a function of the applied temperature difference ΔT . As mentioned, the right side compares all the concentration series (dotted lines) of all the different molar masses (referenced colors), to each other. The largest concentration, in each molar mass, is the highest curve, with the largest diffusion coefficient. The smaller concentrations follow in order underneath. We can see, that the different concentration series of the small molar masses are stacked very narrowly, whereas the curves of the larger molar masses are further apart from each other. That is, as we will see in fig. 4.38, due to the much smaller overlap concentrations c^* of the larger molar masses. In addition, we can state that all curves show for large temperature differences a similar deviation towards smaller values. For a closer look on this thermal effect, the left illustration is an isolated zoom on the $M = 17.9$ kg/mol curve progressions. First of all, the large gray arrow demonstrates the mentioned concentration stacking. Additionally, we can see again the comparison of the simulated and experimental $c = 1\%$ curves, which we know from the left panel of fig. 4.16. As it applied for all molar masses, the smallest concentrations are deviating with increasing temperature difference ΔT the strongest from the calculated reference value $D_{sim}(T_0)$. This

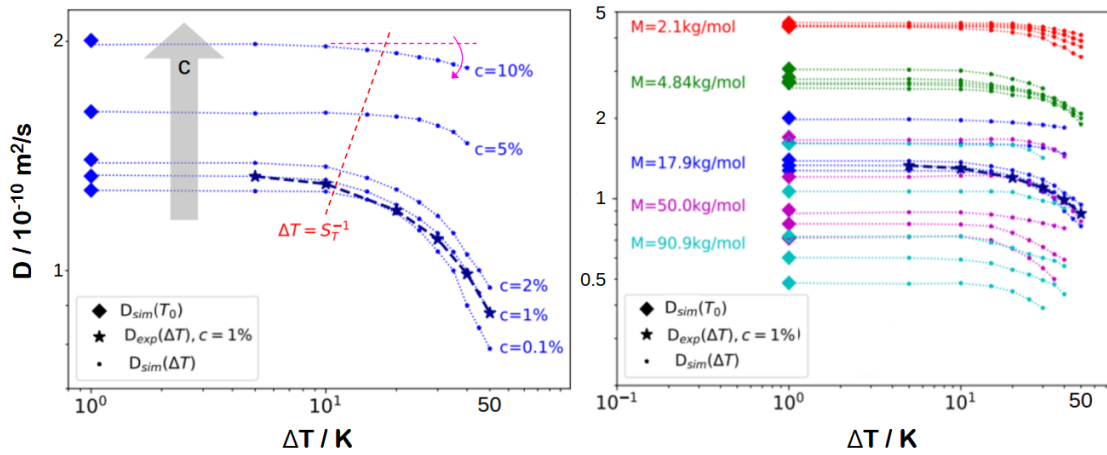


Fig. 4.33: Both illustrations show the simulated diffusion coefficient $D(\Delta T)$ (small dot symbols) as a function of the temperature difference ΔT . The different molar masses M are color coded and labeled in the right panel. The concentration c increases from bottom to top, for each molar mass. Additionally the known experimental thermal series ($M = 17.9 \text{ kg/mol}$, $c = 0.01 \text{ [w/w]}$) is demonstrated with the stars (dark blue). The diamonds reflect the simulated (literature) values for T_0 , of each series. The left side is specifically focusing on the molar mass of $M = 17.9 \text{ kg/mol}$ and shows how the different concentrations progress with the temperature differences. The red dashed line is the $|S_T \Delta T| = 1$ limit of fig. 4.35.

effects reduces with increasing concentration and is illustrated especially for the 10% curve with the pink arrow. The deviation starts at the threshold $\Delta T = |S_T^{-1}|$ (red dashed line, guide to the eye), which will be discussed in more detail in the discussion of the Soret coefficient. The bottom line, which we know from the simulation section is, that for large applied temperature differences the cold cell side grows in dominance, which leads to slower processes. This consequentially means, smaller diffusion coefficients D and larger Soret coefficients S_T (due to $S_T \sim D^{-1}$).

Soret coefficient

Next we want to focus on fig. 4.34, where all the associated Soret coefficients S_T are shown as a function of ΔT . Similar to the diffusion plot, the right plot demonstrates all concentration series of all the different molar masses (same color scheme) and the left side again focuses on the molar mass of 17.9 kg/mol . The different concentrations are stacked this time from top (smallest) to bottom (largest) and we see similar to fig. 4.33, that the smaller the molar mass, the narrower the different

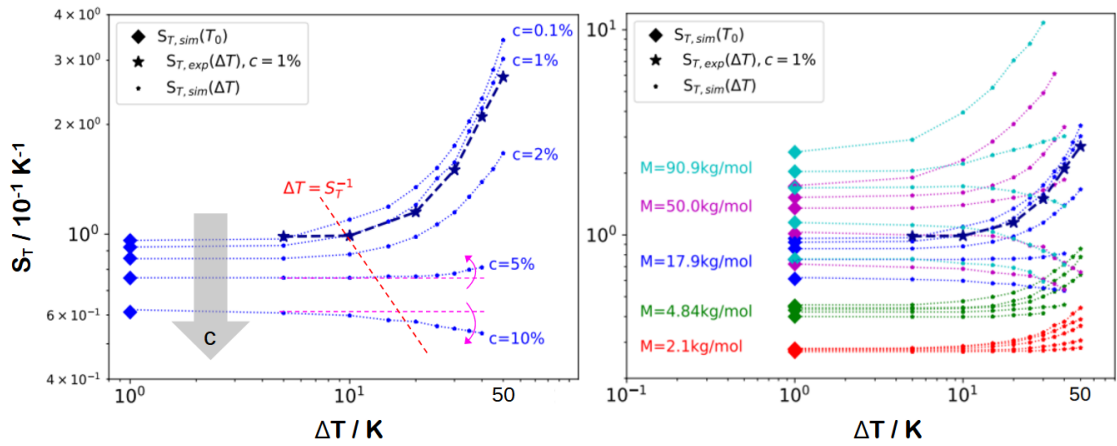


Fig. 4.34: Both illustrations show the simulated Soret coefficient $S_T(\Delta T)$ (small dot symbols) as a function of the temperature difference ΔT . The different molar masses M are color coded in the same way as in fig. 4.33. The concentration c in every molar mass collection increase from top to bottom. Additionally the known experimental thermal series ($M = 17.9 \text{ kg/mol}$, $c = 0.01 \text{ [w/w]}$) is demonstrated by the stars (dark blue). The diamonds reflect the simulated (literature) values for T_0 . The left side is specific focusing on the molar mass of $M = 17.9 \text{ kg/mol}$ and shows how the different concentrations progress with the temperature difference. For the largest c we see for the first time a progression of S_T , which decreases with increasing temperature ΔT . Further the red dashed line is the $|S_T \Delta T| = 1$ limit of fig. 4.35, where the fanning out starts.

concentration series are. However, it is noticeable that some curves deviate from the general increasing direction and deflect downwards. More on that will follow shortly. The left plot demonstrates the known affect, that the smallest concentrations are affected the most by the rising temperature difference, which results in the strong deviations towards increasing Soret coefficients. These deviations start again at the red dashed line, which represents the threshold of $\Delta T = |S_T^{-1}|$. This time, we can quantify this effect better. To do this, we analyze the plot of fig. 4.35, which shows for all the curves of fig. 4.34, the $|S_T \Delta T|$ (ΔT) pendants. The plot is divided into two areas, with the common boundary line of the threshold $|S_T \Delta T| = 1$. The area above, for $|S_T \Delta T| > 1$, we called 'temperature sensitive region' and the area below (for $|S_T \Delta T| < 1$), 'temperature insensitive region'. The simple answer is, that below this dimensionless threshold the linear approximation of the diffusion equation is usable and above the non linearity must be taken into account. In the 'temperature insensitive region' all the curves show a linear dependence on ΔT . This

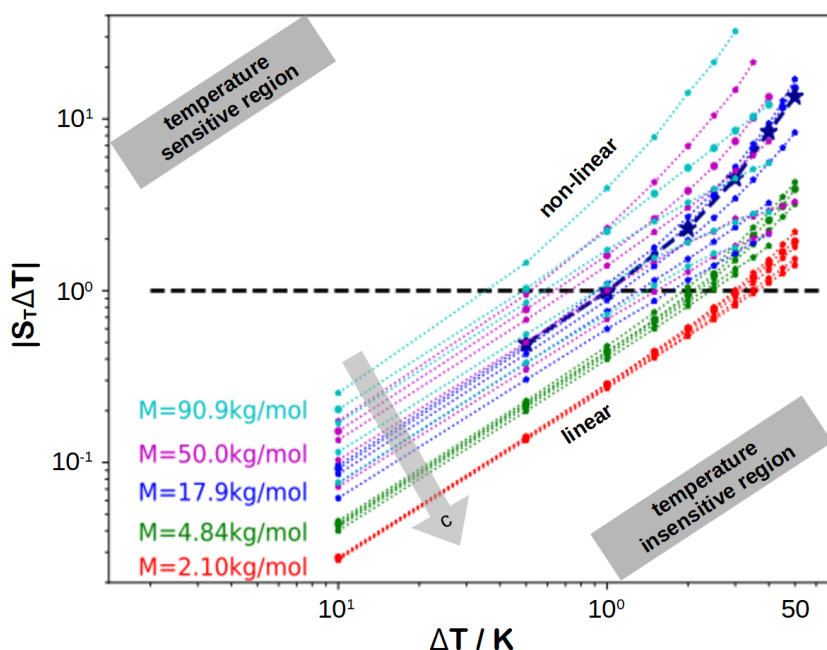


Fig. 4.35: Illustration of $|S_T \Delta T|$ (ΔT) as a function of ΔT . Shown are all the Soret coefficients of fig. 4.34. The plot is divided into two areas, with the common boundary $|S_T \Delta T| = 1$. For $|S_T \Delta T| < 1$ is the 'temperature insensitive region', where a linear relationship of $|S_T \Delta T|$ (ΔT) is found. Above, for $|S_T \Delta T| > 1$, on the other hand, is the 'temperature sensitive region', where a non linear relationship occurs.

linear relationship of $|S_T \Delta T|$ reflects the constancy of S_T , in the left illustration of fig. 4.34, before the red dashed line. In the 'temperature sensitive region' we can see a non linear relationship of $|S_T \Delta T|$ (ΔT), which corresponds to the fanning out of the curves in fig. 4.34. It is the now known nonlinearity effect, which we have explained in the simulation section. Here, however, broken down for several molar masses and concentrations. The other, before mentioned, noteworthy effect is indicated with pink arrows in the left panel of fig. 4.34. The 10% curve of the blue 17.9 kg/mol collection is the first curve with a downward directed deviation (to smaller S_T values). It is also noticeable that the higher the molar mass, the more frequently this type of deviation occurs. These decreasing curves are also visible in fig. 4.35. They deviate from the linear progression of the curves (in the 'temperature sensitive region'), but not towards increasing values, rather the curves flatten. Fig. 4.36 shows an overview of all the discussed curves and demonstrates the direction of the curvature with the arrows. Upward pointing arrows (\nearrow) demonstrate an

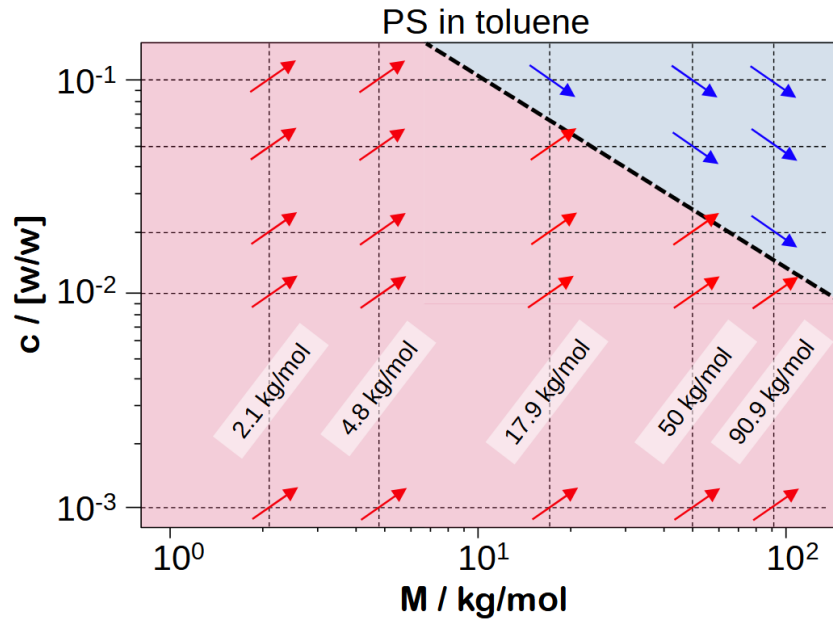


Fig. 4.36: Illustration of the increasing (\nearrow) or decreasing (\searrow) progression of the Soret coefficient curves ($S_T(\Delta T)$) as a phase diagram. In the red area the non linearity of the diffusion equation is the dominating effect, which leads to increasing Soret coefficients. Contrary, in the blue area there is a dominance of temperature dependency, which leads to decreasing Soret coefficients.

increasing progression of the associated Soret coefficient curve $S_T(\Delta T)$ and vice versa a downward directed arrow (\searrow) the opposite. Thereby a kind of phase diagram is created that gives the impression that the upper right corner, with high molar masses and concentrations, is very susceptible to this additional effect. We attribute this to the blue marked temperature dependency of the Soret coefficients, which was before demonstrated in fig. 4.24 and should be kept in mind. It is an opposing effect to the nonlinearity of the diffusion equation, that becomes dominant for large solutal parameters (c, M). The red area demonstrates Soret coefficients which deviate towards increasing values driven by the nonlinearity effect and the blue area decreasing ones due to the temperature dependence. If we look at the phase diagram and compare it with fig. 4.34, we can see that the further away the solutal compositions are from the thick black dashed phase boundary, the stronger the curvatures and the deviations from the literature value are. For example, in the case of the $M = 17.9$ kg/mol collection, the boundary is between $c = 5\%$ and

10%, resulting in slight upward and downward bending curves in [fig. 4.34](#). It must be noted that this result has not yet been confirmed experimentally and is only determined from the simulations.

Thermodiffusion coefficient

Finally, [fig. 4.37](#) shows the thermodiffusion coefficient $D_T(\Delta T) = S_T(\Delta T) \cdot D(\Delta T)$

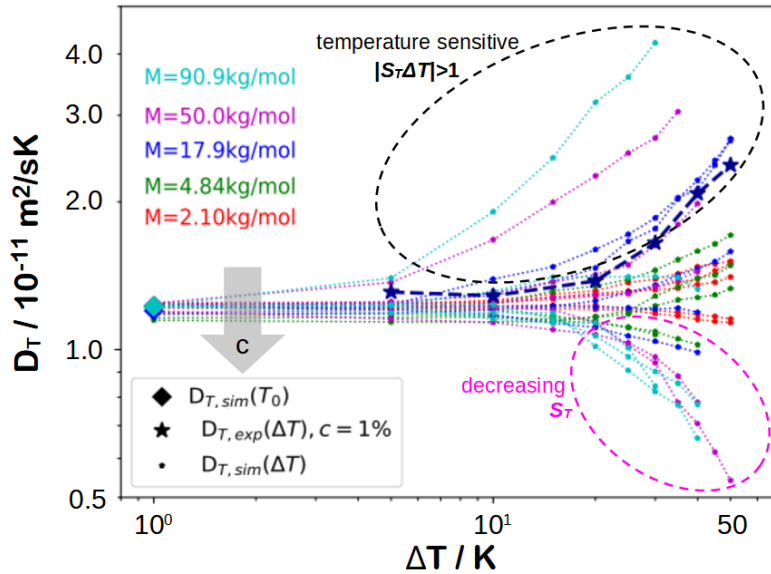


[Fig. 4.37](#): The illustration shows the simulated thermodiffusion coefficient $D_T(\Delta T)$ (small dot symbols) as a function of the temperature differences ΔT . The different molar masses M are color coded in the same way as in [fig. 4.33](#) and [fig. 4.34](#). The concentration c in every molar mass collection increases from top to bottom. Additionally the known experimental thermal series ($M = 17.9 \text{ kg/mol}$, $c = 0.01$ [w/w]) is demonstrated with the stars (dark blue). The diamonds reflect the simulated (literature) values for T_0 . Specifically the high molar masses are critical to thermal deviations from the literature values. We also see the decreasing progression of S_T , especially for the highest c values in the large M curves (pinkish highlighted) and the 'temperature sensitive area' for small c (black highlighted).

as a function of ΔT . It should be a constant value, which is, depending on the accepted error tolerance, true for most simulated curves. The two highlighted circles show the two effects, which were introduced before. They are the reasons for the additional temperature dependencies in the otherwise constant parameter. We can see the strong temperature sensitivity of the small concentrations (black dashed ellipse), caused by the large values of $|S_T \Delta T| > 1$. Indicated by the pink dashed

ellipse are falling thermodiffusion coefficient due to the decreasing Soret coefficients curvature. If we ignore these two extremal effects and consider, for example, small temperature differences ΔT or samples with small Soret coefficients, the expected constancy fits very well. Conversely, this also means that research of the glass transition in particular is afflicted with the additional problems. This needs to be investigated further. With that, we end the thermal analysis of the transport coefficients and come to the solutal dependencies in the following sub-section.

4.4.2 Concentration and molar mass dependence

The concentration and molar mass dependence of the transport coefficients is the focus of this second section. The considered quantities are again the diffusion $D(c, M)$, Soret $S_T(c, M)$ and thermodiffusion coefficients $D_T(c, M)$. The associated numerical values of the measured quantities are listed in the [appendix 6.2-6.7](#). For the sake of completeness and a better understanding, we refer sometimes to the simulated quantities of [tab. 4.6](#) and include them in the considerations. [Section 4.4.2](#) starts with the molar mass series, afterwards [section 4.4.2](#) shows the concentration series.

a) Concentration dependence

In a molar mass series the transport properties ($D(c)$, $S_T(c)$, $D_T(c)$) for the different molar masses M are shown as functions of the concentration c . The color scheme of this sub-section is the same for all included plots and separates M in color. The molar mass range varies from 2.1 kg/mol to 1070 kg/mol. The associated simulations (index: *sim*) are shown in the same colors but with small dots and thin dotted lines, instead of the stars and dashed lines of experimental measurements (index: *exp*). The simulated reference values (as in D_{sim}, T_0) result from the simulations for $\Delta T = 1 \text{ K}$ ²⁴ and are separately shown with diamonds and solid lines. As literature references (index: *lit*) we used values from *Zhang*^[82], marked with a Z and shown with upwards pointing triangles. As well as values from *Rauch*^[68] (R), illustrated with downwards pointing triangles.

²⁴ $S_T^{-1} < 1\text{K}$ applies to all samples.

Diffusion coefficient

Fig. 4.38 starts the solutal analysis and illustrates the resulting diffusion coeffi-

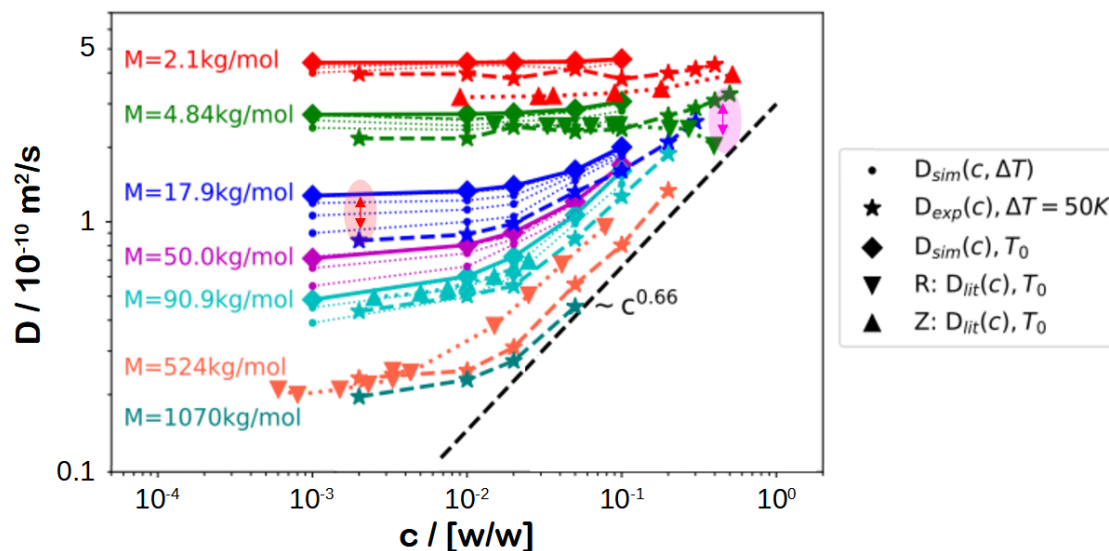


Fig. 4.38: Demonstration of the resulting experimental diffusion coefficients $D(c)$ (star symbols) as a function of the concentration c . The different molar masses M are color coded and named in the plot. The diamonds reflect the simulated literature values for T_0 . The small dots represent the different thermal series, which connect the literature values with the measured ones. The upwards pointing triangles are literature values of Zhang^[82] (red: 2.6 kg/mol, turquoise: 96 kg/mol) and the downwards pointing triangles from Rauch^[68] (green: 4.7 kg/mol, orange: 532 kg/mol). The dashed black line is the scale law of the entangled polymer state, which follows [68]. Listed in tab. 6.2-6.7.

icients of all experiments $D_{exp}(c)$, simulations $D_{sim}(c)$ and includes additionally the literature references $D_{lit}(c)$. This type of plot can be found in the literature very often^[68,72,82,83]. It demonstrates the dilute and semidilute polymer state (dashed black line) of different molar masses and as a function of c . The left panel of fig. 4.18, which was shown in the simulation section, was an isolated illustration of the here demonstrated blue group of $M = 17.9$ kg/mol. We see that all molar masses show a similar concentration dependence. They start with a constant plateau and converge with increasing concentration towards the entangled polymer state ($\sim c^{0.66}$), where they become molar mass independent. Except for the smallest molar mass of 2.1 kg/mol, the simulated values $D_{sim}(T_0)$ (diamonds) and the literature ones $D_{lit}(T_0)$ (triangles) match nearly perfectly. The important point is the already

known difference between these reference values and our experimental quantities $D_{exp}(c)$ (stars, measured with $\vec{\nabla}T_0 = 10^4\text{K/m}$), which, however, is bridged by the various temperature simulations and is therefore understood (highlighted by the red arrow). As explained in the simulation section, the differences in the resulting experimental diffusion coefficient are caused by the nonlinear diffusion equation, which causes itself strong nonlinear concentration profiles inside the cells. These concentration distributions prioritize the cold cell sides and deliver thereby diffusion and especially Soret-coefficients of denser system states than the original sample composition. With the pink arrow, in [fig. 4.38](#) a second already mentioned effect is visible, where for high concentrations the experimental results are for the first time larger than the literature counterparts. This can be traced back to the in [fig. 4.36](#) mentioned effect. For these system compositions the Soret coefficient is dominated by the temperature dependent effect, which leads to decreasing Soret values. Since we are still in the entangled system state, the thermodiffusion coefficient D_T is constant and the diffusion coefficient $D \sim S_T^{-1}$ can be described as the inverse of the Soret coefficients S_T . Therefore, the now decreasing Soret coefficient values lead to increasing diffusion coefficient values.

Soret coefficient

Similar to [fig. 4.38](#), [fig. 4.39](#) illustrates the associated Soret coefficients of our experiments $S_{T,exp}(c)$, simulations $S_{T,sim}(c)$ and the literature $S_{T,lit}(c)$ as a function of c . The color and symbol code remains the same. The various thermal simulations are again presented for the three smallest molar masses, but avoided for larger ones, since the curves overlap and can not be identified easily. The full thermal set of the blue 17.9 kg/mol collection was already shown in [fig. 4.18](#). Just as in the case of the diffusion coefficient, this type of representation is well established, therefore we will only present the essential points. All curves start again in the diluted plateau ($c \rightarrow 0$) and fall collectively to the entangled polymer state, which is represented by the dashed black line ($\sim c^{-0.77}$). Once there, the Soret coefficients become molar masses independent (analogous to the $D(c)$). A noteworthy and unique effect is, that, the larger the molar mass, the more the experimental values $S_{T,exp}(c)$ (stars) deviate from the literature ones $S_{T,sim}(T_0)$ (diamonds). This is highlighted by the red ellipse and the included arrows. This is especially true for the smallest

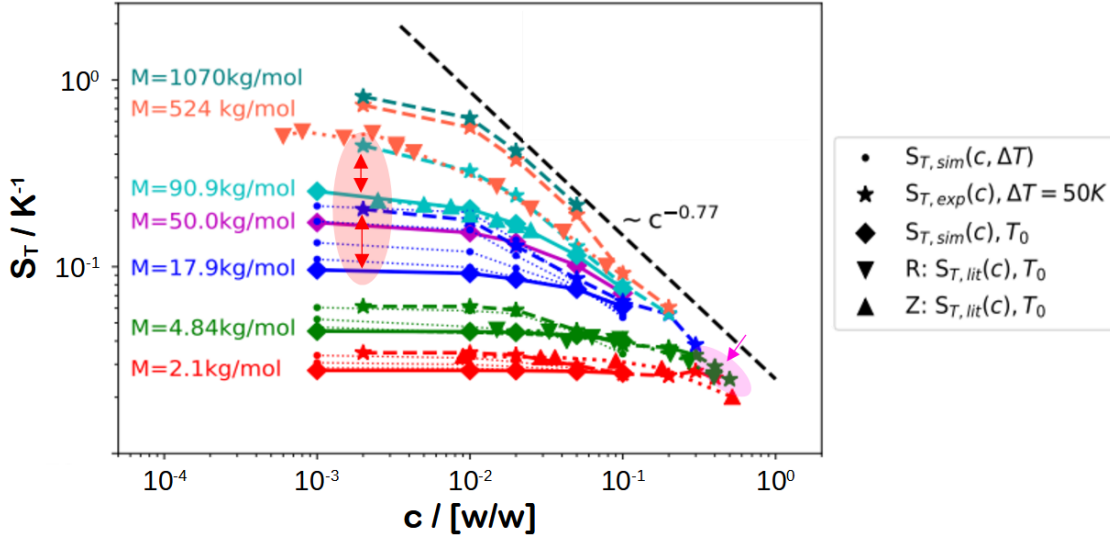


Fig. 4.39: Demonstration of the resulting experimental Soret coefficients $S_T(c)$ (star symbols) as a function of the concentration c . The different molar masses M are color coded and named in the plot. The diamonds reflect the simulated (literature) values for T_0 . For the smallest two molar masses, the small dots show the different thermal series, which connect the literature values to the measured ones. The upwards directing triangles are literature values of Zhang^[82] (red: 2.6 kg/mol, turquoise: 96 kg/mol) and the downwards triangles from Rauch^[68] (green: 4.7 kg/mol, orange: 532 kg/mol). The dashed black line is the scale law of the entangled polymer state, which follows [68]. Listed in tab. 6.2-6.7.

concentrations. Only shown for the smallest molar masses ($M = 2.1, 4.84$ kg/mol), but there very clearly visible is, that the thermal simulations can explain the gap between the literature and experimental values perfectly. It is important to know that all samples shown (even $c_{min} = 0.2\%$) have in our strong temperature field of $\vec{\nabla}T_0 = 10^4 K/m$ an $|S_T \Delta T|$ value greater than one. This means they all contain the nonlinearity effect of the diffusion equation. If we remember fig. 4.34 and the deviations-size of the smallest concentrations, which decreased with increasing concentration, we can understand the curves shown here (fig. 4.39). If we primarily want to use the NEF shadowgraphy experiments to measure transport coefficients, we see, that smaller temperature differences ΔT generate more accurate results. Furthermore, it should be noted that the greater the molar mass, the greater the differences are to be expected, especially in the case of small concentrations. If we follow the curves and extrapolate them to large concentrations, we can see that

the differences are becoming smaller and smaller, which means that the entangled polymer state up to the glass temperature could deliver better results with small differences to the literature values. However, we have already discussed in the structure factor section that the NEF amplitudes decrease with increasing molar masses and concentrations, which in turn could lead to measurement difficulties. In addition the pinkish arrow at the highest concentrations of $M = 4840$ kg/mol references the mentioned effect of dominance change, from nonlinear effected, to temperature dependent thermally decreasing Soret coefficients S_T . This can be explained again due to the decreasing Soret values of these measurements, which was shown in the phase diagram [fig. 4.36](#).

Thermodiffusion coefficient

The missing quantity, the thermodiffusion coefficient D_T , can be seen in [fig. 4.40](#). The experimental measurements $D_{T,exp}(c)$ (stars), the literature values $D_{T,lit}(c)$

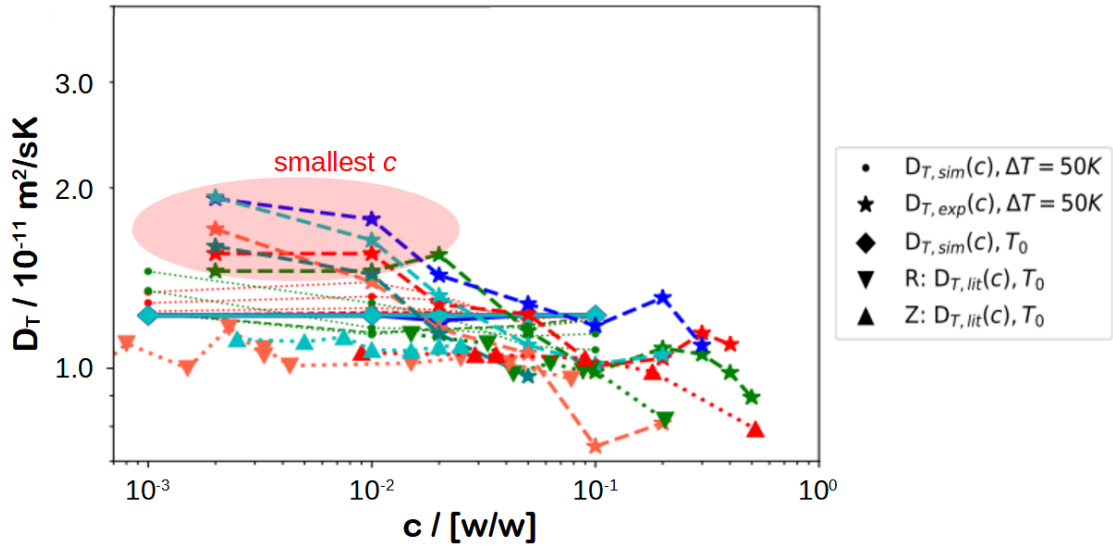


[Fig. 4.40](#): Demonstration of the resulting experimental thermodiffusion coefficients $D_T(c)$ (star symbols) as a function of the concentration c . The different molar masses M are color coded. The diamonds reflect the simulated (literature) values for T_0 . For the smallest two molar masses, the small dots show the different thermal series, which connect the literature values to the measured ones. The upwards directing triangles are literature values of [Zhang^{\[82\]}](#) (red: 2.6 kg/mol, turquoise: 96 kg/mol) and the downwards triangle from [Rauch^{\[68\]}](#) (green: 4.7 kg/mol, orange: 532 kg/mol).

(triangles) from *Zhang* (Z) and *Rauch* (R) and the simulated values $D_{T,sim}(T_0)$ (diamonds) are shown again in the established color and symbol scheme of [figs. 4.38](#) and [4.39](#). In the dilute and entangled polymer regime the thermodiffusion coefficient is molar mass M and concentration c independent. Only for very large concentrations (> 0.8 ^[72]) the curves drop dramatically through the glass transition. However, the first curvature effects can already be seen for concentrations around $c \approx 40\%$, which explains the slight collective decrease in the curves at large concentrations. The largest deviations (factor ~ 2 , highlighted by the red ellipse) from the literature value (diamonds) of $D_T = 1.10 \cdot 10^{-11} \text{m}^2/\text{sK}$ can be seen again at the smallest concentrations and can be traced back to the deviations of the Soret coefficient S_T there. However, it should be noted that this plot covers a much smaller value range and thus represents a stronger zoom. This explains the apparently large variations in the curves. If we consider this and include the mentioned nonlinearity effects, we can verify the general molar mass and concentration independence.

Sub-section (a) has shown the concentration dependence of the transport coefficients in the three associated plots, each for one specific quantity (D , S_T , D_T). In particular, the non linearity in the diffusion equation is included in the resulting coefficients and was mentioned again and again as the reason for the differences of our experimental values and the literature benchmarks. In the following sub-section, a similar explanation style is chosen, but this time for the dependencies on the molar mass.

b) Molar mass dependence

For the concentration series of this sub-section, we show, the diffusion $D(M)$, the Soret $S_T(M)$ and the thermodiffusion coefficient $D_T(M)$ as functions of the molar mass M . Therefore we must change the established color scheme and reference the different concentrations c by color. The actual values are listed again in the [tabs. 6.2-6.7](#). As the table of [4.7](#) demonstrates, the concentration varies from 0.2% to 30%. The two points of 40% and the single measurement of $c = 50\%$ are not shown in the following plots. The symbol code stays the same. With the same upwards and downwards pointing triangles the literature values (index: *lit*) of

Zhang^[82] (Z) and *Rauch*^[68] (R) are shown respectively. These quantities are values for the infinite-diluted compositions ($c \rightarrow 0$) of a polystyrene/toluene mixture. Additionally included are the simulated values (index: *sim*) for $\Delta T = 1$ K, they are demonstrated in the same concentration colors and with diamond symbols. We need these values for better comparisons, since the literature ones only describe the infinitely diluted solutions.

Diffusion coefficient

As for every analysis, we start in [fig. 4.41](#) with the diffusion coefficients $D(M)$. For small molar masses $M \rightarrow 0$ (left side) all concentrations are very close to the

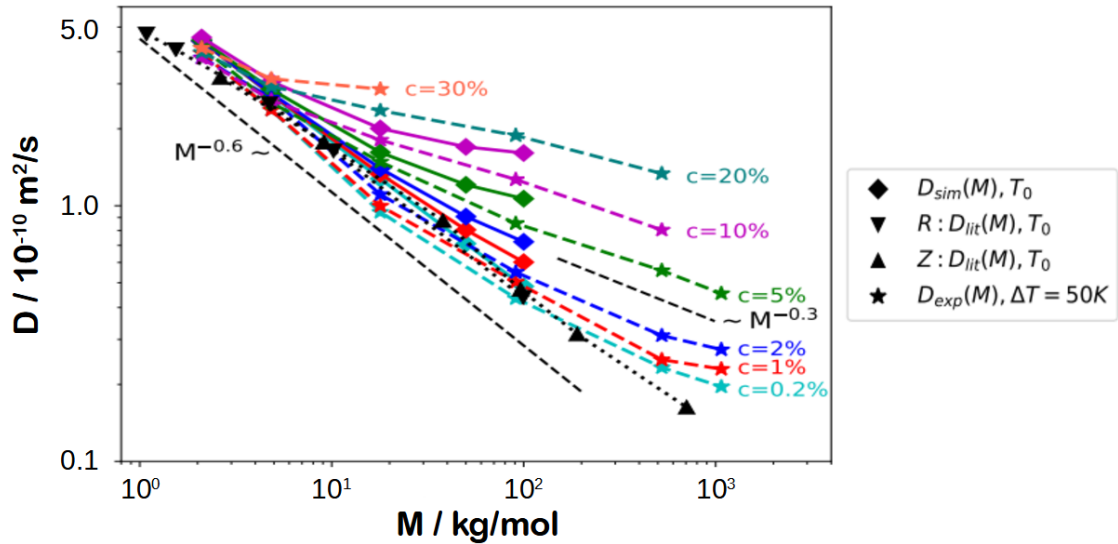


Fig. 4.41: Demonstration of the resulting experimental diffusion coefficients $D_{exp}(M)$ (star symbols) as a function of the molar mass M . The different concentrations c are color coded and named in the plot. The diamonds reflect the simulated (literature) values for T_0 . The literature values of *Zhang*^[82] (Z, upwards triangles) and *Rauch and Köhler*^[68] (R, downwards triangles) show the infinite-diluted values.

literature values and they follow the implemented scale law $\sim M^{-0.6}$, which we used in [eq. 4.70](#) of the structure factor analysis. This scale law originates from *Rauch*^[68] and is shown by the dashed black line. It represents the diffusivity of diluted polymer coils as a function of polymer molar mass (M), which influences ($R_H \sim M^{0.6}$) the effective hydrodynamic radius^[57] (Einstein-Stokes-equation^[84]: $D(c \rightarrow 0) \sim R_H^{-1}$). As the molar mass increases, the largest concentrations initially

deviate from this behavior. The smallest concentrations, on the other hand, follow the scale law up to much large molar masses. It is only very late that they deviate from the infinitely diluted values. This can also be seen in the simulated curves. The moment the curves leave the scale law is $M^*(c)$, the so called overlap molar mass, where for a fixed concentration the volumes of the individual polymer coils touch each other and the entangled state begins²⁵. The gap between the simulated values $D_{lit}|_c(M)$ and the associated experimental ones $D_{exp}|_c(M)$ increases with increasing molar mass and can once more be traced back to the nonlinearity effect. Since the smallest concentrations have the smallest $|S_T\Delta T|$ values, the gap is also the smallest. In addition to the scaling law ($\sim M^{-0.6}$) mentioned and confirmed by the literature, there is a tendency in the entangled polymer state, that all curves propagate proportional to $\sim M^{-0.3}$. It is shown due to the second black dashed line. This proportionality may provide further results on the diffusion coefficient in the limited entangled polymer state in future investigations.

Soret coefficient

In [fig. 4.42](#) the Soret coefficient $S_T(M)$ is shown for the same molar mass range and in the same color scheme as [fig. 4.41](#). Again we see the infinitely diluted literature values $S_{T,lit}(M)$, represented by the black triangles, following a increasing scale law of $\sim M^{0.6}$ (left black dashed line). This was the before used proportionality of [eq. 4.71](#) and is the inverse of the diffusion scale law of $\sim M^{-0.6}$. This was to be expected, since in the diluted regime, the Soret coefficient is determined as the inverse of the diffusion coefficient. The different concentrations behave principally in the same way as seen before, the largest concentrations leave the scale law at the smallest molar masses and vice versa, the smallest concentrations follow the scale law for a long time. This is again due to the different overlap molar masses $M^*(c)$. This effect is superimposed by a second mechanism, which leads to the red highlighted deviations. Since it is especially visible for the smallest concentrations, it can be traced back to the included nonlinearity effect of these curves. As seen before, the smallest concentrations are the most susceptible to the nonlinearity distortion of the concentration profile in the cell due to their large $|S_T\Delta T|$ values.

²⁵To be understood similarly to the overlap concentration c^* at fixed molar masses.

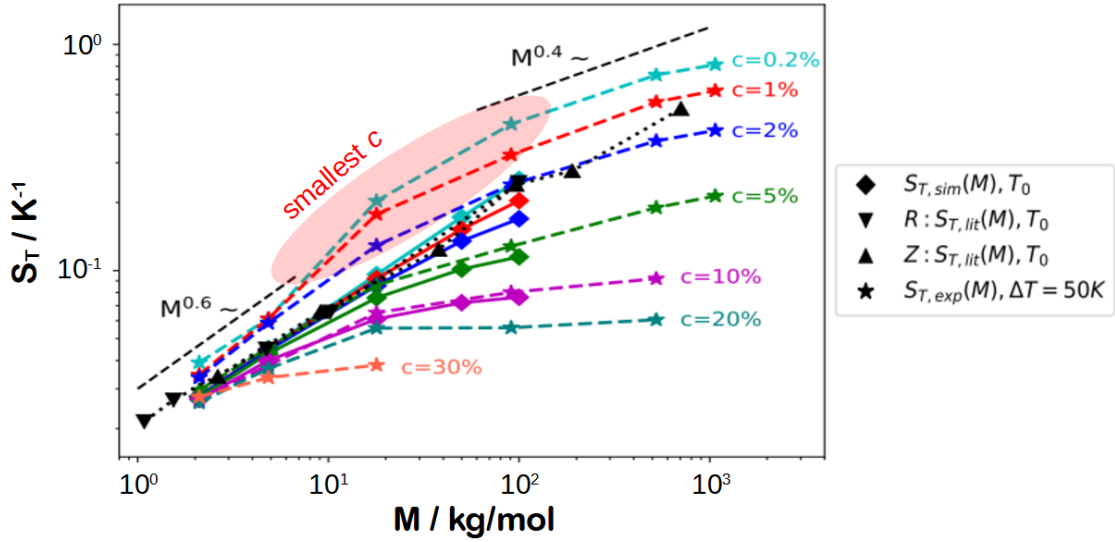


Fig. 4.42: Demonstration of the resulting experimental Soret coefficients $S_T(M)$ (star symbols) as a function of the molar mass M . The different concentrations c are color coded. The diamonds reflect the simulated (literature) values for T_0 , of each series. The literature values of *Zhang*^[82] (Z, upwards triangles) and *Rauch*^[68] (R, downwards triangles) show the infinite-diluted values.

For very large molar masses it seems that all concentrations run into a constant plateau. Finally, we see a behavior of the Soret coefficient proportional to $\sim M^{0.4}$ (right black dashed line), which we were able to calculate in eq. 4.84, as already mentioned in the structure factor section 4.3. It applies to small concentrations $c_- = c < 5\%$ in the limit of large molar masses (\hat{M}).

Thermodiffusion coefficient

Finally fig. 4.43 shows the calculated thermodiffusion coefficients $D_T(M) = S_T(M) \cdot D(M)$ as functions of the molar mass M . The experimental $D_{T,exp}(M)$, simulated $D_{T,sim}(T_0)$ (for $\Delta T = 1$ K) and reference values $D_{T,lit}(M)$ (of *Zhang*^[82] (Z) and *Rauch*^[68] (R)) are demonstrated in the same color and symbol code as seen before in fig. 4.41 and 4.42. Again, this should provide a constant value of $D_T = 1.10 \cdot 10^{-11} \text{m}^2/\text{Ks}$, which is independent of molar masses. For the most part we can confirm this. As has often been seen, the smallest concentrations, $c = 0.2\%$ in turquoise, 1% in red and 2% in blue, show the greatest deviations from the literature values (black triangles, calculated ones: diamonds). This can again

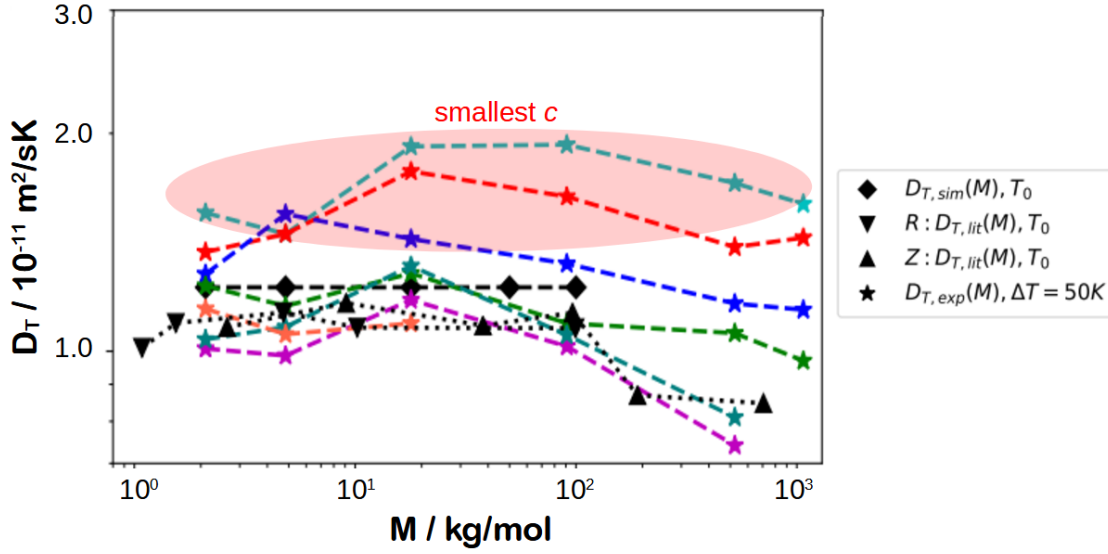


Fig. 4.43: Demonstration of the resulting experimental diffusion coefficients $D_T(M)$ (star symbols) as a function of the molar mass M . The different concentrations c are color coded. The diamonds reflect the simulated (literature) values for T_0 , of each series. The literature values of Zhang^[82] (Z, upwards triangles) and Rauch^[68] (R, downwards triangles) show the infinite-diluted values.

be attributed to the included nonlinearity effects of these large Soret coefficients combined with the strong temperature gradient.

This section presented the resulting diffusion $D(\Delta T, c, M)$, Soret $S_T(\Delta T, c, M)$ and thermodiffusion coefficients $D_T(\Delta T, c, M)$ as isolated functions of applied temperature difference ΔT , concentration c and molar mass M . These are the first results with our new shadowgraphy setup, using large temperature gradients to achieve strong amplitude signals. The focus was not on providing as many new values as possible, but on the explanation of our experimental results, which showed differences to the literature ones. The cause was found in the included nonlinearity shift of the resulting transport quantities, which itself was explained in the previous section 4.2.

5 Summary and outlook

Non equilibrium fluctuations (NEFs) in liquid mixtures are fundamentally different from their equilibrium counterparts (EFs, Brownian motion of the molecules) and represent a completely new class of fluctuations. In liquids exposed to external temperature and concentration gradients they are caused by randomly occurring velocity fluctuations, where the associated displacements of the local temperature and concentration conditions are called NEFs. Not only are the amplitudes many magnitudes stronger than the equilibrium counterparts, they are also long-ranged with a characteristic q^{-4} dependence of the associated wavevectors. The strongest amplitudes of the largest NEFs are, however, on earth quenched by gravity. The current state of research provides a linearized hydrodynamic description of benign, simple systems. The goal is to investigate complex systems such as naturally more relevant ternary mixtures^[6,85] and strongly asymmetric polymer solutions close to the glass transition^[68,72]. This work is part of the BT-Giant project of the German Aerospace Center (DLR), which in turn is part of the GIANT-FLUCTUATIONS project, formerly called 'Non-Equilibrium Fluctuations during Diffusion in complex liquids' (NEUF-DIX), of the European Space Agency (ESA). The laboratory measurements serve as ground base reference measurements for future experiments in microgravity conditions.

Our first task was to design, build and put into operation our own measurement setup, which is inspired by existing instruments of our partner groups in Milan and Anglet. The heterodyne, small-angle, near-field light scattering in the longitudinal direction, called shadowgraphy, is the experiment of choice for studying of NEFs. Therefore the experimental section provides a description of our shadowgraphy setup with a special focus on the Soret-cell. This cell type is a liquid container, which allows the application of strong, uniform temperature and concentration gradients. It is own built in the machine shop of the University of Bayreuth.

In addition to the setup, the analysis program/script for the structure functions of the NEFs was also completely revised and own written. It is based on a 'differential dynamic analysis' (DDA) method.

After the calibration, the first measurements were on already known binary polystyrene in toluene mixtures, of various concentrations and molar masses. During this process, we were already able to improve existing descriptions with a new, alternative and considerably better description of the structure function for our samples. This description, unlike the existing ones, is not based on empirical approximations, but rather directly on the fundamental correlation function of the visible refractive index fluctuations. Through the consideration of the thermal mode in the entire structure function and with an analogous, equal description of the thermal and solutal mode, both solutal and thermal transport processes could be explained. Furthermore, the diffusion, Soret and thermodiffusion coefficient as well as the thermal diffusivity could be determined from the experiment. Beyond that, a further publication was recently submitted that addresses the relevance of a nonlinear description of the concentration distribution inside the cell, which is usually neglected or linearized. Using own written simulations that include both the nonlinearity of the concentration distribution and temperature as well as concentration dependencies of the involved thermophysical parameters, we were able to replicate our experimental measurements almost exactly and showed that measurements with strong temperature differences can by no means neglect the involved nonlinearity. The simulations also showed the interaction of the opposing mechanisms of nonlinearity effect and temperature dependence in the Soret coefficient. Sample compositions were calculated in which, with increasing temperature difference, the apparent Soret coefficient increases, which can be attributed to the nonlinearity, and on the other hand there are also decreasing values due to the dominance of the temperature dependency.

Various unknown dependencies of NEFs as a function of applied temperature difference, polymer concentration, and molar mass were demonstrated. These include the behaviors of the two wavevector thresholds. These are the limits for small q values, where gravitational quenching begins and the threshold for large wavevectors, where NEFs are no longer distinguishable from EFs. Depending on the sample composition and the applied temperature difference, effects such as the shifts of the

quenching to significantly smaller wavevectors can be observed. The same applies to the NEF amplitudes, compositions were shown which had significantly stronger amplitudes than others at the same temperature difference. Finally, a similar temperature, concentration and molar mass analysis of the involved transport coefficients was performed. These are the diffusion, Soret and thermodiffusion coefficients. In particular, for small concentrations and large molar masses, our measurements with strong temperature differences showed deviations from the literature values. In a first analysis, these could be attributed to the mentioned nonlinearity effects. In addition, a large number of dependencies could be identified for which there are still no conclusive explanations.

A variety of unknown effects and dependencies on certain parameters, which are not considered in the existing theory, were already found in these first measurements and the corresponding simulations. Therefore, further investigations and comparison with microgravity experiments are essential to recover the full amplitude divergence at small q -values. It is advisable to either investigate first dilute systems in ternary mixtures or to stay with the binary systems and work towards the glass transition temperature.

6 Appendix

6.1 Structure function comparison with literature

In all the previous literature^[43,66,86] the total time depended structure factor is calculated as:

$$S(q, \Delta t) = S_0(q) [1 - f(q, \Delta t)] + B . \quad (6.1)$$

That representation deviates a little bit, from that one which we derived in [eq. 2.54](#) and [2.55](#):

$$S(q, \Delta t) = \sum_{i=T,c} S^i(q) [1 - f(\Delta t, \tau^i(q))] + B^i \quad (6.2)$$

but can be transformed into it¹. In this appendix we will briefly build the bridge between [eq. 6.1](#) and our structure function of [eq. 6.2](#). For this, the following connections must be introduced:

$$S_0(q) = \sum_{i=T,c} S^i(q) \quad (6.3)$$

$$B = \sum_{i=T,c} B^i \quad (6.4)$$

$$f(q, \Delta t) = \sum_{i=T,c} \frac{S^i(q)}{S_0(q)} f(\Delta t, \tau^i(q)) . \quad (6.5)$$

As we can see, the necessary equations are sums of our thermal and solutal parts ($i = T, c$). The main difference is that the intermediate scattering function $f(q, \Delta t)$ of [eq. 6.1](#) is not a mono-exponential function with only one relaxation time. It is a sum of these exponential's with included normalized amplitudes.

¹Without the indices NE .

6.2 Sealing of the inner cell

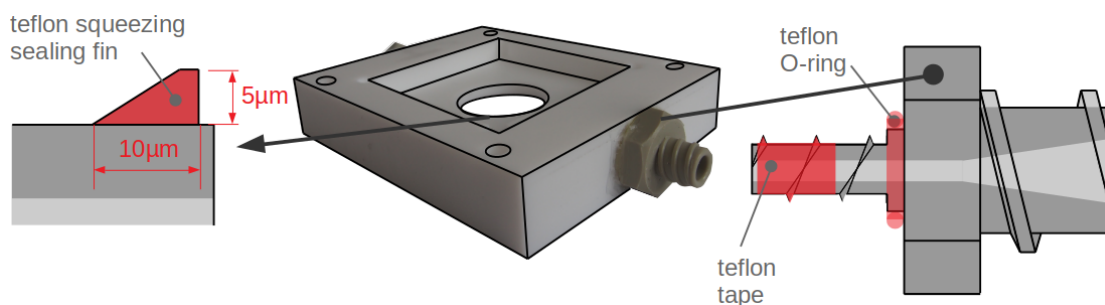


Fig. 6.1: To seal the fluid volume several mechanisms are implemented, which are shown in red. First of all, the sealing up to the sapphire glasses is guaranteed by a little fin at the rim, which is squeezed together (left part). The syringe adapters (right part) is sealed by an soft Teflon O-ring between the adapter and the frame and a Teflon wrapping tape around the threads.

The illustration of [fig. 6.1](#) shows the two import sealing mechanisms of our sample volume (Teflon-frame). The left one is a sketch of the little fin, which is manufactured on top of the Teflon-frame. This fin will be squeezed together by the sapphire windows and guaranteed the sealing². The second and third sealing mechanisms are at the Teflon-adapters for the syringes. The thread of the adapter (yellowish component), which is screwed into the Teflon-frame is wrapped with Teflon-tape³ and seals the cavities in the thread. Finally a soft Teflon O-ring sits between the two parts and is also squeezed together to guarantee an additional sealing. It should also be mentioned that all syringe connections are additionally wrapped with Parafilm⁴ ([fig. 3.5](#)) on the outside.

²All of the four screws of the inner cell are tighten with exact $M = 60 \cdot 10^{-2}\text{Nm}$.

³Teflon-tape is known from water installations.

⁴Parafilm® M All-Purpose Laboratory Film

6.3 Alignment of the Soret-cell

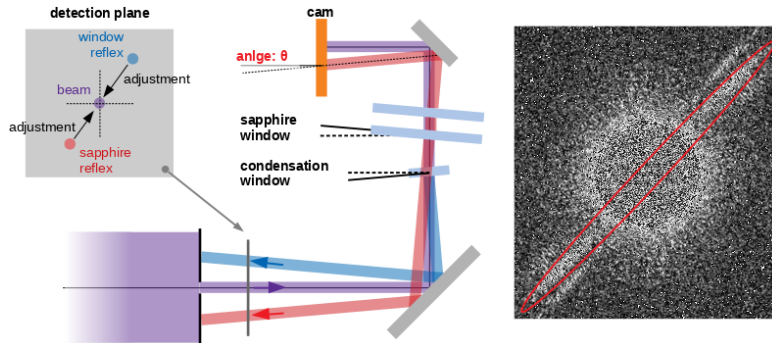


Fig. 6.2: Alignment of the condensation window and the cell due to the glass reflection of the individual elements. The cell sits on a horizontal arranged mirror mount with two micrometer screws. The three glasses are perfectly perpendicular aligned in the beam path, if the reflexes are congruent with the incoming beam.

A very important part of the alignments is the perfect horizontal orientation of the cell, to measure the fluctuations parallel to the direction of gravity. The first step is achieved by a bubble leveling glass. But therefore it is very important that the inner cell windows are parallel aligned, this is guaranteed by step wise tightening of the mentioned cell screws and controlling of the cell height at several points.

The second step is to check the reflections of the two sapphire windows and a third window, which sits right below of Soret-cell and connects a tempered air volume to the cold cell side. This is to prevent the setup for water condensation drops. As in [fig. 6.2](#) illustrated, it is important to align the windows perfectly perpendicular in the light path, otherwise an undesired (additional) refraction angle will be detected. As a result we find the indicated lines (highlighted by red ellipse) in our Fourier images of the correlation functions⁵. In our alignments we search the window reflections in backwards direction and orientate the cell in such a way that these reflexes are congruent to the incoming beam. As a second step we look at the center position of the incoming light beam, if it is not at the marked camera point (detected without the windows) we have an angle in the cell orientation. The last step is to measure a couple of images and calculate the Fourier transformation. If the orientation is not perfect we find the shown lines in the images.

⁵These lines are known from image editing in Fourier space.

6.4 Alignment of the camera mirror

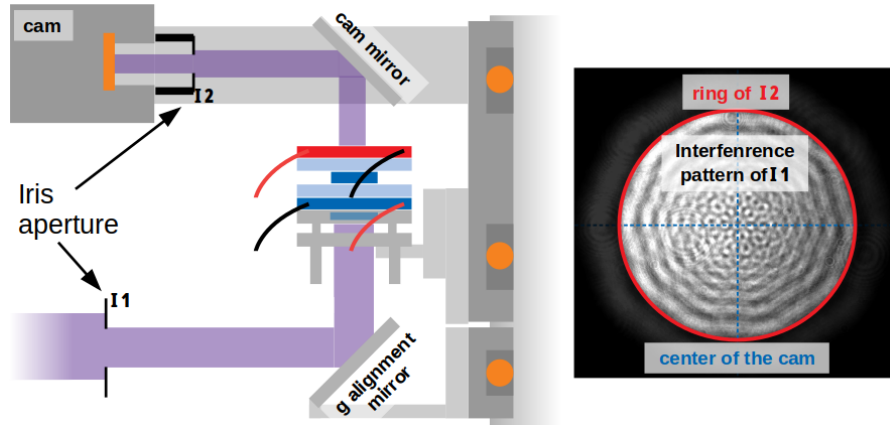


Fig. 6.3: To align the cam mirror, two irises are used. The first iris I1 constructs a circle interference pattern, which is shown in the right image. The second iris I2 is in the front of the cam and we only see the corresponding ring (red ring). The cam mirror is perfectly aligned if the interference pattern is centered in the camera and also the ring pattern is congruent with the ring of the second iris.

If the alignment of the cam-mirror (the last mirror before the camera) isn't perfect, then the light reaches the sensor in a slide angle and that causes additional interference patterns in the Fourier-images. These patterns look like a four leaf clover, which is located in the middle of the image.

For the alignment we use two irises, one before and one after the mirror. If we reduces the diameters, these irises generate a interference ring pattern on the camera. Our mirror orientation is in a ideal $\theta = 90^\circ$ configuration, if the inner diameter of the second iris fits congruent to the ring pattern of the first and if the center of the light beam is in the center of the camera. This is shown in the right illustration of [fig. 6.3](#).

6.5 Camera telescope control

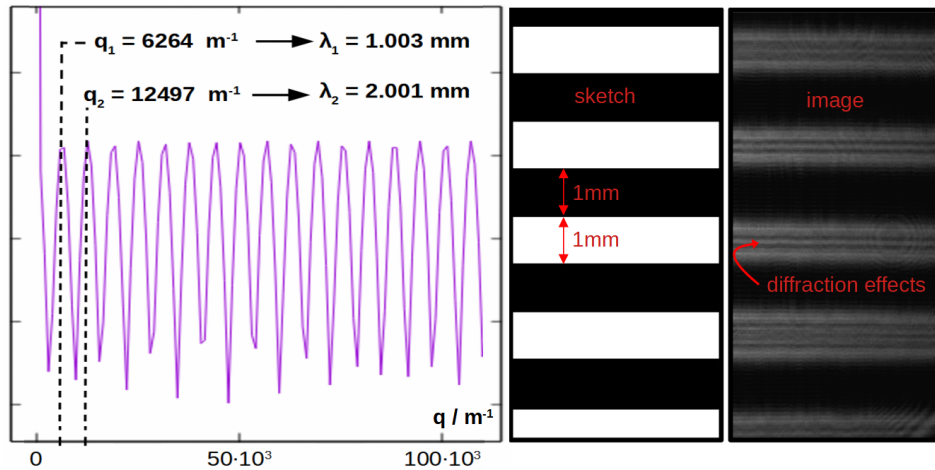


Fig. 6.4: The right illustration is the Fourier transformation of the left image of a scale with a gap width and a gap distance of 1 mm. In addition, the resulting q values were transformed using eq. 3.3. The resulting spatial frequency corresponds to the spatial distance in real space.

The camera telescope⁶, explained in section 3.1.3, and the defined transformation of eq. 3.3, should be controlled in this section. When using, the correct sensor distance is decisive, this is guaranteed by the C-mount adapter. For the control purpose, an image of a scale was taken. The scale has a slit pattern with a 1 mm gap width and also a 1 mm gap spacing. This is shown on the right in fig. 6.4. The connected sketch is an idealized representation of the measured image, without the diffraction effects occurring at the slit edges, which are visible on the right. We use two control mechanisms, first a real space image, where the pixel number from slit-center to slit-center is read out. This number calculated with the transformed pixel size must match 1 mm. Second, we Fourier transform this image. The associated intensities of the central column is shown on the left in fig. 6.4. The resulting spatial frequency suits also the inverse of the 1 mm^{-1} gap. Both control procedures turned out to be correct, which confirms our assumption that the developed q value transformation provides the correct outcomes.

⁶KOPPACE, 0.5x C-mount camera adapter.

6.6 Pixel illustration of the normalization steps

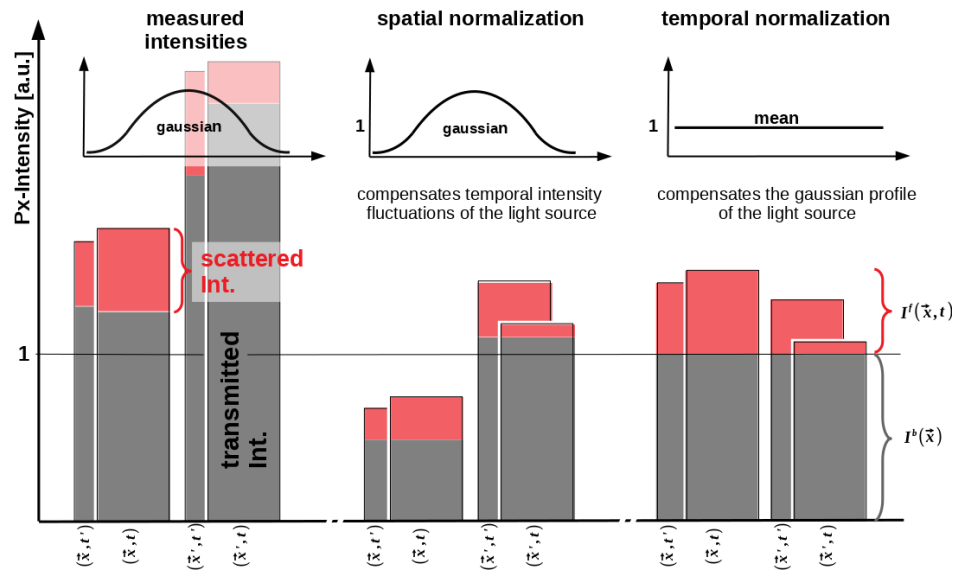


Fig. 6.5: Summary representation, in which two different pixels (\vec{x} / \vec{x}') of an image and their temporally shifted pairs ($(\vec{x}, t) / (\vec{x}', t')$) demonstrate the normalization steps. The spatial normalization compensates power fluctuations of the light source, which is shown in the equal background intensities (grey portion). The temporal normalization compensates intensity differences due to the Gaussian beam profile of the detection light.

The illustration of [fig. 6.5](#) shows how the calculations of [section 3.3](#) effects the pixel intensities. For this purpose, two pixels (\vec{x}, \vec{x}') and the same pixels at different times (t, t') are displayed in each step. We can see the total intensity as a sum of the background part (grey) and the fluctuation part (red). Additionally, we can see the shape of the intensities above.

In the first step, the spatial averaging (elimination on temporal power fluctuations of the light source), normalizes the average intensity value to one. We can see that the ratio between the fluctuating and the background part does not change. What changes, however, is that the temporally shifted pixels have now the same background value. In the second step, the temporal averaging (elimination of the Gaussian beam profile), we normalize all pixels with the average Gaussian beam profile. By doing so, all background contributions are regulated to a constant value of one. On top only the fluctuation intensity remains, which can then be extracted.

6.7 Normalized A^c , q_{ro}^c illustrations

Fig. 6.6 is an alternative, normed illustration of fig. 4.30, where all known values of the concentration series (left) and the molar mass series (right) are normalized with their first values. These are on the left the associated roll-off values q_{ro}^c of the $M = 2.1$ kg/mol series and on the right of $c = 0.002$ g/g. Especially on the

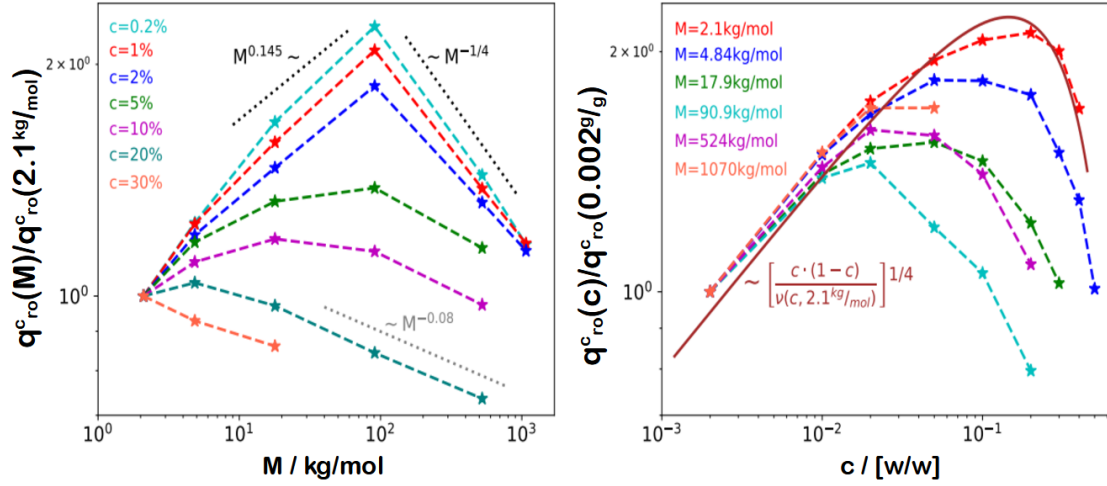


Fig. 6.6: Normed solutal roll-off values q_{ro}^c of fig. 4.30. On the left as a function of the molar mass M , on the right as a function of the concentration c . The values of both plots are normalized with their smallest variable value, which on the left $q_{ro}^c(2.1 \text{ kg/mol})$ and on the right $q_{ro}^c(0.002 \text{ g/g})$. The known proportionality of fig. 4.30 are shown with the dotted lines. In the right plot the additional dark red line is a fit of the in plot mentioned function and fits to the smallest molar mass a pure viscosity dependency.

left side, this type of presentation gives a sense of how the slope of the curves changes with increasing concentration. The right side shows that all curves follow a common $\sim c^2$ proportionality, but it is molar mass dependent when they deviate from the increasing process and start falling. In addition, in the right panel the solid dark red line shows a fit of the $M = 2.1$ kg/mol curve, which only includes the viscosity. For larger molar masses this very simple approximation becomes progressively inefficient, indicating that additional concentration and molar mass dependencies play a further role.

Similar to fig. 6.6 demonstrates fig. 6.7 a normed illustration of fig. 4.31, where again all known values of the concentration series (left) and the molar mass series (right) are normalized with their smallest values. The left figure is again a demonstration

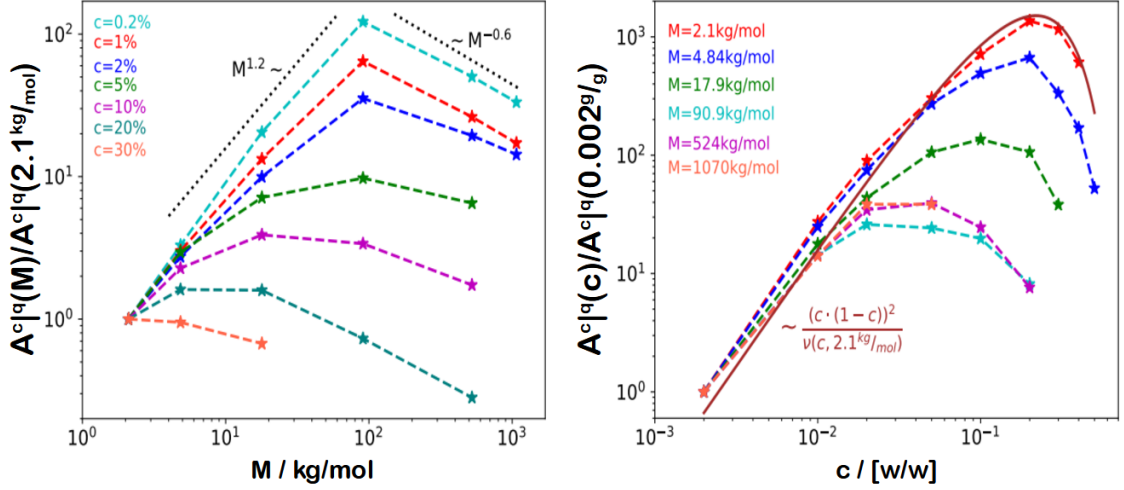


Fig. 6.7: Normed solutal NEF amplitudes A_{NE}^c of a certain $q = 367 \text{ cm}^{-1}$ value, known from fig. 4.31. On the left as a function of the molar mass M , on the right as a function of the concentration c . The values of both plots are normalized with their smallest variable value, which on the left $A^c|q(2.1 \text{ kg/mol})$ and on the right $A^c|q(0.002 \text{ g/g})$. The known proportionality of fig. 4.31 are shown with the dotted lines. In the right plot the additional dark red line is a fit of the in plot mentioned function and fits to the smallest molar mass a pure viscosity dependency.

of how the slope of the curves changes with increasing concentration. It is also interesting that the plots of this illustration are so similar to those of fig. 6.6, which shows the similarity of the underlying functions. These are the two equations 4.66 and 4.67, in which, except for the exponents, the quantities contained are the same. The right figure again contains a fit of the viscosity dependence for the $M = 2.1 \text{ kg/mol}$ curve, which fits the experimental progression nicely.

6.8 TDFRS measured simulation data

For the simulations we need a full set of thermal depended transport coefficients. Therefore *J. Kantelhardt* used our 'Thermal diffusion forced Rayleigh scattering' (TDFRS) setup, a multi-wavelength refractometer and an interferometer to measure these values. TDFRS is a heterodyne measurement technique, which allows to

T / K	$D(T)$ / $10^{-10}\text{m}^2/\text{s}$	$S_T(T)$ / 10^{-2}K^{-1}	$D_{th}(T)$ / $10^{-8}\text{m}^2/\text{s}$	$\left.\frac{\partial n}{\partial c}\right _{p,T}(T)$ / 10^{-1}	$\left.\frac{\partial n}{\partial T}\right _{p,c}(T)$ / 10^{-4}K^{-1}
283.15	2.0494	5.3126	8.75	0.9564	-5.6232
288.15	2.2463	5.0492	8.11	0.9673	-5.6287
293.15	2.4380	4.8045	7.43	0.9457	-5.6364
298.15	2.6063	4.5278	6.85	0.9936	-5.6461
303.15	2.8376	4.3876	6.53	0.9631	-5.6579
308.15	3.0026	4.3862	6.41	1.0291	-5.6719
313.15	3.2638	4.1437	6.16	0.9958	-5.6878
318.15	3.3834	4.0848	5.96	1.0214	-5.7060
323.15	3.7140	3.7270	5.78	1.0408	-5.7262

Tab. 6.1: Measured values of the important experimental quantities. Therefore $D(T)$, $S_T(T)$ and $D_{th}(T)$ is measured with TDFRS by *J. Kantelhardt*. The solutal contrast factor $\partial n/\partial c$ is measured with refractometer by *J. Kantelhardt* and the thermal contrast factor $\partial n/\partial T$ is measured with a temperature-ramp controlled interferometer by *J. Kantelhardt*. The used sample is $c_0 = 1\%$ polystyrene ($M = 4.84 \text{ kg/mol}$) in toluene.

measure Fickian and heat diffusion (D and D_{th}). In principle the technique works with two different laser beams, one which creates a holographic grating in the sample and a second which extracts the information under the Bragg-angle. The technique is explained in detail in [51]. For binary mixtures, the fit function

$$\zeta(t) = A_{th} \left\{ 1 - e^{-\frac{t}{\tau_{th}}} - A_{sol}(\tau_{sol} - \tau_{th})^{-1} \left[\tau_{sol} \left(1 - e^{-\frac{t}{\tau_{sol}}} \right) - \tau_{th} \left(1 - e^{-\frac{t}{\tau_{th}}} \right) \right] \right\} \quad (6.6)$$

yields two amplitudes (A_{sol} , A_{th}) and two relaxation times (τ_{sol} , τ_{th}) of the thermal ($i = th$) and solutal sample component ($i = sol$). From the relaxation times τ_i the associated diffusion coefficients D and D_{th} can be calculated as:

$$D_i = \frac{d^2}{4\pi^2\tau_i} . \quad (6.7)$$

Here d is the grating constant, which is measured and included directly in the experiment. Another important variable is the Soret-coefficient

$$S_T \equiv \frac{D_T}{D} = \frac{A \left[\frac{\partial n}{\partial T} \right]_{p,c}}{c_0(1 - c_0) \left[\frac{\partial n}{\partial c} \right]_{p,T}}, \quad (6.8)$$

the quotient of the thermodiffusion D_T and the diffusion coefficient D . Here the equilibrium concentration c_0 of the polymer component and the two contrast factors $\partial n/\partial c$ and $\partial n/\partial T$ are used. By measuring the refractive index $n(c)$ with a refractometer (multi-wavelengths, Anton Paar, Abbemat), for different concentrations and the derivation of the fitted linear function we can calculate $\partial n/\partial c$. Separately, a standard interferometer setup calculates from the increasing to decreasing temperature phase shift, the values of $\partial n/\partial T$.

6.9 List of transport coefficients

List of all measured transport coefficients. The first six [tables 6.2-6.7](#) show for a specific molar mass M (given in the caption), dependent on the polymer concentration c (rows), the related the diffusion (D), Soret (S_T) and thermodiffusion coefficients (D_T). Additionally, the last column demonstrates the $|S_T \Delta T|$ values. All shown experimental values are measured with the same temperature difference of $\Delta T = 50$ K between the upper and lower plate. The cell height remains therefore at a constant value of $h = 5$ mm. The last [tab. 6.8](#) demonstrates for each temperature difference ΔT the resulting transport coefficients of the thermal series. No error tolerance is given in the tables because it is difficult to determine and the dominant contribution is a systematic error. In generally, as an educated guess, 10% can be assumed.

The associated raw data for all of the measurements shown here, are available at: `'NAS/btpw33/Bayreuth/Setup24'` and `'NAS/btpw33/Messdaten'`. Furthermore, the evaluation files of the fitted parameters can be found in my home-directory (`'btpw33'`), under: `'~/DOC/Messungen/Bayreuth/Combi_Results'`.

Tab. 6.2: Measured with $\vec{\nabla}T_0 = 10^4\text{K/m}$. All value have an error of approximately 10%.

c [w/w]	$M = 2.1 \text{ kg/mol}$			
	D $10^{-10}\text{m}^2/\text{s}$	S_T 10^{-2}K^{-1}	D_T $10^{-11}\text{m}^2/\text{Ks}$	$ S_T\Delta T $
0.002	3.96	3.92	1.55	1.96
0.01	3.96	3.46	1.37	1.73
0.02	3.80	3.36	1.28	1.68
0.05	4.16	2.96	1.23	1.48
0.10	3.78	2.67	1.01	1.34
0.20	3.99	2.61	1.04	1.31
0.30	4.14	2.76	1.14	1.38
0.40	4.32	2.54	1.09	1.27

Tab. 6.3: Measured with $\vec{\nabla}T_0 = 10^4\text{K/m}$. All value have an error of approximately 10%.

c [w/w]	$M = 4.84 \text{ kg/mol}$			
	D $10^{-10}\text{m}^2/\text{s}$	S_T 10^{-2}K^{-1}	D_T $10^{-11}\text{m}^2/\text{Ks}$	$ S_T\Delta T $
0.002	2.09	6.01	1.45	3.07
0.01	2.13	5.82	1.45	3.07
0.02	2.32	5.22	1.54	2.93
0.05	2.24	4.57	1.15	2.28
0.10	2.28	3.99	0.98	1.91
0.20	2.63	3.73	1.08	1.85
0.30	2.77	3.34	1.05	1.68
0.40	2.92	2.92	0.98	1.46
0.50	3.11	2.49	0.89	1.25

Tab. 6.4: Measured with $\vec{\nabla}T_0 = 10^4\text{K/m}$. All value have an error of approximately 10%.

c [w/w]	$M = 17.9 \text{ kg/mol}$			
	D $10^{-10}\text{m}^2/\text{s}$	S_T 10^{-2}K^{-1}	D_T $10^{-11}\text{m}^2/\text{Ks}$	$ S_T\Delta T $
0.002	0.82	20.4	1.92	10.15
0.01	0.87	17.9	1.78	8.85
0.02	0.94	12.8	1.43	6.45
0.05	1.28	8.74	1.28	4.32
0.10	1.55	6.69	1.18	3.26
0.20	2.06	5.84	1.32	2.79
0.30	2.45	3.91	1.09	1.91

Tab. 6.5: Measured with $\vec{\nabla}T_0 = 10^4\text{K/m}$. All value have an error of approximately 10%.

c [w/w]	$M = 90.9\text{ kg/mol}$			
	D $10^{-10}\text{m}^2/\text{s}$	S_T 10^{-2}K^{-1}	D_T $10^{-11}\text{m}^2/\text{Ks}$	$ S_T\Delta T $
0.002	0.43	44.4	1.93	22.2
0.01	0.50	32.5	1.64	16.25
0.02	0.55	24.0	1.33	12.00
0.05	0.85	12.8	1.09	6.40
0.10	1.27	8.02	1.01	4.01
0.20	1.88	5.59	1.05	2.80

Tab. 6.6: Measured with $\vec{\nabla}T_0 = 10^4\text{K/m}$. All value have an error of approximately 10%.

c [w/w]	$M = 524\text{ kg/mol}$			
	D $10^{-10}\text{m}^2/\text{s}$	S_T 10^{-2}K^{-1}	D_T $10^{-11}\text{m}^2/\text{Ks}$	$ S_T\Delta T $
0.002	0.23	73.3	1.71	36.65
0.01	0.25	55.7	1.39	27.85
0.02	0.31	37.4	1.16	18.70
0.05	0.56	19.0	1.06	9.50
0.10	0.80	9.21	0.73	4.61
0.20	1.34	6.06	0.81	3.03

Tab. 6.7: Measured with $\vec{\nabla}T_0 = 10^4\text{K/m}$. All value have an error of approximately 10%.

c [w/w]	$M = 1070\text{ kg/mol}$			
	D $10^{-10}\text{m}^2/\text{s}$	S_T 10^{-2}K^{-1}	D_T $10^{-11}\text{m}^2/\text{Ks}$	$ S_T\Delta T $
0.002	0.20	81.5	1.60	40.75
0.01	0.23	62.4	1.44	31.20
0.02	0.27	41.7	1.14	20.85
0.05	0.45	21.4	0.97	10.70

Tab. 6.8: Thermal measurements of the mixture: $M = 17.9$ kg/mol, $c = 0.01$ [w/w]. All values have an error of approximately 10%.

ΔT	$\vec{\nabla}T_0$	D	S_T	D_T	$ S_T\Delta T $
in K	in K/m	in $10^{-10}\text{m}^2/\text{s}$	in 10^{-2}K^{-1}	in $10^{-11}\text{m}^2/\text{Ks}$	
5	$1 \cdot 10^3$	1.33	9.90	1.31	0.50
10	$2 \cdot 10^3$	1.30	9.85	1.29	0.99
20	$4 \cdot 10^3$	1.20	11.5	1.38	2.30
30	$6 \cdot 10^3$	1.11	14.9	1.65	4.47
40	$8 \cdot 10^3$	0.99	21.1	2.08	8.44
50	$10 \cdot 10^3$	0.87	27.2	2.38	13.6

List of figures

2.1	Brownian fluctuations.	6
2.2	Gaussian relaxation.	7
2.3	Sketch of the scattering vector.	7
2.4	Non-equilibrium state and fluctuation.	9
2.5	Combination of diffusive relaxation and sedimentation of a fluctuation.	10
2.6	Fourier transformation.	15
2.7	Fluctuation direction.	16
2.8	Correlation function and relaxation time of EF(without g).	21
2.9	Correlation function and relaxation time of NEF(without g).	23
2.10	Correlation function and relaxation time of EF(with g).	25
2.11	Total static structure factor.	28
2.12	2D comparison of the static and dynamic structure function.	29
2.13	3D structure function illustration.	30
3.1	Setup sketch.	32
3.2	3D sketch of the light path.	33
3.3	Illustration of the Kepler-telescope arrangement.	34
3.4	Illustration of the Soret-cell.	36
3.5	Image of the assembled inner cell.	37
3.6	Near field vs far field scattering.	39
3.7	Camera telescope.	40
3.8	Comparing plot of the q_{meas} and q_{real}	41
3.9	Measurements of the expansion coefficients.	44
3.10	Binary mixture of two glass formers.	45
3.11	Combination of the different interval times.	48
3.12	Illustration of the different interval times of real measurements.	49

3.13	3D illustration of the image preparation.	50
3.14	Windowing.	51
3.15	Splitting of the fluctuations due to the Fourier-transformation.	52
3.16	Time shift illustration.	53
3.17	Experimental and theoretical connection of the q -values.	55
3.18	Azimuthal averaging and anti-aliasing of the inverse pixel.	56
3.19	Real 3D structure function.	57
4.1	Temporal structure functions ($c = 0.02$ [w/w], $M = 90.9$ kg/mol, $\Delta T = 50$ K).	61
4.2	Relaxation dynamics ($c = 0.02$ [w/w], $M = 90.9$ kg/mol, $\Delta T = 50$ K).	62
4.3	Static structure factor ($c = 0.02$ [w/w], $M = 90.9$ kg/mol, $\Delta T = 50$ K).	63
4.4	Relaxation times and structure function of first paper.	66
4.5	Multi-exponential simulated correlation functions of all layers.	68
4.6	Thermal dependencies of the simulated transport properties.	69
4.7	Thermal dependencies of β_i , ν and ρ	72
4.8	Cell profiles $T(z)$, $c(z)$ and cell gradients $\vec{\nabla}T(z)$, $\vec{\nabla}c(z)$	76
4.9	Simulated relaxation times and structure functions of all layers.	80
4.10	Simulated relaxation times and structure functions of all layers.	82
4.11	Evaluation of the simulated correlation functions.	83
4.12	Evaluated relaxation times of the simulation.	85
4.13	Evaluated NEF structure functions of the simulation.	86
4.14	Comparison of the simulated $\tau(q)$ and actual measurements.	88
4.15	Comparison of the simulated $S(q)$ and actual measurements.	89
4.16	Comparison of the simulated and experimental $D(\Delta T)$ and $S_T(\Delta T)$ values.	90
4.17	Comparison of the simulated and experimental $D_T(\Delta T)$ and $D_{th}(\Delta T)$ values.	91
4.18	Comparison of the simulated and experimental $D(c)$ and $S_T(c)$ values.	92
4.19	$T(z)$, $c(z)$ of the 'total' simulation and the 'constant' simulation.	95
4.20	Comparison of $C_i(q, \Delta t, z)$ of the 'total' simulation and the 'constant' simulation.	96

4.21	Comparison of $S_i(q, z)$ of the 'total' simulation and the 'constant' simulation.	97
4.22	Comparison of $\tau_i(q, z)$ of the 'total' simulation and the 'constant' simulation.	98
4.23	Combi-illustration of the two simulated and the experimental $D(\Delta T)$ and $D_{th}(\Delta T)$ values.	99
4.24	Combi-illustration of the two simulated and the experimental $D(\Delta T)$ and $S_T(\Delta T)$ values.	100
4.25	Structure function sketch.	101
4.26	Thermal series of the total structure function.	104
4.27	Slope coefficients $a(q)$ of the amplitudes.	105
4.28	Thermal progression of the roll-off and cut-off values.	106
4.29	Molar mass and concentration series of the structure functions.	109
4.30	Solutal analysis of the q roll-off values.	110
4.31	Solutal analysis of the NEF amplitudes.	114
4.32	Solutal analysis of the scale laws of the c, M limits.	117
4.33	Illustration of all simulated thermal dependencies of D	123
4.34	Illustration of all simulated thermal dependencies of S_T	124
4.35	Illustration of all $ S_T \Delta T (\Delta T)$	125
4.36	$S_T(\Delta T)$ curve progression phase diagram.	126
4.37	Illustration of all simulated thermal dependencies of D_T	127
4.38	Illustration of all experimental concentration series of D	129
4.39	Illustration of all experimental concentration series of S_T	131
4.40	Illustration of all experimental concentration series of D_T	132
4.41	Illustration of all experimental molar mass series of D	134
4.42	Illustration of all experimental molar mass series of S_T	136
4.43	Illustration of all experimental molar mass series of D_T	137
6.1	Cell sealing.	144
6.2	Horizontal cell alignment.	145
6.3	Cam mirror alignment.	146
6.4	Cam Telescope scale control.	147
6.5	Spatial and temporal normalization of several pixels.	148

6.6	Normed solutal analysis of the q roll-off values.	149
6.7	Normed solutal analysis of the NEF amplitudes.	150

List of tables

2.1	Onsager Coefficients.	18
2.2	Correlation function amplitudes of EF (without g).	21
2.3	Correlation function amplitudes of NEF (without g).	23
2.4	Correlation function amplitudes of NEF (with g).	25
3.1	Pure components of the binary mixtures.	43
3.2	List of all mixtures.	43
4.1	Comparison of the experimental results of $c = 0.02$ [w/w], $M = 90.9$ kg/mol.	64
4.3	Breakdown of fig. 4.8.	77
4.4	Comparison of the experimental results of $c = 0.02$ [w/w], $M = 90.9$ kg/mol with the simulation.	93
4.5	Constant parameter of the 'constant' simulation.	94
4.6	Overview of all simulated samples.	120
4.7	Overview of all experimental samples, measured with $\Delta T = 50$ K.	121
4.8	Thermal experimental series.	121
6.1	TDFRS data of $c_0 = 1\%$, $M = 4.84$ kg/mol.	151
6.2	Measured with $\vec{\nabla}T_0 = 10^4$ K/m. All value have an error of approximately 10%.	153
6.3	Measured with $\vec{\nabla}T_0 = 10^4$ K/m. All value have an error of approximately 10%.	153
6.4	Measured with $\vec{\nabla}T_0 = 10^4$ K/m. All value have an error of approximately 10%.	153
6.5	Measured with $\vec{\nabla}T_0 = 10^4$ K/m. All value have an error of approximately 10%.	154

6.6	Measured with $\vec{\nabla}T_0 = 10^4\text{K/m}$. All value have an error of approximately 10%.	154
6.7	Measured with $\vec{\nabla}T_0 = 10^4\text{K/m}$. All value have an error of approximately 10%.	154
6.8	Thermal measurements of the mixture: $M = 17.9\text{kg/mol}$, $c = 0.01$ [w/w]. All value have an error of approximately 10%.	155

Bibliography

- [1] Helmut R Brand. Was interessiert den physiker heute an fluiden? *Physikalische Blätter*, 47(11):983–989, 1991.
- [2] JM Ortiz de Zárate, R Pérez Cordón, and JV Sengers. Finite-size effects on fluctuations in a fluid out of thermal equilibrium. *Physica A: Statistical Mechanics and its Applications*, 291(1-4):113–130, 2001.
- [3] Alberto Vailati and Marzio Giglio. q divergence of nonequilibrium fluctuations and its gravity-induced frustration in a temperature stressed liquid mixture. *Physical review letters*, 77(8):1484, 1996.
- [4] Fabrizio Croccolo, Cédric Giraudet, Henri Bataller, Roberto Cerbino, and Alberto Vailati. Shadowgraph analysis of non-equilibrium fluctuations for measuring transport properties in microgravity in the gradflex experiment. *Microgravity Science and Technology*, 28(4):467–475, 2016.
- [5] W Wu, JH Jander, MH Rausch, AP Fröba, and C Giraudet. Simultaneous determination of multiple transport properties over a wide range of temperatures and pressures from the analysis of non-equilibrium fluctuations by the shadowgraph method. *The Journal of Chemical Physics*, 153(14):144201, 2020.
- [6] Fabrizio Croccolo, Henri Bataller, and Frank Scheffold. A light scattering study of non equilibrium fluctuations in liquid mixtures to measure the soret and mass diffusion coefficient. *The Journal of chemical physics*, 137(23):234202, 2012.
- [7] Fabrizio Croccolo, Frank Scheffold, and Henri Bataller. Mass transport properties of the tetrahydronaphthalene/n-dodecane mixture measured by investigating non-equilibrium fluctuations. *Comptes Rendus Mécanique*, 341(4-5): 378–385, 2013.

- [8] Ion Lizarraga, Cédric Giraudet, Fabrizio Croccolo, M Mounir Bou-Ali, and Henri Bataller. Mass diffusion and thermal diffusivity of the decane-pentane mixture under high pressure as a ground-based study for scco project. *Microgravity Science and Technology*, 28(5):545–552, 2016.
- [9] Henri Bataller, Thomas Triller, Bastian Pur, Werner Köhler, José Maria Ortiz de Zárate, and Fabrizio Croccolo. Dynamic analysis of the light scattered by the non-equilibrium fluctuations of a ternary mixture of polystyrene-toluene-hexane. *The European Physical Journal E*, 40(3):1–10, 2017.
- [10] Gerhard Wittko and Werner Köhler. Precise determination of the soret, thermal diffusion and mass diffusion coefficients of binary mixtures of dodecane, isobutylbenzene and 1, 2, 3, 4-tetrahydronaphthalene by a holographic grating technique. *Philosophical Magazine*, 83(17-18):1973–1987, 2003.
- [11] Werner Köhler and P Rossmanith. Aspects of thermal diffusion forced rayleigh scattering: Heterodyne detection, active phase tracking, and experimental constraints. *The Journal of Physical Chemistry*, 99(16):5838–5847, 1995.
- [12] Simone Wiegand, Hui Ning, and Hartmut Kriegs. Thermal diffusion forced rayleigh scattering setup optimized for aqueous mixtures. *The Journal of Physical Chemistry B*, 111(51):14169–14174, 2007.
- [13] M Giglio and A Vendramini. Soret-type motion of macromolecules in solution. *Physical Review Letters*, 38(1):26, 1977.
- [14] Roberto Piazza and Andrea Guarino. Soret effect in interacting micellar solutions. *Physical review letters*, 88(20):208302, 2002.
- [15] Andreas Königer, Börn Meier, and Werner Köhler. Measurement of the soret, diffusion, and thermal diffusion coefficients of three binary organic benchmark mixtures and of ethanol–water mixtures using a beam deflection technique. *Philosophical Magazine*, 89(10):907–923, 2009.
- [16] D Bedeaux and P Mazur. Brownian motion and fluctuating hydrodynamics. *Physica*, 76(2):247–258, 1974.
- [17] OP Singh and J Srinivasan. Effect of rayleigh numbers on the evolution of double-diffusive salt fingers. *Physics of Fluids*, 26(6):062104, 2014.
- [18] EH Hauge and A Martin-Löf. Fluctuating hydrodynamics and brownian motion. *Journal of Statistical Physics*, 7(3):259–281, 1973.

-
- [19] Ilja N Bronstein, Juraj Hromkovic, Bernd Luderer, Hans-Rudolf Schwarz, Jochen Blath, Alexander Schied, Stephan Dempe, Gert Wanka, and Siegfried Gottwald. *Taschenbuch der mathematik*, volume 1. Springer-Verlag, 2012.
- [20] HN Ritland. Relation between refractive index and density of a glass at constant temperature. *Journal of the American Ceramic Society*, 38(2):86–88, 1955.
- [21] Hermann Haken and Hans Christoph Wolf. *The physics of atoms and quanta: introduction to experiments and theory*, volume 1439. Springer Science & Business Media, 2005.
- [22] ED Eastman. Theory of the soiret effect. *Journal of the American Chemical Society*, 50(2):283–291, 1928.
- [23] John Stewart Turner and John Stewart Turner. *Buoyancy effects in fluids*. Cambridge university press, 1979.
- [24] Cédric Giraudet, Henri Bataller, Yifei Sun, Aleksandar Donev, José María Ortiz De Zárate, and Fabrizio Croccolo. Slowing-down of non-equilibrium concentration fluctuations in confinement. *EPL (Europhysics Letters)*, 111(6):60013, 2015.
- [25] BM Law and JC Nieuwoudt. Noncritical liquid mixtures far from equilibrium: the rayleigh line. *Physical Review A*, 40(7):3880, 1989.
- [26] Cx K Batchelor and GK Batchelor. *An introduction to fluid dynamics*. Cambridge university press, 2000.
- [27] Peter Constantin and Ciprian Foias. *Navier-stokes equations*. University of Chicago Press, 1988.
- [28] Franco Bassani. *Encyclopedia of condensed matter physics*. Elsevier acad. press, 2005.
- [29] Don S Lemons. *A student's guide to entropy*. Cambridge University Press, 2013.
- [30] Gerd Wedler and Hans-Joachim Freund. *Lehrbuch der physikalischen Chemie*, volume 1. John Wiley & Sons, 2012.
- [31] John Crank. *The mathematics of diffusion*. Oxford university press, 1979.

- [32] Kiyoshi Maruyama. Mass flux density, momentum, and flow velocity. 2015.
- [33] Lawrence C Evans. Partial differential equations. *Graduate studies in mathematics*, 19(2), 1998.
- [34] Herbert B Callen. Thermodynamics and an introduction to thermostatistics, 1998.
- [35] Martin Baily. *A survey of thermodynamics*. AIP, 1994.
- [36] Marianne Hartung. *A detailed treatment of the measurement of transport coefficients in transient grating experiments*. PhD thesis, 2007.
- [37] Nicolas Garnier and Sergio Ciliberto. Nonequilibrium fluctuations in a resistor. *Physical Review E*, 71(6):060101, 2005.
- [38] Dilip Kondepudi and Ilya Prigogine. *Modern thermodynamics: from heat engines to dissipative structures*. John Wiley & Sons, 2014.
- [39] Alberto Vailati and Marzio Giglio. Nonequilibrium fluctuations in time-dependent diffusion processes. *Physical Review E*, 58(4):4361, 1998.
- [40] H Fischer and H Kaul. *Mathematik für physiker-band 2: Gewöhnliche und partielle differentialgleichungen, mathematische grundlagen der quantenmechanik. 2. Auflage, Teubner, 2004.*
- [41] Gregory L Eyink and Katepalli R Sreenivasan. Onsager and the theory of hydrodynamic turbulence. *Reviews of modern physics*, 78(1):87, 2006.
- [42] H Eugene Stanley and Guenter Ahlers. Introduction to phase transitions and critical phenomena. *Physics Today*, 26(1):71, 1973.
- [43] Henri Bataller, Cédric Giraudet, Fabrizio Croccolo, and José Maria Ortiz De Zárate. Analysis of non-equilibrium fluctuations in a ternary liquid mixture. *Microgravity Science and Technology*, 28(6):611–619, 2016.
- [44] Cédric Giraudet, Henri Bataller, and Fabrizio Croccolo. High-pressure mass transport properties measured by dynamic near-field scattering of non-equilibrium fluctuations. *The European Physical Journal E*, 37(11):1–7, 2014.
- [45] Fabrizio Croccolo, JM Ortiz de Zarate, and JV Sengers. Non-local fluctuation phenomena in liquids. *The European Physical Journal E*, 39(12):1–12, 2016.

-
- [46] PN Segre, RW Gammon, and JV Sengers. Light-scattering measurements of nonequilibrium fluctuations in a liquid mixture. *Physical Review E*, 47(2):1026, 1993.
- [47] D Zapf and W Köhler. Thermal and solutal non-equilibrium fluctuations in a polymer solution. *The Journal of Chemical Physics*, 153(22):224902, 2020.
- [48] EO Schulz-DuBois and I Rehberg. Structure function in lieu of correlation function. *Applied Physics A*, 24(4):323–329, 1981.
- [49] Gary S Settles. *Schlieren and shadowgraph techniques: visualizing phenomena in transparent media*. Springer Science & Business Media, 2001.
- [50] Matthias Gebhardt and Werner Köhler. What can be learned from optical two-color diffusion and thermodiffusion experiments on ternary fluid mixtures? *The Journal of chemical physics*, 142(8):084506, 2015.
- [51] Werner Köhler and R Schäfer. Polymer analysis by thermal-diffusion forced rayleigh scattering. *New Developments in Polymer Analytics II*, pages 1–59, 2000.
- [52] Clayton A Gearhart. Specific heats and the equipartition law in introductory textbooks. *American Journal of Physics*, 64(8):995–1000, 1996.
- [53] Zhong Lin Wang. *Nanowires and nanobelts: materials, properties and devices. Volume 1: Metal and Semiconductor Nanowires*. Springer Science & Business Media, 2013.
- [54] Dorian Brogioli, Alberto Vailati, and Marzio Giglio. Heterodyne near-field scattering. *Applied physics letters*, 81(22):4109–4111, 2002.
- [55] Steven P Trainoff and David S Cannell. Physical optics treatment of the shadowgraph. *Physics of Fluids*, 14(4):1340–1363, 2002.
- [56] Fabrizio Crocco, Dorian Brogioli, Alberto Vailati, Marzio Giglio, and David S Cannell. Effect of gravity on the dynamics of nonequilibrium fluctuations in a free-diffusion experiment. *Annals of the New York Academy of Sciences*, 1077(1):365–379, 2006.
- [57] Gert Strobl. *Physik kondensierter Materie: Kristalle, Flüssigkeiten, Flüssigkristalle und Polymere*. Springer-Verlag, 2013.

- [58] Thomas G Fox. Influence of diluent and of copolymer composition on the glass temperature of a poly-mer system. *Bull. Am. Phys. Soc.*, 1:123, 1956.
- [59] Manfred Gordon and James S Taylor. Ideal copolymers and the second-order transitions of synthetic rubbers. i. non-crystalline copolymers. *Journal of Applied Chemistry*, 2(9):493–500, 1952.
- [60] Lindong Weng, Ranganathan Vijayaraghavan, Douglas R MacFarlane, and Gloria D Elliott. Application of the kwei equation to model the tg behavior of binary blends of sugars and salts. *Cryobiology*, 68(1):155–158, 2014.
- [61] Thomas Körber. *Relaxation behavior of pure and binary glass formers—studied by Dielectric and NMR spectroscopy*. PhD thesis, 2022.
- [62] Florian Schwaiger, Walter Zimmermann, and Werner Köhler. Transient cage formation around hot gold colloids dispersed in polymer solutions. *The Journal of chemical physics*, 135(22):224905, 2011.
- [63] Fabio Giavazzi, Dorian Brogioli, Veronique Trappe, Tommaso Bellini, and Roberto Cerbino. Scattering information obtained by optical microscopy: differential dynamic microscopy and beyond. *Physical Review E*, 80(3):031403, 2009.
- [64] Prajoy Podder, Tanvir Zaman Khan, Mamdudul Haque Khan, and M Muk-tadir Rahman. Comparative performance analysis of hamming, hanning and blackman window. *International Journal of Computer Applications*, 96(18), 2014.
- [65] Adolf W Lohmann and DE Silva. An interferometer based on the talbot effect. *Optics Communications*, 2(9):413–415, 1971.
- [66] Fabrizio Croccolo, Henri Bataller, and Frank Scheffold. Static versus dynamic analysis of the influence of gravity on concentration non-equilibrium fluctuations. *The European Physical Journal E*, 37(11):1–5, 2014.
- [67] Florian Schwaiger and Werner Köhler. Ueber lasergeheizte kolloidale goldnanopartikel in polymerlösungen. *Universitaet Bayreuth*, 1(1):104, 2013.
- [68] Jürgen Rauch and Werner Köhler. Collective and thermal diffusion in dilute, semidilute, and concentrated solutions of polystyrene in toluene. *The Journal of chemical physics*, 119(22):11977–11988, 2003.

-
- [69] Stefano Mazzoni, Roberto Cerbino, Alberto Vailati, and Marzio Giglio. Fluctuations in diffusion processes in microgravity. *Annals of the New York Academy of Sciences*, 1077(1):351–364, 2006.
- [70] Daniel Zapf, Jannik Kantelhardt, and Werner Köhler. Nonlinearities in shadowgraphy experiments on non-equilibrium fluctuations in polymer solutions. *The European Physical Journal E*, 45(4):1–11, 2022.
- [71] Florian Schwaiger. Ueber lasergeheizte kolloidale goldnanopartikel in polymerlösungen. *Universitaet Bayreuth*, 1(1):147, 1981.
- [72] Jürgen Rauch and Werner Köhler. Diffusion and thermal diffusion of semidilute to concentrated solutions of polystyrene in toluene in the vicinity of the glass transition. *Physical review letters*, 88(18):185901, 2002.
- [73] H Kashiwagi, T Hashimoto, Y Tanaka, H Kubota, and T Makita. Thermal conductivity and density of toluene in the temperature range 273–373 k at pressures up to 250 mpa. *International Journal of Thermophysics*, 3(3):201–215, 1982.
- [74] S Matsuoka and MK Cowman. Equation of state for polymer solution. *Polymer*, 43(12):3447–3453, 2002.
- [75] Fernando JV Santos, Carlos A Nieto de Castro, John H Dymond, Natassa K Dalaouti, Marc J Assael, and Akira Nagashima. Standard reference data for the viscosity of toluene. *Journal of physical and chemical reference data*, 35(1):1–8, 2006.
- [76] Herman L Wagner. The mark–houwink–sakurada equation for the viscosity of linear polyethylene. *Journal of physical and chemical reference data*, 14(2):611–617, 1985.
- [77] Rainer Braun. *Experimentelle Bestimmung der Wärmeleitfähigkeit von Flüssigkeiten mit einem konvektionsfreien Verfahren unter Berücksichtigung der thermischen Strahlung*. PhD thesis, 1980.
- [78] Brian Higgins. Heat conduction with variable thermal conductivity. 05 2021. doi: 10.13140/RG.2.2.17178.36805.
- [79] Andrei D Polyenin. *Handbook of linear partial differential equations for engineers and scientists*. Chapman and hall/crc, 2001.

- [80] Cédric Giraudet, Henri Bataller, Yifei Sun, Aleksandar Donev, José M Ortiz de Zárate, and Fabrizio Croccolo. Confinement effect on the dynamics of non-equilibrium concentration fluctuations far from the onset of convection. *The European Physical Journal E*, 39(12):1–13, 2016.
- [81] Paul J Flory. *Principles of polymer chemistry*. Cornell University Press, 1953.
- [82] KJ Zhang, ME Briggs, RW Gammon, JV Sengers, and Jack F Douglas. Thermal and mass diffusion in a semidilute good solvent-polymer solution. *The Journal of chemical physics*, 111(5):2270–2282, 1999.
- [83] Matthias Gebhardt, Werner Köhler, Aliaksandr Mialdun, Viktor Yasnou, and Valentina Shevtsova. Diffusion, thermal diffusion, and soret coefficients and optical contrast factors of the binary mixtures of dodecane, isobutylbenzene, and 1, 2, 3, 4-tetrahydronaphthalene. *The Journal of chemical physics*, 138(11):114503, 2013.
- [84] Steffan Puwal, Bradley J Roth, and Peter J Basser. Heterogeneous anisotropic magnetic susceptibility of the myelin-water layers causes local magnetic field perturbations in axons. *NMR in Biomedicine*, 30(4):e3628, 2017.
- [85] José M Ortiz de Zárate, Cédric Giraudet, Henri Bataller, and Fabrizio Croccolo. Non-equilibrium fluctuations induced by the soret effect in a ternary mixture. *The European Physical Journal E*, 37(8):1–7, 2014.
- [86] L García-Fernández, P Fruton, Henri Bataller, JM Ortiz de Zárate, and Fabrizio Croccolo. Coupled non-equilibrium fluctuations in a polymeric ternary mixture. *The European Physical Journal E*, 42(9):1–13, 2019.
- [87] M Braibanti, P-A Artola, P Baaske, Henri Bataller, J-P Bazile, MM Bou-Ali, DS Cannell, M Carpineti, R Cerbino, F Croccolo, et al. European space agency experiments on thermodiffusion of fluid mixtures in space. *The European Physical Journal E*, 42(7):1–11, 2019.
- [88] Alberto Vailati, Philipp Baaske, Henri Bataller, Serena Bolis, Marco Braibanti, Marina Carpineti, Roberto Cerbino, Fabrizio Croccolo, Jean-Luc Dewandel, Aleksandar Donev, et al. Giant fluctuations induced by thermal diffusion in complex liquids. *Microgravity science and technology*, 32(5):873–887, 2020.

- [89] Michael Orlishausen, Lorenz Butzhammer, Daniel Schlotbohm, Daniel Zapf, and Werner Köhler. Particle accumulation and depletion in a microfluidic marangoni flow. *Soft matter*, 13(39):7053–7060, 2017.

7 List of publications

Directly related publications

- Zapf and Köhler. Thermal and solutal non-equilibrium fluctuations in a polymer solution. *The Journal of Chemical Physics* 153(22):224902, 2020
- Zapf, Kantelhardt, and Köhler. Non linearities in shadowgraphy experiments on non-equilibrium fluctuations in polymer solutions. *The European Physical Journal E*, Submitted, 2022
- Braibanti, Artola, Baaske, Bataller, Bazile, Bou-Ali, Cannell, Carpineti, Cerbino, Croccolo, et al.. European Space Agency experiments on thermodiffusion of fluid mixtures in space. *The European Physical Journal E*, 42(7):1-11, 2019
- Vailati, Baaske, Bataller, Bolis, Braibanti, Carpineti, Cerbino, Croccolo, Dewandel, Donev, et al.. Giant Fluctuations Induced by Thermal Diffusion in Complex Liquids. *Microgravity science and technology*, 32(5):873-887, 2020

Further publication

- Orlishausen, Butzhammer, Schlotbohm, Zapf, and Köhler. Particle accumulation and depletion in a microfluidic Marangoni flow. *Soft matter*, 13(39):7053–7060, 2017

Danksagung

Viele Menschen haben mich in meinem Studium und den letzten Jahren der Promotion auf unterschiedlichste Weise unterstützt. Einigen Auserwählten möchte ich mit den nächsten Zeilen besonders danken.

Beginnen möchte ich mit Professor Dr. Werner Köhler, der mir nach meiner Bachelor- und Masterarbeit ebenfalls die Möglichkeit der Promotion in seiner Arbeitsgruppe bot. Seine stets freundliche und hilfsbereite Art hilft ungemein, in ungezwungenen, konstruktiven und zielführenden Gesprächen, die Arbeit zu lenken und voran treiben.

Anschließend gilt mein Dank Herren Professor Dr. Lothar Kador für seine Zweitkorrektur dieser langen und sehr spezialisierten Arbeit. Ebenfalls danke ich den beteiligten Wissenschaftler des Giant-Fluctuation Projekts, der ESA und des verbundenen BT-Giant Projekts, des DLR. Unter Ihnen besonders Prof. Alberto Vailati und Dr. Marina Carpineti, der Università degli Studi di Milano, wie auch Prof. Fabrizio Croccolo und Prof. Henri Bataller, der Université de Pau et des Pays de l'Adour.

Ganz besonders am Herzen liegt mir der Dank an meine Eltern und meiner Familie, selbst in den unruhigen Phasen bietet die Familie einen unumstößlichen Anker an dem man sich immer wieder hochziehen kann und auf deren Hilfe immer Verlass ist. Gleiches gilt für meine guten Freunde Jan Christian 'Chrischan' Glauber und Dr. Kevin 'Diggerle' Wilma. Sie darf ich schon lange meine besten Freunde nennen. Ohne euch wäre mein Studium und die Promotion nicht das Gleiche Erlebnis gewesen. Zuletzt gilt mein größter Dank meiner Theresa. Du bist mein Fels in der Brandung, meine große Liebe und meine baldige Frau. Wir kennen uns schon viele Jahre und ohne dich wäre mein Leben nicht das Gleiche. Du hast mir in den stressigen Zeiten liebevoll zur Seite gestanden und war der Tag noch so kompliziert oder nervenaufreibend, wusste ich immer du wartest auf mich mit einem Lächeln. Dafür und noch für soviel mehr, möchte ich dir nochmals von Herzen danken.

Eidesstattliche Erklärung

Hiermit versichere ich, Daniel Zapf, an Eides statt, dass ich die vorliegende Arbeit selbstständig verfasst und keine anderen als die angegebenen Quellen und Hilfsmittel verwendet habe.

Weiterhin erkläre ich, dass ich die Hilfe von gewerblichen Promotionsberatern bzw.- vermittlern oder ähnlichen Dienstleistern weder bisher in Anspruch genommen habe, noch künftig in Anspruch nehmen werde.

Zusätzlich erkläre ich hiermit, dass ich keinerlei frühere Promotionsversuche unternommen habe.

Bayreuth, den

.....
Daniel Zapf